Regional-Scale Coseismic Landslide Hazard Modeling and Consequence Analysis

alex grant

A dissertation

submitted in partial fulfillment of the

requirements for the degree of

Doctor of Philosophy

University of Washington

2017

Reading Committee:

Joseph Wartman, Chair

Alison Duvall

Arthur Frankel

Program Authorized to Offer Degree:

Civil and Environmental Engineering

University of Washington

Abstract

Regional-Scale Coseismic Landslide Hazard Modeling and Consequence Analysis

alex grant

Chair of the Supervisory Committee:

Professor Joseph Wartman

Department of Civil and Environmental Engineering

Earthquake-induced, or *coseismic*, landslides occur in great number during moderate to large (>M5) earthquakes. These landslides typically occur across regions spanning hundreds to thousands of square kilometers. The widespread geographic distribution of coseismic landslides makes them, by definition, regional-scale events. Current regional-scale landslide hazard analyses are typically based solely on the analysis of shallow translational landslides, neglecting many mechanistically-diverse types of landslides triggered by earthquakes that have historically driven coseismic-losses. Existing landslide hazard models are then difficult to translate into coseismic landslide risk, the likelihood of loss of life or property due to such a landslide, as the modeled landslide is not representative of many observed landslides, and virtually no quantitative data on the consequences and vulnerability of structures are available for landslides.

Here a new multi-modal framework for coseismic landslide hazard analysis is presented. Coseismic landslide hazard is developed from multiple, distinct, types of landslides to explicitly account for differences in failure mechanism, susceptible terrain, and consequences of each landslide. This work improves regional-scale coseismic landslide hazard and consequence analyses by developing mode-based hazard analyses to explicitly account for mechanistic differences in coseismic landslides and developing unique mode-specific landslide consequence data. These advances in modeling and knowledge of coseismic landslide consequences, paired with an assessment of the effect of anthropogenic modification on landslide susceptibility, provide a greatly improved framework in which coseismic landslide risk can be quantitatively assessed. Improved quantitative risk analyses will better enable mitigation strategies and

decisions to be made to protect individuals, communities, and the built environment from future coseismic landslide losses.

The multi-modal framework was developed to compute coseismic landslide hazard for Lebanon considering four landslide modes with unique source regions, failure mechanisms, and implications to human and economic risk. Coseismic landslide hazard was computed for 10% in 50-year probabilistic seismic hazard peak ground accelerations, as well as historic scenario earthquakes, to assess the model's ability to match field observations of historic landslide activity and mapped coseismic landslides. High-quality empirical data on the physical consequences of coseismic rock impacts to residential dwellings is presented from the 2010-2011 Canterbury earthquake sequence. These quantitative measures of rock impacts are a critical missing piece in the analysis of quantitative risk assessment, and provide a foundation for life-safety decision-making anywhere residential homes are exposed to falling rock.

Landslides triggered by the 2011 M9.0 Tohoku, Japan earthquake were mapped and analyzed to assess the role of topographic, climatic, anthropogenic, and ground motion parameters in the initiation of different landslide failure modes as well as the consequences to the built environment caused by each landslide type. A physically-based framework, based on a common simplified landslide initiation model, was found to describe the observed concentrations of landslides triggered by the Tohoku earthquake, whereas commonly-held explanatory metrics such as peak ground acceleration did not. Anthropogenic modification was found to significantly alter expected material strengths, and landslide susceptibility to failure, for debris slides triggered by the Tohoku earthquake. 42% of all Tohoku-triggered landslides impacted the built environment, destroying roadways and structures, and causing significant economic losses. 67% of all Tohoku-triggered landslides occurred in anthropogenically modified hillslopes. These data suggest many of the risks associated with large magnitude subduction zone earthquake-induced landslides may be of our own design, threatening many aggressively developed regions with decreased slope resistance to landslides and increased potential for loss. Probabilistic coseismic landslide hazard analyses are presented for Seattle, Washington based on a suite of 30 synthetic M9.0 Cascadia Subduction Zone earthquakes, the 2001 M6.8 Nisqually earthquake, and a scenario M7.0 synthetic Seattle Fault earthquake. A simplified 475-year return period probabilistic coseismic landslide hazard analysis, combining multiple sources of seismicity, was then developed for Seattle. The multi-modal coseismic landslide hazard analysis, combined with probabilistic estimates of material strength and ground shaking and empirical ground saturation data, is presented as a state-of-the-art regional-scale coseismic landslide hazard analysis, and as a basis for future analyses assessing Cascadia Subduction Zone coseismic landslide hazard across the Pacific Northwest.

TABLE OF CONTENTS

LIST OF FIGURES

LIST OF TABLES

DEDICATION

for Doris

INTRODUCTION

Coseismic landslides occur in great number during moderate to large (>M5) earthquakes (Keefer, 2002; Xu et al., 2014; Havenith et al., 2016). Earthquake-induced landslides (hereafter coseismic landslides) are frequently the most damaging secondary hazard following an earthquake (Kramer, 1996). For example, more than 1000 landslides triggered by the M9.0 Tohoku, Japan earthquake impacted roadways, buildings, and the built environment (Chapter 2), and rockfalls and debris avalanches triggered by earthquakes during the 2010-2011 Canterbury earthquake sequence killed five people and impacted 200 homes (Dellow et al., 2011). Observed losses to life and property caused by coseismic landslides, and the potential for many more future landslides to impact exposed populations and infrastructure, motivates the need for high-quality quantitative risk analyses over a regional-scale of hundreds to thousands of square kilometers that can be affected by coseismic landslides (Keefer, 1984). Quantitative risk analyses, the annualized likelihood of loss of life or property due to such landslides, enable informed mitigation strategies to protect against loss of life, damage to buildings and infrastructure, and disruption of society. Quantitative risk analyses rely on two fundamental sources of information: an analysis of hazard and of the resulting consequences on an element at risk.

Current regional-scale hazard analyses consider a single type of landslide failure to compute coseismic landslide hazard estimates for a single shaking intensity input. Landslide consequences are typically adopted from heuristic estimates based on little available data. Taken together, current methodologies for coseismic landslide hazard assessment and consequence data on a regional-scale make quantitative risk analyses nearly impossible, or highly approximate, producing instead *qualitative* risk assessments.

To facilitate future regional-scale quantitative risk assessment of potential losses due to diverse modes of coseismic landslides, I developed and implemented a multi-modal coseismic landslide analysis framework, as well as quantitative landslide consequence data.

In Chapter 1, a multi-modal analysis procedure for coseismic landslides is developed and applied to the country of Lebanon. First, susceptibility to each landslide mode was evaluated based on topography and historical observations of portions of the landscape susceptible to different coseismic landslide types. Second, coseismic landslide hazards were assessed using mode-specific geotechnical models within each susceptible region based on peak ground accelerations for a 10% in 50-years exceedance level, as well as two historic scenario earthquakes in which severe damages were recorded.

In Chapter 2, the multi-modal concept for coseismic landslide evaluation is expanded to assess the causal factors and consequences of landslides triggered by the 2011 M9.0 Tohoku, Japan earthquake. Two parallel analyses of the developed Tohoku landslide dataset were conducted. First, the patterns of observed coseismic landslides with respect to potential causal factors (e.g. topographic slope, lithology, peak ground velocity) are assessed based on the remapping and reclassification of landslides triggered by the Tohoku earthquake. A physically-based relationship between driving and resisting forces to landslide triggering is proposed as a means to explain the distribution of all landslide types triggered by the Tohoku earthquake, and then is verified against a second coseismic landslide inventory from the M6.6 2011 Iwaki earthquake. Second, the qualitative and quantitative effects of anthropogenic modification on landslide susceptibility and triggering for debris slides triggered by the Tohoku earthquake are assessed. Coseismic landslides

were mapped based on mechanistic differences between types, considering landslides originating in both natural and modified terrain, and cataloging landslide impacts to the built environment.

In Chapter 3, the multi-modal analysis framework is refined and implemented probabilistically in the cities of Seattle and Mercer Island, WA for a suite of synthetic M9.0 Cascadia Subduction Zone earthquakes. Uncertainties in input material properties, empirical ground saturation conditions, and variability in expected ground motions within the suite of synthetics were combined with a megathrust-earthquake-specific sliding block displacement model to predict the probability of landslide occurrence (hazard) for two modes of landslides. Predicted coseismic landslide hazard modeling was verified against mapped coseismic landslides triggered by the 2001 M6.8 Nisqually earthquake and compared with hazard forecasts for a synthetic M7.0 Seattle fault earthquake.

Chapter 4 presents the results of the analysis of a high-quality database of 61 individual rockfall impacts on 29 dwellings in the Port Hills of Christchurch, New Zealand. Rockfall impacts on dwellings in this chapter were observed to follow a power-law relationship between kinetic energy and: (1) the runout distance into and through the dwelling; and (2) the impacted area within the dwelling. The results have been quantified and are presented as a "damage proportion," which was defined as the proportion of the area affected by an individual rock-block inside the dwelling divided by the total area of the dwelling. These data provide a fundamental input for rockfall risk analysis and will allow the losses from rockfall impacts to be better constrained.

Chapters 1, 2, and 3 reflect an advancement of coseismic landslide hazard analyses via the explicit characterization and assessment of different types of landslide failure. Insights from the Tohoku earthquake, particularly on the relationship between anthropogenic modification and landslide susceptibility and modes of landslides, make this work particularly useful for earthquakes affecting heavily developed regions, such as a future Cascadia Subduction Zone earthquake affecting the Pacific Northwest or future offshore Japanese earthquakes. Chapter 4, supplemented with observations of consequences from Chapter 2, provides new insight and data on the consequences to the built environment of different landslide types, enabling regional-scale quantitative risk analyses. Collectively, this work provides the tools and data necessary for the advancement of quantitative risk assessment for coseismic landslides and informed mitigation strategies to reduce preventable losses from these landslides.

References

Dellow, G., Yetton, M., Massey, C., Archibald, G., Barrell, D. J. A., Bell, D., ... & Easton, M. (2011). Landslides caused by the 22 February 2011 Christchurch earthquake and management of landslide risk in the immediate aftermath. *Bulletin of the New Zealand Society for Earthquake Engineering*,*44*(4), 227-238.

Havenith, H. B., Torgoev, A., Braun, A., Schlögel, R., & Micu, M. (2016). A new classification of earthquake-induced landslide event sizes based on seismotectonic, topographic, climatic and geologic factors. *Geoenvironmental Disasters*, *3*(1), 1.

Keefer DK (1984) Landslides caused by earthquakes. Geological Society of America Bulletin 95, 406–421

Keefer DK (2002) Investigating landslides caused by earthquakes–a historical review. Surveys in geophysics, 23(6), 473-510

Kramer SL (1996) Geotechnical Earthquake Engineering, Prentice Hall, Upper Saddle River, NJ

Xu, C., Shyu, J. B. H., & Xu, X. W. (2014). Landslides triggered by the 12 January 2010 Port-au-Prince, Haiti, Mw= 7.0 earthquake: visual interpretation, inventory compiling, and spatial distribution statistical analysis. *Nat Hazards Earth Syst Sci*, *14*(7), 1789-1818.

Chapter 1 – Multimodal method for coseismic landslide hazard assessment

The content of this chapter was published in:

Grant, A., Wartman, J., & Abou-Jaoude, G. (2016). Multimodal method for coseismic landslide hazard assessment. *Engineering Geology*, *212*, 146-160.

Abstract

Regional-scale coseismic landslide hazard assessments have traditionally been based on infinite-slope analyses, considering only a single mode of failure. Inventories and landslide reconnaissance work have shown a diverse range of coseismic landslide modes with significantly different consequences of failure. This chapter presents a multimodal approach for regional-scale coseismic landslide hazard assessment. Through a two-step procedure, the multimodal method explicitly accounts for four general landslide types commonly observed during earthquakes: rock-slope failures, disrupted soil slides, coherent rotational slides, and lateral spreads. First, the susceptibility to each landslide mode is evaluated based on topography. Second, coseismic landslide hazards are assessed using mode-specific geotechnical models. A trial multimodal landslide assessment is presented for the seismically active country of Lebanon. Results show that the computed coseismic landslide hazard closely matches field-verified slope activity across different regions of the country exhibiting a range of failure modes. These results qualitatively demonstrate the efficacy of the procedure and suggest that multimodal coseismic landslide hazard analysis is especially well-suited for regions with varying terrain and where landslide inventories are not available.

1.1 Introduction

Earthquake-induced, or *coseismic*, landslides occur in great number during moderate to large (M^1>5) earthquakes (Keefer, 2013; Rodríguez et al., 1999). These landslides typically occur across regions spanning hundreds to thousands of square kilometers (Keefer, 1984). The widespread geographic distribution of coseismic landslides makes them, by definition, regional-scale events. For this reason, coseismic landslide hazards are usually assessed using regional-scale (i.e., 1:250,000 – 1:25,000, Corominas et al., 2014) forecasting models. These models are valuable because they indicate the spatial distribution of coseismic landslides and additionally have the potential to capture seismic performance and propagation of risk across a region. This is especially important when considering the effects of slope failures on geographically distributed critical infrastructure systems, which are highly vulnerable to coseismic landslides (e.g. Wartman et al., 2003).

Regional-scale coseismic landslide hazard assessments are typically based on infinite-slope analyses (e.g. Wieczorek et al., 1985; Khazai and Sitar, 2000; Jibson et al., 2000; Saygili and Rathje, 2008), which theoretically limit their applicability to shallow landslides (Corominas et al., 2014). While infinite-slope based models have been shown to perform adequately for events where landslides primarily consist of shallow disrupted soil slides (e.g. the 1994 Northridge earthquake, Dreyfus et al., 2013), post-earthquake field investigations of other earthquakes reveal a diverse styles of coseismic landslides including rock-slope failures, rotational slumps, and lateral spreads

[1] Note: unless otherwise stated, all earthquake magnitudes reported in this text are moment magnitude, abbreviated as M.

(e.g. Keefer, 1984; Rodríguez et al., 1999; Sitar and Khazai, 2001; Bommer and Rodríguez, 2002; Keefer, 2002; Dai et al., 2011; Wartman et al., 2013). Ideally, landslide hazard assessments should capture the full range of coseismic failure modes.

In this chapter, I present a regional-scale coseismic landslide hazard assessment method that explicitly accounts for different modes of failure. This *multimodal* method considers four general modes (or types) of landslides commonly observed during earthquakes: (1) rock-slope failures, (2) disrupted soil slides, (3) coherent rotational slides, and (4) lateral spreads. Application of the multimodal method follows a two-step procedure: first, susceptibility to each landslide mode is evaluated based on topography; then, coseismic landslide hazards are assessed using mode-specific geotechnical models. The multimodal approach was developed for regions where inventories of coseismic landslides are incomplete or otherwise not available. In such regions, it is often possible to estimate geologic strength parameters and acquire digital elevation model (DEM) data, but impractical to apply regression-based assessment procedures trained on coseismic landslide databases from a specific geographic area (e.g. Lee et al., 2008).

I conducted a trial multimodal landslide hazard assessment for Lebanon, which has good quality geologic and topographic data. The discovery and mapping of the offshore Mount Lebanon Thrust Fault (Elias et al., 2007), linked to a historic ~M7.2 earthquake, has significantly raised the seismic hazard in Lebanon (Huijer 2010; Huijer et al., 2011) and suggests the potential for coseismic landslides across the country. Results from this trial application show that the computed coseismic landslide hazard closely matches field-verified slope activity across different regions of the country exhibiting widely varied terrains. The results demonstrate the efficacy of the procedure and suggest that multimodal coseismic landslide hazard analysis is well suited for regions of varied

terrain where landslide inventories are not available. A unique benefit of the multimodal method is that it provides a spatial disaggregation of coseismic landslide mode across a region, which offers a cursory assessment of risk since each landslide failure mode will have different impacts on human populations and different consequences for infrastructure systems and the built environment.

1.1.1 Coseismic Landslide Types and Consequences

Keefer (1984) identified fourteen commonly occurring coseismic landslide modes of failure, which were simplified and refined in later work to three main categories: disrupted slides, coherent landslides, and lateral spreads and flows (Keefer, 1999). This range of coseismic failure modes has been reported in many post-event landslide investigations. For example, Keefer (2000) mapped ~1,300 coseismic landslides within a 2,000km^2 zone that was highly impacted by the 1989 M6.9 Loma Prieta, California earthquake. Keefer (2000) observed that while most landslides were disrupted but that a considerable fraction (26%) classified as coherent failures. Similarly, Khazai and Sitar (2004) found a majority of the landslides initiated by the 1999 M7.6 Chi-Chi, Taiwan earthquake to be disrupted failures, with coherent (11%) and "other" (4%) types of landslides also being significant (lateral spreads were omitted from the Loma Prieta and Chi-Chi datasets.) Wartman et al. (2013) mapped coseismic landslides triggered by the 2011 M9.0 Tohoku earthquake across a 28,000 km^2 region and found most landslides to be disrupted (63%), with a lesser but significant fraction to be lateral spreads (34%) and coherent failures (3%). However, taken in the context of "sediment mobilization" or landslide erosion volume, lateral spreads were the dominant mode of coseismic landslides (Wartman et al., 2013). Unlike disrupted failures, lateral spreads are not captured by traditional infinite-slope based landslide hazard analyses.

Coseismic landslide failure modes are each associated with unique consequences of failure (e.g. Wartman et al. 2013; Keefer, 2013). For example, during the 2010-2011 Canterbury, New Zealand earthquake sequence, widespread liquefaction and associated lateral spreading resulted in significant damage to buildings and infrastructure systems (economic losses of ~$15B NZD, Cubrinovski et al., 2014) but did not cause human losses. In contrast, rock-slope failures, which occurred in many locations in the Christchurch region, resulted in both highly localized damage and significant loss-of-life (Massey et al., 2012).

1.2. Multimodal Model Development

The multimodal method was developed to assess susceptibility to four common types of landslides and to compute the mode-specific coseismic landslide hazard on a regional scale. Topographic slope was adopted as an indicator to determine terrain susceptible to landslides, and where indicated, the landslide mode(s) most likely to occur. A geospatially continuous mode-specific model was used to compute potential coseismic displacements based on the local ground shaking intensity. The coseismic landslide hazard was then defined based on computed displacements for all modes of failure following previous landslide studies (e.g. Godt et al., 2008; Jibson and Michael, 2009) and recognizing that coseismic displacement ultimately governs the serviceability of a slope after an earthquake (Kramer, 1996). The following sections describe the procedure used to identify landslide susceptibility and the geotechnical models used to assess each landslide mode.

1.2.1 Types of Landslides

Keefer (1984) studied 40 coseismic landslide datasets and found several types of landslides to be "very abundant" or "abundant," including rock falls and slides, disrupted soil slides, soil slumps, and soil lateral spreads. To capture this variation in coseismic landslide type, I focused on four

fundamental modes of failure. Referencing Keefer's (1984) coseismic landslide classification system, these are: (1) rock slides and falls, (2) disrupted soil slides, (3) coherent rotational slides (i.e., soil and rock slumps), and (4) lateral spreads (Fig. 1.1). Table 1.1 summarizes the landslide modes, as well their commonly observed characteristics and typical source zone slope inclinations. Figure 1.2 shows an example of each type of landslide. Other less common modes of failure, such as soil falls or earth flows, were omitted as they are unlikely to contribute significantly to the overall landslide hazard.

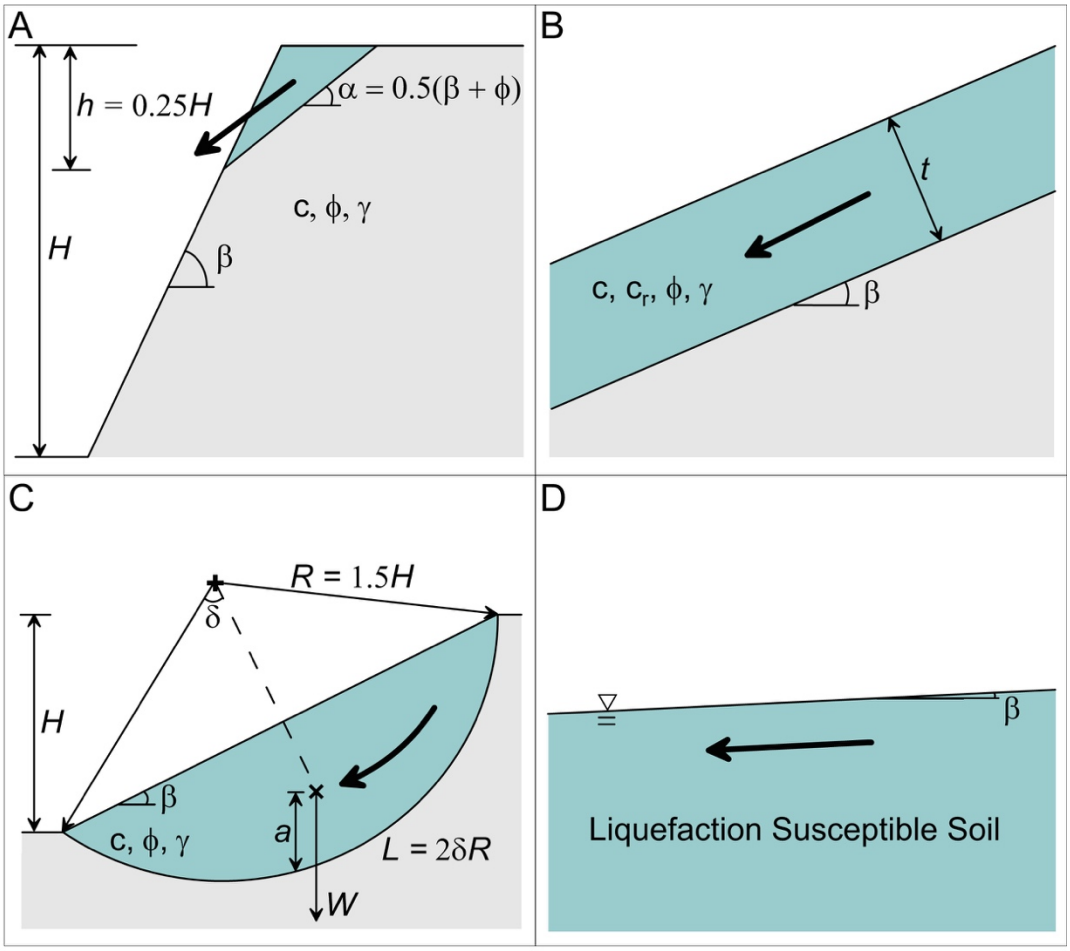

Figure 1.1 Geometry used for each mode of failure A. Rock Slope Failures, B. Disrupted Soil Slides, C. Coherent Soil Failures, D. Lateral Spreads

Landslide Category	Modeled Geometry	Slope Range	Characteristics
Rock-Slope Failures	Wedge	35° - 90°	Movement by free fall, sliding, and/or rolling. Run-out often long, tens of meters to km.
Disrupted Soil Slides	Infinite Slope	15° - 50°	Movement by sliding. Displacements of meters to a hundred meters common.
Coherent Rotational Slides	Circular-Rotational	20° - 35°	Movement by slumping or rotational sliding of a coherent mass. Displacement often small (<2m), but large displacements have been reported in many instances
Lateral Spreads	Empirically Developed	0° - 6°	Movement by the translational movement of a semi-liquid mass. Displacements typically small (<2m), but may be large in the case of flow failures

Table 1.1 Summary of modes of failure considered in this study. Modified from Wartman et al., (2013).

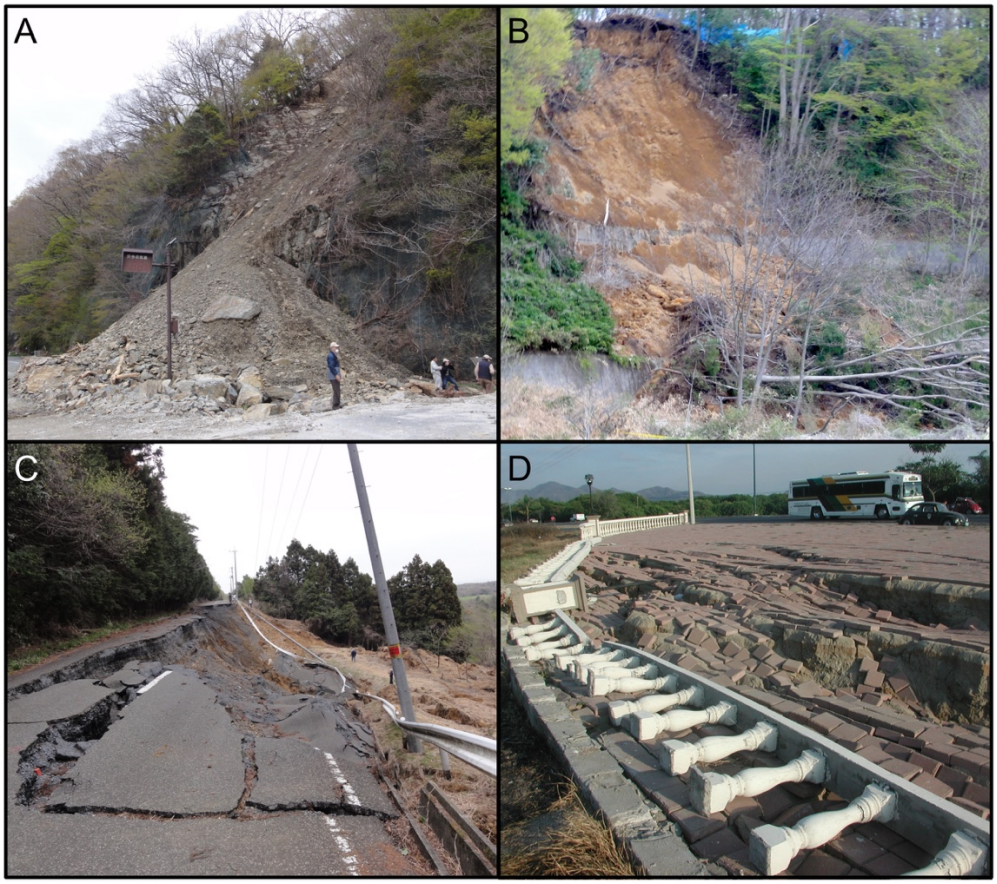

Figure 1.2 Examples of the four modes of landsliding considered in this study. (A) Rock-Slope Failure (B) Disrupted Soil Slide (C) Coherent Rotational Slide, and (D) Lateral Spread. Photos by Joseph Wartman and Scott Deaton following the 2011 Tohoku, Japan (A – C) and 2003 Colima, Mexico (D) earthquakes.

1.2.1.1 Mode of Failure Susceptibility Zonation

For many landslide susceptible regions in the world, detailed inventories are not available, thus preventing the use of region-specific statistical measures of future landslide susceptibility. However, previous studies and landslide reconnaissance investigations have identified clear relationships between mode of failure and slope of landslide source areas (e.g. Keefer, 1984; Keefer 2013). I adopted these findings to delineate the most likely coseismic mode(s) of failure within a study region within specific slope bounds. Lateral spread susceptibility was restricted to slopes of 0° – 6° based on Bartlett and Youd (1995) who found that liquefaction in slopes > 6° would likely produce flow slides, which are not considered in this work. Slopes from 15° – 50° are assumed to be susceptible to disrupted soil sliding based on observations of Keefer (1984) and the assumption that slopes steeper than 50° exhibit rock-like behavior. Terrain susceptible to potentially significant coherent rotational sliding movements was limited to slopes from 20° - 35°. While coseismic rock and soil rotational slides failures have been observed in gentler slopes in past events, I constrained failures based on my assumed slip surface geometry (section 1.2.2.3) and an assumed transition from deep to shallow soil and rock failures above 35° slopes. Rock-slope failures were considered for only slopes steeper than 35° based on the observations of Toppe (1987), Lee (2013), and Keefer (2013).

Slopes from 6° - 15° were assumed to have low susceptibility to the considered coseismic landslide modes. Low susceptibility terrain was assigned to reflect the relative scarcity of coseismic landslides in modest slopes (below 20°) in datasets with respect to steeper slopes (e.g. Northridge, Harp and Jibson, 1996; Wenchuan, Dai et al., 2011; multiple other events, Meunier et al., 2007) and to eliminate the need to characterize the geotechnical properties of soil and rock for regions unlikely to experience significant coseismic deformation. The upper bound of 15° was selected to

be consistent with the observations of Keefer (1984, 2013) that shallow disrupted soil slides, which often dominate coseismic landslide occurrence, may trigger in slopes as shallow as 15°. Low susceptibility terrain was not considered in later analyses based on the assumption that they would negligibly contribute to the overall coseismic hazard.

1.2.2 Mode-Specific Coseismic Hazard Assessment

1.2.2.1 Rock-slope Failures

Rock-slope failures –including the block slides and falls frequently observed in earthquakes (e.g. Massey et al., 2012)– were modeled as Culmann wedge-like masses (Duncan et al., 2014). This methodology captures both the brittle behavior typically associated with rock-slope failures and the planar nature of structural controls (i.e., discontinuities) common in rock masses. To constrain individual block geometries in a geographic information system (GIS) environment, local relief (*H*) was calculated for each susceptible pixel location based on a moving window analysis. This window size should be selected to best capture the major hillslope features within a study area. Window sizes that do not fully capture hillslopes will underestimate hazard, while overly broad windows will provide overestimates of coseismic hazards. Rock-slope failures were then assumed to potentially occur within the upper quarter of local relief based on observations from past earthquakes (Meunier et al., 2008; Massey et al., 2014). The static factor-of-safety (*FS*) for was then computed for each pixel as:

$$FS = \frac{2csin\beta}{\gamma hsin(\beta-\alpha)sin\alpha} + \frac{tan\phi}{tan\alpha} \qquad \text{Equation 1.1}$$

where β is the slope angle [rad], ϕ and c are the friction angle [rad] and cohesion [kPa] of the rock mass, α is the slope's critical angle given by: $\alpha = \left(\frac{\beta+\phi}{2}\right)$, h is the vertical height of the failure mass [m] ($h=0.25H$), and γ is the unit weight of rock (kN/m^3).

Static factors-of-safety were converted to yield acceleration values as (Newmark, 1965):

$$k_y = (FS - 1)gsin\theta \qquad \text{Equation 1.2}$$

where g is the acceleration of gravity [m/sec^2], and θ is the failure plane angle, $\theta = \alpha$ for rock-slope failures and $\theta = \beta$ for infinite slope conditions as described below. Coseismic displacements [cm] were then estimated using Jibson's (2007) sliding block displacement regression equation, which is a function of the yield acceleration (k_y) and peak ground acceleration (PGA) [both computed in units of g]:

$$logD_N = 0.215 + log\left[\left(1 - \frac{k_y}{PGA}\right)^{2.341}\left(\frac{k_y}{PGA}\right)^{-1.438}\right] \qquad \text{Equation 1.3}$$

1.2.2.2 Disrupted Soil Slides

As in previous regional-scale coseismic landslide studies (e.g. Wieczorek et al., 1985; Jibson et al., 2000; Allstadt et al., 2013), the static factor-of-safety (*FS*) for shallow disrupted sliding was calculated assuming dry infinite slope-like failure conditions. Schmidt et al. (2001) found that root systems of vegetated hillslopes can provide a significant degree of "root cohesion" to the upper layer of regolith. To assess the potential contribution of root cohesion (c_r) to coseismic slope resistance, I compared the Northridge earthquake inventory (Harp and Jibson, 1996) with pre-earthquake LANDSAT 5 satellite data of the region. I observed a clear relationship between the relative normalized difference vegetation index (NDVI) values and the intensity of coseismic

landslides within terrain susceptible to disrupted slides (Fig. 1.3). Specifically, heavily vegetated sloping terrain (20° - 50°) was found to be virtually free of landslides (1% of the mapped landslides occurred in the top decile [most vegetated] of relative NDVI values). In contrast, minimally vegetated sloping terrain (bottom half of relative NDVI values) accounted for the majority of landslides (73%.) Accordingly, I modified the general infinite slope equation (Duncan et al., 2014, Fig. 1.1B) to include the contribution of root cohesion:

$$FS = \frac{c+c_r}{\gamma t sin\beta} + \frac{tan\phi}{tan\beta} \qquad \text{Equation 1.4}$$

Here, c_r is root cohesion [kPa], t is the thickness of failure mass [m], γ is the soil unit weight [kN/m^3], and other terms are as defined for Equation 1. Jibson et al., (2000) found that disrupted soil slides typically extended to depths of 1 to 2 m and Sitar and Clough (1983) similarly observed that such failures rarely exceeded 2 to 3 m for slopes of 30° - 60°. Therefore, I assumed a failure plane thickness of t = 2 m for this work. I also adopted a conservative root cohesion value of c_r = 2 kPa based on empirical estimates provided by Terwilliger and Waldron (1991) and Schmidt et al. (2001) for Southern California, where vegetation is similar to that in this study area of Lebanon. Static factor-of-safety values were related to expected coseismic displacements using Equations 1.2 and 1.3.

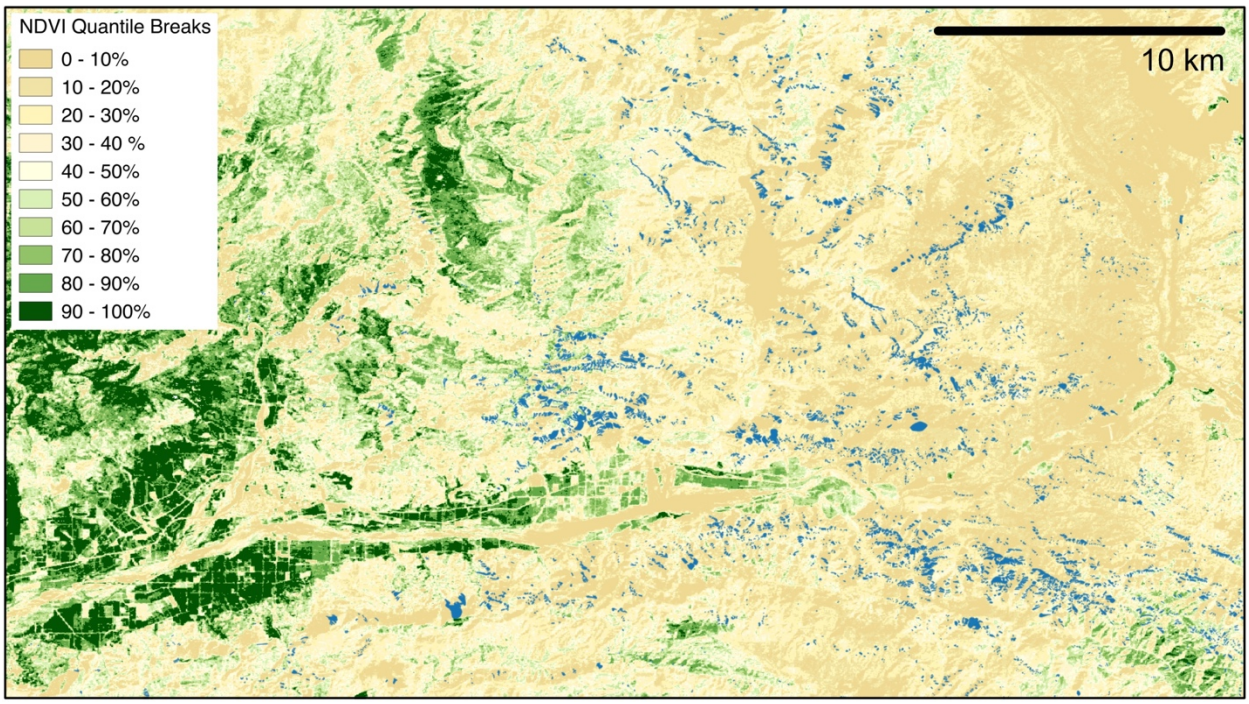

Figure 1.3 Normalized Difference Vegetation Index percentiles prior to the 1994 Northridge, California Earthquake. Blue polygons represent mapped landslides (Harp and Jibson, 1996).

1.2.2.3 Coherent rotational slides

To analyze coherent, slump-like, rotational slides in a pixel-based GIS platform I developed a uniform idealized failure surface that combines larger hillslope conditions with individual pixel properties (i.e. c and ϕ). I first determined local hillslope relief (H) via moving window analysis of varying sizes to best capture the scale of the local landscape. I then assumed the radius of a circular failure plane (R) acting through a dry homogeneous hillslope would be one and a half times the local relief ($R = 1.5H$, Fig. 1.1C). By constraining R and assuming a circular-segment shaped failure body, I compute the internal angle ($\delta = \sin^{-1}\frac{1}{3sin\beta}$, for $\beta > 20°$) and failure plane length ($L = 2\delta R$ [m]). Adopting the solution for yield acceleration developed by Kim and Sitar (2004) for an ordinary method of slices analysis, and projecting the 2D circular failure across each pixel as a cylindrical surface of width y, yield accelerations were computed on a per-pixel basis for dry slopes using a single slice calculation as:

$$k_y = \frac{cLy + W(cos\beta tan\phi - sin\beta)}{W\left(\frac{a}{R} + sin\beta tan\phi\right)}$$ Equation 1.5

Here, a is the vertical distance between the center of the slip circle and the landslide body's centroid ($a = \left(\frac{4Rsin^3\delta}{3(2\delta - sin2\delta)} - R\right) cos\delta$ [m]), W is the weight of the sliding mass ($W = \frac{1}{2}\gamma y R^2(2\delta - sin2\delta)$ [kN]), and y is the cell size of the assessed pixel. Other terms β, c, and ϕ are as defined in Equations 1 and 4. Coseismic displacements were then estimated using Equation 3, with a 50% reduction factor applied to the PGA to account for the compliant (i.e., non-rigid) nature of large coherent failure masses. In compliant materials, ground motion incoherence serves to reduce the destabilizing inertial forces within the soil failure mass (e.g. Kramer and Smith, 1997; Wartman et al., 2003). The 50% reduction value was chosen based on a comprehensive series of dynamic response analyses by Cetin et al. (2004).

1.2.2.4 Lateral Spreads

Due to the limited subsurface information typically available for regional scale assessments, I adopted a simplified lateral spread hazard assessment procedure based on liquefaction susceptibility indices and displacement estimation procedures developed for HAZUS (FEMA, 2003). As a soil liquefaction-related phenomenon, lateral spreading fundamentally differs from other coseismic failure modes due to its dependency on pore water pressure generation in soils that are encountered in a narrow range of depositional settings. I assumed that only low-lying soils (elevation <25 m) or deposits found near (within 25 m) rivers would be susceptible to lateral spreading. I assigned Youd and Perkins (1978) PGA thresholds for liquefaction triggering to susceptible soil units based on depositional conditions, ages, and sand-clay-gravel contents. These PGA triggering thresholds (T_{PGA}) ranged from a low of 0.12 g for highly susceptible soils (e.g.

recent sandy alluvium) to 0.26 g for soils having a lower susceptibility to liquefaction (e.g. Holocene-age cohesionless marine terraces). A magnitude correction factor (K_{Δ}) for lateral spread displacements was assumed to be 1.0 (FEMA, 2003) for probabilistic seismic hazard-based calculations based on a modal earthquake of ~M7.0. For scenario events, K_{Δ} was computed as (FEMA, 2003):

$$K_{\Delta} = 0.0086M^3 - 0.0914M^2 + 0.4698M - 0.9835 \qquad \text{Equation 1.6}$$

Where M is the earthquake moment magnitude for each scenario event.

For soils undergoing liquefaction, I estimated lateral spread displacements (*D*) based on relationships developed by FEMA (2003):

$$D = K_{\Delta} a \quad \text{where:} \quad \begin{array}{ll} a = 12r - 12 & \text{for } 1 < r < 2 \\ a = 18r - 24 & \text{for } 2 < r < 3 \\ a = 70r - 180 & \text{for } 3 < r < 4 \end{array} \quad \text{and } r = \frac{PGA}{T_{PGA}} \qquad \text{Equation 1.7}$$

1.2.3 Relating Coseismic Displacements to Relative Landslide Hazard

Coseismic displacements were assigned landslide hazard levels (Table 1.2) based on recommendations in the literature, but also from field observations of the seismic performance of slopes during major earthquakes (e.g. Wartman et al., 2003; Wartman et al., 2005). For brittle, disaggregated materials, such as those susceptible to disrupted soil sliding and rock-slope failure, Jibson and Michael (2009) designated regions with as low as 1 cm of sliding block displacement as having a moderate likelihood of landslide occurrence. By contrast, the California Geologic Survey (2008) concluded that more ductile materials, such as those found in rotational slides, can undergo significantly more coseismic deformation (15 cm) before posing a significant hazard to the built environment that I adopt as a threshold between low and moderate rotational slide hazard.

For lateral spreading, Youd and Perkins (1987) observed that events with $D < 13$ cm were typically associated with little structural damage, while events with $D = 13 – 50$ cm caused moderate to severe damage, and events with $D > 75$ cm resulted in major damage. I adopted a threshold of 50 cm for high lateral spreading hazard as a more conservative measure than the major damage limit of 75 cm.

	Low Hazard	Moderate Hazard	High Hazard	Primary Reference
Rock-Slope Failures	1 – 5 cm	5 – 15 cm	>15 cm	Jibson and Michael (2009)
Disrupted Soil Slides	1 – 5 cm	5 – 15 cm	>15 cm	Jibson and Michael (2009)
Coherent Rotational Slides	5 – 15 cm	15 cm – 1 m	>1 m	CGS (2008)
Lateral Spreads	0 – 15 cm	15 – 50 cm	>50 cm	Youd and Perkins (1987)

Table 1.2 Hazard levels assigned to coseismic displacements for each mode of landsliding

1.3. Application to Lebanon

The nation of Lebanon was adopted a test location to apply the multimodal coseismic landslide hazard method. Lebanon was principally selected because of its steep topography, history of large (>M6) earthquakes, and rapidly growing population, which together may produce significant coseismic landslide risks. Coseismic landslide inventories were not available for Lebanon, precluding the use of regression-based modeling techniques, as is the case for many parts of the world. After describing application and results of the multimodal modeling, I discuss observations from a field reconnaissance across the region that was subsequently undertaken to assess and test the landslide hazard mapping.

1.3.1 Geologic and Tectonic Setting

Lebanon is a small (10,452 km^2), mountainous country located along the eastern Mediterranean (Fig. 1.4). The landscape rises steeply from a narrow (5-15 km) shelf along the coast where major

cities in Lebanon are found (Beirut, Tripoli, and Tyre) to elevations of 2,500 – 3,000 m in the Mount Lebanon Range. Numerous deeply incised east-west trending river valleys divide the western slopes of the Mount Lebanon Range, exposing extensive cliffs of sandstone and limestone. East of the Mount Lebanon Range, the landscape drops steeply over sparsely vegetated slopes to the Yammouneh fault, the major left-lateral restraining bend of the Levant Fault System. From the Levant Fault System, the terrain slopes gently to the Bekaa Valley, a major agricultural region. Continuing east, the relatively barren limestone mountains of the Anti-Lebanon Range rise to ~2,500 m over rolling hillslopes that form Lebanon's border with Syria.

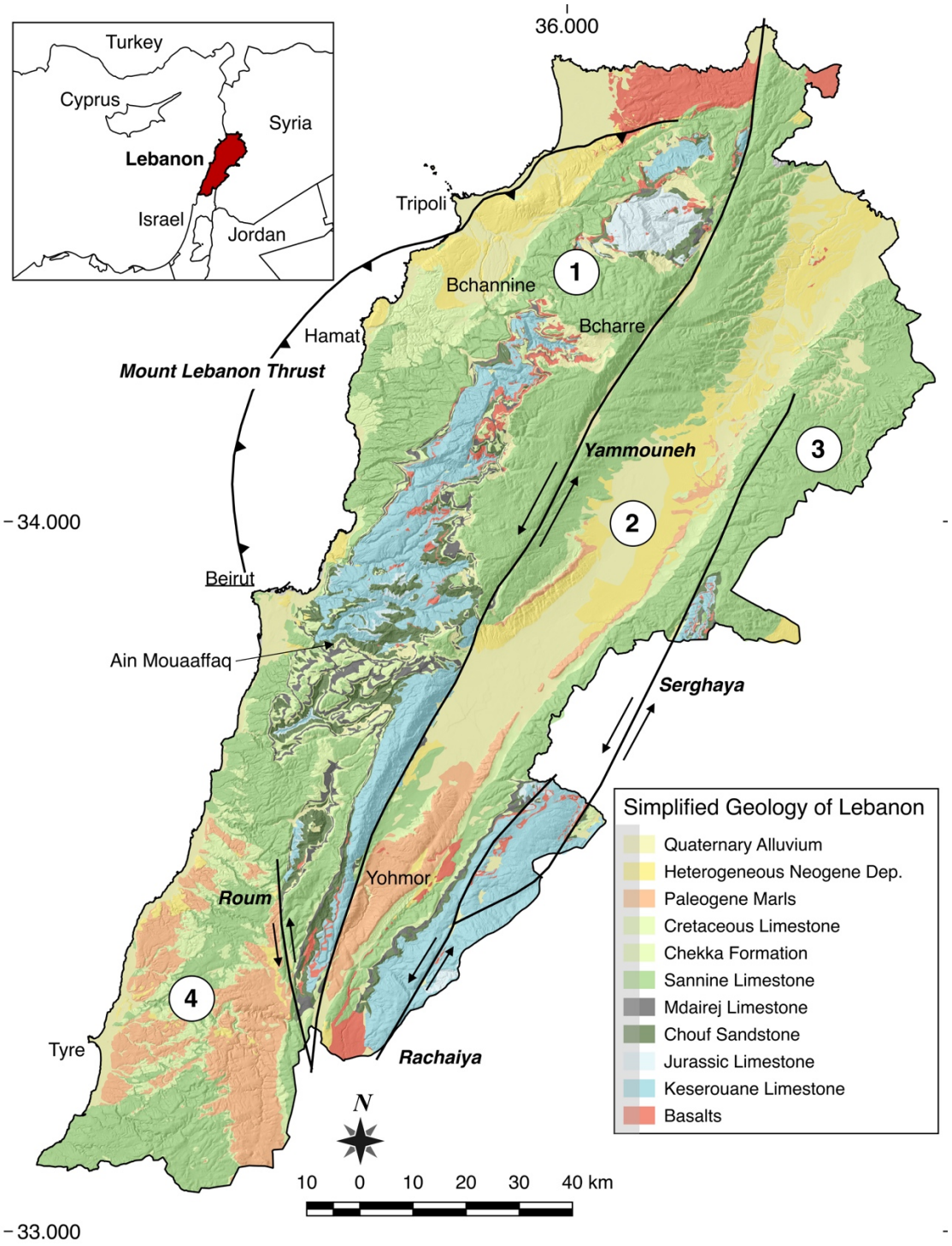

Figure 1.4 Major geologic units and faults (bold) of Lebanon and locations referenced in this work. Mount Lebanon Range (1) and its foothills are bound by the Yammouneh fault to the East, Mount Lebanon Thrust (MLT) fault to the North, and the Roum fault to the South. The Bekaa Valley (2) divides the high Mount Lebanon Range from the lower Anti-Lebanon Range (3). Rolling southern alluvial valleys and lowlands (4) extend across Lebanon south of the Roum fault. Geology after Dubertret (1945)

Geologic units in Lebanon are principally limestone and sandstone, dating back to the Early Jurassic. Four of these units, Kesrouane Limestone, Sannine Limestone, Chouf Sandstone, and the Mdairej Limestone, dominate the landscape. The early Jurassic Kesrouane Limestone was deposited in a shallow sea during a period of tectonic quiescence in the region (Walley, 1988; 1998) and today is a structurally complex and often thick limestone unit that underlies much of the mid-elevation Mount Lebanon region. Uplift of Lebanon in the early Cretaceous allowed for the deposition of the Chouf Sandstone across a then flat, low lying region. The Chouf Sandstone unit, which overlies Jurassic limestone, is widespread and highly fractured. Sea-level rise during the Late Cretaceous led to the further deposition of limestones (Sannine and Mdairej), which were later uplifted to form the modern Mount Lebanon and Anti-Lebanon ranges. This sea-level rise was followed by lateral offset of the Levant Fault System beginning about 10 m.y. ago (Walley, 1988). Today, the Sannine Limestones form the highest slopes of the Mount Lebanon range and are largely structurally intact. The older Mdjairej Limestones form a nearly continuous band of cliffs at mid to high elevations and are a major source of rockfall.

The regional tectonics shaping Lebanon are dominated by three zones of movement. The offshore Mount Lebanon Thrust (MLT) is undergoing compressional displacements of 1.0-2.0 mm/y (Elias et al., 2007). The most significant historic earthquake along the Mount Lebanon Thrust was a tsunamigenic ~M7.2 earthquake in 551C.E. that triggered large landslides in the Hamat area near the coast (Abdallah, 2007). The Yammouneh fault, which bisects the length of Lebanon and bends eastward to compress and uplift the Mount Lebanon Range, is slipping at an estimated rate of 5.1±1.3 mm/y and has been linked to historic M>7 earthquakes (e.g. 1202C.E., Daëron et al., 2004). The coupled Rachaiya-Serghaya fault system, a left-lateral strain-partitioning complex through the Anti-Lebanon Range, shows 1.4±0.1 mm/y of movement (Gomez et al., 2003) and

produced estimated M6.7 and M7.2 earthquakes in 1759 that destroyed much of the region (Elnashai and El-Khoury, 2004). Overall, the nearly 1000-year historic record of the region reveals a pattern of large earthquakes clustered in time (with decade intervals, most recently in the late 1700s) between longer 200 – 350 year periods of quiescence (Ambraseys and Barzangi, 1989). Huijer (2010) and Huijer el al. (2011) aggregated the three major seismic sources in the region to produce the PGA values used in this work.

1.3.2 Landslide Susceptibility Zones

I studied the coseismic landslide hazard across the entire countryside of Lebanon. Previous work in Lebanon on landslide susceptibility and detection (e.g. Abdallah, 2010; Abdallah et al., 2007; Khawlie and Hassanain, 1984) has focused on the rugged western slopes of the Mount Lebanon Range, where near-vertical limestone cliffs, long talus slopes, and extensive hillslopes of relatively steep (>20°) terrain cover the landscape. East of Ain Mouaaffaq, near Hammana, Khawlie and Hassanain (1984) identified active and former slope failures involving translational and rotational slides, block failures, toppling, and complex failures, while Abdallah (2010) identified slides and falls of unknown origin across the northwest of Lebanon. Less well studied were the gently sloping Bekaa Valley, the karstic Anti-Lebanon Mountains, and the alluvial valleys in the south of Lebanon (Fig. 1.4). I estimated soil and rock strength parameters (c and ϕ) based on available geologic and soil mapping and data presented in published studies (Dubertret, 1945; Geze, 1956; Abdallah, 2007), unpublished engineering consulting reports, and in consultation with geotechnical professionals practicing in the area. Rock and soil parameters used in this chapter are summarized in Table 3. A DEM was developed at a resolution of 15 m by digitizing contours from 1:20,000 scale topographic map of the country (DGA, 1963). For rock-slope failures and coherent rotational slides a range of window sizes were tested to best capture relevant topographic features

for local relief calculations. For both landslide types a window of 75 m was selected to best represent the scale of hillslopes active in these failure modes. The unit weight of all rock materials was assigned a nominal value of 23 kN/m^3, which is typical of the limestone, sandstone, and marl units that occur throughout the region. Soil unit weights were assigned a uniform value of 20 kN/m^3 based on typical values for sands and gravels (Lambe and Whitman, 1969). As a first order attempt to incorporate the reinforcing effects of vegetation on a hillslope, relative NDVI values were used to identify regions of vegetation cover across the study region based on Landsat 8 images from May 2014. Given the similarities in climate and vegetation between Lebanon and southern California, I assumed a conservative value of root cohesion of 2 kPa, which was applied over the most heavily vegetated portions of the study region (i.e., regions in the top 10% of relative NDVI for Lebanon).

Age	Formation or Description	Mapped Geologic Units	Rock-Slope Failures Coherent Rotational Slumps		Disrupted Soil Slides	
			Cohesion (kPa)	Phi (deg)	Cohesion (kPa)	Phi (deg)
Quaternary	Quaternary Heterogeneous Deposits	qd, qm	20	20	20	20
		ql, qs, qta,qaoi	20	30	20	30
		q, qcg, ql1	20	25	20	25
		qar	20	18	20	18
		a, ad	15	33	15	33
		Alluvium	15	33	15	33
		Gravel Slopes	15	33	15	33
		Alluvial Fans	15	33	15	33
		Silt and Mud	15	33	15	33
		Rocky	25	33	25	33
		Fill	15	33	15	33
		Scree	25	33	25	33
	Quaternary Basalt	qb	20	20	26	24
Neogene	Misc. Miocene Units	m	48	21	32	25
		m2,m2a,m2b	55	25	35	22
		mcg,ml,ml1	48	21	14	26
	Misc. Pliocene Units	p	57	25	67	22
		p1	62	32	57	26
	Misc. Neogene Units	n2,n	58	30	62	25
		ncg	62	32	57	26
	Neogene Basalt	bp,bp1-2,bp3	62	27	27	30
		bn	52	24	26	24
Paleogene	Numilitic Eocene Formation	e2, e2a	42	18	18	21
		e2b	44	20	24	20
Cretaceous	Chouf Sandstone	c1, c1-2, c1-2a, c2	48	21	18	21
	Abieh Formation	C2a	42	18	47	20
	Mdairej Formation	c2b	77	34	35	25
	Hammana Formation	c3, c3b, c3-4	48	21	17	21
	Sannine Formation	c4, c4-5	59	24	34	18
	Maameltain Formation	c5	59	24	35	25
	Chekka Formation	c6	48	21	18	21
	Cretaceous Basalt	bc, bc1, bc2a, bc2b, Bc	56	27	13	24
Jurassic	Chouane Formation	j1-3, j2, j3, j	61	26	53	28
	Keserouane Formation	j4, j6	61	26	35	20
	Bikkfaya Formation	j6a	84	38	113	34
	Salima Formation	j7	45	21	35	20
	Jurassic Basalt	bj, bj6, bj5	52	24	13	24

Table 1.3 Geologic units and geotechnical properties used in this study. Geologic mapping adopted from Dubertret (1945).

Fig. 1.5 shows landslide susceptibility modes based on topographic criteria. Steep (> 35°), highly susceptible terrain comprises 5% of the country, while areas assumed to have a low susceptibility coseismic landslide hazard (i.e., slopes from 6° to 15°) is found across 45% of the country. When lateral spread susceptibility criteria (i.e., age of deposit and setting; section 1.2.2.4) are applied,

approximately 75% of the region classifies as having a low susceptibility to coseismic landslides. Of the zones categorized as being susceptible to shallow disrupted slides, about 8% were assigned root cohesion-enhanced soil strengths based on the NDVI criterion. These vegetation-reinforced slopes are concentrated along the alluvial valleys of western Lebanon. In the rugged Mount Lebanon Range, hillslopes steeper than 35° slopes extend for many kilometers along the repeating east-west alluvial valleys located below scattered cliff bands. Field observations of these steep hillslopes in the Mount Lebanon Range revealed localized areas of actively eroding rock cliffs above long, steep, and loose talus deposits. Observations from past seismic events in other regions suggest that these steep slopes would be highly susceptible to rock-slope failure (e.g. Wartman et al. 2013). Further east, below the bare scree slopes of the eastern Mount Lebanon Range slope lies the flat Bekaa Valley, where lateral spreading susceptibility was indicated along the major rivers. The sparsely vegetated, open slopes of the Anti-Lebanon Range (eastern portions of Fig. 1.5), where gently sloped (<35°) ridges trend from northeast-southwest to east-west, were shown to be susceptible to disrupted and coherent rotational slides. To the south, shallow alluvial valleys meander across gentle (6° - 35°) slopes, with only the region's major river, the Litani, producing slopes prone to localized rock-slope failures or more widely distributed disrupted soil slides.

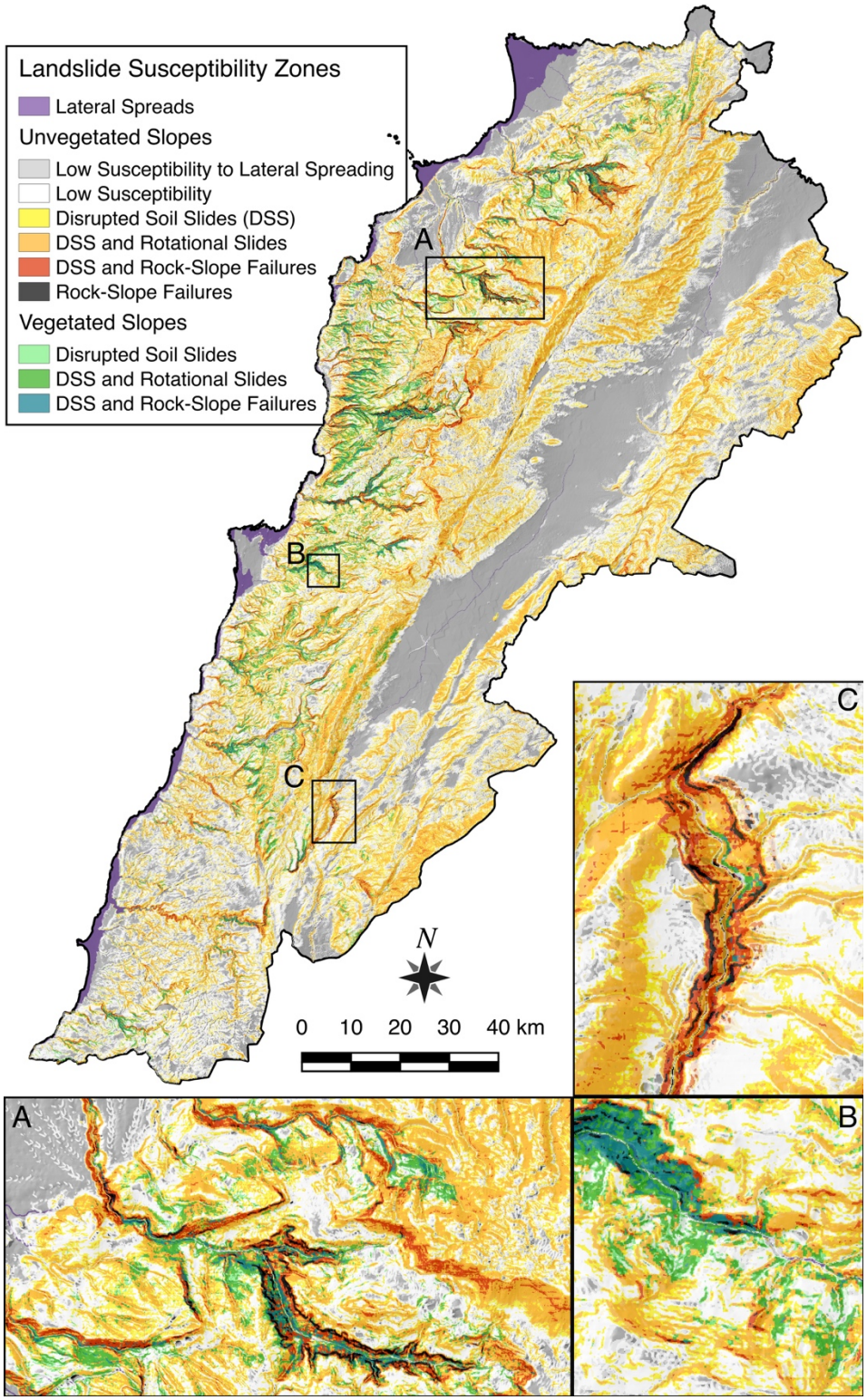

Figure 1.5 Landslide mode of failure susceptibility zones for Lebanon. (A) Steep cliff-lined valleys of the Mount Lebanon Range. (B) Ain Mouaaffaq region outside of Beirut where highly vegetated river valleys divide the more arid highlands. (C) Yohmor Valley in southeastern Lebanon where extensive cliffs and talus are indicated as susceptible to rock and disrupted soil slides.

1.3.3 Coseismic Landslide Hazards

Huijer (2010) and Huijer et al. (2011) conducted probabilistic seismic hazard analyses (PSHA) for Lebanon and developed the 10% chance of exceedance in 50 years (475-year return period) peak ground acceleration estimate that was adopted for this study (Fig. 1.6). For 475-year return period PSHA peak ground accelerations, my analysis identified areas having a high disrupted soil slide and rock-slope failure hazard along the steeply incised river valleys of the Mount Lebanon Range (Fig. 1.6A, near Bcharre) and along the Litani River canyon near Yohmor (Fig. 1.6B). I did not find densely concentrated high coseismic landslide hazard zones for these disrupted modes of failure in other parts of the country. Isolated cliff bands and talus slopes across the western portion of the country exhibit a low to moderate hazard that is limited to small, localized zones. For 475-year return period ground motion inputs, no significant (low, moderate, or high) hazard was predicted for coherent rotational sliding. Moderate to high lateral spreading hazard was shown in recent deposits located along the coast and Litani River of the Bekaa Valley (Fig. 1.6B near Yohmor). The highest concentration of high lateral spread hazard was identified near Beirut, where anthropogenic fill and alluvial deposits lie close to the MLT fault, which produces high PGA values in this local area.

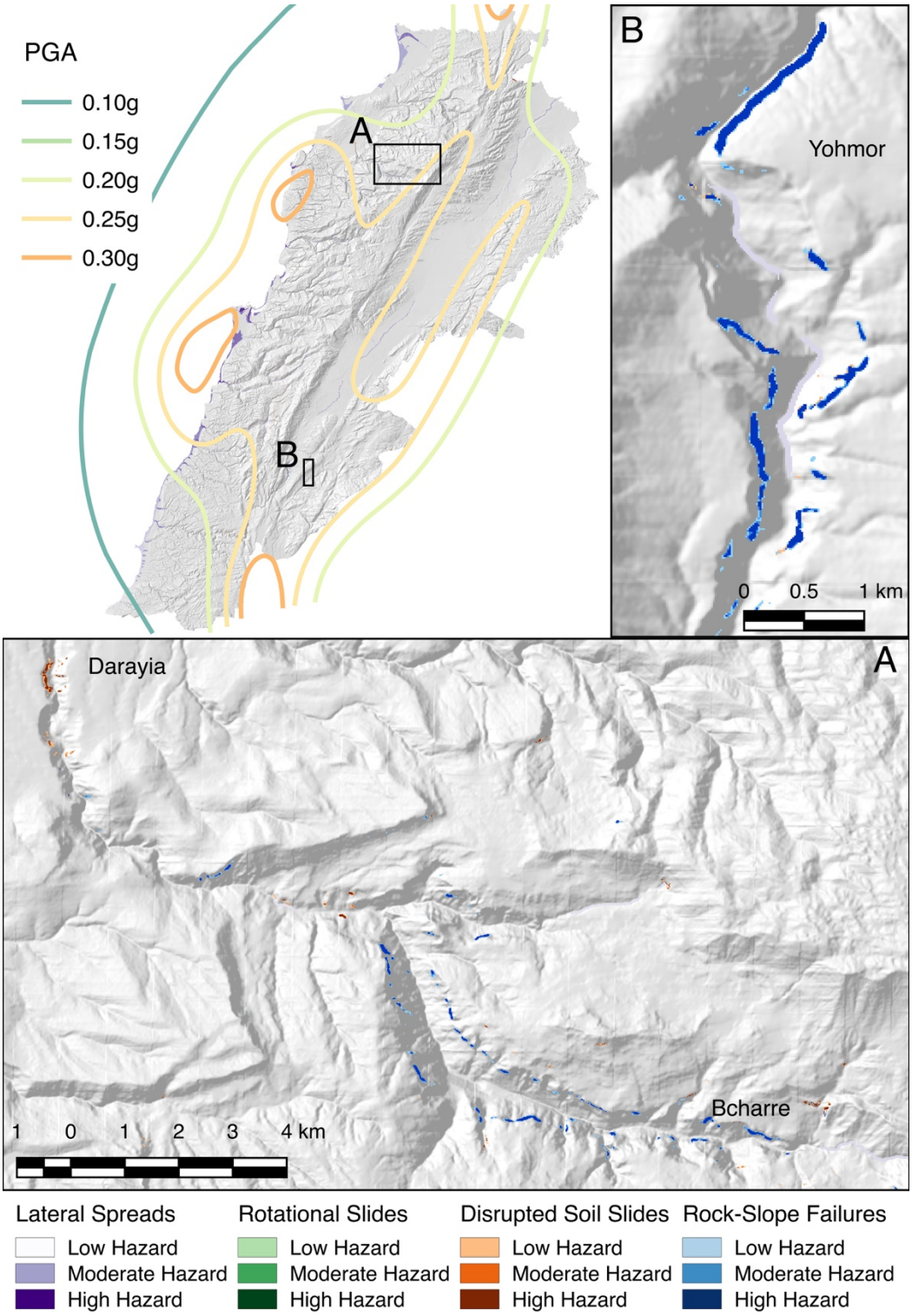

Figure 1.6 Multimodal landslide hazard output for 475-year (10% in 50 years) return period PSHA ground shaking intensities. (A) Incised river valley with rock slope and disrupted soil hazard near Bcharre, and disrupted soil slide hazard in the northeast near Darayia. (B), High rock-slope failure hazard is mapped along the edge of the Litani River canyon near Yohmor, while low levels of lateral spreading hazard are predicted along the river banks.

Strong motion recordings of significant (>M6.0) earthquakes in Lebanon's history do not exist, but the long history of estimated M6.5+ earthquakes in the region motivated an analysis of specific seismic scenarios to further explore potential landslide hazards. I considered several deterministic scenario events that dominate the seismic hazard of the region. Figures 1.7 and 1.8 present results for two such PSHA disaggregation-derived scenarios: a M7.2 Mount Lebanon Thrust and M6.6 Rachaiya fault events. For both events, PGA distributions were estimated using the Scenario Shakemap application (Field et al., 2003).

The Mount Lebanon Thrust (MLT) scenario earthquake (Fig. 1.7) was modeled as occurring on an 80 km long fault plane that dips 45° towards the coast. Fault geometry was based on the work of Arango and Lubkowski (2012) and Elias et al. (2007). This event produced shaking intensities and distributions that are probably similar to the 551C.E. M7.2 earthquake on the MLT that destroyed many coastal cities, included Beirut and Tripoli. Widespread moderate and high hazard is predicted for disrupted soil slides and rock-slope failures is indicated in the steep, unvegetated valley walls west of Bcharre (Fig. 1.7A), where only limited hazard is shown for PSHA shaking (Fig. 1.6A). Along the coast near Journieh (Fig. 1.7B), where modeled shaking is locally in excess of 0.5g, pockets of low – high hazard is indicated for disrupted soil slides and rock-slope failures. A band of low rotational slide hazard is shown just east of Jounieh but not along the more inland alluvial valleys susceptible to this mode of failure near Darayia (Fig. 1.7A) where predicted shaking is ~0.2g.

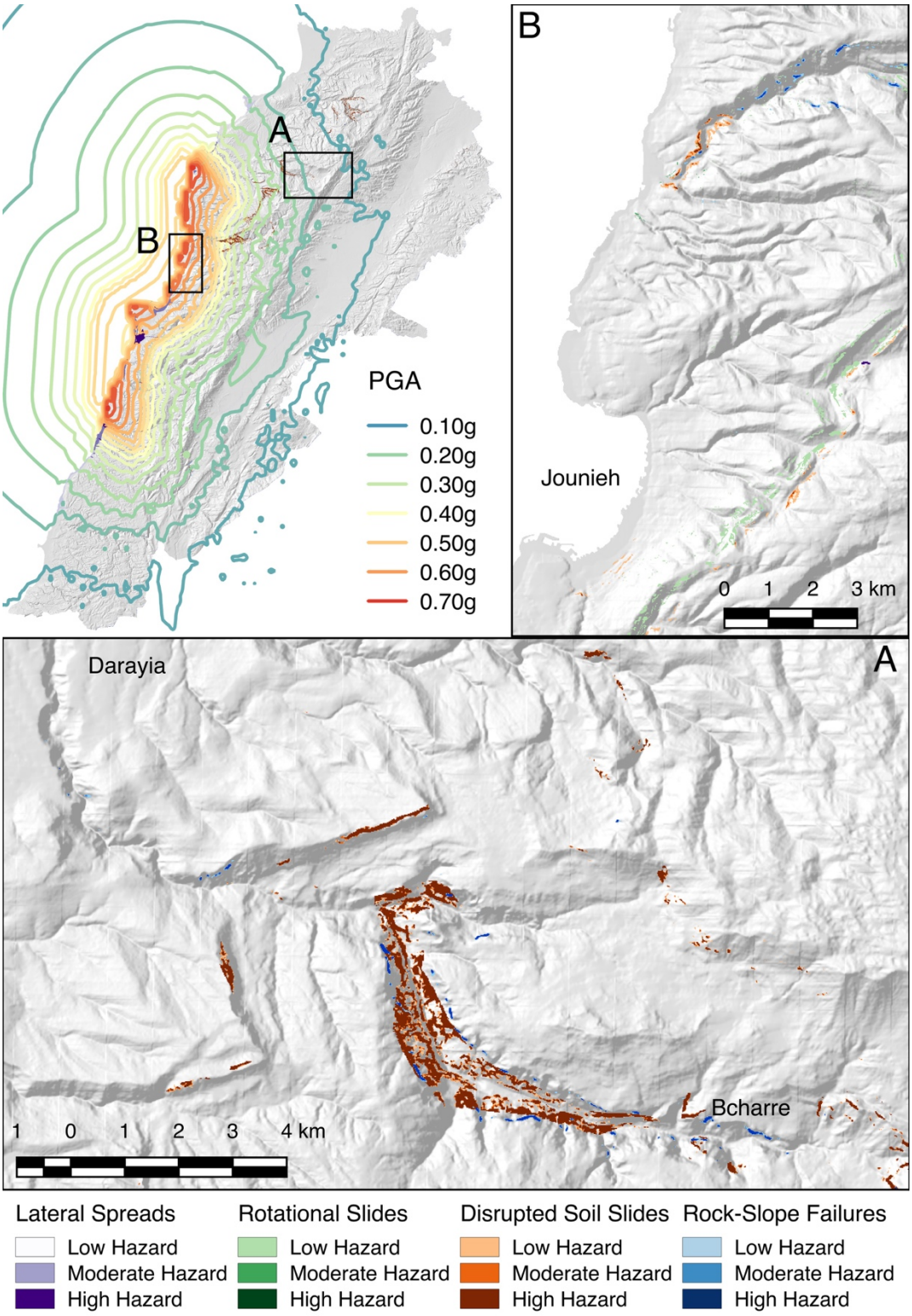

Figure 1.7 M7.2 Mount Lebanon Thrust scenario earthquake. (A) Increased disrupted soil and rock slope failure hazard along the steep valleys and cliffs of the Mount Lebanon Range. (B) High coastal peak ground accelerations develop predicted multimodal landsliding hazard in vegetated hillslopes near Jounieh north of Lebanon where PSHA-based landslide hazard is not predicted

The Rachaiya earthquake scenario was modeled as a 55 km long, left-lateral strike-slip event rupturing vertically from 5 to 10 km below the ground surface. The location and trace of the fault were selected to approximate the M6.6 earthquake that occurred in October of 1759 along the Rachaiya fault (Nemer et al., 2008). Few high hazard zones for all modes of landslides are found as most hillslopes are more weakly shaken in comparison to the PSHA (Fig. 1.6). High and moderate levels of hazard are predicted in rock-slope failure and disrupted soil sliding modes along isolated slopes near Yohmore and Ouardiye (Fig. 1.8A) where predicted shaking ranges from 0.2 – 0.4g. Low hazard predictions were also made in isolated locations for coherent rotational sliding. Results from this scenario suggest that earthquakes within the Anti-Lebanon Range, although large, may not produce the widespread landslide damage that would occur from a coastal or Yammouneh fault earthquake.

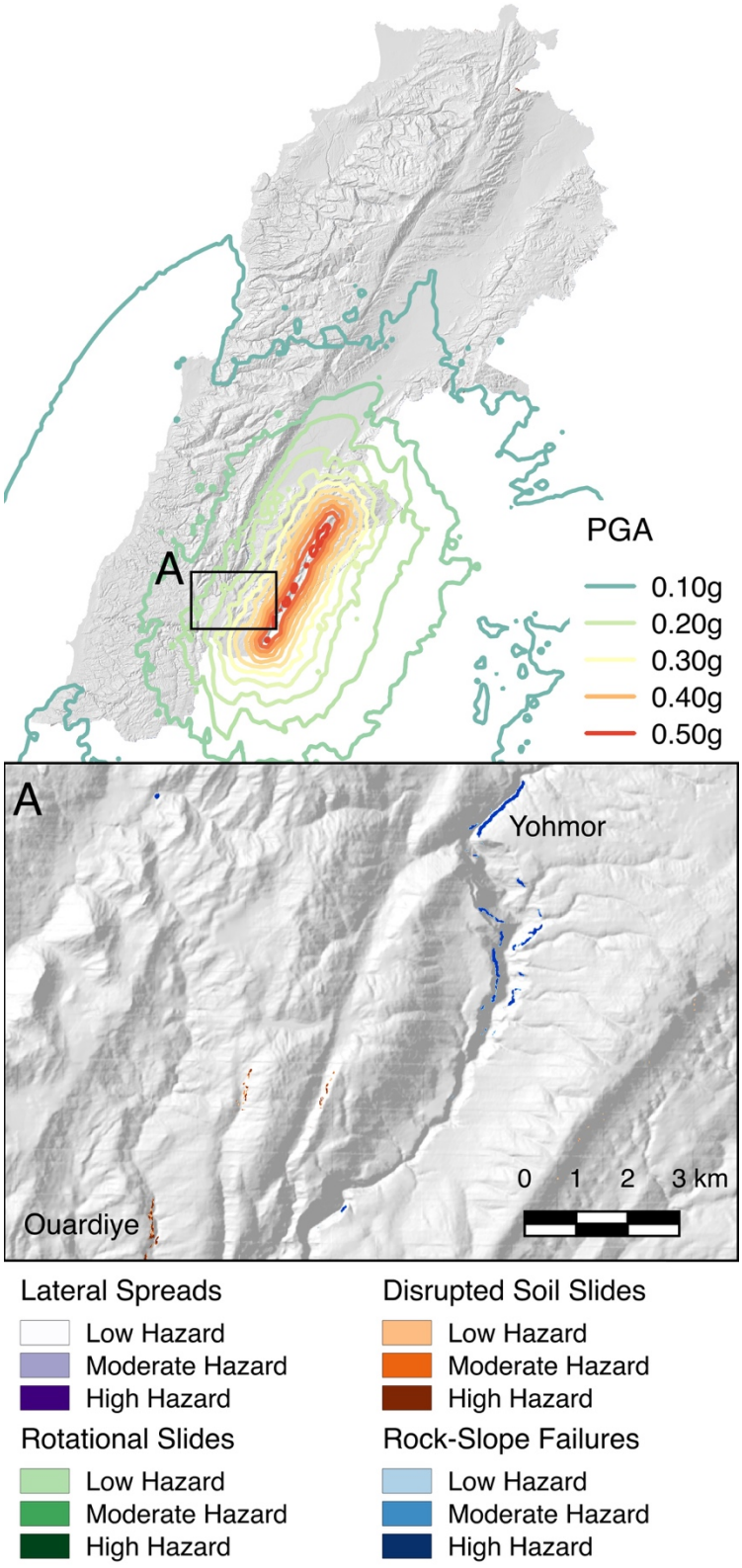

Figure 1.8 M6.6 Rachaiya earthquake scenario output. (A) Sparse landslide hazard estimated in the South of Lebanon near Yohmor for both rock slope failures and disrupted sliding.

1.3.4 Field Assessment

Following the development of multimodal coseismic landslide hazard maps for Lebanon, we (Joseph Wartman, Grace Abou-Jaoude, Angela Saade, and myself) undertook a multiday field reconnaissance across the region to qualitatively assess the results. In addition to the broader-scale reconnaissance across the region, we stopped to make comprehensive assessments at 30 specific sites. These assessment sites were selected such that all predicted modes of failure would be observed in the field. Additionally, this allowed us to more closely investigate local areas where our knowledge of the region suggested that landslide hazards may have been over-estimated, or conversely, omitted. During the fieldwork, we recorded evidence of past slope instability and assessed landslide susceptibility and likely mode of failure based on our professional experience from past post-earthquake reconnaissance investigations. We then compared our field observations to the multimodal landslide hazard maps.

Overall, we found that locations designated as having a high hazard corresponded closely to the observed landslide-susceptible terrain. For example, active rock sources, such as the Mdairej limestone cliffs across the Mount Lebanon Range, were consistently mapped as moderate to high rock-slope failure hazards. Soils developed from the Chouf Sandstone and steep talus slopes were found in most regions of high disrupted soil slide hazard. Coherent rotational landslides were only observed across limited regions near Bcharre, Darayia (Fig. 1.7A), and Hamat (Fig. 1.9A). The large rotational landslides observed near Hamat have been linked to the 551C.E. MLT M7.2 earthquake (Abdallah, 2007), although no clear triggering mechanism is associated with other observed slides. We found no surficial evidence of lateral spreading or liquefaction, as these subtle morphological features are unlikely to survive after the last major earthquake in Lebanon (1759).

Nonetheless, the locations exhibiting a lateral spread hazard corresponded closely to the types of settings where this phenomenon has been routinely observed in past earthquakes.

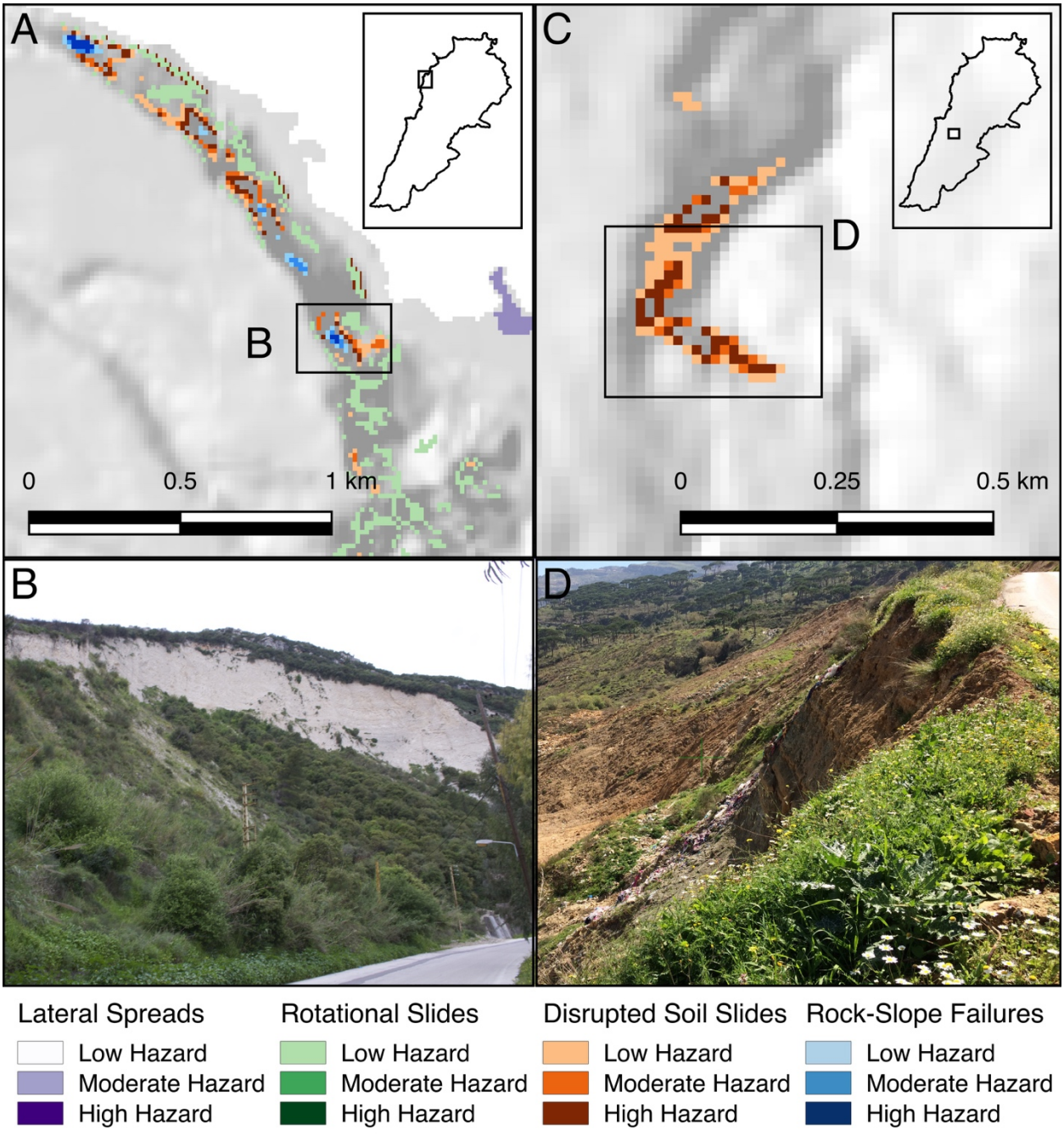

Figure 1.9 (A) Multimodal hazard output for a MLT scenario earthquake on the near Hamat. (B) Hillslope near Hamat susceptible to multiple modes of landsliding. (C) 475-year return period PSHA landslide hazard prediction for location near Ain Mouaaffaq and (D) hillslope showing active sliding.

Our detailed site evaluations were conducted at 30 individual sites; however, for brevity I will limit discussion to two locations that provide site-specific scale examples of how the terrain classified within our multimodal landslide hazard method.

Hamat: Near Hamat (Fig. 1.9A-B) we observed hillslopes susceptible to all considered landslide modes. Hillslopes near Hamat were observed to have short, near vertical, cliffs above alternating zones of planar talus and heavily tree-covered material at angles of ~30° in slope. Hillslopes in this location are ~150m tall and are composed of the weak Cretaceous Chekka Formation (off white unit exposed as a cliff in Fig. 1.9B) capped by a thin gray Miocene age limestone (top-left of Fig. 1.9B.) Abdallah (2007) linked large coherent landslides near Hamat with large MLT earthquakes. In my MLT scenario output, we predict low levels of hazard for coherent rotational slides similar to large rotational movements observed in Hamat, as well as low to high levels of rock-slope failure and disrupted soil slide hazard in the headscarp-cliff and talus portions of the slopes.

Ain Mouaaffaq: At this site we observed complex soil failures in residual soils of the Cretaceous Chouf Sandstone below a major roadway (Fig. 1.9C-D). Landslide movement was observed to be primarily translational over the entire slope, developing locally over-steepened soil and weathered rock-slopes. Susceptibility mapping identified the potential for disrupted soil sliding, without applying root cohesion, and rock-slope failures. PSHA-based hazard analysis predicted low to high disrupted soil landslide hazard increasing with local slope, but no rock-slope failure hazard in the over-steepened soil-rock cliffs observed in the slide.

1.4 Discussion

Across Lebanon, coseismic landslide hazard assessment matched both the anticipated mode of failure based on field reconnaissance and the expected location of potential instability. I found that the mapping was able to resolve many small (single 15 m pixel), localized outcrops (often with recent or incipient landslides) and to correctly identify these as hazards. Similarly, larger kilometer-long stretches of highly localized slope hazard were found to properly corresponded to extensive stretches of potentially unstable cliffs. Distinctive landforms, from limestone cliffs and talus to soil-mantled alluvial valleys, were consistently matched to predicted or observed modes of failure following the multimodal procedure. Overall, the field observations suggest that the multimodal assessment method is capable of identifying the location, expected mode, and coseismic landslide hazard level.

In addition to utilizing geotechnical models tailored to a specific mode of failure, the multimodal method allows explicit consideration of the possible consequences of failure and thus could be used to support regional-scale coseismic landslide risk assessment. For example, widespread lateral spread potential along the Hamat coast (Fig. 1.10A) may be expected to cause structural damage to structures and infrastructure without posing any significant human fatality risk. In contrast, the combination of the high rock-slope failure hazard and steep underlying slopes near the village of Kfour El Aarbi (Fig. 1.10B) may produce numerous rockfalls capable of impacting homes in the village, thus posing a risk to life. Coherent rotational landslide hazards near Hamat (Fig. 1.9B) could damage a small coastal road, but likely pose a lesser risk to life and private property.

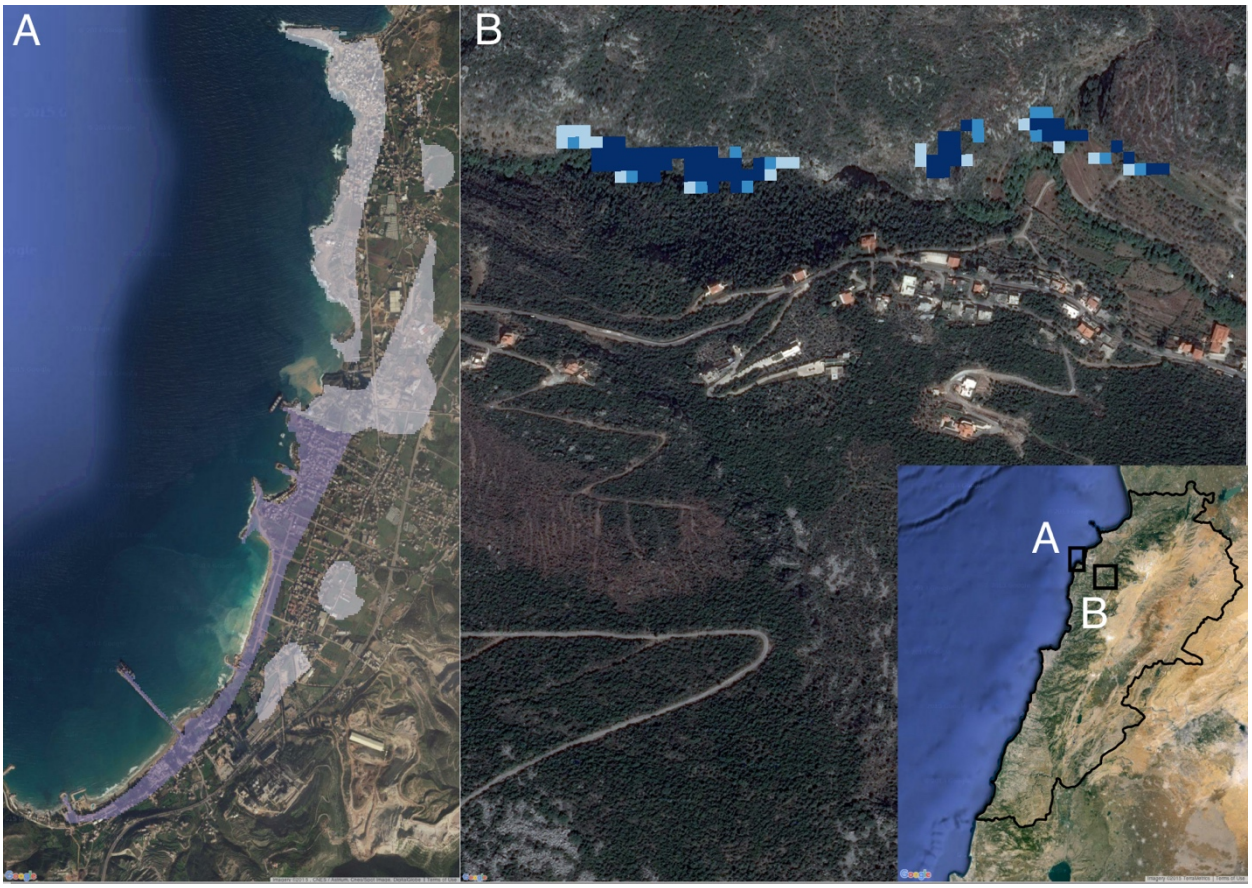

Figure 1.10 Potential consequences due to lateral spread displacements along the Hamat coastline (A) and rock slope failure runouts above Kfour El Aarbi (B). Base Images from Google Earth™

The PSHA and deterministic earthquake events each produce different landslide hazard patterns and highlight insights provided by considering a range of seismic scenarios. As an aggregate of multiple potential earthquakes across a large region, the PSHA-derived ground shaking intensities provided an understanding of the long-term, collective hazard across Lebanon. In contrast, single scenarios such as the potential Rachaiya and MLT events produce tightly constrained regions of mapped landslide hazard and delineate sub-areas where specific types of landslides are likely to occur for a given event. Scenario earthquakes also allow for the distributions of lateral spreading susceptibility to be investigated since PSHA-derived PGA values produce geospatial patterns of lateral spreading potential that appear to under-predict the hazard when compared to scenario events. It should be recognized that the probabilistic and deterministic assessments are associated

with events having different seismic hazard levels (i.e., return periods), and therefore a direct comparison of results is not possible.

Traditionally, regional-scale coseismic hazards assessments have assumed all landslides fail as shallow infinite slopes. This assumption oversimplifies the landslide hazard and fails to consider other common modes of failure and their respective characteristics and consequences. Therefore, worth comparing the results of the multimodal hazard assessment with that of a traditional infinite slope based model. Figure 1.11 presents the infinite slope hazard predictions with results of the multimodal analysis near Hamat. Adopting my disrupted soil slide displacements for hazard predictions of infinite slope analysis, the overall patterns of hazard prediction are similar for the two approaches, but the multimodal analysis provides a richer and more descriptive mapping of landslide hazards along the valley. The multimodal method indicates coherent rotational landslide hazards throughout the hillslopes near Hamat, while the corresponding infinite-slope based approach shows no landslide hazard at this location. Both the multimodal and traditional infinite slope methods indicate a shallow soil sliding hazard throughout the hillslope, but this zone is significantly more localized and narrow for the multimodal assessment as a result of the slope thresholds adopted in this work. In the northern and southern portions of the hillslope, isolated cliffs develop rock-slope failure hazard in the multimodal method that is captured, but not differentiated, by the infinite slope analysis. Finally, in the northern portion of Fig. 1.11, sandy beach deposits are shown as a potential lateral spread hazard while the infinite slope analysis indicates no hazard at this location. Discrepancies between the multimodal and traditional infinite slope methods are principally due to the use of mode-specific geotechnical models (versus solely infinite slope formulations) across the region.

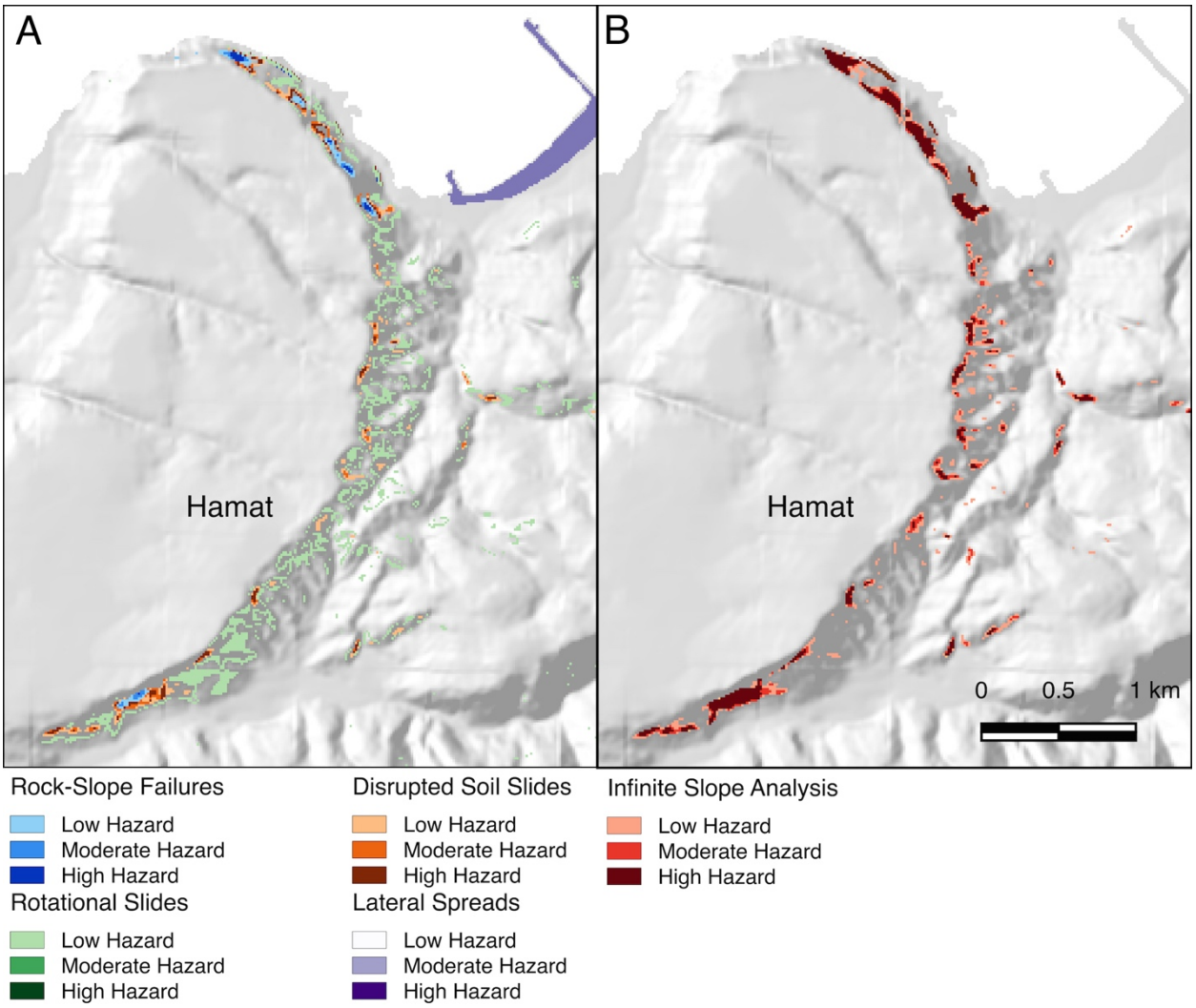

Figure 1.11 Comparison of multimodal analyses results (A) with single mode infinite-slope analysis (B) in the vicinity of Hamat.

Given the relative lack of data traditionally used to assess liquefaction (e.g. geotechnical test borings), several simplifying and conservative assumptions were adopted to evaluate lateral spread potential at a regional scale. Among these were that low-lying elevations along the Mediterranean Sea and locations along rivers were assumed to be uniformly saturated. Clearly, groundwater conditions at these sites are more complex and likely to fluctuate in time. In the event of an earthquake it is expected that some fraction of areas mapped as lateral spread hazards will fully

liquefy and subsequently spread. Thus, the spatial accuracy of the lateral spread hazard mapping will likely be less than that of other modes of coseismic landslides.

I utilized a 15 m resolution DEM for this work, which was able to capture a range of terrain features across Lebanon, including steep river channels in the north, long cliff bands through the central region, and rolling valleys to the south. Although Lebanon served as a test location for this research, we believe the multimodal procedure can also be used in other places where DEM data and information on geologic properties are available. For areas where only coarser resolution DEMs (>15 m) are available, I expect that the slope thresholds may need to be decreased (or increased for higher resolution data) to reflect the resolution with which the DEM cam represent the true morphology of the land surface (Zhang et al., 1999) and zones susceptible to landslides. It should also be recognized that the window dimension used to determine slope heights for rock-slope failures and coherent rotational slides (75 m) reflects the general scale of terrain features in Lebanon. This dimension may require modification for use in locations having significantly different landforms.

1.5 Conclusions

Landslides are a significant and widely distributed secondary seismic hazard during earthquakes. Landslide reconnaissance following past earthquakes has revealed a range of coseismic failure modes. In this chapter, I presented a new multimodal landslide hazard assessment methodology that considers four common modes of coseismic failure: rock-slope failures, disrupted soil slides, coherent rotational slides, and lateral spreads. Susceptibility to a specific landslide mode is determined by topographic slope, which is shown to correspond closely with observed landslide activity across Lebanon. Geotechnical models specific to each mode of failure are then used to

assess stability and estimate coseismic displacements based on probabilistic or deterministic seismic scenarios. Across Lebanon, field verification of ~30 sites showed close agreement between the landslide susceptible terrain and hazard mapping, and the expected seismic performance of slopes. The multimodal method thus provides an inexpensive, rapid, automated procedure for assessing coseismic landslide hazards over a regional scale.

Acknowledgments

Financial support for this research was provided by the U. S. National Science Foundation under Grant Nos. 0936602 and 1548552 and the U. S. Agency for International Development (USAID) under PEER grant 1-163. The opinions, findings, and recommendations expressed in this article are those of the authors and do not necessarily reflect the views of these agencies. The thoughtful comments provided by anonymous reviewers improved this paper.

References

Abdallah C (2007) Application of remote sensing and geographic information systems in the study of ground movements in Lebanon. Dissertation, University Pierre et Marie Curie-Paris VI

Abdallah C (2010) Spatial distribution of block falls using volumetric GIS–decision-tree models. International Journal of Applied Earth Observation and Geoinformation, 12(5), 393-403

Abdallah C, Chorowicz J, Boukheir R, Dhont D (2007) Comparative use of processed satellite images in remote sensing of mass movements: Lebanon as a case study. International Journal of Remote Sensing, 28(19), 4409-4427

Allstadt K, Vidale JE, Frankel AD (2013) A scenario study of seismically induced landsliding in Seattle using broadband synthetic seismograms. Bulletin of the Seismological Society of America. 103(6): 2971

Ambraseys NN, Barazangi, M. (1989) The 1759 earthquake in the Bekaa Valley: implications for earthquake hazard assessment in the Eastern Mediterranean region. Journal of Geophysical Research: Solid Earth (1978–2012), 94(B4), 4007-4013

Arango, M. C., Lubkowski, Z. A. (2012) Seismic Hazard Assessment and Design Requirements for Beirut, Lebanon. In 15th World Conference in Earthquake Engineering.

Bartlett SF, Youd TL (1995) Empirical prediction of liquefaction-induced lateral spread. Journal of Geotechnical Engineering, 121(4), 316-329

Bommer JJ, Rodríguez CE (2002) Earthquake-induced landslides in Central America. Engineering Geology, 63(3), 189-220

California Geological Survey (2004) Recommended criteria for delineating seismic hazard zones in California: California Geological Survey Special Publication, 118 (12 pp.)

California Geological Survey (2008) Guidelines for Evaluation and Mitigating Seismic Hazards in California: California Geological Survey Special Publication, 117A (98pp.)

Cetin KO, Seed RB, Der Kiureghian A, Tokimatsu K, Harder Jr LF, Kayen RE, Moss RE (2004) Standard penetration test-based probabilistic and deterministic assessment of seismic soil liquefaction potential. Journal of Geotechnical and Geoenvironmental Engineering, 130(12), 1314-1340

Corominas J, Van Westen C, Frattini P, et al., (2014) Recommendations for the quantitative analysis of landslide risk. Bulletin of engineering geology and the environment, 73(2), 209-263

Cubrinovski M, Taylor M, Robinson K, et al. (2014) Key factors in the liquefaction-induced damage to buildings and infrastructure in Christchurch: Preliminary findings. Auckland, New Zealand: 2014 New Zealand Society for Earthquake Engineering Conference (NZSEE), 21-23 Mar 2014. 9pp.

Daëron M, Benedetti L, Tapponnier P, Sursock A, Finkel RC (2004) Constraints on the post~ 25-ka slip rate of the Yammoûneh fault (Lebanon) using in situ cosmogenic 36Cl dating of offset limestone-clast fans. Earth and Planetary Science Letters, 227(1), 105-119

Dai FC, Xu C, Yao X, Xu L, Tu XB, Gong QM (2011) Spatial distribution of landslides triggered by the 2008 Ms 8.0 Wenchuan earthquake, China. Journal of Asian Earth Sciences, 40(4), 883-895

de Magistris FS, Lanzano G, Forte G, Fabbrocino G (2013) A database for PGA threshold in liquefaction occurrence. Soil Dynamics and Earthquake Engineering, 54, 17-19

DGA, Direction of geographic affairs (1963) Topographic maps at a scale 1:20,000. Republic of Lebanon

Dreyfus D, Rathje EM, Jibson RW (2013) The influence of different simplified sliding-block models and input parameters on regional predictions of seismic landslides triggered by the Northridge earthquake. Engineering Geology, 163, 41-54

Dubertret L (1945) Cartes géologiques à l'échelle de 1/50 000 (Hamidieh, Halba, Batroun, Tripoli, Sir El Dannieh, Jbail, Qartaba, Baalbeck, Beirut, Zahle, Rayak, Saida, Jezzine, Rachaya). République Libanaise, Ministère des Travaux publics, Beyrouth, Liban.

Duncan JM, Wright SG, Brandon TL (2014) Soil strength and slope stability. John Wiley & Sons, Hoboken

Elias A, Tapponnier P, Singh SC, et al. (2007) Active thrusting offshore Mount Lebanon: Source of the tsunamigenic AD 551 Beirut-Tripoli earthquake. Geology, 35(8), 755-758

Elnashai A, El-Khoury R (2004) Earthquake hazard in Lebanon. Imperial College Press, London

Field EH, Jordan TH, Cornell CA (2003) OpenSHA: A Developing Community-Modeling Evnironment for Seismic Hazard Analysis, Seismological Research Letters, 74, no. 4, p. 406-419

Federal Emergency Management Agency (2003) Multi-Hazard Loss Estimation Methodology. Earthquake Model, HAZUS® MH Technical Manual, National Institute of Building Sciences and Federal Emergency Management Agency, Washington, DC, 690

Godt JW, Sener B, Verdin K, Wald D, Earle P, Harp E, Jibson R. (2008) Rapid assessment of earthquake-induced landsliding. In Proceedings of the First World Landslide Forum, United Nations University, Tokyo 2008 Nov (Vol. 4, pp. 3166-1)

Gomez F, Meghraoui M, Darkal AN, et al., (2003) Holocene faulting and earthquake recurrence along the Serghaya branch of the Dead Sea Fault system in Syria and Lebanon. Geophysical Journal International, 153(3), 658-674

Harp EL, Jibson RW (1996) Landslides triggered by the 1994 Northridge, California, earthquake. Bulletin of the Seismological Society of America, 86(1B), S319-S332

Huijer CE (2010) Implications of the recent mapping of the offshore thrust fault system on the seismic hazard of Lebanon. Dissertation, American University of Beirut

Huijer C, Harajli M, Sadek S (2011) Upgrading the seismic hazard of Lebanon in light of the recent discovery of the offshore thrust fault system. Lebanese Science Journal, 12(2), 67

Jibson RW (2007) Regression models for estimating coseismic landslide displacement. Engineering Geology, 91(2), 209-218

Jibson RW, Harp EL, Michael JA (2000) A method for producing digital probabilistic seismic landslide hazard maps. Engineering Geology 58, 271–289

Jibson RW, Michael JA (2009) Maps showing seismic landslide hazards in Anchorage, Alaska: U.S. Geological Survey Scientific Investigations Map 3077, scale 1:25,000, 11-p. pamphlet

Keefer DK (1984) Landslides caused by earthquakes. Geological Society of America Bulletin 95, 406–421

Keefer DK (1999) Earthquake-induced landslides and their effects on alluvial fans. Journal of Sedimentary Research, 69(1)

Keefer DK (2000) Statistical analysis of an earthquake-induced landslide distribution—the 1989 Loma Prieta, California event. Engineering geology, 58(3), 231-249

Keefer DK (2002) Investigating landslides caused by earthquakes–a historical review. Surveys in geophysics, 23(6), 473-510

Keefer DK, (2013) Landslides generated by earthquakes: immediate and long-term effects. In:
Shroder, J. (Editor in Chief), Owen LA (Ed.), Treatise on Geomorphology. Academic Press, San Diego, CA, vol. 5, Tectonic Geomorphology, pp. 250–266

Khazai B, Sitar N (2000) Assessment of seismic slope stability using GIS modeling. Geographic Information Sciences, 6(2), 121-128

Khazai B, Sitar N (2004) Evaluation of factors controlling earthquake-induced landslides caused by Chi-Chi earthquake and comparison with the Northridge and Loma Prieta events. Engineering geology, 71(1), 79-95

Khawlie MR, Hassanain HI (1984) Failure phenomena and environmental control of the relatively unstable Hammana area, Lebanon. Engineering geology, 20(3), 253-264

Kim J, Sitar N (2004) Direct estimation of yield acceleration in slope stability analyses. Journal of geotechnical and geoenvironmental engineering,130(1), 111-115

Kramer SL (1996) Geotechnical Earthquake Engineering, Prentice Hall, Upper Saddle River, NJ

Kramer SL, and Smith MW (1997) Modified Newmark model for seismic displacements of compliant slopes.'' *J. Geotech. Geoenviron. Eng.,* 123 (7), 635 - 644

Lambe TW, Whitman RV (1969) Soil Mechanics. John Wiley & Sons, New York

Lee CT (2013) Re-evaluation of Factors Controlling Landslides Triggered by the 1999 Chi- Chi Earthquake. In: Ugai, K., Yagi, H., Wakai, A. (eds.) Earthquake-Induced Landslides, Springer Berlin Heidelberg, 213-224.

Lee CT, Huang CC, Lee JF, Pan KL, Lin ML, Dong JJ (2008) Statistical approach to earthquake-induced landslide susceptibility Engineering Geology 100 (1), 43-58

Massey CI, McSaveney MJ, Yetton MD, Heron D, Lukovic B, Bruce ZRV (2012) Canterbury Earthquakes 2010/11 Port Hills Slope Stability: Pilot study for assessing life- safety risk from cliff collapse, GNS Science Consultancy Report 2012/57

Massey CI, McSaveney MJ, Taig T, et al. (2014) Determining rockfall risk in Christchurch using rockfalls triggered by the 2010-2011 Canterbury earthquake sequence. Earthquake Spectra, 30(1), 155-181

Meunier P, Hovius N, Haines AJ (2007) Regional patterns of earthquake-triggered landslides and their relation to ground motion. Geophysical Research Letters, 34(20)

Meunier P, Hovius N, Haines JA (2008) Topographic site effects and the location of earthquake induced landslides. Earth and Planetary Science Letters, 275(3), 221-232

Nemer T, Gomez F, Al Haddad S, Tabet C (2008) Coseismic growth of sedimentary basins along the Yammouneh strike-slip fault (Lebanon). Geophysical Journal International, 175(3), 1023-1039

Newmark N, 1965. Effects of earthquakes on dams and embankments. Geotechnique 15, 139–160

Rodrıguez CE, Bommer JJ, Chandler RJ (1999) Earthquake-induced landslides: 1980–1997. Soil Dynamics and Earthquake Engineering, 18(5), 325-346

Saygili G, Rathje EM (2008) Empirical predictive models for earthquake-induced sliding displacements of slopes. Journal of Geotechnical and Geoenvironmental Engineering. 134(6), 790 - 803

Schmidt KM, Roering JJ, Stock JD, Dietrich WE, Montgomery DR, Schaub T (2001) The variability of root cohesion as an influence on shallow landslide susceptibility in the Oregon Coast Range. Canadian Geotechnical Journal, 38(5), 995-1024

Sitar N, Clough GW (1983) Seismic response of steep slopes in cemented soils. Journal of Geotechnical Engineering, 109(2), 210-227

Sitar N, Khazai, B, (2001) Characteristics of Seismically Induced Landslides in Recent Earthquakes, Invited Keynote Paper, Proc. Int. Conf. on Landslides: Causes, Impacts and Countermeasures, M. Kuhne et al., editors, Verlag Gluckauf GmbH, Essen, 227-237

Terwilliger VJ, Waldron LJ (1991) Effects of root reinforcement on soil-slip patterns in the Transverse Ranges of southern California. Geological Society of America Bulletin, 103(6), 775-785

Toppe R, (1987) Terrain models-A tool for natural hazard mapping. Avalanche formation, movement and effects, IAHS Publ, 162, 629-638

Walley CD (1988) A braided strike-slip model for the northern continuation of the Dead Sea Fault and its implications for Levantine tectonics. Tectonophysics, 145(1), 63-72

Walley CD (1998) Some outstanding issues in the geology of Lebanon and their importance in the tectonic evolution of the Levantine region. Tectonophysics, 298(1), 37-62

Wartman J, Rodriguez-Marek A, Repetto P, Keefer DK (2003) Ground Failure. Southern Peru

Earthquake of June 21, 2001 Reconnaissance Report, Earthquake Spectra, Vol. 19(A), No. 1, pp. 35-56

Wartman J, Rodriguez-Marek A, Macari EJ, et al. (2005) Geotechnical Aspects of the January 2003 Tecomán, Mexico, Earthquake. Earthquake Spectra, Vol. 21, No. 2, pp. 493-538

Wartman J, Dunham L, Tiwari B, Pradel D (2013) Landslides in eastern Honshu induced by the 2011 Tohoku earthquake. Bulletin of the Seismological Society of America, 103(2B), 1503-1521

Wieczorek GF, Wilson RC, Harp EL (1985) Map showing slope stability during earthquakes in San Mateo Count, California. U.S. Geological Survey Miscellaneous Investigations Map I-1257-e, scale 1:62, 500

Youd TL, Perkins DM (1978) Mapping liquefaction-induced ground failure potential. Journal of the Geotechnical Engineering Division, 104(4), 433-446

Youd TL, Perkins DM (1987) Mapping of liquefaction severity index. *Journal of Geotechnical Engineering*, *113*(11), 1374-1392.

Zhang X, Drake NA, Wainwright J, Mulligan M (1999) Comparison of slope estimates from low resolution DEMs: Scaling issues and a fractal method for their solution. Earth Surface Processes and Landforms. Aug 1;24(9):763-79.

Chapter 2 – Patterns and modes of coseismic landslides during the 2011 M9.0 Tohoku, Japan earthquake

The content of this chapter are being prepared for publication as:

Grant, Wartman, and Liu. Patterns and modes of coseismic landslides during the Tohkou, Japan M9.0 earthquake

Grant and Wartman. The role of anthropogenic modification on landsliding triggering and type

Chapter 2: Patterns and modes of coseismic landslides during the 2011 M9.0 Tohoku, Japan earthquake

2.1 Introduction

The March 11, 2011, M9.0 off the Pacific Coast of Tohoku Earthquake (hereafter referred to as the Tohoku earthquake) triggered more than 3,500 landslides mapped within an area of 21,808km^2. These coseismic landslides caused at least fourteen deaths (Wartman et al., 2013). Overall, the earthquake and associated secondary hazards caused over 15,000 deaths, left ~4,000 people missing, destroyed 128,530 homes and damaged an additional 240,332. Total losses were in the range of 300 billion 2011 US dollars (Kazama and Noda, 2012). Eighteen seismic recording stations, spread over 364km along eastern Honshu, recorded extreme peak ground accelerations (PGA) in excess of 1.0g. Significant ground shaking continued for several minutes in many locations, contributing to widespread liquefaction and lateral spreading (Goto and Morikawa, 2012; Bhattacharya et al., 2011). Despite the size of the Tohoku earthquake and the intensity of ground shaking on land, the distribution and concentrations of mapped coseismic landslides show no correlation to ground motion intensity measures (Wartman et al., 2013; Miyagi et al., 2011) as is commonly observed in crustal earthquakes (e.g., Khazai and Sitar, 2004; Meunier et al., 2007; Lee et al., 2008; Wang et al., 2007; Dai et al., 2011; Collins et al., 2012; Xu et al., 2014; Kritikos et al., 2015.) Structural damage caused by the Tohoku earthquake were also found to show no strong correlation with recorded ground motion intensity measures (Goto and Morikawa, 2012).

This chapter discusses the methods and results of two parallel studies of a coseismic landslide database from the Tohoku earthquake. First, the patterns of observed coseismic landslides with

respect to potential causal factors (e.g. topographic slope, lithology, peak ground velocity) are assessed based on the remapping and reclassification of landslides reported by Wartman et al. (2013). A physically-based relationship between driving and resisting forces to landslide triggering is proposed to explain the distribution of landslides triggered by the Tohoku earthquake. This approach is verified against a second coseismic landslide inventory from the M6.6 2011 Iwaki earthquake, which occurred as an aftershock to the Tohoku earthquake. Second, the effects of anthropogenic modification on landslide susceptibility and triggering for debris slides triggered by the Tohoku earthquake are assessed. In both studies, coseismic landslides are mapped based on mechanistic differences between types, considering landslides originating in both natural and modified terrain, and cataloging landslide impacts to the built environment.

Patterns and types of landslides triggered by the Tohoku earthquake were analyzed based on the remapping, reclassification, and expansion of the original Wartman (2013) landslide inventory within a ~600km long by 70km wide corridor along the eastern coast of Honshu, Japan (Fig. 2.1). Five distinct landslide types – debris slides, flow slides, lateral spreads, rotational slides, and rock irregular slides – were mapped to better facilitate analyses of potential causal factors in landslide initiation, recognizing that each landslide mode is controlled by a different set of factors. Each coseismic landslide was also assigned a degree of anthropogenic modification and of impact to the built environment to facilitate a comparative analysis of natural versus anthropogenically modified landslides and to increase our understanding on the consequences and future risk due to coseismic landslides.

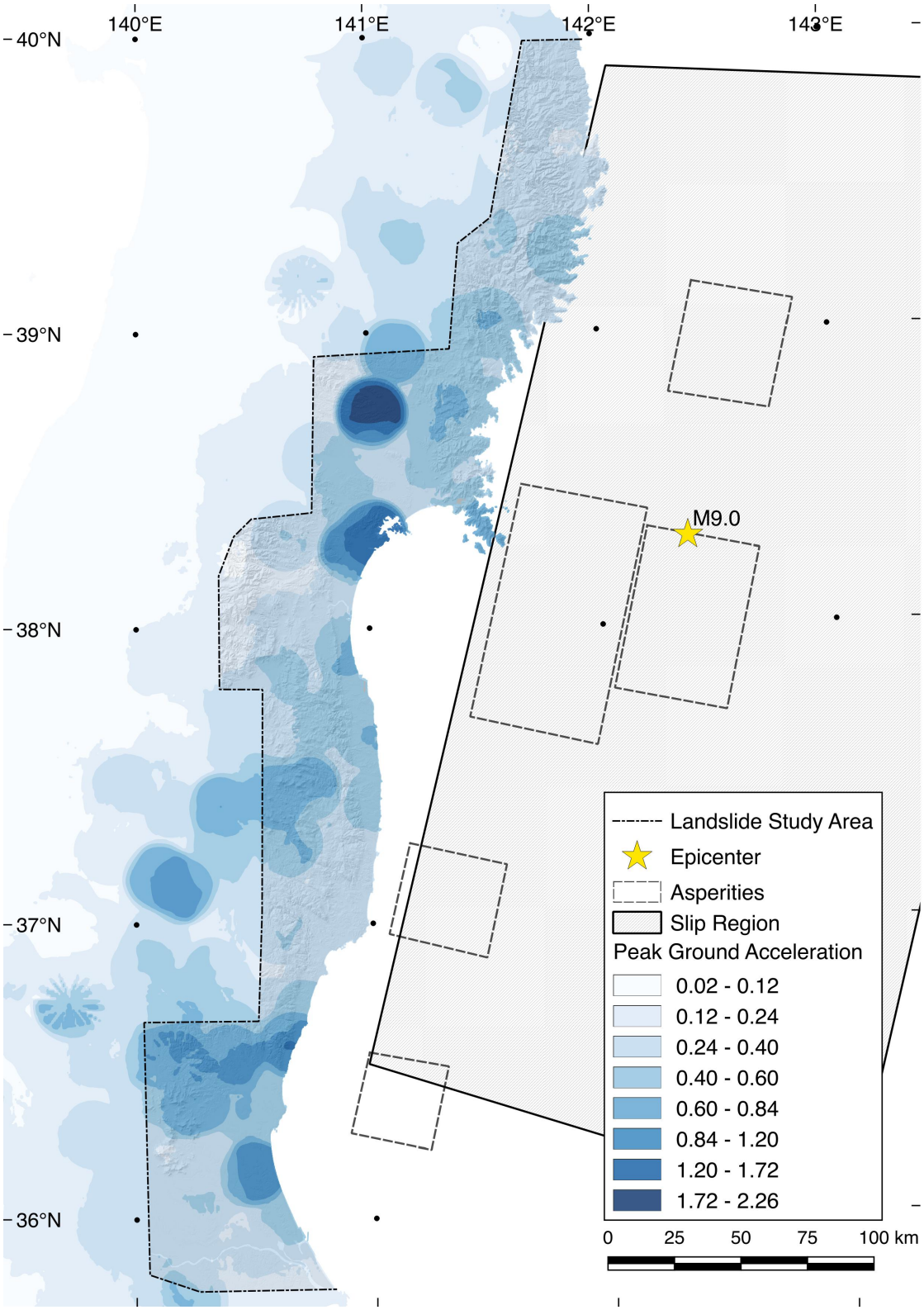

Figure 2.1 Peak ground accelerations during the 2011 M9.0 Tohoku earthquake. Landslide study region shown as a solid black line. Earthquake epicenter, peak ground accelerations, and slip region via the USGS (https://earthquake.usgs.gov/earthquakes/eventpage/official20110311054624120_30#shakemap), strong motion generation areas (asperities) adapted from Kurahashi and Irikura (2011).

To determine the relative importance of different coseismic landslide susceptibility and triggering factors, nearly all existing landslide inventories have been subject to some form of factor analysis (e.g., Lee et al., 2008; García-Rodríguez et al., 2008; Nowicki et al., 2014). Methods for determining the significance of susceptibility (slope, elevation, geology, etc.) and triggering (ground shaking, precipitation) factors include generalized linear modeling (e.g., Atkinson and Massari, 1998), frequency ratios and logistic regression (e.g., Lee and Pradhan, 2007; García-Rodríguez et al., 2008; Lee et al., 2008), and Bayesian or artificial neural networks (e.g., Pradhan and Lee, 2010; Song et al., 2012).

This work utilizes factor analysis (FA) and logistic regression (LR) to test (1) bivariate relationships between causal factors (e.g., topographic slope, PGA, etc.) and landslide concentration, and (2) the predictive capacity of those factors on landslide occurrence. LR was also utilized to test for potential differences between natural and modified slope failure with respect to causal parameters. Artificial neural networks (ANN) and machine learning (ML) algorithms were not applied to the Tohoku or Iwaki coseismic landslide datasets. While ANN and ML are capable of finding high-order patterns within data for a variety of desired response variables (e.g., occurrence/non-occurrence of landslides), they do not, in clear terms, describe the system being evaluated. These, and other, high-level statistical methods operate as a 'black-box', while simple bivariate and multivariate analyses performed in this study can be constructed in a physically meaningful manner. As the purposes of this work were to both understand the distribution of landslides triggered by large magnitude subduction zone earthquakes, and apply those lessons in hazard forecasting models, simpler FA and LR methods are preferred as they better facilitate interpretation and application of potential insights from these data.

Studies of coseismic landslide inventories from shallow crustal earthquakes (e.g., Khazai and Sitar, 2004; Meunier et al., 2007; Lee et al., 2008; Wang et al., 2007; Dai et al., 2011; Collins et al., 2012; Xu et al., 2014; Kritikos et al., 2015; Marc et al., 2016) suggest ground motion intensity measures (such as peak ground acceleration, Modified Mercalli Index, etc.) or distance to the earthquake source (as epicentral distance or nearest distance to the rupture plane) control over the observed coseismic landslide distributions. Studying landslides triggered by the megathrust Tohoku earthquake, Wartman et al. (2013) found no statistically-significant correlation between ground motion intensity and mapped coseismic landslides, finding instead geologic age, as a proxy for material strength, to be the dominant factor in explaining landslide concentration. Here these two disparate findings, the dominance of either shaking intensity or geology as explanatory factors for coseismic landslide concentrations, are reconciled within a physically-based model for landslide triggering based on the ratio of yield acceleration (a function of geologic strength, landslide geology, and topographic slope) to peak ground acceleration. Landslide concentrations of all modes triggered by the M9.0 Tohoku earthquake were found to strongly correlate to the ratio k_y/PGA, where k_y (yield acceleration) is the physically derived acceleration above which the slope can no longer resist downslope movement (failure), and PGA is the observed peak ground acceleration. This proposed physical framework for landslide triggering likelihood based on the mapped distribution of landslides from the Tohoku earthquake was then verified against an independently mapped set of coseismic landslides triggered by a large (M6.6) aftershock earthquake in April, 2011 in coastal Japan.

On April 11, 2011, the M6.6 Fukushima Hamadori aftershock (hereafter Iwaki earthquake, Fig. 2.2) generated strong shaking near Iwaki City and triggered more than 450 additional landslides

(Sato et al., 2013; 2015). Extension is believed to have occurred simultaneously (or near synchronously) along two sub-parallel normal faults, the Itozawa and Yunodake, that strike approximately NW-SE through the Abukuma Mountains (see Fig. 2.5, Toda and Tsutsumi, 2013; Tanaka et al., 2014). Landslides identified by Sato et al. (2015) and during field reconnaissance were distributed over an area of 550km^2 where peak ground accelerations ranged from 0.15 – 0.7g (Fig. 2.2). Utilizing the Iwaki coseismic landslide inventory of Sato et al. (2015), combined with Iwaki aftershock landslides mapped in this study, the physical landslide likelihood (k_y/PGA) framework for assessing triggered landslide intensities was tested. The Iwaki aftershock, with a different style of faulting and smaller magnitude, affected a small subarea of the original study region at a similar time, providing a useful test as to whether findings from Tohoku are specific to large magnitude subduction zone earthquakes or whether they reveal a more universal finding on the nature of coseismic landslide triggering. Patterns of landslide concentration for the Tohoku and Iwaki landslide datasets are in close agreement when viewed within the k_y/PGA framework, with different or divergent trends with respect to all other parameters.

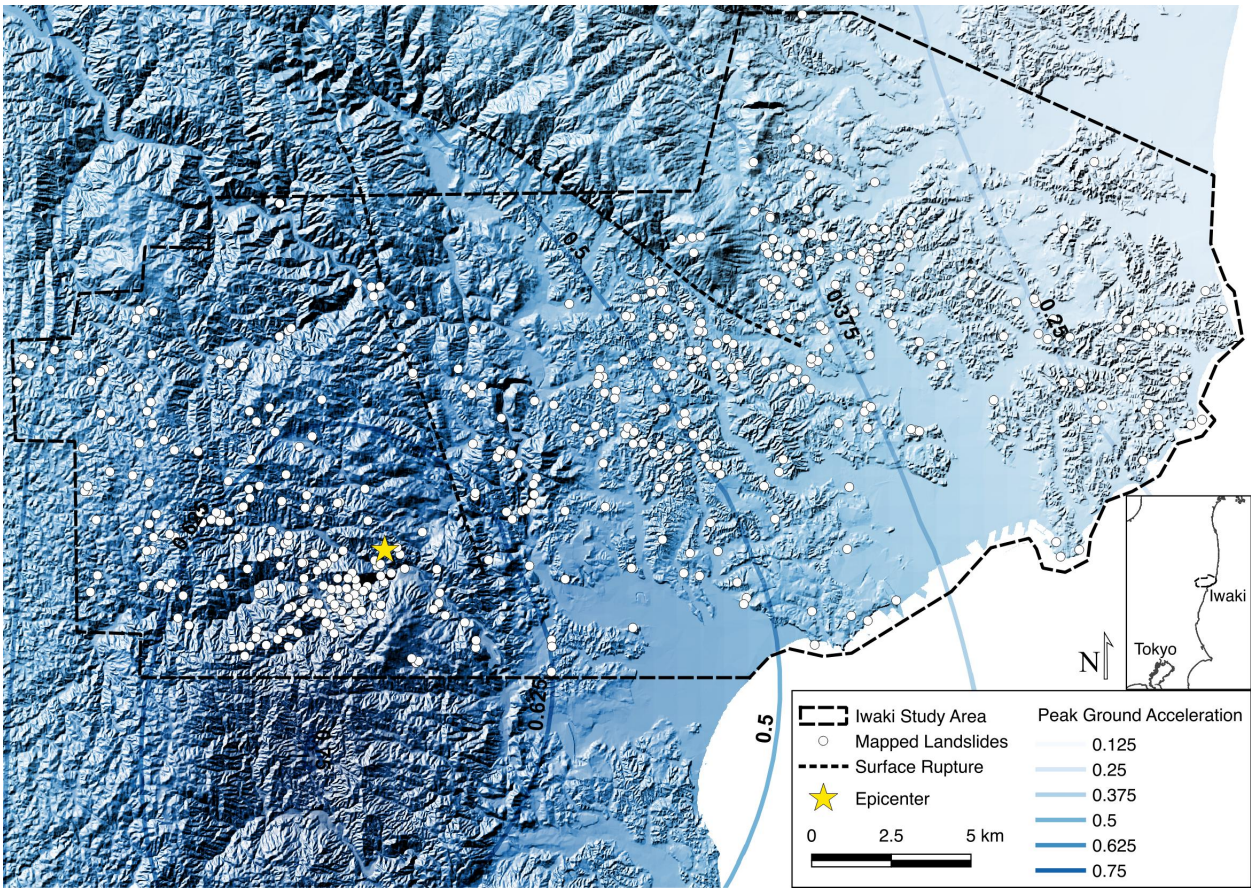

Figure 2.2 Coseismic landslides triggered by the April 11 2011 M6.6 Iwaki aftershock earthquake (Sato et al. 2013, 2015). Dashed line shows the combined study regions of Sato et al. (2015) and this study. Surface rupture along the Yunadake (northest) and Itozawa (southwest) mapped from Toda and Tsutsumi (2013).

Consideration of anthropogenic modification on the landscape as a factor for landslide susceptibility and hazard is often neglected or assessed by proxy (e.g., 'Distance to Roads' as a causal factor for landslide susceptibility, e.g., Yalcin, 2007; Song et al., 2012). Anthropogenic modification may include deforestation via development, fires, or forestry – known to increase landslide volume and occurrence by reducing root cohesion in the years to decades following removal (e.g., Schmidt et al., 2001; Lave and Burbank, 2004; Meusburger and Alewell, 2008)—or the reshaping of the landscape through slope removal and the placement of fill. In the context of coseismic landslide hazard, only Katz and Crouvi (2007) have explicitly considered the effects

of anthropogenic fill while forecasting coseismic landslide hazard. Katz and Crouvi (2007) found that the weak, loose, anthropogenic fill beneath Zefat, Israel may trigger landslides even during relatively minor earthquake shaking while nearby natural slopes remained stable, but lacked detailed coseismic inventories to confirm these findings. Previously, anthropogenic modification of the landscape has been linked to liquefaction and lateral spread damages during the Tohoku earthquake (Pradel et al., 2012). To my knowledge, no existing coseismic landslide inventory has systematically identified and mapped landslides as occurring in natural or anthropogenically modified terrain. In this study, all landslides are classified as initiating in either 'natural' or 'modified' regions to provide as yet unavailable data on the association between different landslide types and anthropogenic modification, assess differences between 'natural' and 'modified' landslides, and provide a foundation for future coseismic landslide hazard forecasting models to better incorporate the effects of anthropogenic modification.

2.2 Study Areas

The main-shock landslide study region[1] consists of an approximately 70km wide zone stretching 600km (from 35.8°N - 40.0°N) along the Pacific coast of the Honshu island of Japan covering an area of 21,808km^2 (Fig. 2.3). This study region corresponds to areas of high landslide concentration observed during a nine-day field reconnaissance conducted in April 2011 and the availability of high-resolution satellite and aerial images collected in the days and weeks following the March 11, 2011, earthquake (Wartman et al. 2013). Hikaki and Abe (2013), similarly found landslides triggered the Tohoku earthquake to stretch over an area approximately

[1] If unspecified, 'landslide study region', 'study region', or references to the landslide inventory refer to the M9.0 Tohoku earthquake and triggered landslide data (Fig. 2.3). Information pertaining to the Iwaki aftershock is always listed as such.

600km along the coastline (fault parallel), and 70km inland, with a maximum distance of 300km from the coast for one flow slide in loose Quaternary volcanic ash. A second, aftershock study region was developed based on field reconnaissance and the work of Sato et al. (2013, 2015), utilizing additional high-resolution post-earthquake images, covering 550km^2 in the Abukuma Mountains near Iwaki City (Fig. 2.3). The main-shock landslide study region includes portions of the Kitakama, Ou, and Abukuma mountain ranges, the Sendai and Kanto plains, and the large population centers of Sendai and Iwaki (Wartman et al., 2013, Fig. 2.5).

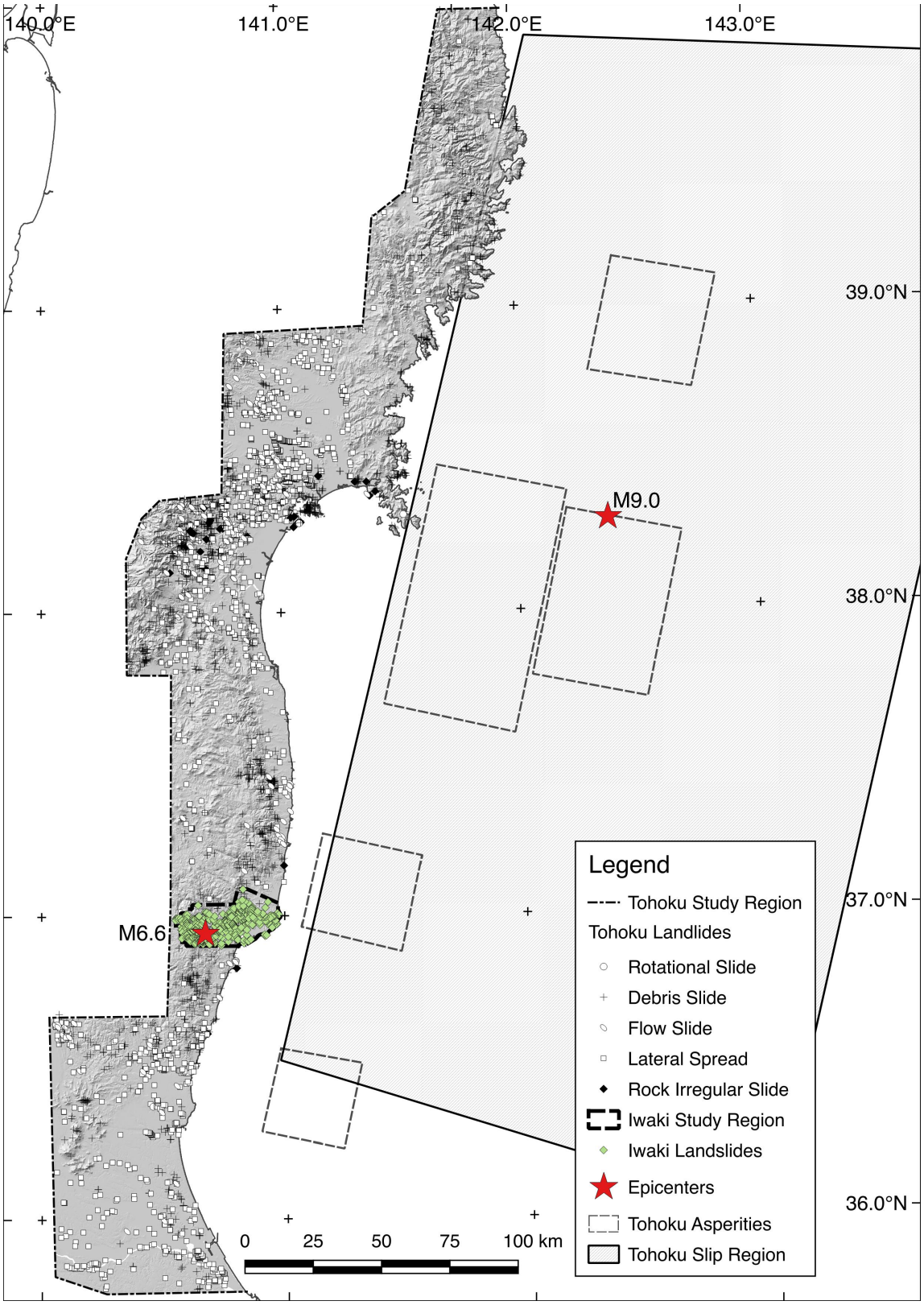

Figure 2.3 Coseismic landslides triggered by the M9.0 Tohoku and M6.6 Iwaki earthquakes. Isolated landslides reported by others outside the study bounds of this work not shown.

Study regions for both earthquakes extend as far throughout potentially landslide-generating zones as possible where high-temporal and spatial resolution images allowed for the identification and delineation of landslides that can confidently be associated with each earthquake. In many locations west of the identified study region (Tohoku), there are no cloud free images months before or after the Tohoku earthquake, making positive landslide identification impossible in a highly active region of precipitation-induced landslides, landslides triggered by other earthquakes, and human activity that quickly removed evidence of landslide activity (Fig. 2.4). Other than Wartman et al. (2013) there have been no full-scale studies of coseismic landslides triggered by the Tohoku earthquake, though several smaller-scope papers in English and Japanese identify key aspects of the landslides as a whole (e.g., Mori et al., 2012; Chigira et al., 2013; Tiwari et al., 2013). In a reconnaissance report of Tohoku landslides, Miyagi et al. (2011) report more than 2,000 small landslides occurred in cut and fill slopes in Sendai city alone despite the overall 'lack' of landslides triggered by the earthquake (Chigira et al., 2013). The 2,000 small landslides of Miyagi et al. (2011) were not presented as a detailed map, and their exact locations are unknown to us. Sendai city is within the scope of this mapping, and for all slides above the detectable limit of mapping here, 1- 4m (depending on lighting and image quality), the landslides of Miyagi et al. (2011) should be included in this dataset. Several large-scale landslides have been published as case studies outside the main study area, primarily in loose pyroclastic flow deposits of the Ou Mountain Range (Miyagi et al., 2011; Mori et al. 2012; Chigira et al., 2013; Higaki and Abe, 2013; Tiwari et al., 2013). These slides were omitted as the inclusion of a small number of extreme landslides while missing all smaller landslides in a greatly enlarged study region (>30,000km^2) would have created two disparate zones of mapping

completeness and quality, invalidating potential correlations with causal factors assessed in this study.

Figure 2.4 Landslides were mapped from the top image collected three weeks after the Tohoku earthquake. In many cases, these damaging landslides have been erased from the landscape (e.g., landslides on the right of the lower image, taken in 2014.) In many instances of smaller landslides, such as lateral spreads, evidence of landslide occurrence was completely erased from the landscape within months of the earthquake.

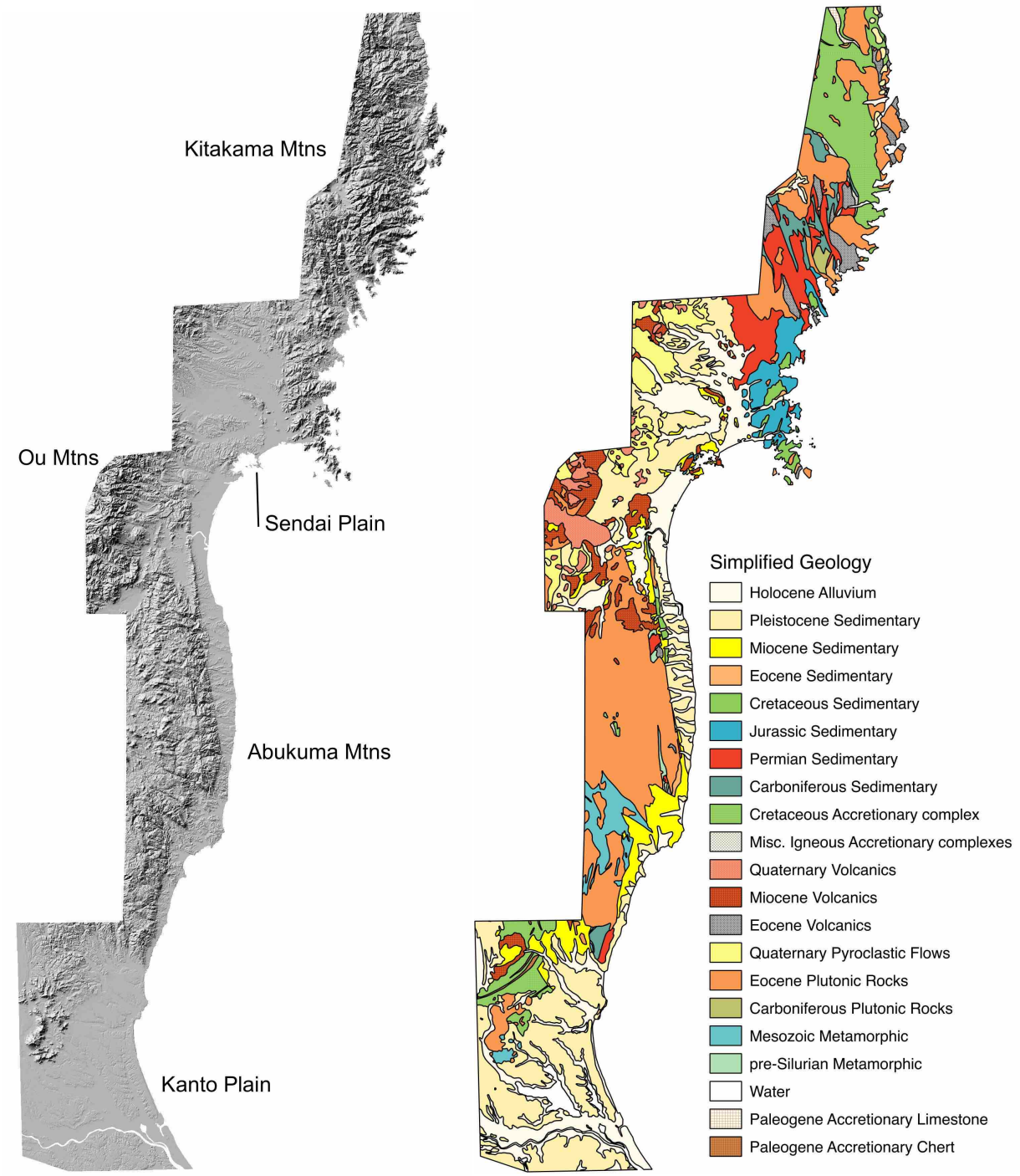

Figure 2.5 Left, Topographic regions of the landslide study region. Right, simplified geology of eastern Honshu. The flat alluvial Sendai Plain bounds the Kitakama Mountains, primarily old sedimentary rocks, to the south. The inland Ou Mountains are a younger and higher sequence of volcanic rocks and pyroclastic flows running along the western margin of the study region. To the South, the Abukuma Mountains mirror the Kitakama to the north, bounded north and south by the Sendai and Kanto Plains.

2.2.1 Geologic and Geomorphic Setting

The island of Honshu is bounded to the east by a highly active subduction margin where the Pacific plate is subducting below the Okhotsk plate at a rate of 73-78mm/year (Ozawa et al., 2011). Its proximity to an active subduction margin results in active volcanism, seismicity, orogeny, and widespread mass wasting across the study region in Honshu (Wartman et al., 2013). The steep but low lying Kitakami Mountains (Fig. 2.5) are a large accretionary complex composed of Mesozoic sedimentary rocks to the north and a Silurian to Cretaceous shallow marine sedimentary sequence to the south (Mikoshiba et al., 2004; Ujiie-Mikoshiba et al., 2006; Minoura and Hasagawa, 1992). Throughout the range, exposures of large Cretaceous plutons are also found (Mikoshiba et al., 2004). Across the Kitakami Mountains, relief is typically 300 – 500m (Yonekura et al., 2001). The Ou Range, the central mountains of Honshu, is an active volcanic front rising to elevations of up to 2000m (Ujiie-Mikoshiba et al., 2006). Only a small portion of the Ou Range is contained within the study area (southwest of the Sendai Plain) and is composed of Miocene to Quaternary volcanic rocks and pyroclastic flows. The Abukuma Mountains are primarily composed of a heavily weathered granitic Cretaceous pluton, interspersed with Cretaceous-age gneiss (Miyashiro, 1958; Faure et al., 1986). The Abukuma Mountains generally dip more gently, and are lower relief (100 – 300m, Yonekura et al., 2001) than the Ou and Kitakama Mountains. Between these mountain ranges are the Sendai and Kanto plains, mantled by unconsolidated Quaternary sediments. Both plains are flat (slopes typically less than 5°), with most of their lowlying modern topography due to anthropogenic modification (<25m in elevation). The Sendai plain is fed sediment by the Abukuma, Natori, and Nanakita rivers, and has experienced rapid progradation in the last five millennia (Matsumoto, 1985; Tamura and Masuda, 2005). The Kanto plain includes older Pleistocene age uplifted terraces in

addition to Quaternary alluvium and is fed by the Tone River, Japan's largest catchment. Both the Sendai and Kanto plains have experienced intense human occupation and development over the past few centuries. The development of cities and towns, extensive infrastructure, and tillage of the land have all permanently altered the shape of the landscape, as well as materials subject to landslides in the near-surface (i.e. Anthropogenic fill). An extraordinary example of anthropogenic change in the Kanto plain is the rerouting of the Tone River, diverted east rather than south through modern Tokyo (Pradel et al., 2012).

2.3 Methods

2.3.1 Coseismic landslide typology

All visible landslides within the study area to a minimum detectable size of 1 – 4m in width, depending on the resolution and lighting of available post-earthquake aerial images, were mapped to achieve the following objectives:

(1) Map coseismic landslides into five mechanistically distinct categories
(2) Describe the level of anthropogenic modification to each landslide source
(3) Describe the consequences, in terms of impacts to the built environment, of each landslide
(4) Revise landslide point locations identified by Wartman et al. (2013) to better reflect each landslide source
(5) Identify and map landslides triggered by the April 11, 2011 Iwaki aftershock earthquake

Distinctions in landslide type were made to reflect mechanistic and morphological differences in coseismic landslides, enable the consideration of unique consequences for each type of landslide, and better facilitate analyses of potentially causal factors for each type of landslide. Coseismic landslides considered in this work are debris slides (Fig. 2.6), flow slides (Fig. 2.7), rock irregular slides (rock slides, Fig. 2.8), rotational slides (coherent slides or slumps, Fig. 2.9), and lateral spreads (Fig. 2.10) based on Hungr et al. (2014) definitions of landslide types (Table 2.1).

Landslide typology was selected to reflect distinct landslide morphologies and failure mechanisms spanning the breadth of triggered coseismic landslide observed following the Tohoku earthquake and commonly observed coseismic landslide failures elsewhere (e.g. Northridge, CA Harp and Jibson, 1996; Chi-Chi, Taiwan, Khazai and Sitar, 2004; Christchurch, NZ Cubrinovski et al., 2011) Each mapped landslide type in this work is mechanistically distinct, and sensitive to different characteristics of the triggering earthquake ground motion. Debris slides, typically 1 – 2m in depth, are associated with high-frequency (e.g. peak ground acceleration) components of ground motions (e.g. Jibson et al., 2004; Harp et al., 2014) Rock irregular slides are highly subject to topographic amplification and the interaction between wavelength and the geometry of the exposed rock slope, but typically respond to high-frequency ground motion energy. Larger rotational slides may exhibit high-frequency wave incoherence, and are typically more sensitive to mid-frequency intensity metrics such as peak ground velocity (e.g. Kramer, 1996). Lateral spreads and flows, occurring in different portions of the landscape, are driven by the accumulation of pore water pressures and cyclic degradation of strength sensitive to a critical combination of ground motion intensity, frequency content, and duration (Kramer, 1996). Additional mechanistically significant distinctions, such as rock falls versus rock wedge failures, were not made due to the inability to make fine-scale distinctions in available aerial images and the lack in availability of data necessary to model such distinctions in a forward-modeling framework at this scale.

Landslide Type	Description
Debris Slide [Disrupted Soil Slide]	Sliding of a mass of granular material on a shallow, planar surface parallel with the ground. Usually, the sliding mass is a veneer of colluvium, weathered soil, or pyroclastic deposits resting on a stronger substrate.
Flow Slide [Rapid soil flow]	Very rapid to extremely rapid flow of sorted or unsorted saturated granular material on moderate slopes, involving excess pore-pressure or liquefaction of material originating from the landslide source.
Rock Irregular Slide [Rock Slide]	Sliding of a rock mass on an irregular rupture surface consisting of a number of randomly-oriented joints, separated by segments of intact rock ("rock bridges"). Occurs in strong rocks with non-systematic structure. Failure mechanism is very complex and often difficult to describe. May include elements of toppling. Definition in this context stretched to include rock slides with more well-defined failure surfaces, from Keefer: "Rock slides are disordered during movement into masses of rock fragments and blocks that slide on planar or gently curved surfaces where joints, bedding planes, or other surfaces of discontinuity dip out of slopes"
Rotational Slide [Soil Slump]	Sliding of a mass of (homogeneous and usually cohesive) soil on a cylindrical or ellipsoidal rupture surface.
Lateral Spread	Extremely rapid lateral spreading of a series of soil blocks, floating on a layer of saturated (loose) granular soil, liquefied by earthquake shaking or spontaneous liquefaction.

Table 2.1 Landslide types and definitions used in this study. Terminology and definitions adapted from Hungr et al. (2014), with equivalent terminology from Keefer (1984) in brackets.

Figure 2.6 Simplified diagram (left) and an example Debris Slide. Often high in the landscape along undeveloped, steep, hillslopes. Shallow failure surfaces with highly displaced and disorganized mobilized material. Figure from Highland and Bobrowsky (2008), based on Cruden and Varnes (1996), photograph by Réjean Couture.

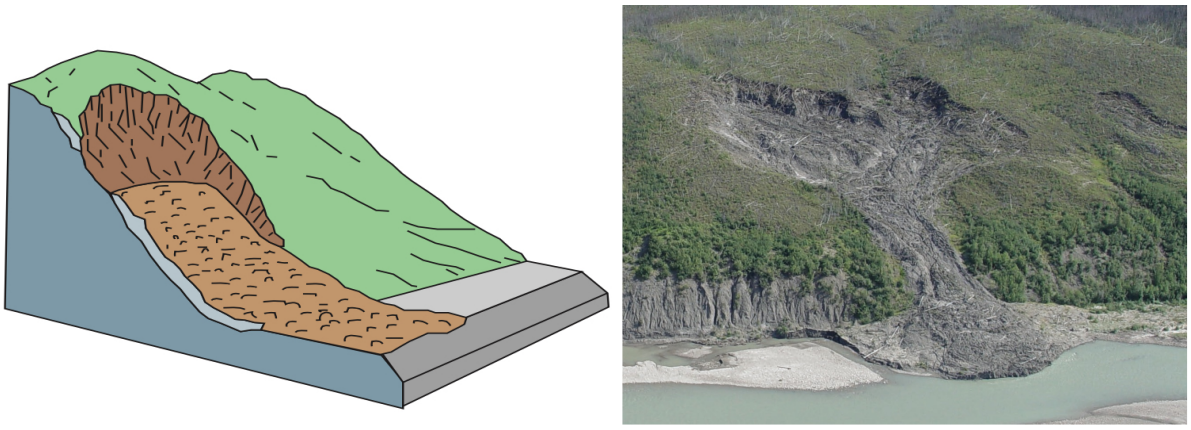

Figure 2.7 Simplified diagram (left) and an example Flow Slide. Source often region similar to lateral spreads, in agricultural or otherwise developed land, large highly disrupted displacements with some evidence of fluidization or semi-fluid like flow. Figure from Highland and Bobrowsky (2008), based on Cruden and Varnes (1996), photograph by Marten Geertsema.

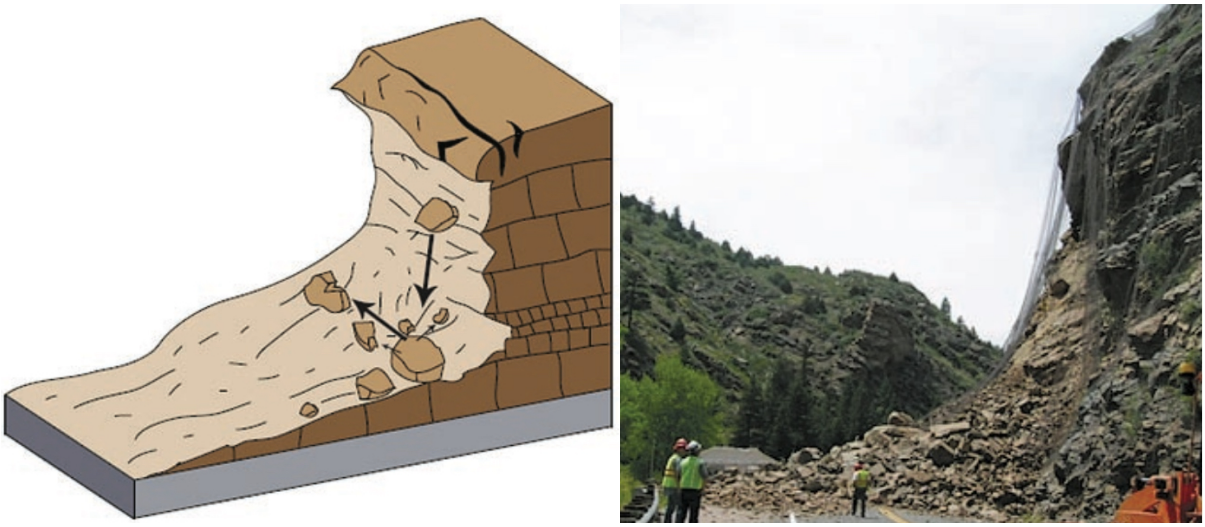

Figure 2.8 Simplified diagram (left) and an example Rock Irregular Slide. Diverse in failure mechanism, all involving large rock masses (boulders pictured are 8 – 10m long) failing from exposed bedrock. Distinguished from debris slides by the size of failed material (>5m blocks) and sense of movement including all falls and topples of intact material. Figure from Highland and Bobrowsky (2008), based on Cruden and Varnes (1996), photograph by the Colorado Geological Survey.

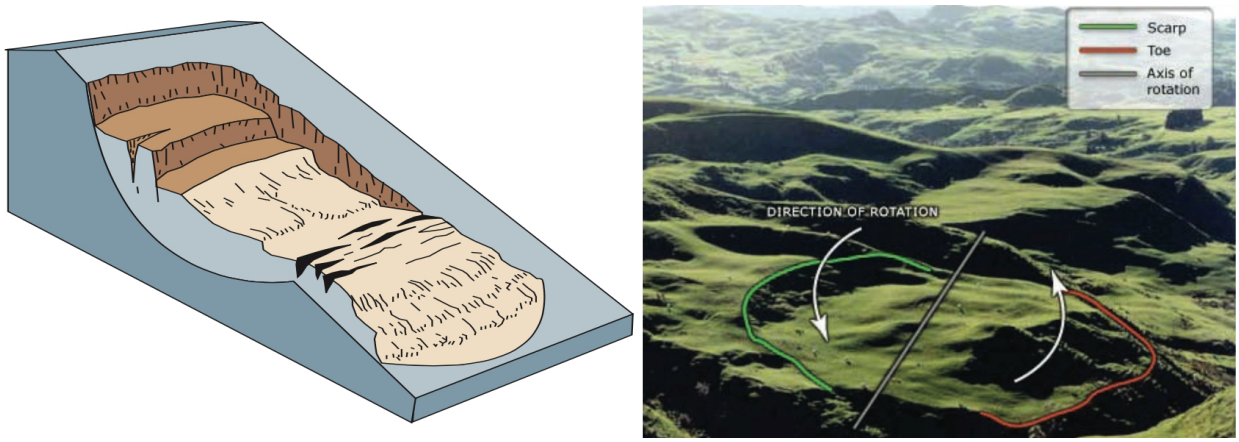

Figure 2.9 Simplified diagram (left) and an example Rotational Slide. Inferred movement along a rotational plane from a distinct head scarp to a largely-intact deposition zone. In the above, a large section of trees appears to have been displaced en masse downslope from the upper head scarp. Retrogressive tension cracks are just visible in the pavement, upper left corner. Figure from Highland and Bobrowsky (2008), based on Cruden and Varnes (1996), photograph by Michael J. Crozier.

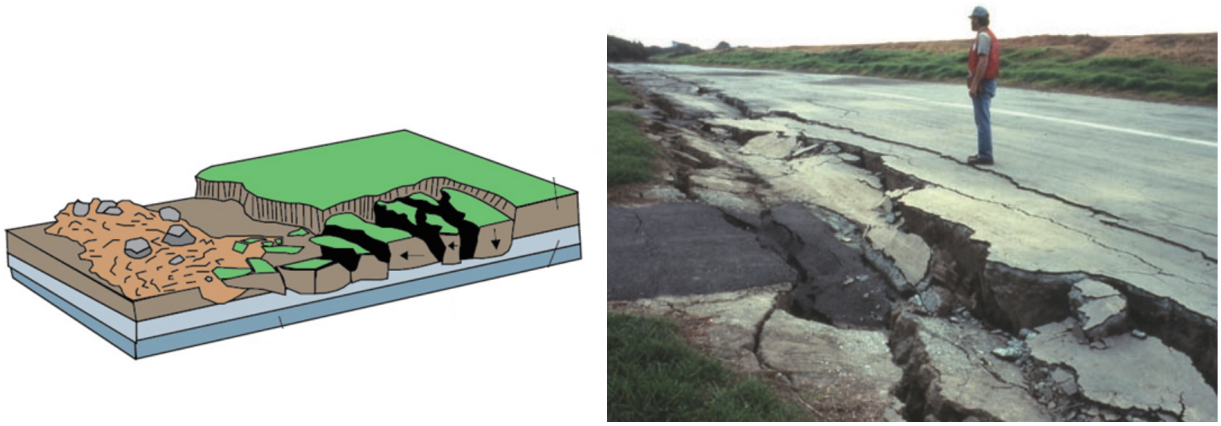

Figure 2.10 Simplified diagram (left) and an example Lateral Spread. Located in modified landscapes (e.g., levees, irrigated fields, and golf courses as in the above). Often extensive, with complex boundaries and movement. Visible deformation correlated with slope or proximity to a free face. Located in near-flat terrain, sometimes transitioning into flows when steep topography is located directly below source zone. Figure from Highland and Bobrowsky (2008), based on Cruden and Varnes (1996), photograph by Steve Ellen.

For each landslide identified in post-earthquake aerial images, a representative point was mapped at the centroid of the source region of the landslide. The source region was defined as the area of material loss or lowering within the observed landslide body. Polygons outlining the landslide source (loss or lowering of the landscape) and depositional zone (areas of material accumulation in the downslope portions of the landslide) were adopted from Wartman et al. (2013) where

possible for landslide size measurements. Landslide type was determined from the descriptions of Hungr et al. (2014), and the morphology of landslide deposits. Landslides where movement clearly occurred along a rotational path, with a single-coherent block comprising the landslide deposit were classified as rotational slides. Disrupted, thin, and planar (non-channelized) landslide deposits were classified as Debris slides. Large individual rock-blocks (>5m) with source regions in exposed bedrock or rock-like material were classified as rock irregular slides. Landslide masses exhibiting evidence of fluidization, or fluid-like flow with significant (>10m) downslope (typically channelized) displacement were classified as flow slides. Lateral spreads were identified by blocky-fractured ground, sometimes with small water-filled depressions, often in relatively flat portions of the landscape. Many lateral spread ground cracks were covered in blue tarps to prevent water infiltration following the Tohoku earthquake, aiding in their identification in available images. Coseismic landslide mapping from the Tohoku earthquake was conducted by Liu and Grant (*unpublished report*) over more than 200-hours to augment and revise the previous coseismic landslide inventory of Wartman et al. (2013).

2.3.2 Anthropogenic modification classification

Anthropogenic modification was initially divided into four categories that were assigned to each landslide: natural slopes, or no observed anthropogenic changes; modified ground, encompassing agricultural areas and unnatural terrain such as golf courses; moderate influence, i.e. logging in steep terrain or roadways above a landslide source; and highly modified slopes, all engineered slopes and cuts into a source area that could directly lead to destabilization (Table 2.2). In later analyses, anthropogenic modification was simplified into two classes: ‘modified’ (low – moderate – high) and ‘unmodified’ (natural slopes). Simplification of classification was done

due to the negligible differences observed between the anthropogenic classes with respect to their effect on explanatory variables such as slope, and the uncertainties in ranking the many types of human modification into different classes.

Initial Classification	Final Classification	Description
Natural Slopes	Natural	no apparent human modification to slope. No part of the landslide source area intersects roadways, fill, or has been reshaped by humans. Landslide source zone is not immediately above a roadway or other cut that may have increased landslide susceptibility, though runout deposits may cover a more distance road or anthropogenic feature.
Low	Modified	Landslide source zone was located fully or partially in modified ground such as golf courses, farms, parks, or other human developed grassland. Ground surface may be grass or sand, and ponds are frequently present; anthropogenic fill is often observed as part of the landslide body.
Moderate		Human-caused changes to the landscape including denuding a steep (>15°) vegetated slope, development of infrastructure above a landslide source, or development of infrastructure at the toe of a landslide source without major modifications to the natural slope.
High		all artificial or "engineered" slopes (e.g., levees, reservoirs, regraded slopes), road cuts in natural or engineered slopes affecting landslide source zones, and slopes in urban areas with infrastructure at both the source and toe of landslide sources.

Table 2.2 Anthropogenic modification scheme used in this study.

Landslides occurred in a wide variety of anthropogenically modified terrain. Many were along roadways or regrading projects where either the toe of the eventual landslide was cut into and thus partially destabilized, or the source region of the landslide was regraded and partially or fully replaced with fill materials (Fig. 2.11). Anthropogenically modified landslide occurred in otherwise stable environments (Fig. 2.12), where changes to the landscape promoted clusters of landslides due to some combination of increased ground saturation via irrigation, comparably weak fill deposits, reshaping and over-steepening of the landscape, and the construction of extensive artificial slopes (e.g., levees). Anthropogenically modified lateral spreads were particularly common along levee systems and canals throughout the study region. Fig. 2.13 shows an area north of Sendai where hundreds of small lateral spreads, triggered in anthropogenic fill, caused widespread damages to levee systems and roadways.

Figure 2.11 Example anthropogenically modified landslides in the foothills of the Ou Mountains west of Sendai, Japan. Landslide bodies outlined in white. For all landslides the source region abuts either a roadway or parking lot, with some landslides failing entirely in anthropogenic fill deposits.

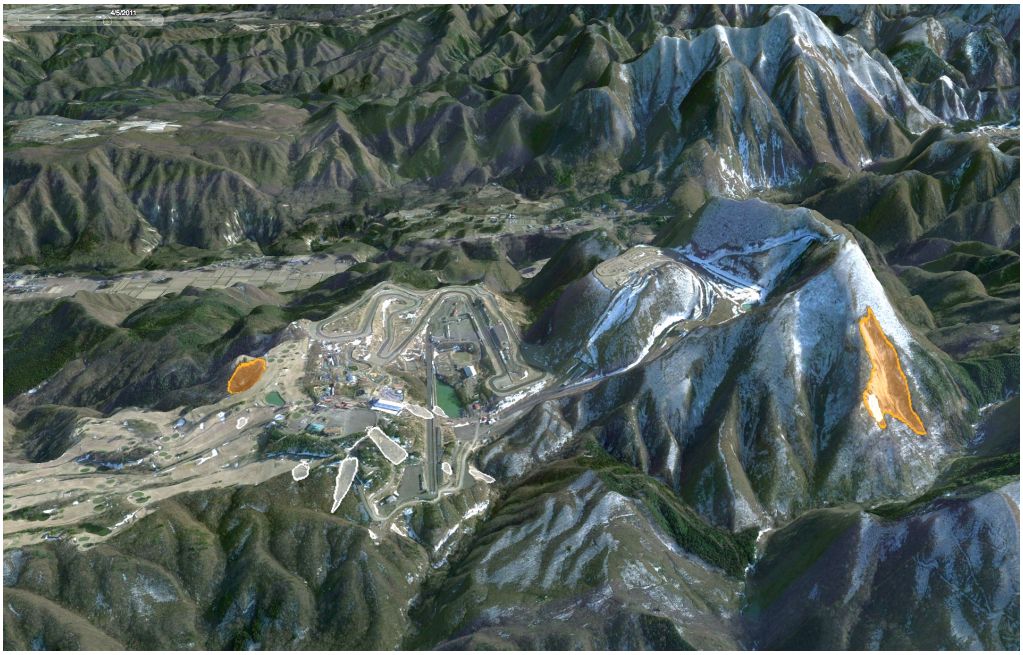

Figure 2.12 Unmodified hillslopes immediately surrounding Fig. 2.11 (Hi-Land race track and golf course) where virtually no coseismic landslides were triggered. Landslides triggered by the Tohoku earthquake shown in white, pre-existing landslides shown in orange. Vertical exaggeration: 2x.

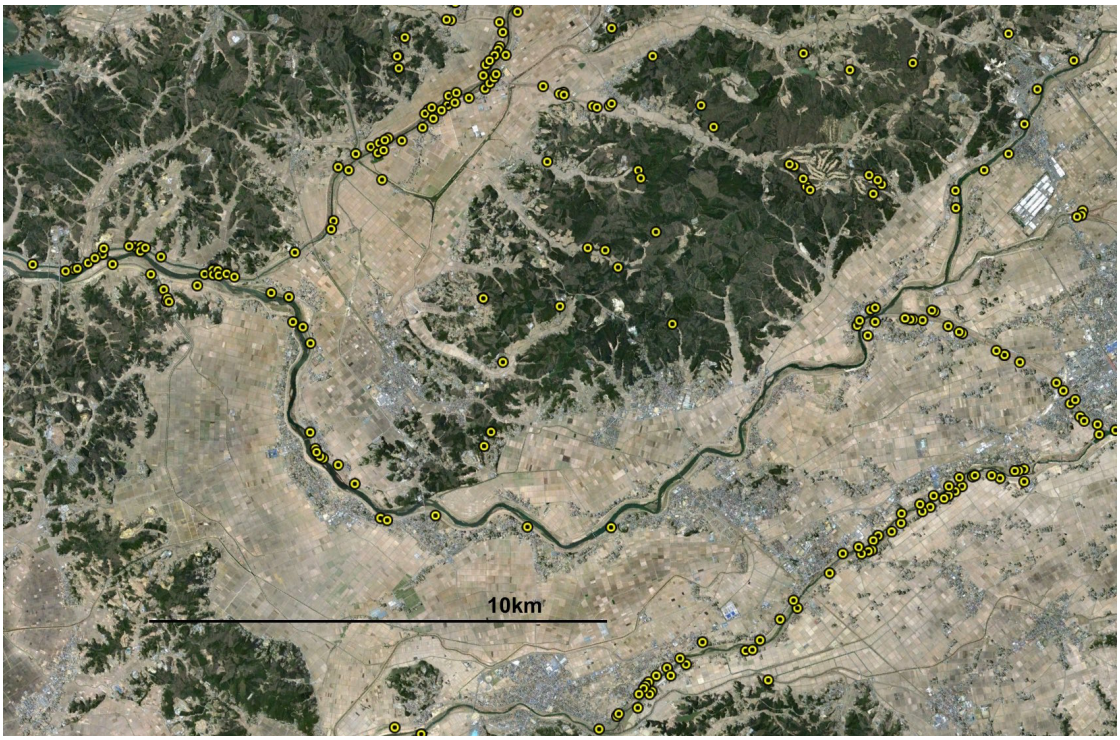

Figure 2.13 Detail from the mapped distribution of landslides highlighting the prevalence of lateral spreads (yellow dots) occurring along river and canal levees.

2.3.3 Landslide consequences to the built environment

Built environment consequences due to landslide impacts were divided into four categories: none, or no impact on the built environment; developed area impact, damage to non-structural and non-roadway elements such as sports fields; road impacts, landslides damaging or destroying major or minor roadways; and structural impacts (Table 2.3). All mapped landslides were assigned an impact category from these definitions to assess the relative significance of each type of landslide on impacts to the built environment. Consequences to the natural environment (e.g., sediment mobilizations, vegetation loss) or direct human losses were not considered in this study.

Landslide Consequences	Description
None	No impact on the built environment
Developed Area Impact	Non-structural damages due to landslides generating economic loss or expenditure, e.g., lateral spreading along a levee that necessitated repair work
Road Impact	Landslide partially or fully covered or destroys a segment of road or major path
Structural Impact	Landslide impact on a residential dwelling, commercial building, or other structure. Damage may be marginal to total

Table 2.3 Classification scheme for assessed consequences of landslide impacts to the built environment.

2.3.4 Iwaki Aftershock Landslides

Twenty landslides mapped in the original Wartman et al. (2013) dataset were attributed to a large (M6.6) aftershock earthquake that occurred in the Iwaki City area on April 11, 2011, based on a comparison of pre- and post-event images and field reconnaissance that occurred following the aftershock. A much larger set of coseismic landslides associated with the April 11 aftershock by Sato et al. (2013, 2015) was digitized from published paper maps and combined with field-identified landslide locations to produce a merged Iwaki coseismic landslide inventory of 456 landslides of undifferentiated type (Fig. 2.14). The Sato et al. (2013, 2015) coseismic landslide dataset was manually mapped from post-April 11 aerial images collected by the Geospatial Information Authority of Japan, consisting of landslides in excess of 5m wide that caused some degree of vegetation damage or removal. Additional landslides presented in Sato et al. (2015) of unknown origin date were not digitized or included in these data as they may have been triggered by rainfall, human interference, or another earthquake.

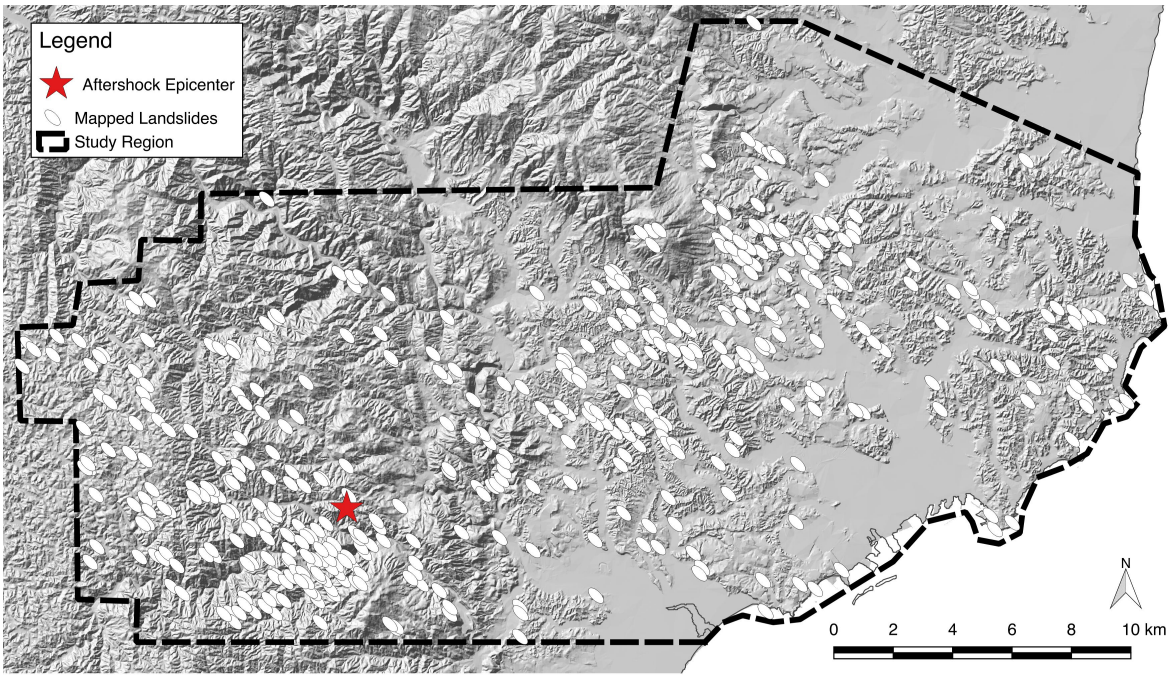

Figure 2.14 Coseismic landslides of the April 11 M6.6 Iwaki aftershock digitized from Sato et al. (2013, 2015) and mapped in this study.

2.3.5 Data resources

Ground motion acceleration time history records from 547 strong motion k-net and kik-net stations were collected from the National Research Institute for Earth Science and Disaster Prevention (NIED) in Japan (obtained at http://www.kyoshin.bosai.go.jp/ last accessed November, 2017). Distributions of peak ground acceleration (PGA), peak ground velocity (PGV), and Modified Mercalli Index (MMI) were adopted from the USGS (2017, Fig. 2.15). The earthquake epicenter and estimated extent of fault rupture were adopted from the USGS. Earthquake asperity (strong motion generation areas) locations were adopted from Kurahashi and Irikura (2011, Fig. 2.1). Epicentet location, fault geometry, and asperities were then used to compute epicentral distance (R_{epi}), closest surface projection distance to the fault (R_{jb}), and closest distance to an asperity (R_{asp}) for all landslides in the study region. A 1:200,000 scale digital geologic map of Japan, developed by the Geological Survey of Japan (2009), along with a 10m Digital Elevation Model (DEM, Geospatial Information Authority of Japan, 2017) were

used for all analyses including the development of secondary topographic measures, e.g., slope. Point source data (e.g., precipitation gauges and seismic ground recordings) were interpolated to generate geospatially continuous data for analyses. Interpolation was performed in ArcGIS via kriging assuming an exponential semivariogram model using default input parameters. In cases where geospatially continuous data were available, e.g., topography, geology, or pre-processed data from the USGS, no interpolation or modification was made.

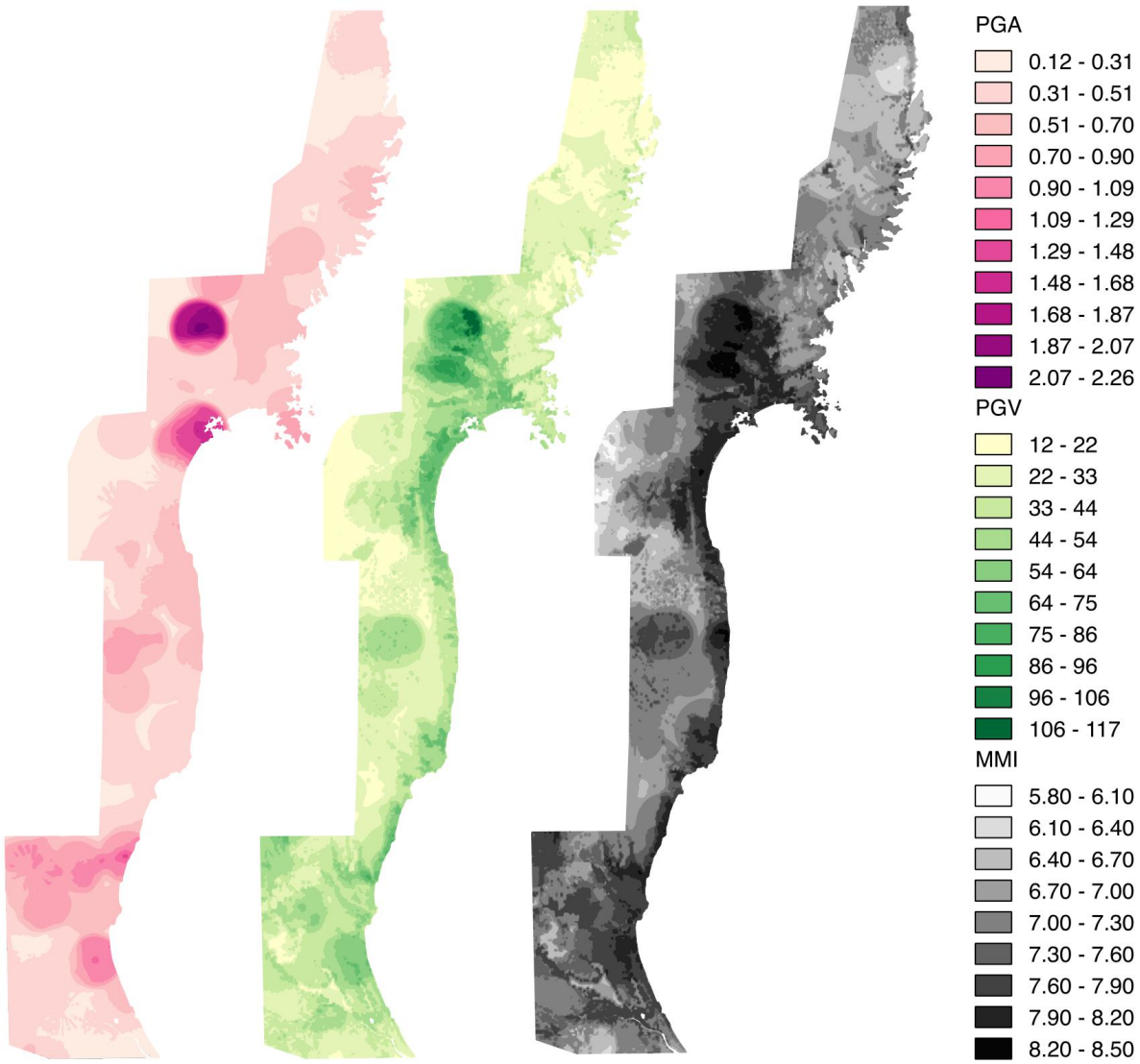

Figure 2.15 Peak ground acceleration, velocity, and Modified Mercalli Index data provided by the USGS for the M9.0 Tohoku earthquake.

Chigira et al. (2013) have suggested the relative lack of 60-day antecedent rainfall (94mm near triggered flows as low as 50mm elsewhere) compared to previous earthquakes was responsible for the perceived lack of large-scale landslides in pyroclastic flow deposits. Previously, Uzuoka et al. (2005) have reported antecedent rainfall effects the number, distribution, and types of landslides triggered in Japan. Similarly, Sassa et al. (2005), comparing two similarly-sized Japanese earthquakes in the same region of Japan found far more and larger landslides triggered by a M6.8 wet-season earthquake than a previous M7.2 dry-season earthquake. Rainfall data were collected from 79 weather stations operated by the Japan Meteorological Agency (2017) to generate antecedent rainfall maps across the study region for 1, 2, and 3-month cumulative rainfall prior to the Tohoku earthquake. These data were collected to supplement the small sample of climatic records (3) presented in Wartman et al. (2013) to assess potential relationships between landslide concentrations, particularly for flow slides and lateral spreads, and antecedent rainfall. Fig. 2.16 shows the 2-month antecedent rainfall totals for the Tohoku landslide study area. 1-month and 3-month time-windows show similar patterns in distribution.

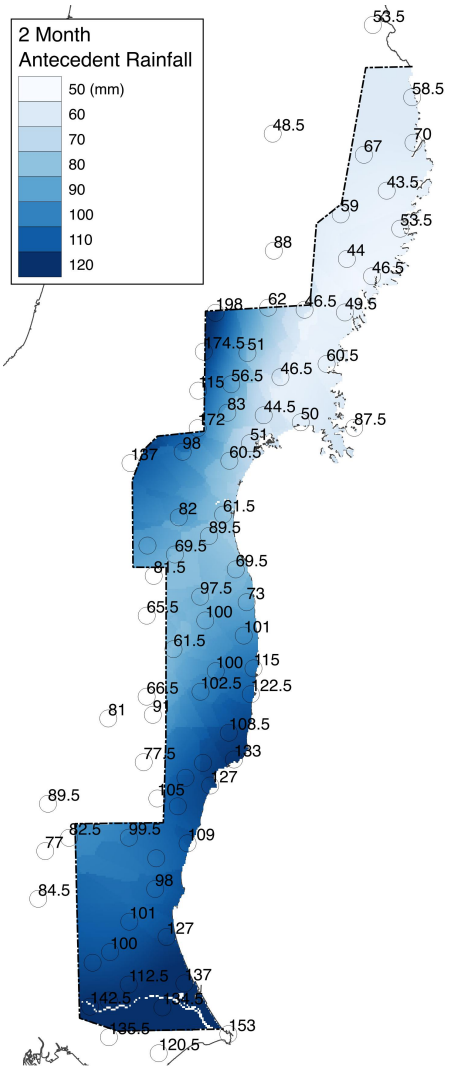

Figure 2.16 2-month antecedent rainfall within the landslide study region. Japan Meteorological Agency stations (open circles) used in this analysis are labeled with 2-month (January and February) rainfall totals in mm.

2.3.6 Analysis Methods

The most common factor analysis method for coseismic landslide inventories is the construction of bivariate statistics between some potentially causal landslide factor and a metric for landslide density or concentration. Utilizing bivariate statistical relationships, many have found strong relationships between landslide intensity or concentration and ground shaking intensity measures, e.g., peak ground acceleration, peak ground velocity, Arias Intensity, and Modified Mercalli Index (MMI): Khazai and Sitar (2004), Meunier et al. (2007), Lee et al. (2008), Wang

et al. (2007), Dai et al. (2011), Collins et al. (2012), Xu et al. (2014), Kritikos et al. (2015). Additional metrics commonly assessed are slope – where landslide concentrations have been found to increase with slope in all cases, often most markedly above 35° (e.g., Dai et al., 2011), Aspect, for very small regions a measure of geologic structure that may preferentially develop failures, Elevation, and geology are often considered.

In this work, three landslide concentration measures were tested.

1. Landslide concentration: defined as the number of landslides per square kilometer (LS/km^2), provides a raw accounting of how many landslides occurred. Landslide concentration is highly sensitive to the number of triggered landslides, and the overall study area extents, making it difficult to compare types of landslides with very different numbers of triggered landslides.
2. Landslide fraction (LF), is the fraction of landslides occurring in a particular intensity measure (IM) range. Landslide fraction directly compares where the majority of landslides occurred given a particular intensity measure (e.g., PGA) but ignores the overall rate of that IM.
3. Frequency Ratio (FR), is the ratio between the fraction of landslides to the fraction of overall study region for a particular IM range. Frequency ratio provides a relative measure across a particular IM where landslides were more or less abundant than the null hypothesis that landslides occur at the same rate as the background weight (FR = 1.0) but is subject to large swings when the total number of landslides is small ($N < 50$).

Landslide fraction (LF) and frequency ratio (FR) data for the distribution of peak ground accelerations (in units of gravity, g) are shown for the entire study area (background rate) and all mapped landslides in Fig. 2.17A. The background and landslide trends with peak ground acceleration are similar with a strong peak at 0.5g but otherwise only small differences are observed. When the distribution of landslides is normalized by the background rate (FR) deviations between landslides and the background are highlighted (Fig. 2.17B), such as the spike in relative landslide occurrence from 1.5 – 1.7g. Fig. 2.17C shows these same data expressed as LS/km^2 revealing the same patterns as FR. In this work, frequency ratio is preferred as it best highlights those regions where landslides disproportionately occurred or didn't occur, relative to the overall study region (Xiaoli et al., 2015).

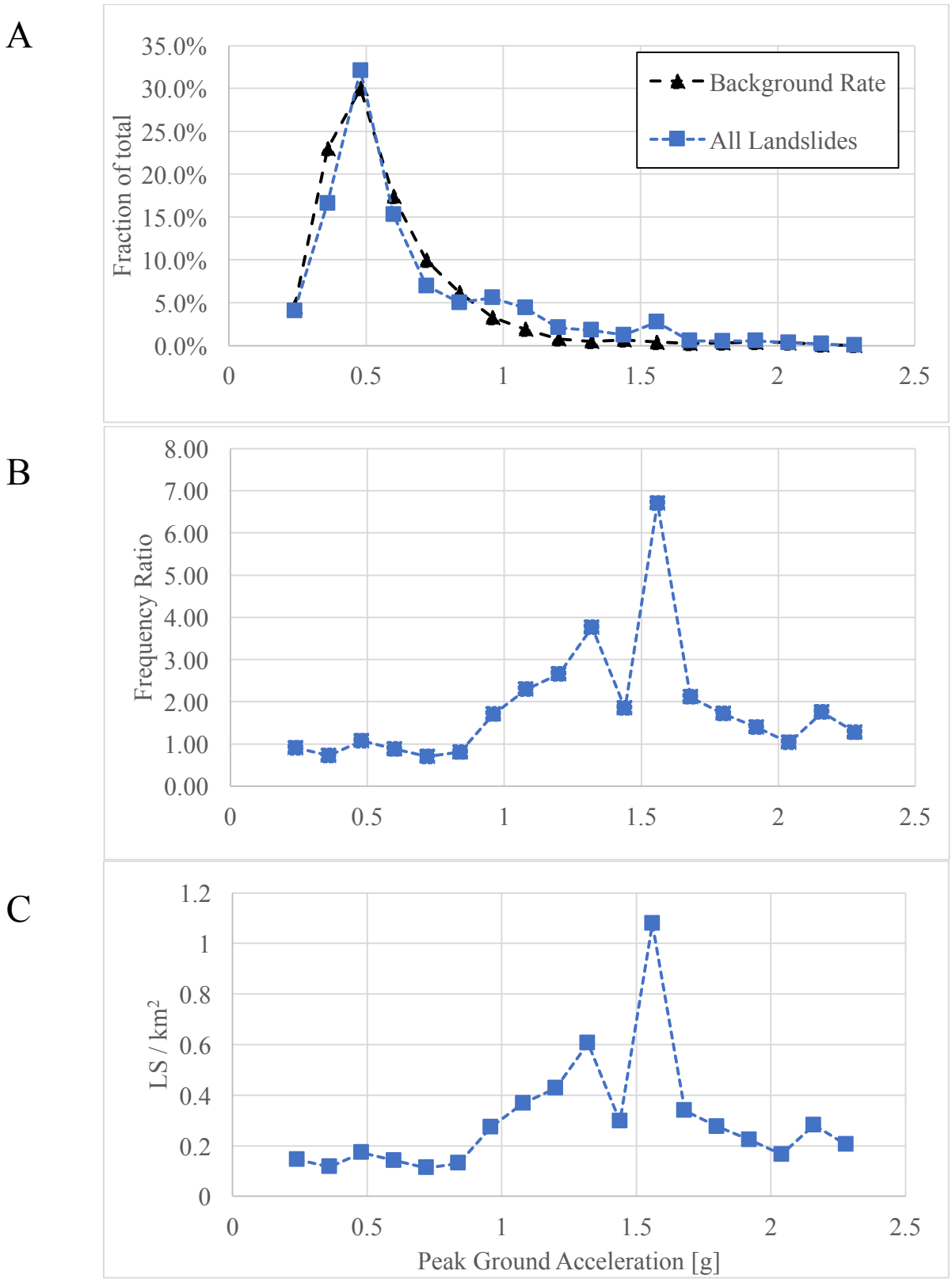

Figure 2.17 A, Landslide fraction and background rate for peak ground accelerations during the Tohoku earthquake. B, Frequency ratios for all landslides derived from A. C, Landslides per square kilometer for all modes of sliding as a function of PGA bins.

Material strengths for geologic units were estimated from known age-strength relationships for Japanese rock (Okamoto et al., 1981, Fig. 2.18) and reasonable estimates based on similar reference materials (e.g., de Vallejo and Ferrer, 2012). For geologic materials with large (N > 50) populations of unmodified debris slides (9 of 21 geologic units, shaded in Table 2.7), the methodology of Gallen et al. (2015, 2017) was adopted to develop quantitative estimates of material strength (internal friction angle and cohesion) occurring in natural slopes.

Relying on well-mapped coseismic landslide inventories, mapped peak ground acceleration from the USGS, digital topography, and surficial geologic mapping, Gallen et al. (2015, 2017) reverse typical landslide hazard mapping procedures to take known landslide distributions to infer the strength of the failed materials. They first assume shallow landslides behave as simple infinite slopes:

$$FS = \frac{c}{\gamma t sin\beta} + \frac{tan\phi}{tan\beta} \qquad \text{Equation 2.1}$$

where FS is the static factor of safety of the slope, γ is the unit weight of the material, t is the thickness of the failed slide, β is the slope angle, and c and ϕ are the material strengths cohesion and friction angle, and that failure is governed by Newmark sliding-block (1965) assumptions:

$$k_y = (FS - 1)sin\beta \qquad \text{Equation 2.2}$$

where k_y is the yield acceleration above which the slope will fail. Since we know the mapped landslides failed, in this formulation $k_y/PGA < 1.0$, we can combine each of these equations:

$$\frac{k_y}{PGA} = \frac{\left(\frac{c}{\gamma t sin\beta} + \frac{tan\phi}{tan\beta} - 1\right) sin\beta}{PGA} \leq 1.0 \qquad \text{Equation 2.3}$$

If we rearrange Eq. 2.3 to solve for cohesional strength of the material (c):

$$c \leq PGAt\gamma - \left(1 - m\frac{\gamma_w}{\gamma}\right)\frac{t\gamma tan\phi}{tan\beta} + t\gamma \qquad \text{Equation 2.4}$$

Assuming typical values for all right-hand values (t = 2m, ϕ = 15°, β from 10m resolution DEM data, m = 2 month antecedent rainfall (mm) / 200, γ = 20kN/m^3, γ_w = 10kN/m^3) the cohesional limit strength was computed for all debris slides. As this method is built upon infinite slope assumptions, back-analyzed material strengths were solely based on *unmodified* debris slides as they most closely resemble infinite slope assumptions and may poorly reflect conditions affecting deeper modes of failure (coherent rotational slides, flow slides) and those driven by liquefaction phenomena (lateral spreads, flow slides). Strengths derived in this manner are a lower bound estimate as the ratio k_y/PGA for many slides may have been much closer to 0 – 0.5 than 1.0 as used in calculations. For quantitative strength estimates, the 20th percentile strength, that is cohesional values above which 80% of landslides were calculated to have occurred, was adopted. Material strength estimates were then modified, or for materials without sufficient unmodified debris slides entirely, based on the findings of Okamoto et al. (1981). Okamoto et al. (1981, Fig. 2.18) found sedimentary rock strength in Japan, measured as unconfined compressive strength (UCS) increase significantly with age due to consolidation, compaction, and cementation of the source grains. Additional modification to material strengths were adopted to

reflect more physically realistic conditions (e.g., water is assigned no strength.) Assigned material strengths are comparable with typical values reported elsewhere (e.g. Goodman, 1989).

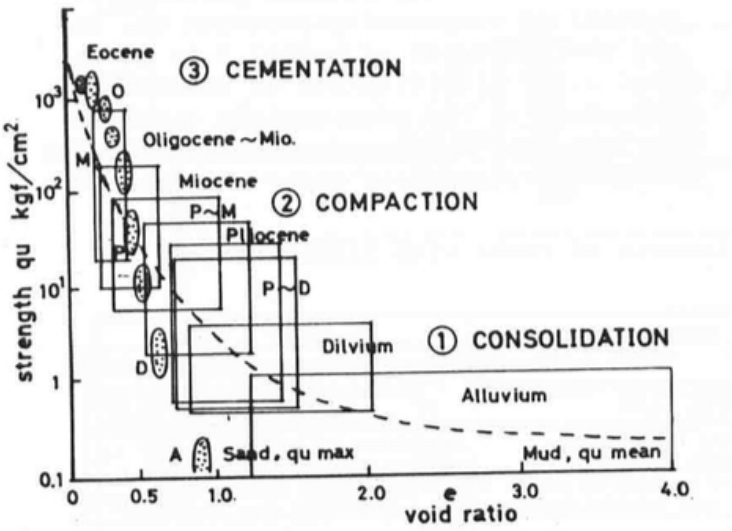

Fig. 1.6 Change in physical properties of Cenozoic sediments in Japan with lithification (qu; unconfined compressive strength)

Figure 2.18 From Okamoto et al. (1981) observing the effects of lithification on rock strength in Japan.

For geologic units with sufficient (>15) numbers of unmodified and modified debris flows, this process was repeated to estimate material strengths for modified debris slides and assess if a difference in computed cohesional strength at failure was present between the two landslide populations.

A multivariate relationship incorporating triggering and resisting factors was then developed to assess landslide concentration (FR). Adopting the same physics-based framework as Chapter 1 (Grant et al., 2016), landslide susceptibility to failure was defined as:

$$k_y = \left(\frac{c}{\gamma t sin\beta} + \frac{tan\phi}{tan\beta} - 1\right) sin\beta \qquad \text{Equation 2.5}$$

where c and ϕ are strength parameters based on age-strength relationships and unmodified disrupted landslides described above, γ is an assumed uniform weight of material 19kN/m^3, β is the DEM derived slope, and t is an assumed failure thickness of 2m. In all cases, ground saturation is neglected, as is potential compliance or strain-softening of the landslide mass. PGA was then applied as a triggering factor to compute the ratio k_y/PGA, reflecting the relative likelihood of landslide occurrence. k_y/PGA values less than approximately 1.0 should indicate landslides, while values much greater than 1.0 should be unconditionally stable given this particular earthquake and setting.

To further quantify the relationship between casual factors and landslide occurrence bivariate and multivariate logistic regression was performed for two sets of analyses. First, to test the predictive power of causal factors on the initiation of all, or particular, modes of landslides. Second, to assess any differences between natural and modified slope failures. Logistic regression enables the modeling of some binary response (slide or no slide) as a function of some set of continuous or qualitative independent variables (e.g., slope, peak ground acceleration, antecedent rainfall). Logistic regression has been applied to landslide and liquefaction susceptibility and hazard assessments by many (e.g., Ayalew and Yamagishi, 2005; Yesilnacar and Topal, 2005; Chang et al., 2007; García-Rodriguez et al., 2008; Nefeslioglu et al., 2008; Yilmaz, 2009; Oommen et al., 2011; Abdulwahid and Pradhan, 2016) and is well suited to describing the relationship between topographic and geologic factors and, in this case, landslide triggering. Logistic regression output was expressed as the increased likelihood of some event (landslide occurrence) given a unit increase in the predictor variable (e.g., 1° increase in

topographic slope). The sign and magnitude of this change in likelihood can be interpreted as the strength of the predictor on the response, and their relative relationship i.e. do increases in slope increase or decrease the likelihood of landslide occurrence, and to what degree (Weisberg, 2005)

2.4 Results

3,508 landslides triggered by the March 11, 2011, M9.0 Tohoku, Japan earthquake were mapped. In the data presented here, 48.3% (1694) of mapped landslides are classified as debris slides, 45.1% (1584) as lateral spreads, 5.2% (181) flow slides, 1.2% (42) irregular rock failures, and 0.2% (7) rotational slides. In preparing this new coseismic landslide dataset 26 landslides of Wartman et al. (2013) were reclassified as aftershock triggered, and 56 additional landslides, compiled from additional aerial images and post-disaster reconnaissance reports, were mapped producing a final revised database of 3,508 coseismic landslides.

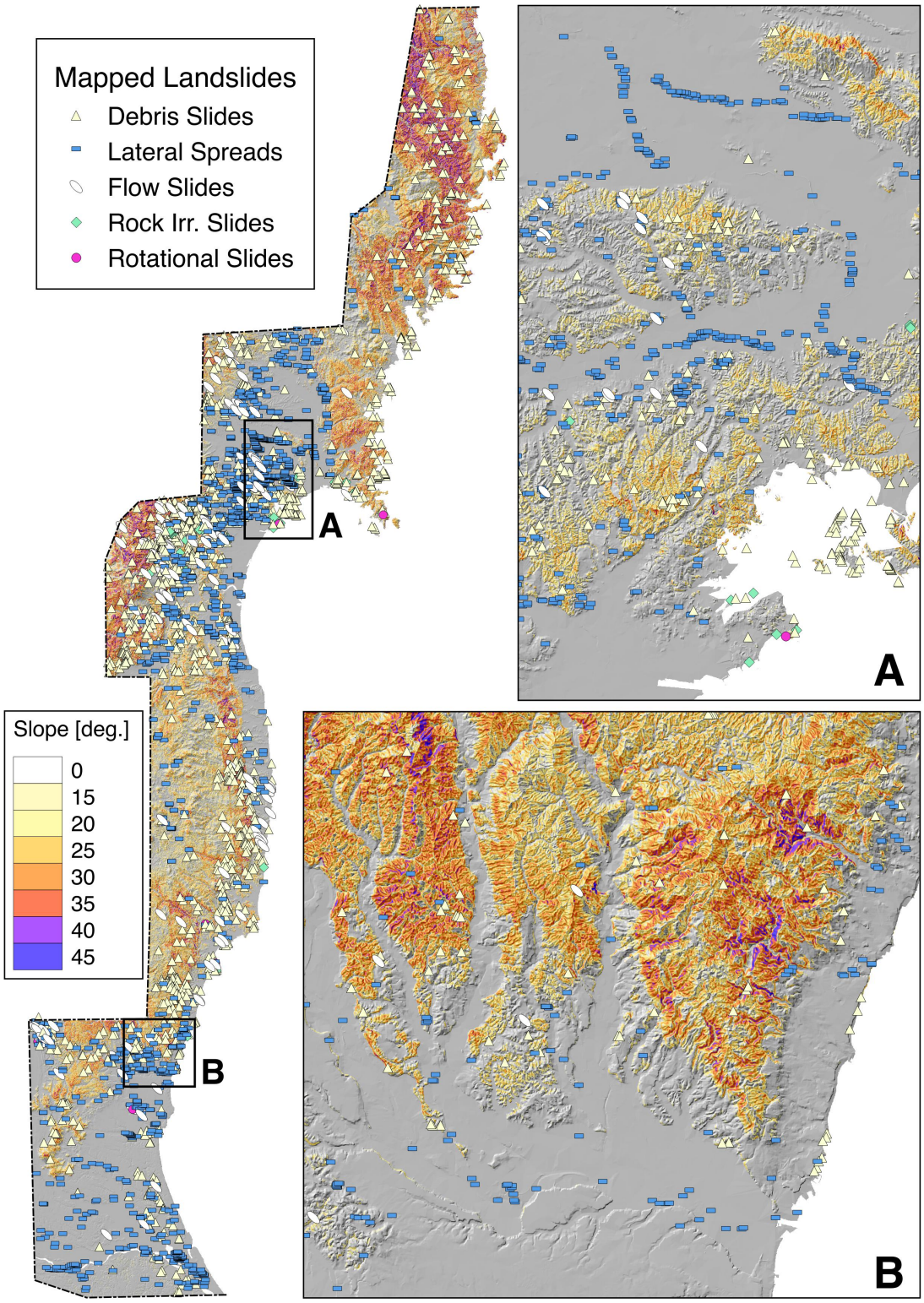

Figure 2.19 Mapped landslides following the M9.0 2011 Tohoku earthquake disaggregated by mode (type) of landslide. A, detail of Sendai showing linear distribution of lateral spread failures (along levees and canals), coastal rock irregular slides, and scattered debris slides in the low topography of the Sendai Plain. B, detail of the southern Abukuma Mountains showing few triggered landslides despite steep topography.

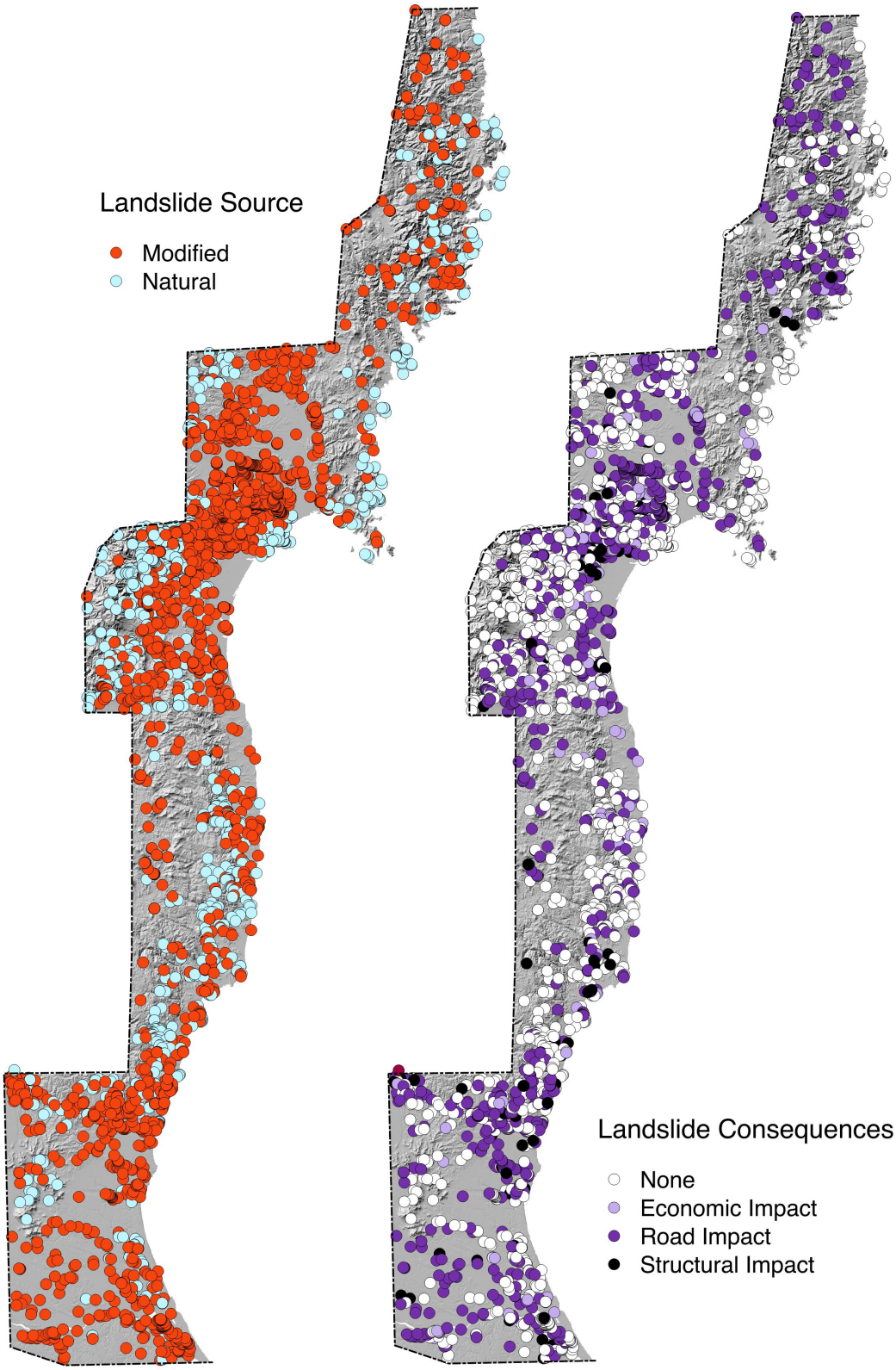

Figure 2.20 Mapped landslides classified by (A) anthropogenic modification and (B) impact to the built environment.

67% (2346) of all mapped landslides triggered by the Tohoku earthquake occurred in anthropogenically modified hillslopes (Table 2.4, Fig. 2.20). One third of all landslides trigged during the Tohoku earthquake caused some degree of damage or complete destruction of a roadway (1168 impacts, 33.3%), with an overall impact rate of 41.8% (1468) for all mapped landslides. In large magnitude subduction zone earthquakes, the destruction of roadways is particularly important as tsunami evacuation routes or emergency response routes may be cut off. In total 163 structures, primarily residential dwellings, were impacted by coseismic landslides (Table 2.4). Lateral spreads (60.4%), rotational slides (57.1%), and flow slides (43.1%) had the highest rates of impacting the built environment, likely caused by their occurrence primarily in manufactured or modified slopes, and not in natural hillslopes away from elements at risk. Nearly 10% of all flow slides were found to have impacted a building or structure, compared to 2.8% of debris slides, and 6.2% of lateral spreads. Consequences to the built environment were very closely associated with anthropogenic modification. Landslides impacting roadways were overwhelmingly undercut by those roads or had source regions along a road that may have focused water into the slope. Similarly, loosely placed artificial materials along levees and engineered slopes were highly susceptible to lateral spreads and flows, which in turn drove economic impacts. Given the lower percentage of rock slides and rotational slides in this dataset, conclusions could not be drawn as to the relationship between these modes and anthropogenic modification or impacts, though rock slides do appear to be primarily natural phenomenon, with exceptions found in quarries and limited steep rock road cuts.

	Natural Slopes	Modified Slopes
Rock Irregular Slides	85.7% (36)	14.3% (6)
Debris Slides	63.5% (1076)	36.5% (618)
Rotational Slides	28.6% (2)	71.4% (5)
Flow Slides	24.9% (45)	75.1% (136)
Lateral Spreads	0.2% (3)	99.8% (1581)

Table 2.4 Rates of natural and modified slope failures for each mapped landslide type sorted by percent of landslides triggered in natural terrain. Landslide counts for each category in parenthesis.

	Non-Impacting	Damage to Structures	Damage to Roadways	Direct Economic Impact	Impact Rate
Rock Slides	97.6% (41)	-	-	2.4% (1)	2.4%
Debris Slides	74.7% (1265)	2.8% (47)	19.2% (326)	3.3% (56)	25.3%
Flow Slides	56.9% (103)	9.9% (18)	30.9% (56)	2.2% (4)	43.1%
Rotational Slides	42.9% (3)	-	42.9% (3)	14.3% (1)	57.1%
Lateral Spreads	39.6% (628)	6.2% (98)	49.4% (783)	4.7% (75)	60.4%

Table 2.5 Consequences to the built environment of landslides triggered by the M9.0 Tohoku, Japan earthquake sorted by fraction of landslides impacting the built environment. Landslide counts for each category in parenthesis.

2.4.1 Size distribution of coseismic landslides

Mapped landslide area distributions, disaggregated by mode of landslide (Fig 2.21), reveal a shift in typical landslide size increasing from lateral spreads and debris slides to flow slides. To facilitate comparison, size-frequency data for each mode of landslide is normalized to the maximum value. Rotational slides and rock falls are not shown in Fig 2.20 due to small sample size. Within each landslide mode, no difference in area was found between modified and natural slope failures.

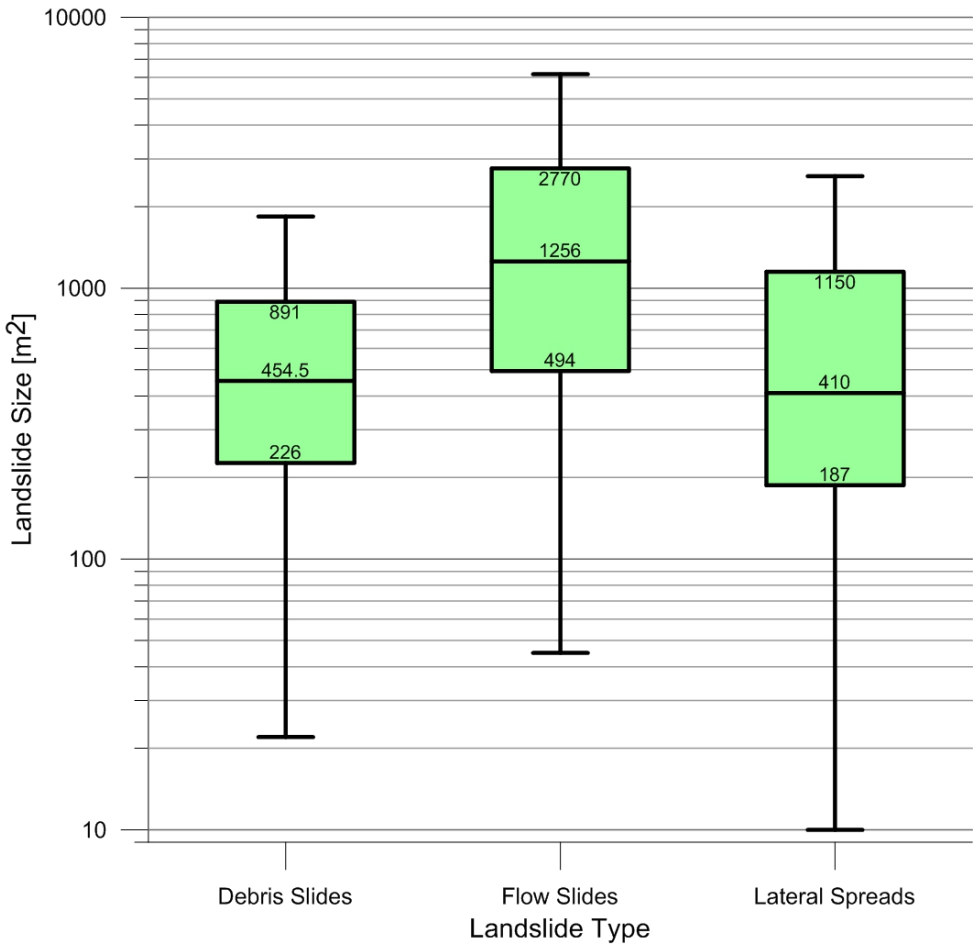

Figure 2.21 Distribution of mapped landslide size for debris slides, flow slides, and lateral spreads, rotational slides and rock irregular slides omitted due to small sample sizes. Labels correspond to 25th, 50th (median), and 75th quantiles of the data. Flow slides were typically larger than debris slides and lateral spreads, while debris slides were found to occur across the narrowest range of sizes. Note these data are plotted logarithmically.

2.4.2 Correlations with ground motion, topographic, and climatic parameters

Mapped distributions of the parameters discussed in this section are shown in Appendix A. For each considered causal landslide parameter, frequency ratios (FR) are shown based on equal-interval bins of the data, i.e. landslide frequency ratios for peak ground accelerations of 0 – 0.12g, 0.12 – 0.24g, 0.24 – 0.36g, etc. Fig. 2.22 shows FR values with respect to peak ground acceleration for each mode of mapped landslide and the overall landslide dataset. Rotational slides and rock irregular slides are dashed to visually unweight these data due to their small

sample sizes (6 and 28 respectively). Elevated frequency ratios are observed for ground accelerations of ~1.5g followed quickly by a drop back to a relatively constant rate. Extreme (>1.5g) ground motions recorded at relatively flat locations in the Sendai plain likely drive the observed misfit between increasing peak ground acceleration and landslide concentrations (here as FR, this trend is also observed in LS/km^2). In bivariate logistic regression space (Fig. 2.23), considering all modes of landslides, PGA is positively correlated with landslide occurrence, showing an increased likelihood of landslides of 2.8% for every 1cm/s^2 increase in shaking (28.2% per 0.1g unit increase, Table 2.6).

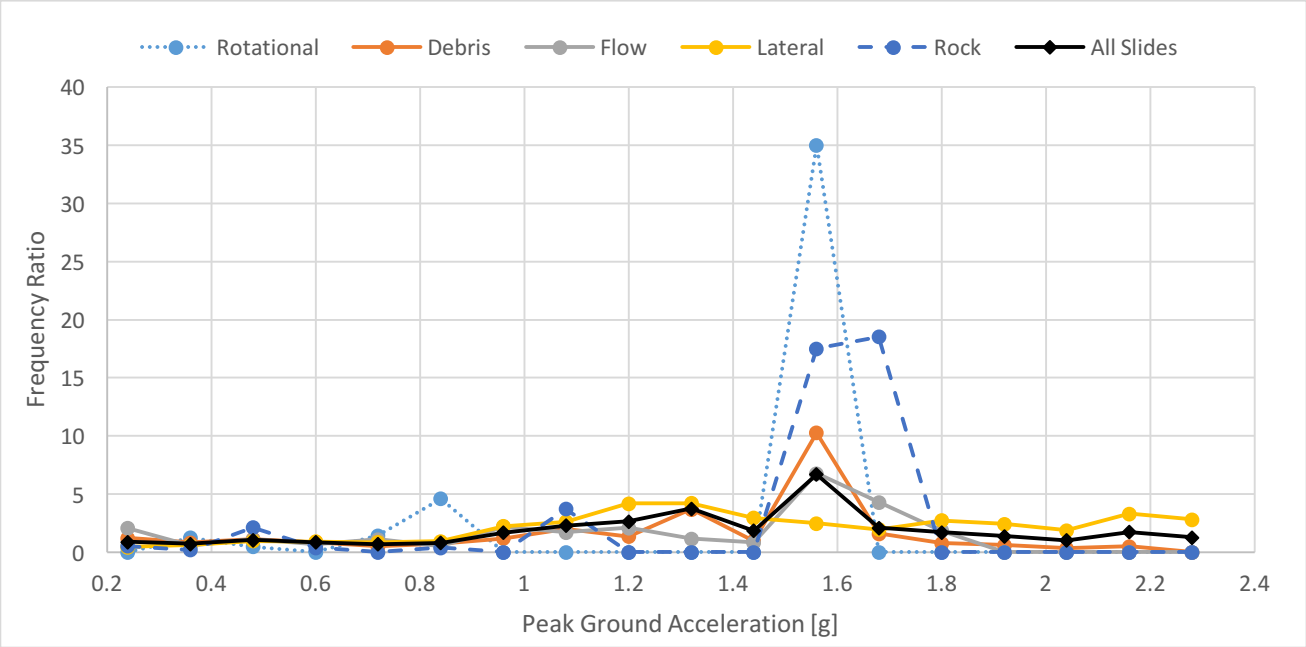

Figure 2.22 Frequency ratio distribution for each landslide mode as a function of peak ground acceleration. With below, landslide types abbreviated for space to the first word of their name. Rotational slides and rock irregular slides dashed to reflect the small sample size for these landslide types.

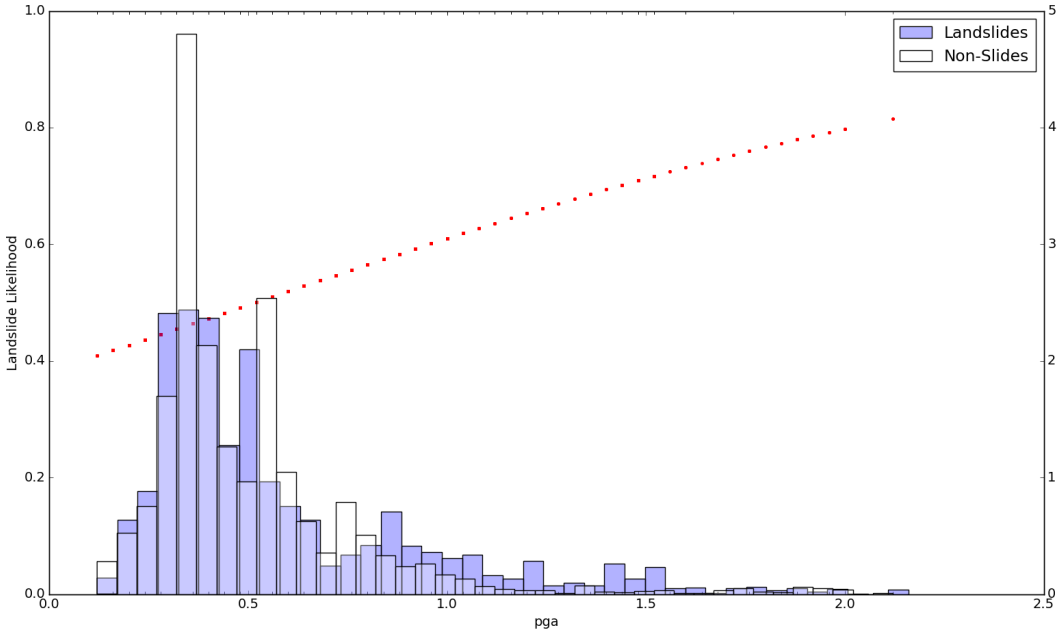

Figure 2.23 Logistic regression output for the occurrence of any type of landslide based on peak ground acceleration. Blue shaded bars show the distribution of observed landslides, white bars reflect the background rate for the entire study area. Computed landslide likelihood as a function of PGA is given by the dotted red line.

Frequency ratio-peak ground velocity (PGV) relationships show a weak increase in mapped landslides with increasing PGV to ~90cm/s before declining sharply (Fig 2.24). Debris slide frequency ratios never exceed 1.8 with respect to PGV, while lateral spreads show a distinct increase from 80 – 90cm/s, driving the overall trend. Logistic regression output shows a relatively strong positive relationship between landslide occurrence and increasing PGV (Fig 2.25).

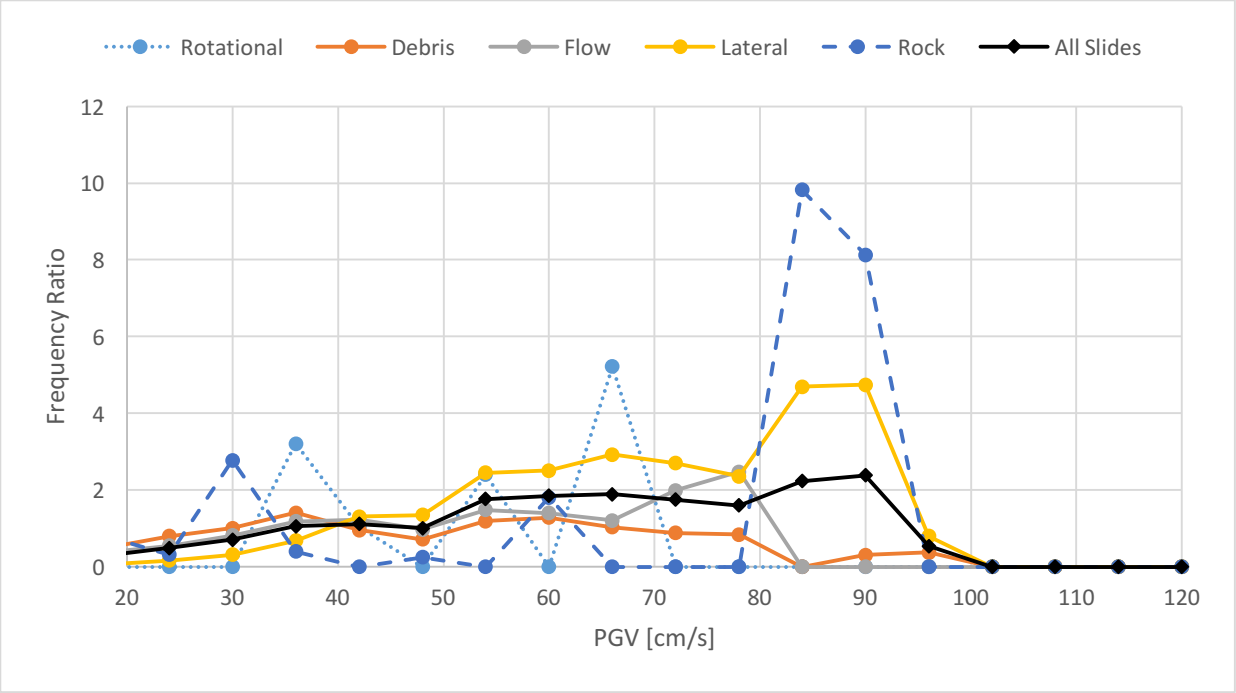

Figure 2.24 Landslide frequency ratios as a function of peak ground velocity (PGV).

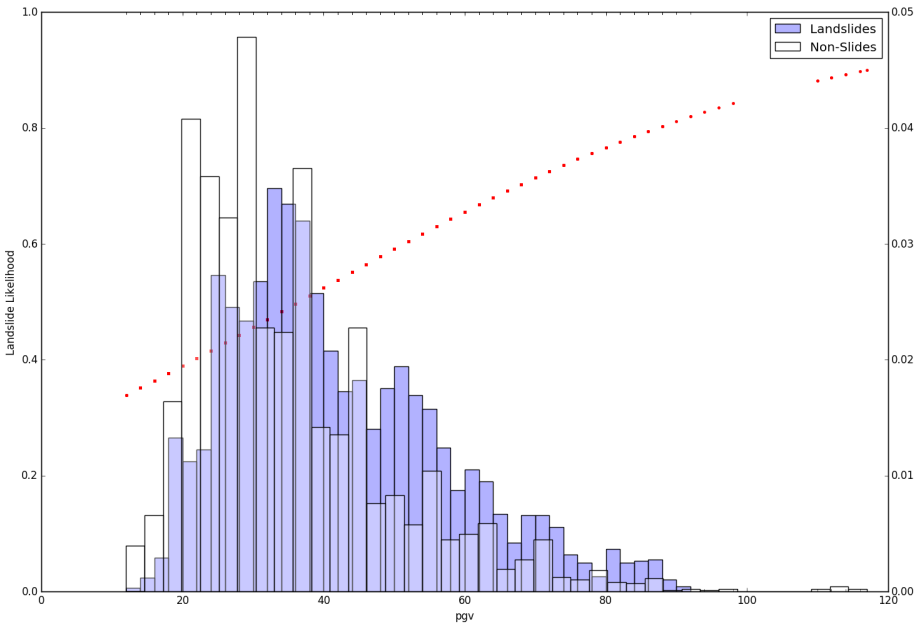

Figure 2.25 Landslide likelihood as a function of PGV.

Parameter	Change in landslide likelihood	Unit change
Peak ground velocity	2.8%	1 cm/s
Peak ground acceleration	1.7%	1 cm/s^2
Distance to fault rupture (R_{jb})	0.9%	1 km
Topographic Slope	0.6%	1°
2mo. Antecedent rainfall	0.1%	1 mm
Distance to Asperities (R_{asp})	-0.2%	1 km
Distance to Epicenter (R_{epi})	-0.3%	1 km
k_y/PGA	-3.7%	0.1 [-]

Table 2.6 Summary table of bivariate logistic regression output. For each unit increase in X the expected change likelihood of a landslide occurrence is shown. E.g., it is 32.7% more likely, given these data, a landslide would occur if shaken 0.6g than one shaken at 0.5g peak ground acceleration.

Frequency ratio as a function of slope (Fig 2.26) increases on average but exhibits significant variability between landslide modes. Lateral spreads were most common at low-angle slopes (0 – 5° and 5 – 10°) dropping rapidly in frequency with increasing slope, and completely missing from the record above 25 – 30° slopes. These data suggest rotational and flow slides show little sensitivity to increases in slope. Debris slides and rock irregular slide frequency ratios strongly respond to increases in slope, particularly above slope angles of 40°. For steep (>55°) slopes, landslide frequency ratios for debris slides and rock irregular slides are ~11 and 100, respectively.

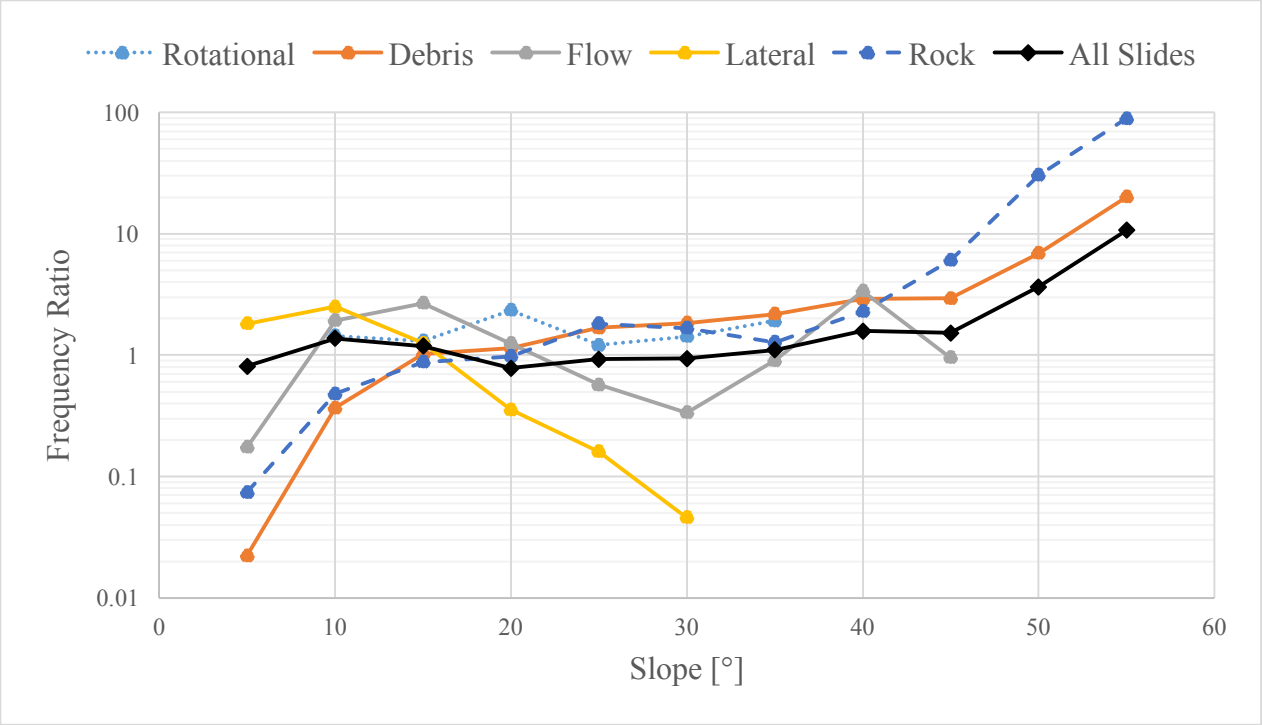

Figure 2.26 Frequency ratio as a function of topographic slope. NB logarithmic y-axis (frequency ratio) ranging from 0.01 – 100.

Figure 2.27 shows the landslide likelihood as a function of slope for all modes of landslides. When aggregated into a single 'landslides' category no significant trend in landslide likelihood is found with respect to slope.

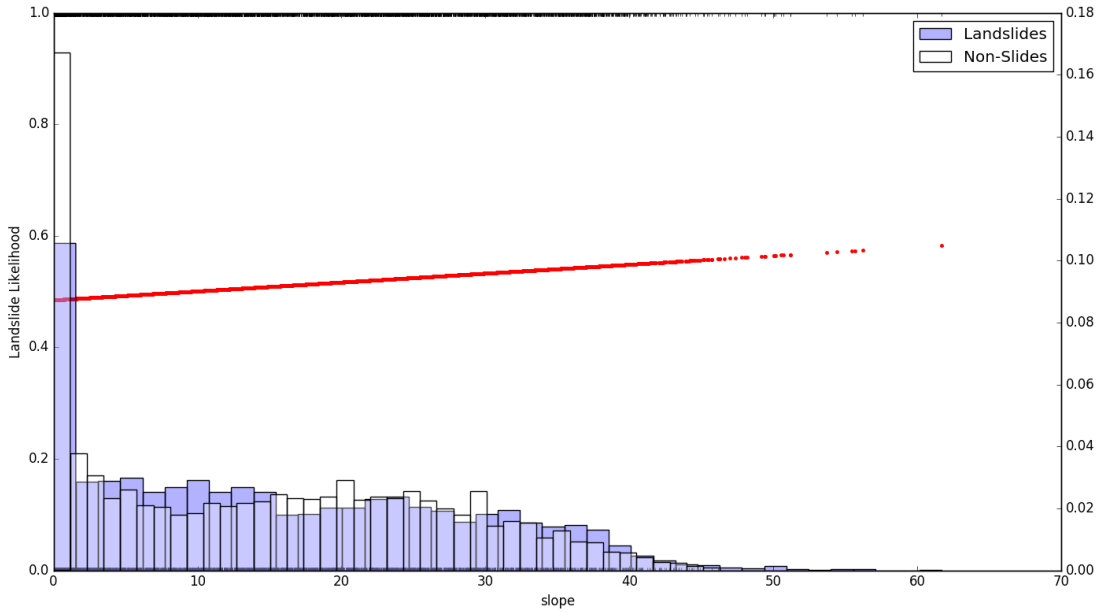

Figure 2.27 Landslide likelihood as a function of slope for all landslide types.

Landslide frequency ratios, for all modes of landslides, as a function of mapped geologic unit are shown in Fig 2.28. As observed in Wartman et al. (2013), areas of high landslide prevalence were typically young sedimentary units (A, B, C and N, Fig. 2.28), while a relative dearth of landslides occurred in older igneous rocks and accretionary complexes (e.g., I, J, P). Lateral spreads preferentially occur in young (Neogene or more recent) material (Wartman et al., 2013), though we note virtually all lateral spreads occur in anthropogenically modified terrain. Table 2.7 shows the landslide rates, frequency ratios, and back calculated cohesional strength (section 2.3.6) for all mapped geologies.

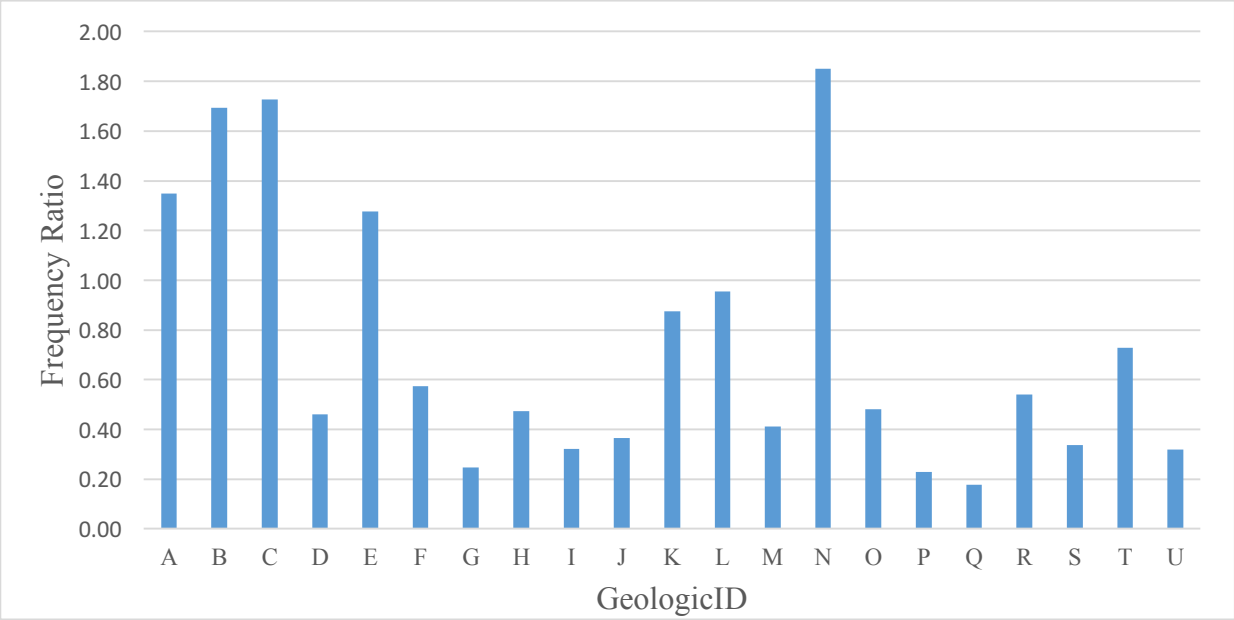

Figure 2.28 Frequency ratio as a function of geologic unit. Mapped units described in Table 2.7.

ID	Sym.	Description	Area [km^2]	**Rot. Slides**	**Deb. Slides**	**Flow Slides**	**Lateral Spreads**	**Rock Slides**	**FR**	**Coh (kPa)**
A	H	Latest Pleistocene to Holocene Sedimentary rocks	3488.5	0	100	10	630	4	1.35	29
B	N2-Q3	Middle Miocene to Latest Pleistocene Sedimentary rocks	4723.0	4	521	93	637	11	1.69	36
C	PG2-N1	Middle Eocene to early Middle Miocene Sedimentary rocks	1035.1	2	189	12	75	5	1.73	38
D	K1-PG1	Early Cretaceous to Early Eocene Sedimentary rocks	82.5	0	6	0	0	0	0.46	78
E	J2-K1	Middle Jurassic to Early Cretaceous Sedimentary rocks	203.1	1	40	0	0	0	1.28	38
F	TR1-J1	Early Triassic to Early Jurassic Sedimentary rocks	595.0	0	50	1	0	3	0.57	42
G	P	Permian Sedimentary rocks	1056.0	0	25	2	14	0	0.25	55
H	S-C	Silurian to Carboniferous Sedimentary rocks	387.5	0	23	0	6	0	0.47	55
I	TR3-K1	Late Triassic to Early Cretaceous Accretionary complexes Mainly sedimentary rocks	1791.6	0	82	0	9	0	0.32	36
J	Cm-H	Cambrian to Holocene Accretionary complexes Ultra-mafic igneous rocks	52.0	0	3	0	0	0	0.36	72
K	N2-H	Middle Miocene to Holocene Volcanic rocks	512.2	0	47	9	14	1	0.88	36
L	PG2-N1	Middle Eocene to early Middle Miocene Volcanic rocks	926.3	0	98	25	16	1	0.95	40
M	K1-PG1	Early Cretaceous to Early Eocene Volcanic rocks	415.0	0	25	0	2	0	0.41	73
N	N3-H	Late Miocene to Holocene Pyro-clastic flow	871.0	0	127	20	105	3	1.85	30
O	K1-PG1	Early Cretaceous to Early Eocene Plutonic rocks	4698.3	0	286	8	64	0	0.48	36
P	S-C	Silurian to Carboniferous Plutonic rocks	55.3	0	2	0	0	0	0.23	55
Q	K1-PG1	Early Jurassic to Early Eocene Metamorphic rocks (Low-middle Pressure)	499.8	0	9	1	4	0	0.18	89
R	pS	pre-Silurian Metamorphic rocks (High Pressure type)	70.3	0	6	0	0	0	0.54	78
S	Water	Water area	262.2	0	8	0	6	0	0.34	0
T	C-PG	Carboniferous to Paleogene Accretionary complexes Exotic limestone blocks	43.4	0	3	0	2	0	0.73	45
U	C-PG	Carboniferous to Paleogene Accretionary complexes Exotic chert blocks	39.7	0	2	0	0	0	0.32	95

Table 2.7 Landslide distribution by type for each mapped geologic unit (Geological Survey of Japan (2009), 1: 200,000 scale geologic map of Japan) with overall landslide frequency ratio (*FR*) and cohesional strengths (*Coh*) used in this work. For all mapped materials (except water) internal friction angle is assumed to be 15°. Shaded rows indicate geologic units used to compute natural and modified material strength, discussed in section 2.4.5.

As a function of epicentral distance (R_{epi}), landslide frequency ratios were found to increase with increasing distance. This behavior is driven by a cluster of lateral spreads occurring along canals and rivers of the Kanto plain, northeast of Tokyo (Fig. 2.29). High observed frequency ratios from 60 – 80km for rotational slides are due to the lack of these landslides, inflating the relative importance of a small handful of slides. Neglecting the anthropogenically influenced lateral spreads at great R_{epi}, no observed distance-frequency ratio (or LS/km^2) relationship is observed. Landslide frequency ratios are found to sharply decline with increasing R_{asp} (closest distance to asperities/strong motion generation areas) for all modes of failure. This finding is not supported by logistic regression output (Fig. 2.30) where the small numbers of landslides occurring on small rocky islands near the earthquake source are insufficient in number to reproduce the frequency-ratio trend. R_{jb} (closest surface projected distance from the fault plane) shows a positive correlation with landslide occurrence (increased likelihood of landslide occurrence with increasing distance).

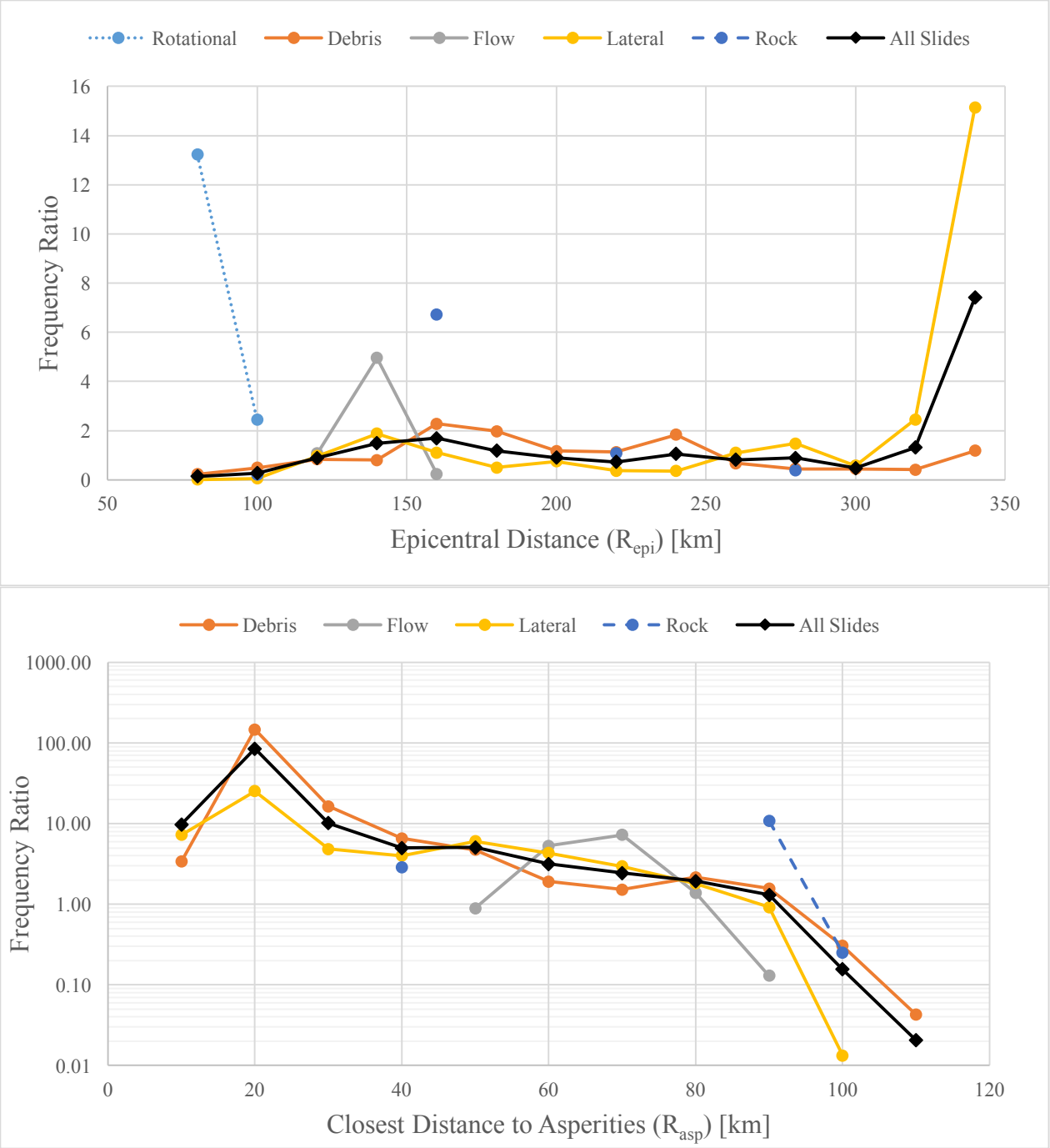

Figure 2.29 Epicentral distance (top) and closest distance to asperities – frequency ratio plots.

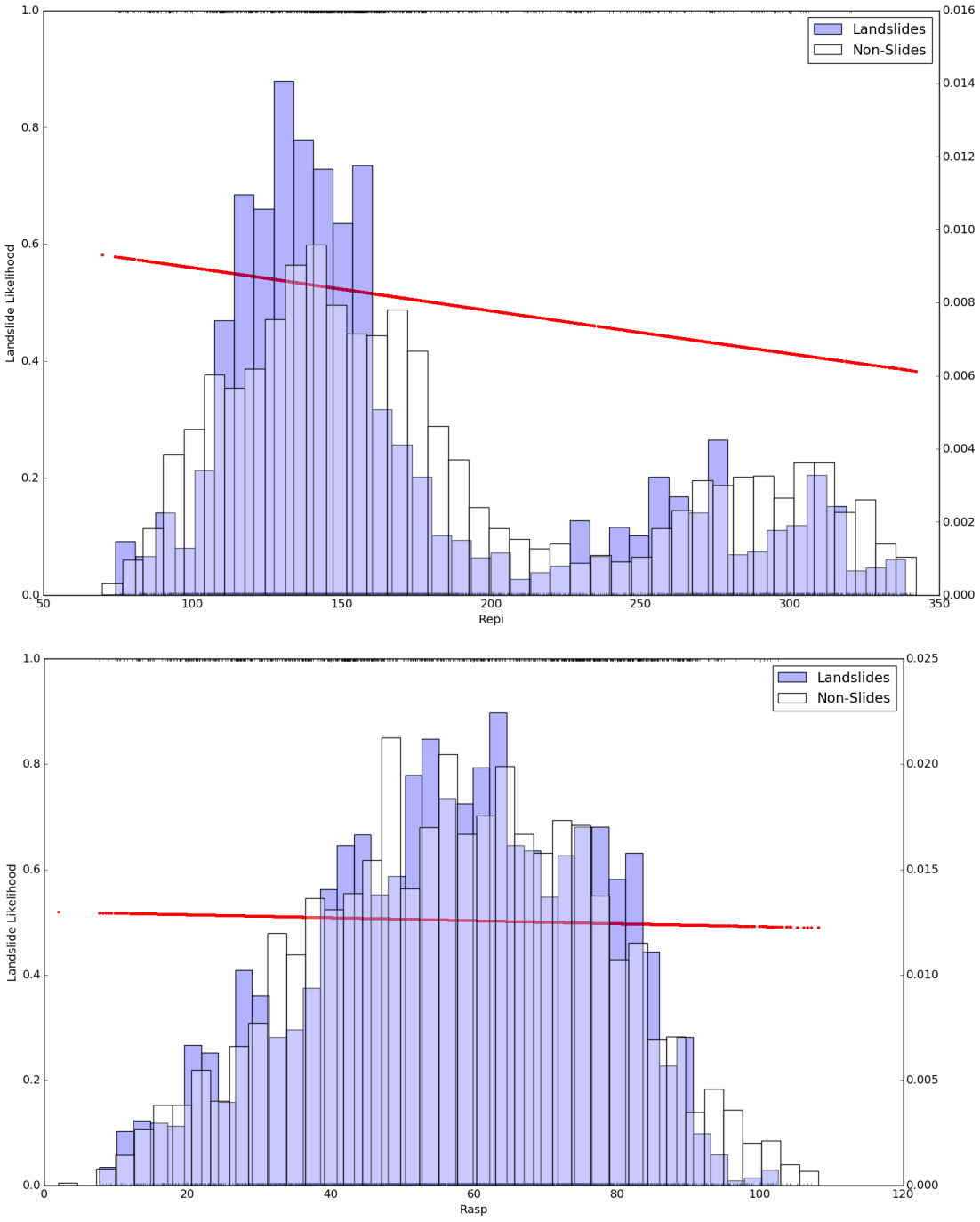

Figure 2.30 Logistic regression output for R_{epi} (top) and R_{asp} showing weakly negative correlations with distance (decreasing landslide likelihood for increasing distance.)

For antecedent rainfall windows of 1, 2, and 3-months prior to the Tohoku earthquake, no relationship is observed between any mode of mapped coseismic landslides and antecedent rainfall. Fig. 2.31, showing data for 2-month antecedent rainfall and landslide frequency ratios, is

representative of each assessed window. While ground saturation, and thus indirectly antecedent rainfall, is physically important in landslide susceptibility and preconditioning, or triggering, of failure, the spatial resolution of these data and more dominant effects of slope, geology, and shaking intensity likely mask any potential relationship between landslide occurrence and antecedent rainfall for hydraulically controlled modes of failure such as flow slides and lateral spreads.

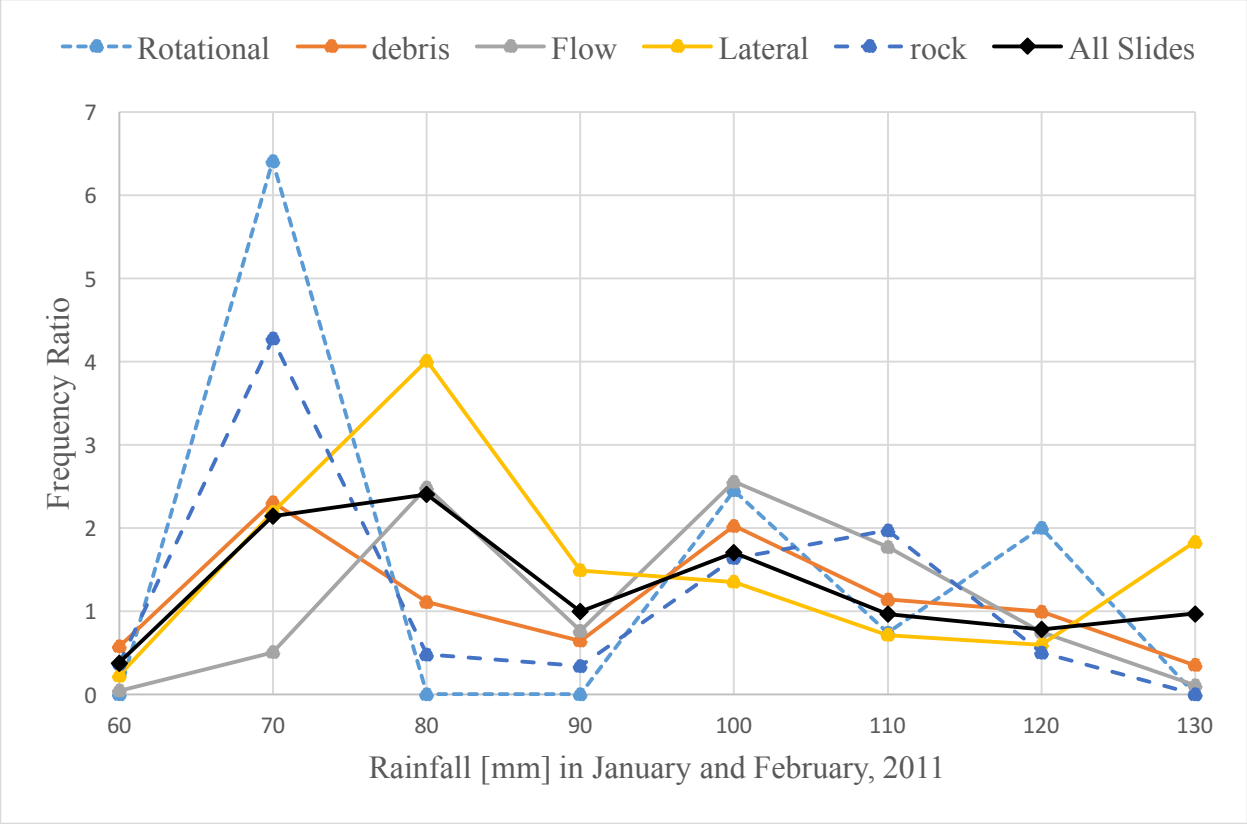

Figure 2.31 Frequency ratio – antecedent rainfall (2-month) plot for all landslide modes.

2.4.3 k_y/PGA

For computed ratios of yield acceleration (k_y) to peak ground acceleration (PGA), frequency ratios of all modes of landslides are found to sharply decline from k_y/PGA = 0.4 – 1.25 before flattening to a null-frequency ratio of 1.0 for all higher values (Fig 2.32). Frequency ratio trends are supported by landslide likelihood predictions from logistic regression, for all modes modified

and natural, where the likelihood of landslide occurrence decreases by 3.7% for each 0.1 increase in k_y/PGA (25% for each 1.0 increase in k_y/PGA.)

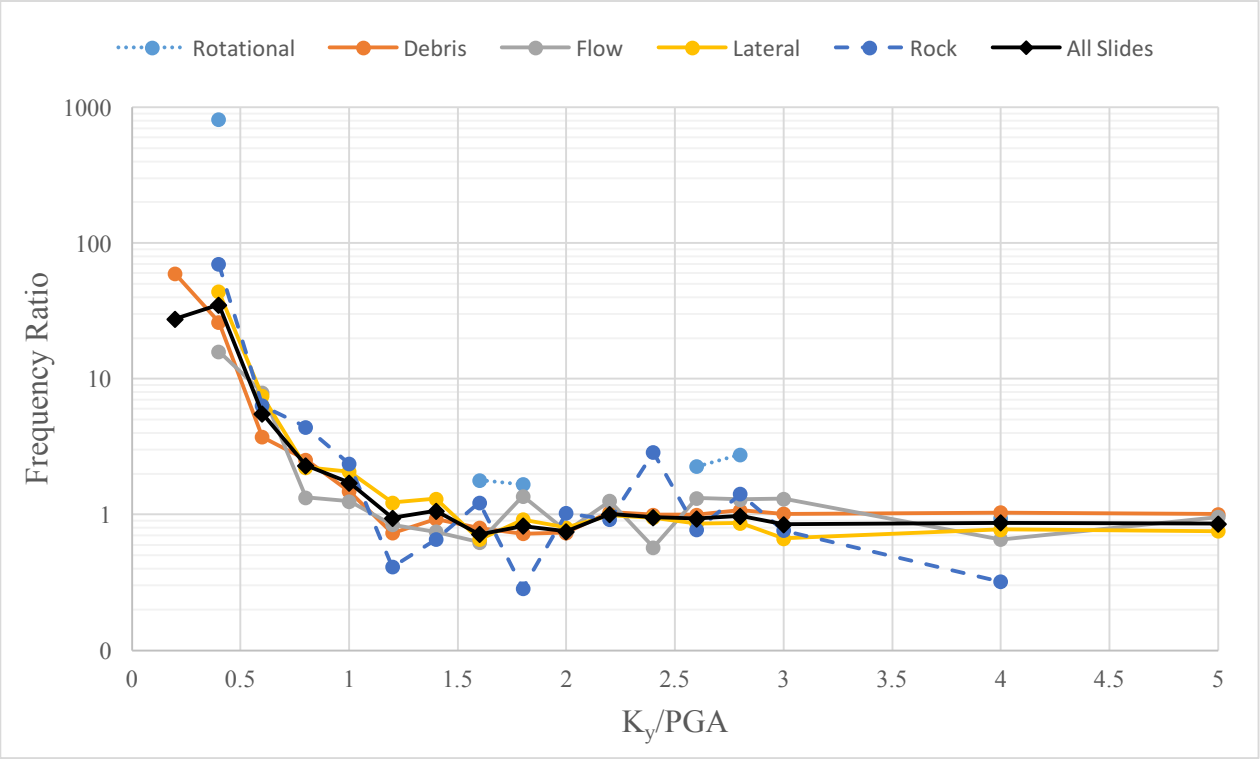

Figure 2.32 Frequency ratio – k_y/PGA plot for all landslide types in the Tohoku, Japan dataset. For all landslide types landslide frequency ratios sharply increase at k_y/PGA ~1.25.

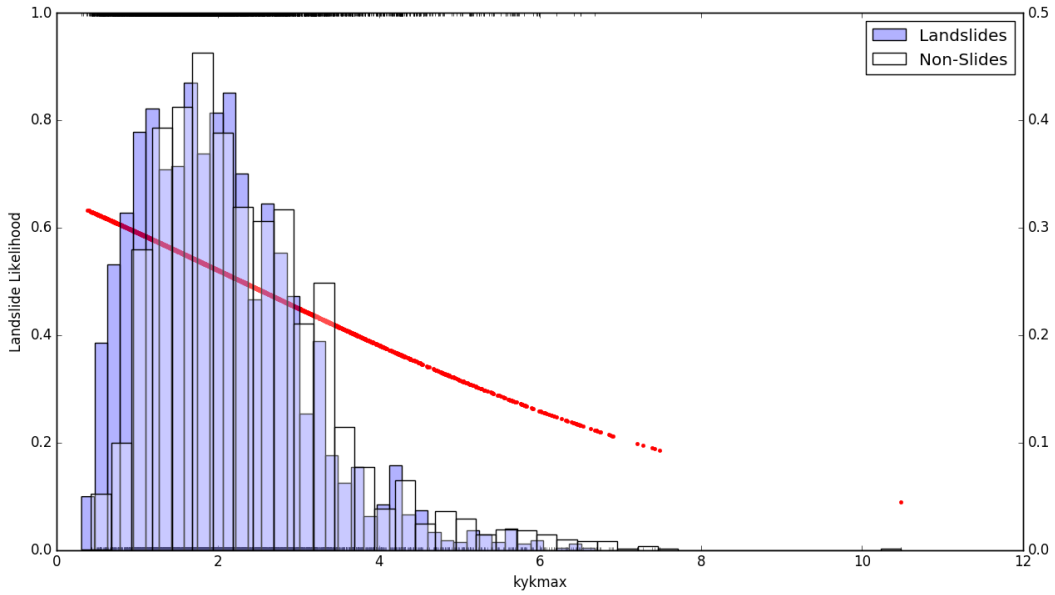

Figure 2.33 Landslide occurrence likelihood as a function of k_y/PGA for all types of landslides, modified and natural.

2.4.4 Landslide correlations for the Iwaki aftershock earthquake

Landslides digitized from Sato et al. (2013, 2015) and mapped landslides from the Iwaki earthquake in this study are shown in Fig 2.14. Digitalization was based on geo-registered images of Sato et al. (2015) and available high-resolution images via Google Earth. Frequency ratio – R_{epi} relationships for the Iwaki aftershock landslides follow a familiar power-law decay with increasing distance from the source (Fig. 2.34). Figure 2.35 shows a slight increase in landslide frequency ratio with increasing peak ground acceleration for the Iwaki coseismic landslides.

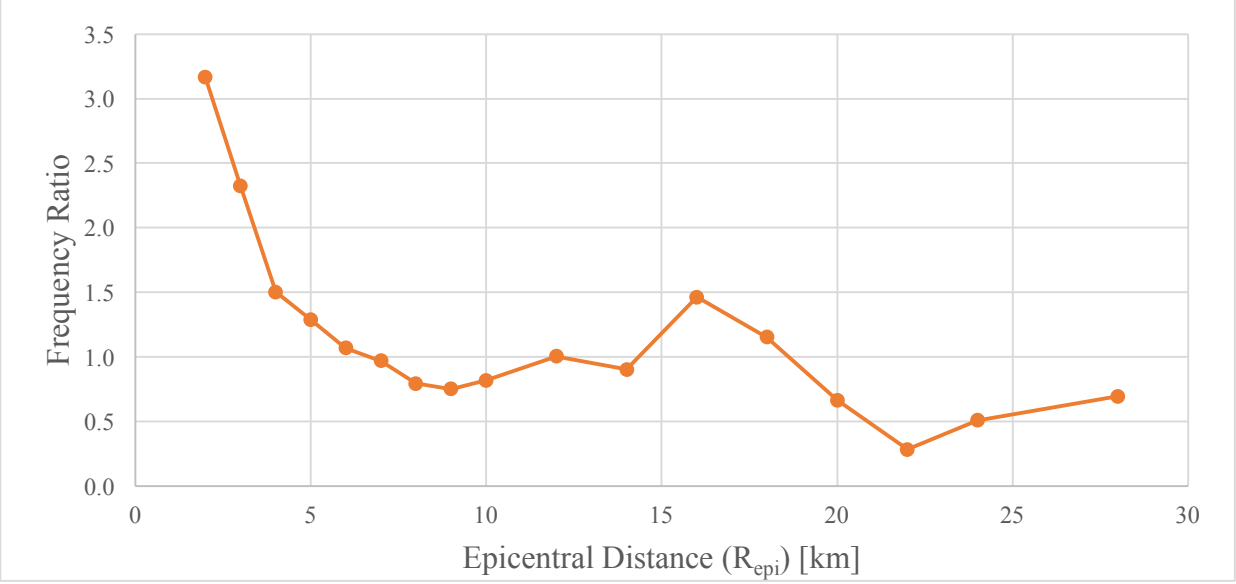

Figure 2.34 Frequency ratio – epicentral distance relationship for the Iwaki aftershock landslides

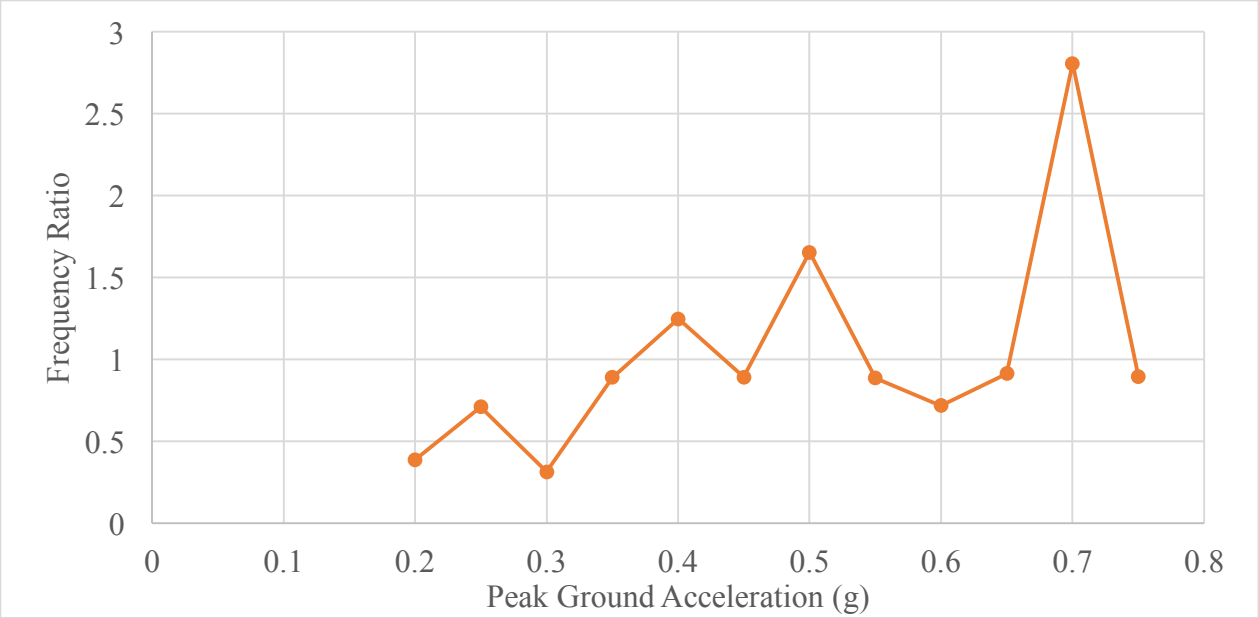

Figure 2.35 Frequency ratio – peak ground acceleration relationship for the Iwaki aftershock landslides.

Geologic strengths, derived from unmodified debris slides and interpolation from depositional age developed for the Tohoku dataset were directly applied to the Iwaki aftershock landslide inventory without modification to compute yield accelerations (k_y) for the Iwaki study area. Resultant k_y/PGA curves for both the Iwaki aftershock and Tohoku mainshock coseismic landslide inventories, expressed as frequency ratio, are shown in Fig. 2.36. Landslides frequency ratios trigged by the Iwaki aftershock follow the same sharp increase in k_y/PGA trend as Tohoku, though shifted to slightly higher values (sharp increase occurs at $k_y/PGA \sim 1.5$). Fig. 3.37 shows the distribution of k_y/PGA for both earthquakes compared to mapped landslides.

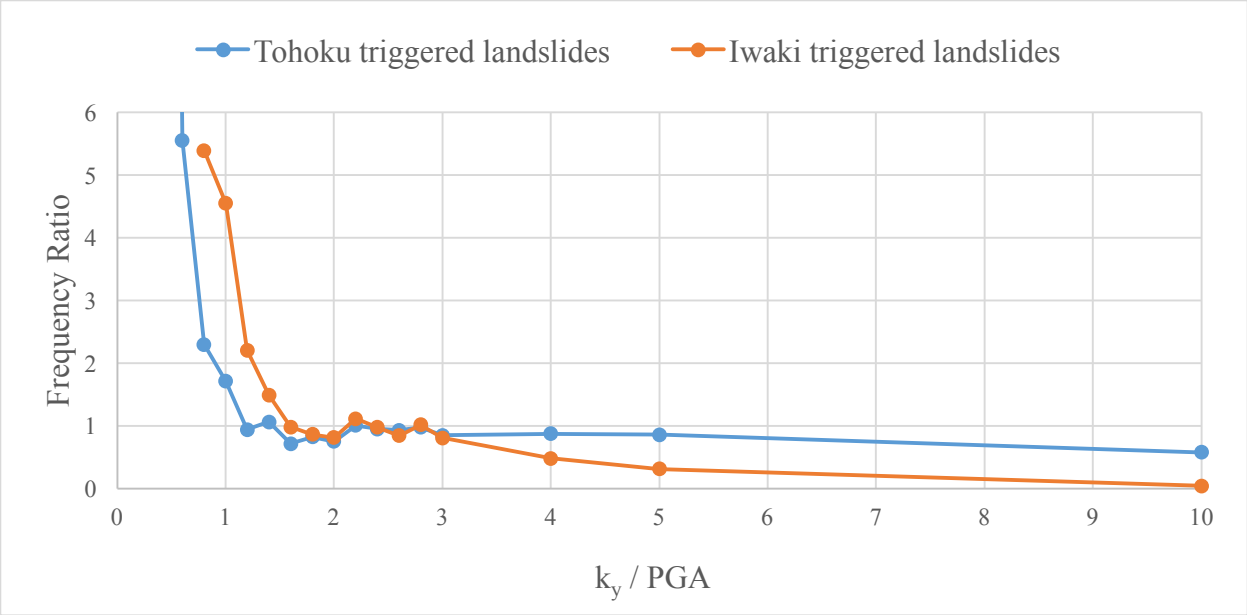

Figure 2.36 Comparison between frequency ratio and k_y/PGA for coseismic landslides trigged by the M9.0 Tohoku and M6.6 Iwaki earthquakes.

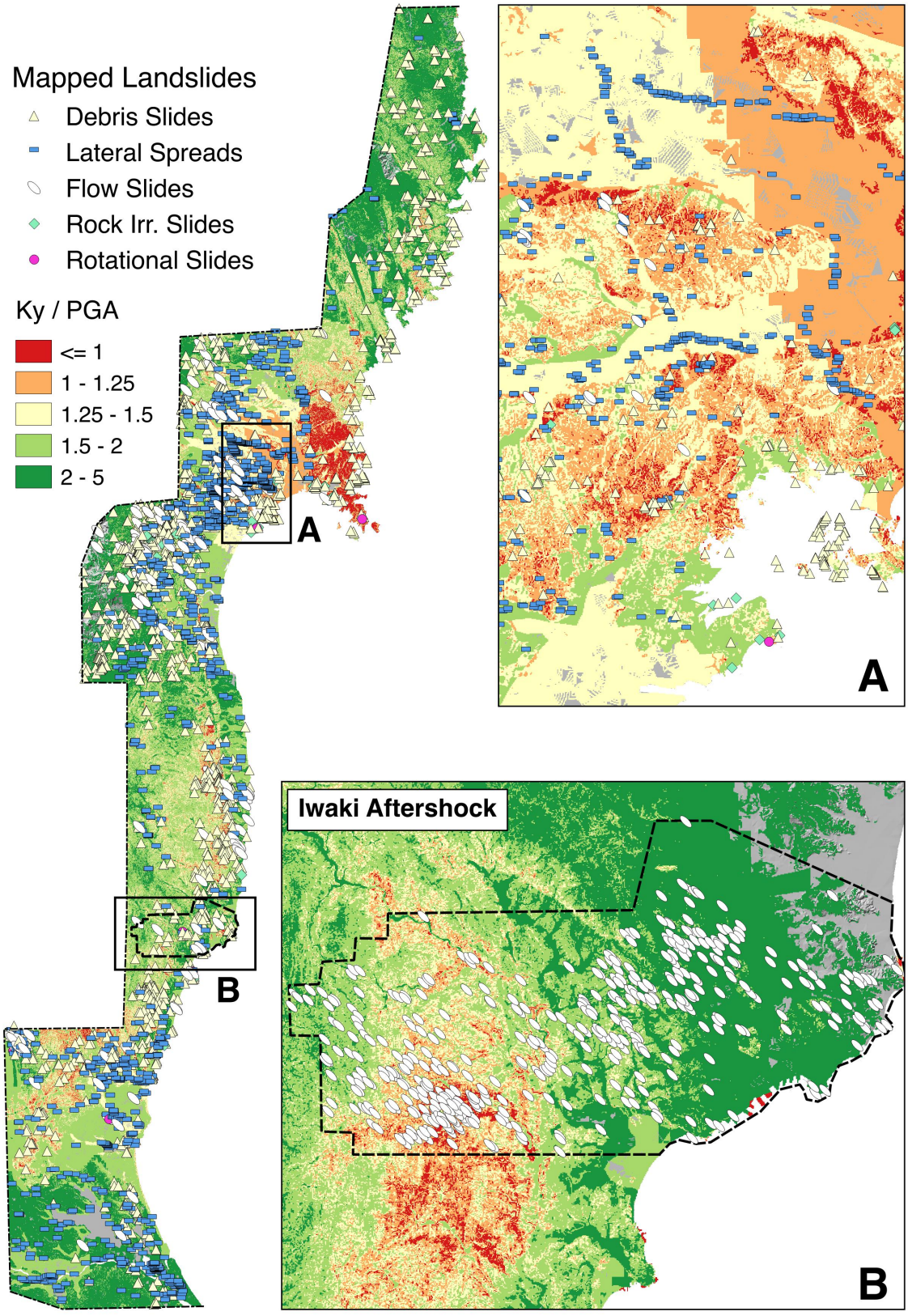

Figure 3.37 k_y/PGA distributions for the Tohoku earthquake (A), and the Iwaki aftershock (B) with mapped distributions of landslides for each earthquake.

2.4.5 Effects of anthropogenic modification on assessed strength

Material cohesional strength estimates (internal friction angle held constant at 15°, for all analyses) for both natural and modified debris slide failures were computed for nine geologic units accounting for 1,500 natural and modified debris slides (91% of all debris slides). The remaining geologic units lacked sufficient numbers of natural, modified, or both, debris slides for this analysis (Table 2.6). Fig. 2.38 shows a sample distribution of modified and natural back-analyzed cohesional strengths for a Neogene to latest Pleistocene sedimentary rock group (Table 2.6, B). Fig. 2.38 reveals that 20% of modified slope failures in unit B were expected to have higher strength at failure than an equivalent natural slope, while the large majority (80%) were expected to be weaker at the time of failure. For unit B, the median expected strength at failure is found to have decreased by 11% for modified slopes with respect to equivalent natural slopes.

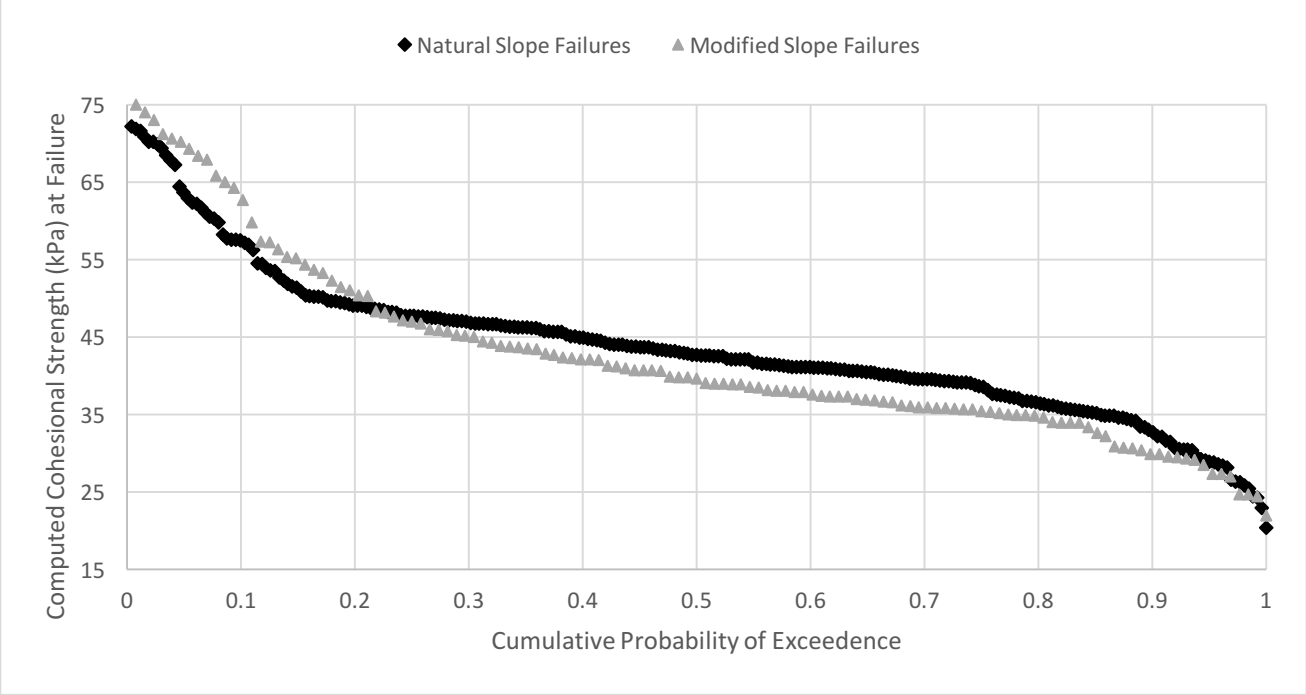

Figure 2.38 Back analyzed cohesional strength (kPa) at failure for natural (black diamonds) and anthropogenically modified (grey triangles) debris slides.

Back-calculated strength was normalized to the median strength of natural debris slide failures (e.g., for unit B the 50^{th} percentile strengths are 1.0 for natural, and 0.89 for modified) to facilitate plotting strength curves for multiple lithologies on a single plot. Fig. 2.39 shows multiple normalized strength curves for natural and modified debris slides grouped by material age. On average, older stronger parent materials show expected decreases in strength at failure when modified whereas young unconsolidated Holocene-age alluvium and pyroclastic flow deposits show expected increases in strength when modified. Fig. 2.40 shows the computed median strength change for each assessed geologic unit as a function of the reported age of the material (for units given an age range, the median of listed ages is taken). For very young (Holocene) materials, an increase in predicted strengths is observed for anthropogenically modified slopes, whereas all older materials see strength loss due to modification, approximately following a logarithmic decay.

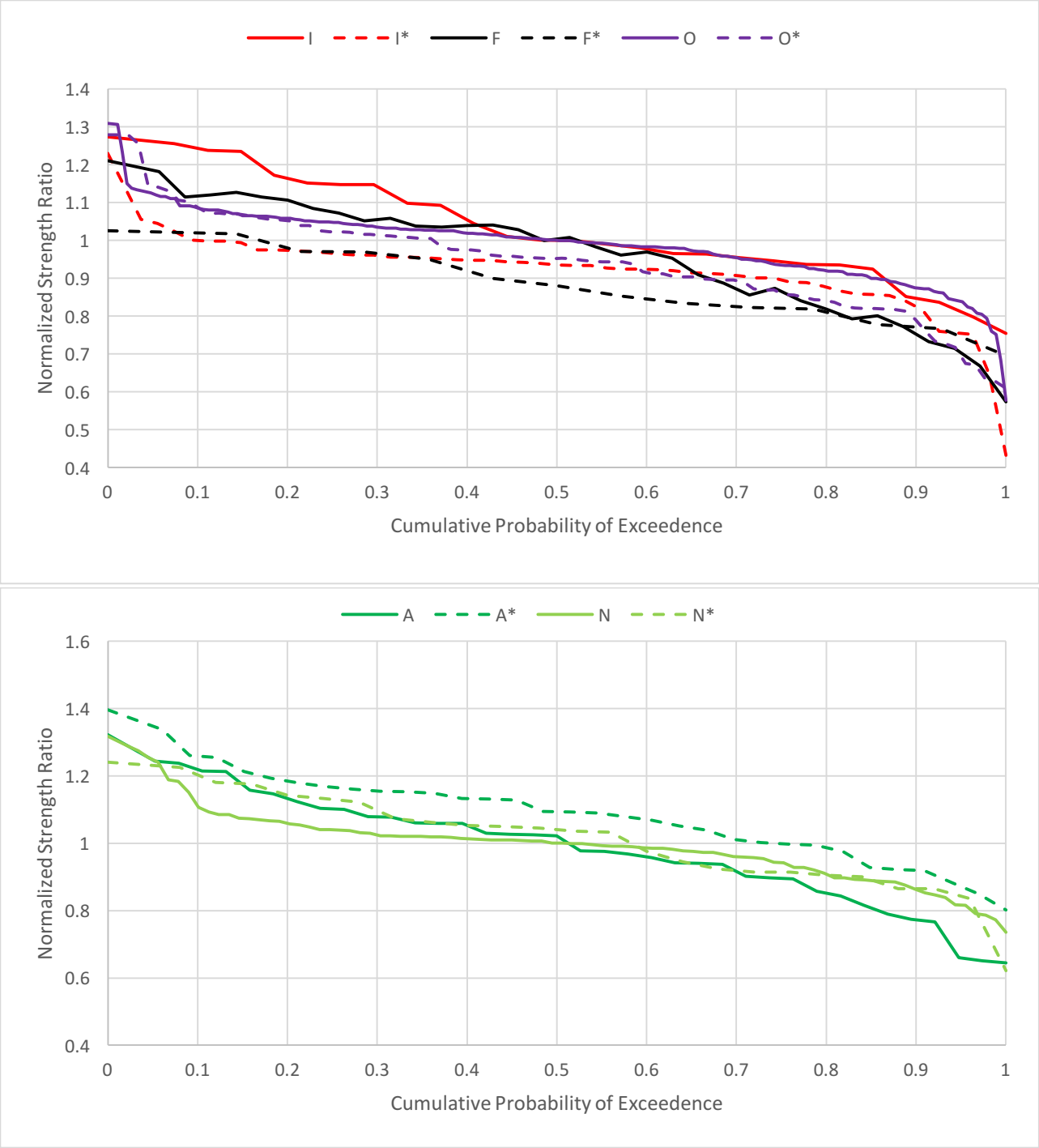

Figure 2.39 Normalized strength ratios for natural (solid lines) and anthropogenically modified (dashed lines) debris slides. Top: old, relatively strong, sedimentary and plutonic rocks showing strength loss due to anthropogenic modification. Bottom: young, weak, alluvium and unconsolidated pyroclastic flows show an increase in expected strength due to anthropogenic modification.

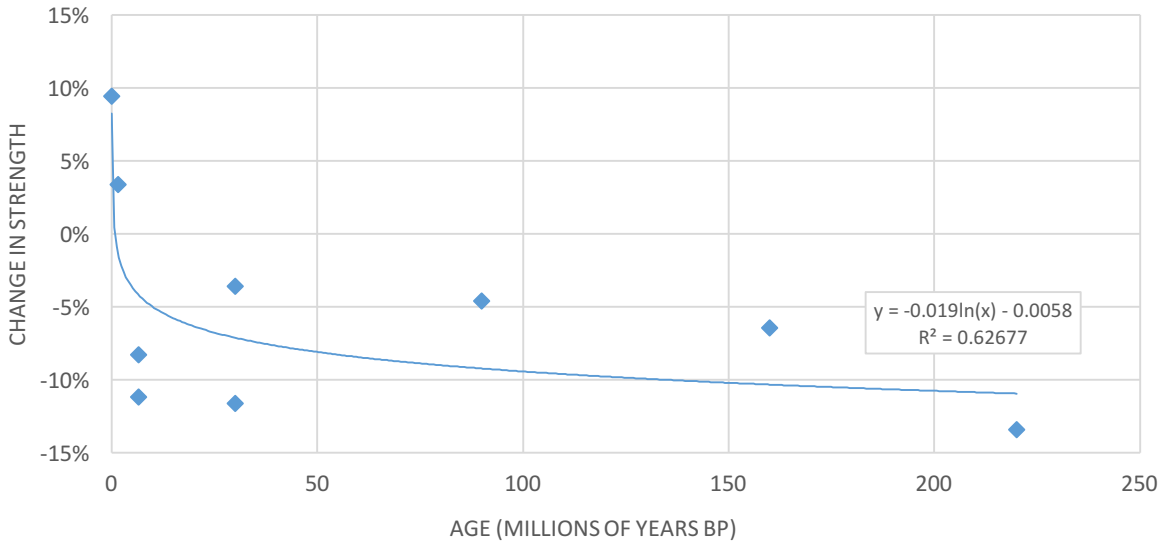

Figure 2.40 Geologic age – strength change predicted from natural and anthropogenically modified debris slides triggered by the Tohoku earthquake.

Natural and modified slope debris slides in all geologic units were compared with respect to single-variate causal factors. Fig. 2.41 shows landslide likelihood output for natural and modified debris slides as a function of slope, R_{epi}, and k_y/PGA. Landslide likelihood trends between modified and natural slope debris slides were found to be similar for most input parameters (e.g., R_{epi}, PGA, k_y/PGA). For slopes greater than 10° (areas typically susceptible to debris slides) modified debris slide likelihood was observed to anti-correlate with increased slope (-2.0% change in landslide likelihood per degree increase in slope), while natural debris slides exhibit a strong correlation with slope (5.4% increase in likelihood per degree increase in slope). These data suggest debris slides are being pushed into more gently sloping portions, and much more of the landscape than previously observed through anthropogenic modification.

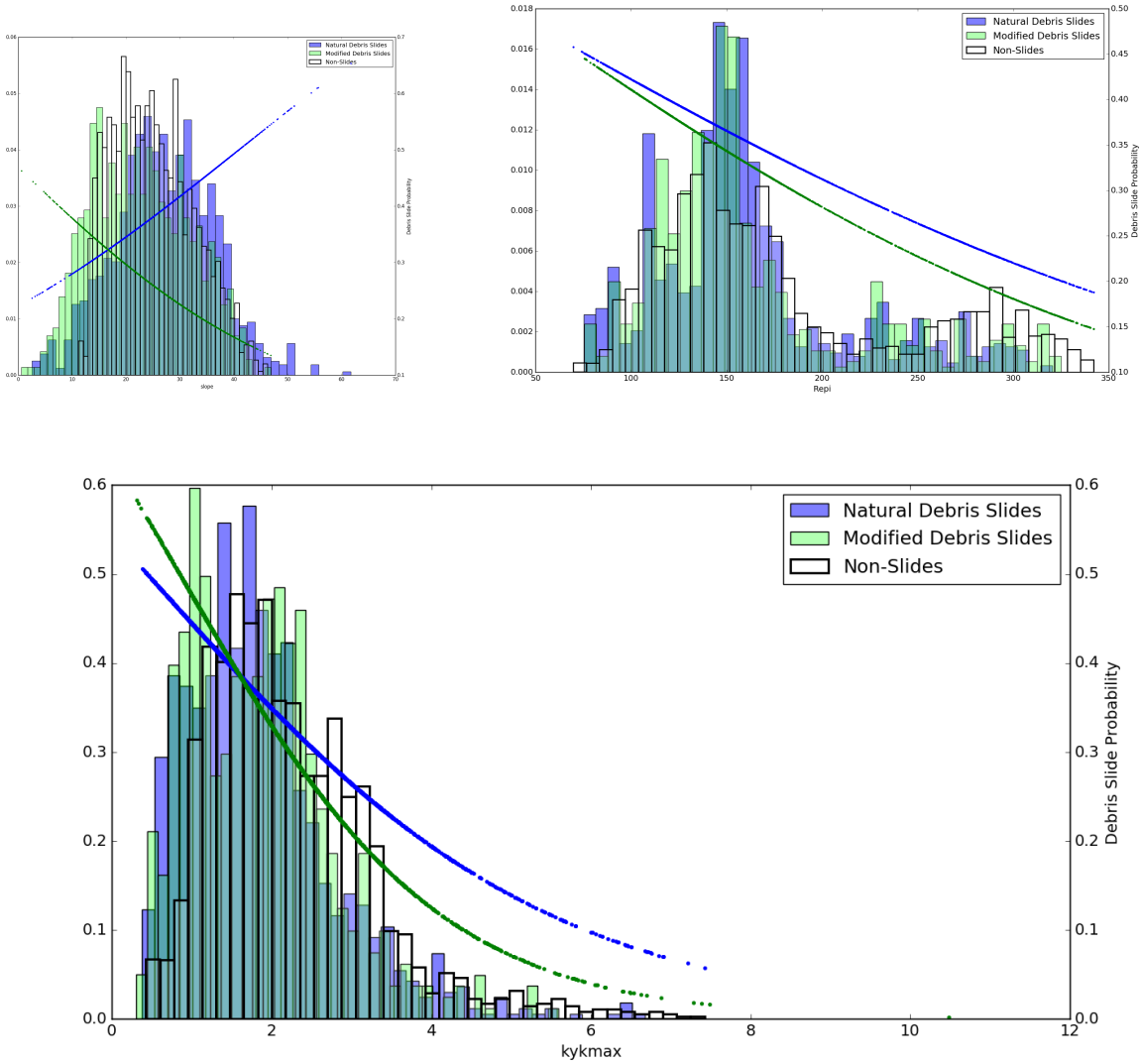

Figure 2.41 Debris slide likelihood as a function of slope (top left), epicentral distance (top right) and k_y/PGA for natural (blue) and anthropogenically modified (green) debris slides. Background slopes trimmed to >10° to better reflect terrains susceptible to debris slides.

2.5 Discussion

2.5.1 Disaggregation of landslide type and consequences

For nearly all crustal earthquake landslide inventories, disrupted (debris slides and irregular rock slides) landslides are the dominant mode of failure observed (e.g., Mammoth Lakes, CA (98%), Harp et al., 1984; Northridge, CA (90%), Harp and Jibson, 1996; Chi-Chi, Taiwan (85%), Khazi and Sitar, 2003, Table 2.8). Landslides triggered by the 2011 M9.0 Tohoku, Japan earthquake

were found to be dominated by two distinct modes of failure, debris slides ('disrupted' in the terminology of Keefer and Wilson (1989), Table 2.8) and lateral spreads, with an additional 5% of the total landslide population of flow slides. Small numbers of rotational slides (a subset of the more general 'coherent' classification) and irregular rock slides were observed. In this study, the number of irregular rock slides is likely under-reported due to coastal tsunami damage preventing definitive landslide mapping in areas containing rockfall susceptible cliffs, and the limits of detection (1 – 4m) of this study. The relative increase in lateral spread fraction for Tohoku may be a combination of several factors. First, lateral spreads are not often systematically mapped across the meizoseismal region, or are ignored in 'landslide' studies. Second, many on-shore crustal earthquakes occur in steep, mountainous, terrain where few areas of relatively flat, loosely deposited, saturated young sandy alluvium are present. Third, the long duration of megathrust earthquakes, even for relatively lower PGA or PGV intensities than near-field crustal earthquakes, enables the development of excess pore water pressure leading to liquefaction or cyclic degradation of strength facilitating flow-like slides (e.g., Kramer, 1996; Greenfield, 2017). Following the Tohoku earthquake, lateral spreads were systematically mapped in high-resolution aerial images, facilitated by emergency response teams covering exposed ground cracks with blue tarps, where thousands of square kilometers of flat alluvial planes were shaken for several minutes, triggering ~1,500 lateral spreads. Most importantly, virtually all lateral spreads in this study occurred in anthropogenically modified ground, from loose irrigated agricultural fields to placed fill and extensive levee systems.

The strong links between lateral spreads and flow slides with anthropogenically modified slopes observed in this study (Table 2.4) is likely to repeat itself in future megathrust earthquakes in the

Pacific Northwest, Japan, and elsewhere where human settlement and anthropogenic modification to the landscape may be subjected to significant ground shaking on the order of 50 – 200 seconds. More commonly observed coseismic landslide modes such as debris slides (shallow translational slides or disrupted slides) are still a significant presence in the Tohoku dataset, and were most strongly associated with steep natural topography. These key modes of landslide failure – lateral spreads, flow slides, and debris slides – are not only associated with different states of the landscape (Table 2.4) but are found to occur in different sections of the landscape (Fig. 2.26) as expressed in the slopes at which different landslide types were triggered. These findings, in addition to the disparate size distribution of each mode of landslide (Fig. 2.21) support the need for a mode-based analysis of coseismic landslide inventories and hazard. Portions of the landscape most susceptible to each type of landslide (e.g., debris slides and lateral spreads) and the mechanics governing their behavior at a site-specific level are unique. Further motivating a mode-based approach to coseismic landslide inventory analyses and hazard forecasting are the disparate impacts to the built environment observed in the Tohoku-triggered landslides (Table 2.5). Lateral spreads and flow slides (predominantly associated with anthropogenically modified slopes) were disproportionately likely to impact the built environment with respect to observed damage/destruction of buildings, roadways, levees or dams, and direct economic costs. Had lateral spreads and flow slides not occurred in anthropogenically modified terrain, significantly fewer impacts to the built environment would have occurred during the Tohoku earthquake: 783 fewer road impacts and 116 fewer destroyed buildings and homes.

The overall rate of landslide impacts on the built environment, 41.8% of all landslides were mapped as causing some degree of loss, 33.3% of slides damaging roadways, was significant. While these data are unrecorded in previous studies, reconnaissance and coseismic landslide inventory reports suggest landslide impact rates from crustal earthquakes more typically in the range of 1 – 5% (e.g. slope failures triggered by the Canterbury earthquake sequence impacted dwellings/structures at a rate of 1.7%, with additional uncounted road impacts (~2-3%), Ch. 2). If observed impact rates from Tohoku are representative of large magnitude subduction zone earthquakes, risk implications for similar regions (e.g., the Pacific Northwest) are significant. Recognizing the link between consequences, mode of failure, and anthropogenic modification future quantitative risk analyses will be better equipped to estimate future mode-based landslide losses, and target mitigation strategies to protect the greatest number of lives and properties.

Earthquake	Date	M	Landslides	Disrupted (%)	Coherent (%)	Lateral Spreads and Flows (%)	Reference
Lorca, Spain	11-May-11	5.1	256	97	3	-	Alfaro et al., 2012
Daly City, CA	22-Mar-57	5.3	23	48	30	22	Bonilla, 1960
San Salvador, El Salvador	10-Oct-86	5.7	216	93	5	2	Rymer, 1987; Rymer and White, 1989
Mt Diablo, CA	24-Jan-80	5.8	103	83	17	-	Wilson et al., 1985; Keefer and Wilson, 1989
Umbria-Marche, Italy	26-Sep-97	6	99	75	22	3	Esposito et al., 2000
Mammoth Lakes, CA	25-May-80	6.2	5,253	98	1	1	Harp et al., 1984
Avaj, Iran	22-Jun-02	6.5	550	98	2	-	Mahdavifar et al., 2006
Coalinga, CA	2-May-83	6.5	9,389	97	2	1	Harp and Keefer, 1990
Niigata Chuetsu	16-Jul-07	6.6	312	84	15	1	Collins et al. 2012
Northridge, CA	17-Jan-94	6.7	11,111	90	9	1	Harp and Jibson, 1996
Iwate-Miyagi, Japan	14-Jun-08	6.9	4,161	91	5	4	Yagi et al., 2009
Kobe, Japan	17-Jan-95	6.9	674	82	14	4	Fukuoka et al., 1997
Loma Prieta, CA	17-Oct-89	6.9	1,500	74	26	-	Keefer and Manson, 1998
Chi-Chi, Taiwan	21-Sep-99	7.7	9,272	85	11	4	Khazi and Sitar, 2003
Tohoku, Japan	**11-Mar-11**	**9**	**3,508**	**49.5**	**0.2**	**50.3**	**This report**

Table 2.8 Coseismic landslide type distributions for 15 historic earthquakes disaggregated by Keefer and Wilson (1989) landslide classes. Disrupted (debris slides and rock irregular slides), Coherent (rotational slides), and Lateral Spreads and Flows. Eight additional coseismic landslide datasets where the authors describe 'most' or 'virtually all' landslides as disrupted (e.g., Tecoman, MX; Keefer et al., 2006) without percentage estimates were omitted (See Appendix B)

2.5.2 Coseismic landslide concentrations

Compared with many studies of shallow crustal earthquake coseismic landslide inventories (e.g., Lee et al., 2008; Xu et al, 2014) single-variate correlations between landslide concentrations (i.e. LS/km^2 or frequency ratio) are weaker for all mapped landslides in the Tohoku dataset. In some cases, widely observed landslide concentration behavior of physical significance (e.g., decreasing landslide concentration with distance from the fault rupture plane, Marc et al., 2016)

are reversed in the Tohoku data (landslide occurrence weakly expected in increase with R_{jb}). While some of these trends (e.g., landslide frequency ratio as a function of slope) improve when disaggregated by landslide type, others (e.g., distance) do not, challenging the perception coseismic landslides can be framed in terms of single-variate thresholds or with respect to seismologically driven frameworks derived from distance to the earthquake source (e.g., Marc et al., 2016). A threshold or single-variate framework for coseismic landslides is an indirect one. Published thresholds of minimum triggering peak ground acceleration of coseismic landslides: 0.18g (Niigata Chuetsu-Oki, Japan, Collins et al., 2012) or 0.15g (Chi-Chi, Taiwan, Khazai and Sitar, 2000), are easily produced (here 0.12g) but are specific to the materials, slopes, and temporally-variable conditions (e.g., ground saturation and anthropogenic modification) at the time of the earthquake. Similarly, statistically informal (e.g., Keefer, 1984) and formal (e.g., Marc et al., 2016) analyses correlating magnitude-distance pairs to limits and concentrations of coseismic landsides implicitly or explicitly assume a uniform earth being acted upon by self-similar earthquakes. As shown exhaustively in the context of individual slope analyses (e.g., Lambe and Whitman, 1969; Hungr et al., 1989) the initiation of landslides results from the imbalance of forces acting to resist downslope movement and those acting to cause movement. These conflicting forces (slope, material strength, pore water pressure, seismic shaking, etc.) can vary in both space in time across a landscape, reshaping expected patterns from a uniform-earth assumption.

In its simplified form presented here, the relative balance between resting forces (material strength, assumed geometry) and driving forces (peak ground acceleration and slope) expressed as the ratio of slope yield acceleration to PGA (k_y/PGA) provides a clear explanation of triggered

landslide concentrations by the Tohoku earthquake in a physically consistent framework. Similar, qualitative, findings adopting a ratio of peak ground acceleration to a landslide susceptibility index (slope), have been made for two earthquakes in New Zealand (Rosser and Carey, 2017). While some material strengths were estimated from unmodified debris slides using a physics-based back analysis process (Gallen et al., 2015), these represent only 27% of all assessed landslides (strengths otherwise estimated from the age of the deposit), and are independent of all other modes of landslide assessed or landslides in modified slopes. If a strong bias effect were present due to similarities between strength estimation and analysis, only natural debris slides would be affected, whereas Fig. 2.32 shows all modes of landslide failure in the Tohoku inventory are well described by k_y/PGA. To further verify this physically-based framework of k_y/PGA, an independently developed coseismic landslide inventory by Sato et al. (2013, 2015) of landslides triggered by the April 11, 2011, M6.6 Iwaki aftershock earthquake was used to test the framework. For all modes of landslides triggered by the Iwaki aftershock, k_y/PGA describes a rapid increase in landslide frequency ratios and landslides per square kilometer for values below 1.5 (Fig. 2.36). Here estimates of strength for each mapped geologic unit were adopted for the Iwaki dataset without modification, and if perfect for both coseismic inventories we would expect rapid landslide frequency increases below 1.0, with no landslide occurrence above 1.0. In these real, heterogeneous, materials across a complex range of failure modes, we observe sharp increases in landslide frequency from a low (non-zero rate) above 1.25 and 1.5 for Tohoku and Iwaki, respectively. The higher inflection point (1.5) between sparse and dense landslide triggering in the aftershock earthquake may be associated with elevated pore water pressures (not considered) or as some have suggested a coseismic weakening of materials

(Parker et al., 2015) during previous shaking, both of which would develop lower than predicted effective hillslope strength at failure, shifting the curve towards an inflection point of 1.0.

Omitted physical parameters such as hillslope hydrology and vegetation, known to play key roles in local hillslope stability and susceptibility to failure, should be included in future analyses. Additional research seeking to bridge between the body of geotechnical research and knowledge at the site-specific scale – where dynamic hydrology and natural and unnatural reinforcement or destabilization of slopes can be readily assessed – and the small-scale analyses performed will be required to more fully capture hillslope dynamics at the scales of large magnitude subduction zone earthquakes. Understanding the interplay between slope, material strength, hydrology, anthropogenic modification, vegetation, and shaking, for multiple modes of landslide failure, will greatly improve our ability to forecast coseismic landslide hazard and risk, and thus facilitate better informed mitigation-strategies.

2.5.3 Effects of anthropogenic modification

The nature of anthropogenic changes for all landslides in Quaternary and Mesozoic units was visually re-inspected to determine if susceptibility to landslide triggering with modification could be described by the type of modification to the landscape, rather than the age of the deposits. Quaternary units were found to have much higher (30 – 55%) rates of anthropogenic stabilization (e.g., engineered slopes or the reduction of surcharge around the source area) than older units (stabilization rates of 7 – 16%). Destabilizing modification was found to be dominated by road cuts with no observed engineered reinforcement. A potential explanation for the observed shift from stabilizing young materials (causing the increase in computed strengths) and destabilization

of old materials (and weakening anthropogenically modified slopes) is the difference in natural slope stability between these two classes of materials. Quaternary units (primarily Holocene alluvium) are relatively weak, causing any road cut to trigger engineered mitigation efforts, while the Mesozoic sedimentary and volcanic rocks were deemed to be statically safe when exposed as road cuts, but were not seismically stable during Tohoku levels of shaking. If we assume Fig. 2.40 (correlating material age to anthropogenic change in expected material strength) is applicable elsewhere, or a simplified case where Quaternary units may experience stabilization with all older materials experiencing destabilization, the changes to our landscape driven by infrastructure, urbanization, and agriculture may significantly affect landslide susceptibility, and their consequences, during future large magnitude earthquakes. In the case of a future megathrust earthquake off the coast of North America on the Cascadia Subduction Zone, widespread steep road cuts along critical lifelines may have seen an effective reduction in strength (via changes to slope geometry) of 5 – 15%, increasing the likelihood that tsunami evacuation and emergency response routes will be impeded by coseismic landslides. Currently, metrics for anthropogenic and vegetation proxies (land use/cover, vegetation type) available at the required scales (state to national-scale) are insufficient in resolution and detail to capture the critical edge effects caused by humans (e.g., road cuts and localized placement of fill.) For the predictive capabilities of these observations to be realized, additional work is required to translate site-specific data on changes to the landscape, or remotely-sensed techniques tailored to these analyses, are needed to assess changes to hazard and risk due to anthrophonic modification to regionally significant scales.

2.6 Conclusions

3,508 landslides triggered by the 2011 M9.0 Tohoku, Japan earthquake have been mapped and classified into five distinct modes of failure. For each mapped landslide, an assessment of the state of its source, anthropogenically modified or natural, and the consequences to the built environment, damages to buildings, roadways, direct economic costs, or no-impact, was made. Lateral spreads and flow slides were found to occur predominantly in anthropogenically modified portions of the landscape and drove observed consequences. Debris slides (alternatively shallow translational slides or disrupted soil slides), often considered to be the dominant mode of coseismic landslides, make up just half of the observed landslides, and were primarily triggered in natural terrain, leading to a disproportionately small impact to the built environment. Rock irregular slides and rotational slumps were minor landslide failure modes for the Tohoku earthquake. Driven by differences in triggered modes of landslides and the heavy influence of anthropogenic modification, commonly observed relationships for landslide concentration triggered by shallow crustal earthquakes (e.g., sharply increasing landslide concentration with peak ground acceleration, slope, or decreasing concentration with distance from faulting) are not strongly observed. Here I introduce a physically-based landslide likelihood framework, based on quantitative estimates of resisting (material strength) and triggering (slope, peak ground acceleration) forces, expressed as the ratio k_y/PGA, where k_y is the slope's yield acceleration, to explain the distribution of mapped coseismic landslides, of all modes, triggered by the Tohoku earthquake. This physically-based framework was then verified using an independently mapped coseismic landslide inventory from the M6.6 Iwaki earthquake within the Tohoku landslide study region, finding a nearly identical distribution of landslide concentrations strongly correlated to k_y/PGA. Future analyses of coseismic landslide inventories should consider this

physically-based framework for landslide stability, as well as catalog landslide type, source area, and consequences to further develop our understanding of the interplay between anthropogenic modification, landslide triggering, and consequences to the built environment.

Acknowledgements

Financial support for this research was provided by the U. S. National Science Foundation under Grant No. 1331412. The opinions, findings, and recommendation expressed in this chapter are those of the author and do not necessarily reflect the views of these agencies. Landslide mapping support was provided by Eddy Liu and Lisa Dunham at the University of Washington.

References

Abdulwahid, W. M., & Pradhan, B. (2016). Landslide vulnerability and risk assessment for multi-hazard scenarios using airborne laser scanning data (LiDAR). *Landslides*, 1-20.

Alfaro, P., Delgado, J., García-Tortosa, F. J., Lenti, L., López, J. A., López-Casado, C., & Martino, S. (2012). Widespread landslides induced by the Mw 5.1 earthquake of 11 May 2011 in Lorca, SE Spain. *Engineering Geology*, *137*, 40-52.

Atkinson, P. M., & Massari, R. (1998). Generalised linear modelling of susceptibility to landsliding in the Central Apennines, Italy. *Computers & Geosciences*, *24*(4), 373-385.

Ayalew, L., & Yamagishi, H. (2005). The application of GIS-based logistic regression for landslide susceptibility mapping in the Kakuda-Yahiko Mountains, Central Japan. *Geomorphology*, *65*(1), 15-31.

Bhattacharya, S., Hyodo, M., Goda, K., Tazoh, T., & Taylor, C. A. (2011). Liquefaction of soil in the Tokyo Bay area from the 2011 Tohoku (Japan) earthquake. *Soil Dynamics and Earthquake Engineering*, *31*(11), 1618-1628.

Bonilla, M. G. (1960). *Landslides in the San Francisco South Quadrangle, California* (No. 60-15). US Geological Survey

Chang, K. T., Chiang, S. H., & Hsu, M. L. (2007). Modeling typhoon-and earthquake-induced landslides in a mountainous watershed using logistic regression. *Geomorphology*, *89*(3), 335-347.

Chigira, M., Nakasuji, A., Fujiwara, S., & Sakagami, M. (2013). Catastrophic landslides of pyroclastics induced by the 2011 off the Pacific coast of Tohoku Earthquake. In *Earthquake-Induced Landslides* (pp. 139-147). Springer Berlin Heidelberg.

Collins, B. D., Kayen, R., & Tanaka, Y. (2012). Spatial distribution of landslides triggered from the 2007 Niigata Chuetsu–Oki Japan Earthquake. *Engineering geology*, *127*, 14-26.

Cruden, D.M, and Varnes, D.J., 1996, Landslide types and processes, *in* Turner, A. Keith, and Schuster, Robert L. eds. Landslides—Investigation and mitigation: Transportation Research Board, Special report no. 247, National Research Council, National Academy Press, Washington, D.C., p. 36–75.

Cubrinovski M, Bradley B, Wotherspoon L, Green R, Bray J, Wood C, Pender M, Allen J, Bradshaw A, Rix G, Taylor M (2011) Geotechnical aspects of the 22 February 2011 Christchurch earthquake. Bull of the New Zealand Society for Earthq Engineering 44(4), 205-226

Dai, F. C., Xu, C., Yao, X., Xu, L., Tu, X. B., & Gong, Q. M. (2011). Spatial distribution of landslides triggered by the 2008 Ms 8.0 Wenchuan earthquake, China. *Journal of Asian Earth Sciences*, *40*(4), 883-895.

de Vallejo, L. G., & Ferrer, M. (2012). *Geological engineering*. CRC Press, London.

Esposito, E., Porfido, S., Simonelli, A. L., Mastrolorenzo, G., & Iaccarino, G. (2000). Landslides and other surface effects induced by the 1997 Umbria–Marche seismic sequence. *Engineering geology*, *58*(3), 353-376.

Faure, M., F. Lalevee, Y. Gusokujima, J. T. Iiyama, and J. P. Cadet (1986). The pre-Cretaceous deep-seated tectonics of the Abukuma massif and its place in the structural framework of Japan, Earth Planet. Sci. Lett. 77, 384–398.

Fukuoka, H., Sassa, K., & Scarascia-Mugnozza, G. (1997). Distribution of landslides triggered by the 1995 Hyogo-ken Nanbu earthquake and long runout mechanism of the Takarazuka Golf Course landslide. *Journal of Physics of the Earth*, *45*(2), 83-90.

Gallen, S. F., Clark, M. K., & Godt, J. W. (2015). Coseismic landslides reveal near-surface rock strength in a high-relief, tectonically active setting. *Geology*, *43*(1), 11-14.

Gallen, S. F., Clark, M. K., Godt, J. W., Roback, K., & Niemi, N. A. (2017). Application and evaluation of a rapid response earthquake-triggered landslide model to the 25 April 2015 Mw 7.8 Gorkha earthquake, Nepal. *Tectonophysics*, *714*, 173-187.

García-Rodríguez, M. J., Malpica, J. A., Benito, B., & Díaz, M. (2008). Susceptibility assessment of earthquake-triggered landslides in El Salvador using logistic regression. *Geomorphology*, *95*(3), 172-191.

Geospatial Information Authority of Japan. Digital elevation models of Honshu, Japan. http://www.gsi.go.jp/gis.html (last accessed November, 2017)

Goodman, R. E. (1989). *Introduction to rock mechanics* (Vol. 2, p. 576). New York: Wiley.

Goto, H., & Morikawa, H. (2012). Ground motion characteristics during the 2011 off the Pacific coast of Tohoku earthquake. *Soils and Foundations*, *52*(5), 769-779.

Greenfield, M. (2017) Effects of Long-duration ground motions on liquefaction hazards. Doctoral Thesis, University of Washington.

Harp E.L., and Keefer, D. K. (1990) Landslides Triggered by the Earthquake. *In The Coalinga, California, Earthquake of May 2, 1983 Rymer, M.J. and Ellsworth, W.L. (eds.)* IS Geological Survey Prof. Paper 1487.

Harp, E. L., & Jibson, R. W. (1996). Landslides triggered by the 1994 Northridge, California, earthquake. *Bulletin of the Seismological Society of America*, *86*(1B), S319-S332.

Harp, E.L., Tanaka, K., Sarmiento, J., & Keefer, D.K. (1984) Landslides from the May 25 – 27, 1980 Mammoth Lakes, California, earthquake sequence. Miscellaneous Investigations Map I-1612. US Geological Survey.

Harp, E. L., Hartzell, S. H., Jibson, R. W., Ramirez-Guzman, L., & Schmitt, R. G. (2014). Relation of Landslides triggered by the kiholo bay earthquake to modeled ground motion. Bulletin of the Seismological Society of America, 104(5), 2529-2540.

Higaki, D., & Abe, S. (2013). Classification of the geomorphology, geology and movement types of earthquake landslides. In *Earthquake-induced landslides* (pp. 37-44). Springer, Berlin, Heidelberg.

Highland, L.M., and Bobrowsky, Peter, 2008, The landslide handbook—A guide to understanding landslides: Reston, Virginia, U.S. Geological Survey Circular 1325, 129 p.

Hungr, O., Leroueil, S., & Picarelli, L. (2014). The Varnes classification of landslide types, an update. *Landslides*, *11*(2), 167-194.

Hungr, O., Salgado, F. M., & Byrne, P. M. (1989). Evaluation of a three-dimensional method of slope stability analysis. *Canadian Geotechnical Journal*, *26*(4), 679-686.

Japan Meteorological Agency (2017). Monthly mean and monthly total tables retrieved from Japan Meteorological Agency at http://www.data.jma.go.jp/obd/stats/data/en/smp/index.html (last accessed November, 2017).

Jibson, R. W., Harp, E. L., Schulz, W., & Keefer, D. K. (2004). Landslides triggered by the 2002 Denali Fault, Alaska, earthquake and the inferred nature of the strong shaking. Earthquake Spectra, 20(3), 669-691.

Katz, O., & Crouvi, O. (2007). The geotechnical effects of long human habitation (2000< years): Earthquake induced landslide hazard in the city of Zefat, northern Israel. *Engineering Geology*, *95*(3), 57-78.

Kazama, M., & Noda, T. (2012). Damage statistics (Summary of the 2011 off the Pacific Coast of Tohoku Earthquake damage). *Soils and Foundations*, *52*(5), 780-792.

Keefer DK (1984) Landslides caused by earthquakes. Geological Society of America Bulletin 95, 406–421
Keefer, D.K., Manson, M.W., 1998. Regional distribution and characteristics of landslides generated by the earthquake. In: Keefer, D.K. (Ed.), The Loma Prieta, California earth- quake of October 17, 1989 — landslides, US Geol. Survey Prof. Paper 1551-C, C7–C32.

Keefer, D. K., & Wilson, R. C. (1989). Predicting earthquake-induced landslides, with emphasis on arid and semi-arid environments. *Landslides in a semi-arid environment*, *2*(PART 1), 118-149.

Keefer, D. K., Wartman, J., Ochoa, C. N., Rodriguez-Marek, A., & Wieczorek, G. F. (2006). Landslides caused by the M 7.6 Tecomán, Mexico earthquake of January 21, 2003. *Engineering Geology*, *86*(2), 183-197.

Khazai, B., & Sitar, N. (2004). Evaluation of factors controlling earthquake-induced landslides caused by Chi-Chi earthquake and comparison with the Northridge and Loma Prieta events. *Engineering geology*, *71*(1), 79-95.

Kramer SL (1996) Geotechnical Earthquake Engineering, Prentice Hall, Upper Saddle River, NJ

Kritikos, T., Robinson, T. R., & Davies, T. R. (2015). Regional coseismic landslide hazard assessment without historical landslide inventories: A new approach. *Journal of Geophysical Research: Earth Surface*, *120*(4), 711-729.

Kurahashi, S., & Irikura, K. (2011). Source model for generating strong ground motions during the 2011 off the Pacific coast of Tohoku Earthquake. *Earth, planets and space*, *63*(7), 11.

Lambe, T. W., & Whitman, R. V. (1969). Soil Mechanics, 553 pp. *John Wiley & Sons, N. York*.

Lavé, J., & Burbank, D. (2004). Denudation processes and rates in the Transverse Ranges, southern California: Erosional response of a transitional landscape to external and anthropogenic forcing. *Journal of Geophysical Research: Earth Surface*, *109*(F1).

Lee, S., & Pradhan, B. (2007). Landslide hazard mapping at Selangor, Malaysia using frequency ratio and logistic regression models. *Landslides*, *4*(1), 33-41.

Lee, C. T., Huang, C. C., Lee, J. F., Pan, K. L., Lin, M. L., & Dong, J. J. (2008). Statistical approach to earthquake-induced landslide susceptibility. *Engineering Geology*, *100*(1), 43-58.

Mahdavifar, M. R., Solaymani, S., & Jafari, M. K. (2006). Landslides triggered by the Avaj, Iran earthquake of June 22, 2002. *Engineering geology*, *86*(2), 166-182.

Marc, O., Hovius, N., Meunier, P., Gorum, T., & Uchida, T. (2016). A seismologically consistent expression for the total area and volume of earthquake-triggered landsliding. *Journal of Geophysical Research: Earth Surface*, *121*(4), 640-663.

Matsumoto, H. (1985). Beach ridge ranges and the Holocene sea-level fluctuations on alluvial coastal plains, northeast Japan, Sci. Rep. Tohoku Univ. 7th series (Geography) 35, 15–46.

Meunier P, Hovius N, Haines AJ (2007) Regional patterns of earthquake-triggered landslides and their relation to ground motion. Geophysical Research Letters, 34(20)

Meusburger, K., & Alewell, C. (2008). Impacts of anthropogenic and environmental factors on the occurrence of shallow landslides in an alpine catchment (Urseren Valley, Switzerland). *Natural Hazards and Earth System Sciences*, *8*, 509-520.

Mikoshiba, M. U., Kanisawa, S., Matsuhisa, Y., & Togashi, S. (2004). Geochemical and isotopic characteristics of the Cretaceous Orikabe Plutonic Complex, Kitakami Mountains, Japan: magmatic evolution in a zoned pluton and significance of a subduction-related mafic parental magma. *Contributions to Mineralogy and Petrology*, *146*(4), 433-449.

Minoura, K., & Hasegawa, A. (1992). Crustal structure and origin of the northeast Japan arc. *Island Arc*, *1*(1), 2-15.

Miyagi, T., Higaki, D., Yagi, H., Doshida, S., Chiba, N., Umemura, J., & Satoh, G. (2011). Reconnaissance report on landslide disasters in northeast Japan following the M 9 Tōhoku earthquake. *Landslides*, *8*(3), 339-342.

Miyashiro, A. (1958). Regional metamorphism of the Gosaisho Takanuki district in the Central Abukuma plateau, J. Facul. Sci. Univ. Tokyo, Sec. 2 11, 219–272.

Mori, T., Tobita, Y., & Okimura, T. (2012). The damage to hillside embankments in Sendai city during The 2011 off the Pacific Coast of Tohoku Earthquake. *Soils and foundations*, *52*(5), 910-928.

Nefeslioglu, H. A., Gokceoglu, C., & Sonmez, H. (2008). An assessment on the use of logistic regression and artificial neural networks with different sampling strategies for the preparation of landslide susceptibility maps. *Engineering Geology*, *97*(3), 171-191.

Nowicki, M. A., Wald, D. J., Hamburger, M. W., Hearne, M., & Thompson, E. M. (2014). Development of a globally applicable model for near real-time prediction of seismically induced landslides. *Engineering Geology*, *173*, 54-65.

Okamoto, R., Kojima, K., & Yoshinaka, R. (1981, January). Distribution and engineering properties of weak rocks in Japan. In *ISRM International Symposium*. International Society for Rock Mechanics.

Oommen, T., Baise, L. G., & Vogel, R. M. (2011). Sampling bias and class imbalance in maximum-likelihood logistic regression. *Mathematical Geosciences*, *43*(1), 99-120.

Ozawa, S., Nishimura, T., Suito, H., Kobayashi, T., Tobita, M., & Imakiire, T. (2011). Coseismic and postseismic slip of the 2011 magnitude-9 Tohoku-Oki earthquake. *Nature*, *475*(7356), 373-376.

Pradel, D., J. Wartman, and B. Tiwari (2012). Impact of anthropogenic changes on liquefaction along the Tone River during the 2011 Tohoku Earthquake, Nat. Hazards Rev., doi: 10.1061/(ASCE)NH.1527- 6996.0000097.

Pradhan, B., & Lee, S. (2010). Landslide susceptibility assessment and factor effect analysis: backpropagation artificial neural networks and their comparison with frequency ratio and bivariate logistic regression modelling. *Environmental Modelling & Software*, *25*(6), 747-759.

Rosser, B. J., & Carey, J. M. (2017). Comparison of landslide inventories from the 1994 Mw 6.8 Arthurs Pass and 2015 Mw 6.0 Wilberforce earthquakes, Canterbury, New Zealand. *Landslides*, 1-10.

Rymer, M. J. (1987). The San Salvador earthquake of October 10, 1986—geologic aspects. *Earthquake Spectra*, *3*(3), 435-463.

Rymer, M. J., & White, R. A. (1989, July). Hazards in El Salvador from earthquake-induced landslides. In *Landslides: extent and economic significance, Proceedings of 28th international geological congress, Washington, DC* (pp. 105-109).

Sassa, K. (2005). Landslide disasters triggered by the 2004 Mid-Niigata Prefecture earthquake in Japan. *Landslides*, *2*(2), 135-142.

Sato, G., Hayashi, K., Yagi, H., & Higaki, D. (2013). Distribution of Landslides Induced in Iwaki City, Japan, by Two Large-scale Earthquakes in 2011. In *Earthquake-Induced Landslides* (pp. 763-767). Springer, Berlin, Heidelberg.

Sato, G., Hayashi, K., Yagi, H., Higaki, D. (2015) Spatial distribution characteristics of landslides caused by the 2011 Fukushima-ken Hamadori earthquake in Japan. *Journal of the Japanese Landslide Society* 52(2), 32 – 36.

Schmidt KM, Roering JJ, Stock JD, Dietrich WE, Montgomery DR, Schaub T (2001) The variability of root cohesion as an influence on shallow landslide susceptibility in the Oregon Coast Range. Canadian Geotechnical Journal, 38(5), 995-1024

Song, Y., Gong, J., Gao, S., Wang, D., Cui, T., Li, Y., & Wei, B. (2012). Susceptibility assessment of earthquake-induced landslides using Bayesian network: a case study in Beichuan, China. *Computers & Geosciences*, *42*, 189-199.

Tamura, T., and F. Masuda (2005). Bed thickness characteristics of inner- shelf storm deposits associated with a transgressive to regressive Holocene wave-dominated shelf, Sendai coastal plain, Japan, Sedimen- tology 52, 1375–1395.

Tanaka, M., Asano, K., Iwata, T., & Kubo, H. (2014). Source rupture process of the 2011 Fukushima-ken Hamadori earthquake: how did the two subparallel faults rupture?. *Earth, Planets and Space*, *66*(1), 101.

Toda, S., & Tsutsumi, H. (2013). Simultaneous Reactivation of Two, Subparallel, Inland Normal Faults during the Mw 6.6 11 April 2011 Iwaki Earthquake Triggered by the Mw 9.0 Tohoku-oki, Japan, Earthquake. *Bulletin of the Seismological Society of America*, *103*(2B), 1584-1602.

Tiwari, B., Wartman, J., & Pradel, D. (2013). Slope Stability Issues After Mw 9.0 Tohoku Earthquake. In *Geo-Congress 2013: Stability and Performance of Slopes and Embankments III* (pp. 1587-1594).

Ujiie-Mikoshiba, M., Imai, N., Terashima, S., Tachibana, Y., & Okai, T. (2006). Geochemical mapping in northern Honshu, Japan. *Applied geochemistry*, *21*(3), 492-514.

United States Geological Survey (2017). Ground motion intensity parameters retrieved from the USGS at https://earthquake.usgs.gov/earthquakes/eventpage/official20110311054624120_30#shakemap (last accessed November, 2017.

Uzuoka, R., Sento, N., Kazama, M., & Unno, T. (2005). Landslides during the earthquakes on May 26 and July 26, 2003 in Miyagi, Japan. *Soils and Foundations*, *45*(4), 149-163.

Wang, H. B., Sassa, K., & Xu, W. Y. (2007). Analysis of a spatial distribution of landslides triggered by the 2004 Chuetsu earthquakes of Niigata Prefecture, Japan. *Natural Hazards*, *41*(1), 43.

Wartman J, Dunham L, Tiwari B, Pradel D (2013) Landslides in eastern Honshu induced by the 2011 Tohoku earthquake. Bulletin of the Seismological Society of America, 103(2B), 1503-1521

Weisberg, S. (2005). *Applied linear regression* (Vol. 528). John Wiley & Sons.

Wilson, R. C., Wieczorek, G. F., Keefer, D. K., Harp, E. L., & Tannaci, N. E. (1985). *Map showing ground failures from the Greenville/Mount Diablo earthquake sequence of January 1980, Northern California* (No. 1711). US Geological Survey.

Xiaoli, C., Qing, Z., & Chunguo, L. (2015). Distribution pattern of coseismic landslides triggered by the 2014 Ludian, Yunnan, China Mw6. 1 earthquake: special controlling conditions of local topography. *Landslides*, *12*(6), 1159-1168.

Xu, C., Xu, X., Yao, X., & Dai, F. (2014). Three (nearly) complete inventories of landslides triggered by the May 12, 2008 Wenchuan Mw 7.9 earthquake of China and their spatial distribution statistical analysis. *Landslides*, *11*(3), 441-461.

Yagi, H., Sato, G., Higaki, D., Yamamoto, M., & Yamasaki, T. (2009). Distribution and characteristics of landslides induced by the Iwate–Miyagi Nairiku Earthquake in 2008 in Tohoku District, Northeast Japan. *Landslides*, *6*(4), 335.

Yalcin, A. (2008). GIS-based landslide susceptibility mapping using analytical hierarchy process and bivariate statistics in Ardesen (Turkey): comparisons of results and confirmations. *Catena*, *72*(1), 1-12.

Yesilnacar, E., & Topal, T. (2005). Landslide susceptibility mapping: a comparison of logistic regression and neural networks methods in a medium scale study, Hendek region (Turkey). *Engineering Geology*, *79*(3), 251-266.

Yilmaz, I. (2009). Landslide susceptibility mapping using frequency ratio, logistic regression, artificial neural networks and their comparison: a case study from Kat landslides (Tokat—Turkey). *Computers & Geosciences*, *35*(6), 1125-1138.

Yonekura, N., S. Kaizuka, M. Nogami, and K. Chinzei (Editors) (2001). Introduction to Japanese Geomorphology, University of Tokyo Press, Tokyo (in Japanese).

Chapter 3 – Probabilistic Coseismic Landslide Hazard Analysis of Seattle, Washington

The contents of this chapter are being prepared for publication as:

Grant and Wartman. Probabilistic coseismic landslide hazard analysis for Seattle, WA

Grant, LaHusen, Wartman, and Duvall (*in review*) Cascadia subduction zone coseismic landslide mapping and hazard forecasting. *Extended Abstract*, 11th National Conference on Earthquake Engineering. Los Angeles, 2018.

Chapter 3: Probabilistic Coseismic Landslide Hazard Analysis (PCLHA) of Seattle, WA

3.1 Introduction

The Cascadia subduction zone (CSZ), offshore of Oregon, Washington, British Columbia and Northern California, has produced a sequence M8-9 earthquakes in the Holocene determined from coastal evidence of shaking, subsidence, and tsunamis (Atwater et al., 2005) as well as off-shore turbidite data (Goldfinger et al., 2012). Earthquakes larger than M8.0 are believed to have a recurrence interval of 250 – 350 years (Frankel, 2011; Goldfinger et al., 2012), with the last great earthquake occurring on January 26, 1700 (e.g., Atwater et al., 2005). The consequences of a great (M9.0) earthquake along the CSZ are highly uncertain due to a lack of available data from previous great earthquakes in North America and the complexities of modeling such a large event over an area the size of the pacific northwest (PNW). From previous megathrust earthquakes in other locations, losses may be many billions of US dollars, and several thousand lives may be lost due to shaking damage, landslides, and tsunamis. Of particular concern are that would affect densely populated areas within the Puget Sound and along the Columbia River, as well as coastal and mountainous communities situated along or below potentially mobile hillslopes. Many communities in coastal British Columbia, Washington, and Oregon are connected to the rest of the region by sparse road networks that cut through steep, and generally, slide-prone topography. Accurate forecasting of coseismic landslide hazards on the scale of the PNW will help identify particularly vulnerable communities to landslide impacts or isolation due to roadway blockage, in addition to direct losses due to landslide impacts to homes, and allow for targeted mitigation prior to the next great Cascadia Subduction Zone earthquake.

Here the cities of Seattle and Mercer Island were assessed in detail as a case study for the application of synthetic M9.0 CSZ earthquake ground motions to the PNW. Two sets of probabilistic analyses for coseismic landslide hazard were developed.

1. Conditional probability of landslide occurrence given a M9.0 Cascadia Subduction Zone earthquake
2. Coseismic landslide hazard due to multiple sources of seismicity for a 10% in 50-year exceedance rate.

In (1), uncertainty in material properties, ground saturation conditions, and shaking intensity were incorporated into a probabilistic estimation of landslide triggering likelihood. Previous probabilistic coseismic landslide hazard analyses have been developed for single landslide types, single seismic sources, and/or heuristic ground water estimates (e.g. Saygili and Rathje, 2009; Allstadt et al., 2013; Lari et al., 2014; Wang and Rathje, 2015), limiting their future applicability to quantitative risk analysis via over-simplification of diverse landslide phenomena, or unrealistic physical conditions leading to landslide triggering and consequences. Here the work of Chapter 1 (Grant et al., 2016) was utilized to develop probabilistic coseismic landslide hazard for two modes of landslides: shallow translational and deep rotational slides. A suite of synthetic ground motions simulating a M9.0 CSZ earthquake (Frankel et al., *in review*) were used in concert with a megathrust-specific coseismic sliding-block displacement model developed for this study to predict probabilities of landslide triggering. Empirical ground saturation conditions from nearby monitoring data (Smith et al., 2017) were used to determine realistic winter and summer ground saturation conditions across the study region. The resultant probabilistic coseismic landslide hazard map for Seattle and Mercer Island reflects advances in failure mechanism modeling, via refined multi-modal procedures, large-magnitude synthetic ground

motion analysis, utilizing a suite of potential M9.0 CSZ synthetics, and ground saturation conditions, utilizing recorded local conditions in regional-scale analyses. The proposed coseismic landslide model was then verified against known landslides triggered by the 2001 M6.8 Nisqually, WA earthquake based on recorded ground motions. Predicted coseismic landslide probabilities of occurrence closely match observed Nisqually-triggered landslides, providing strong support for the applicability of these models.

In (2), coseismic landslide hazard is analyzed for multiple sources of seismicity and combined into a Probabilistic Coseismic Landslide Hazard Analysis (PCLHA) based on the relative seismic hazard for each earthquake source affecting Seattle. Coseismic landslide hazard developed from a synthetic M7.0 Seattle Fault earthquake (Allstadt et al., 2013), deep Benioff earthquakes, and the Cascadia Subduction Zone were compared as scenario events and then combined based on their relative contributions to the 10% in 50-year probability of exceedance peak ground acceleration hazard in Seattle. Combined with long-term estimates for ground water saturation conditions, the resultant map reflects the overall probabilities of coseismic landslide occurrence within Seattle for a timeframe of 475-years. Mapped probabilities of coseismic landslide hazard were found to generally match observed precipitation and anthropogenically-triggered landslides mapped within Seattle.

3.2 Background

3.2.1 Cascadia subduction zone landslides

To date, no landslides have been directly dated to the ~M9 1700 CSZ earthquake. Compiling Native oral histories about the 1700 earthquake, Ludwin et al. (2005) record evidence of a large-scale landslide triggered by the earthquake in southern Vancouver Island, BC, near present-day Nanaimo (Hill-Tout, 1978; Ludwin et al., 2005):

> It began about the middle of one night … threw down … houses and brought great masses of rock down from the mountains. One village was completely buried beneath a landslide. It was a very terrible experience; the people could neither stand nor sit for the extreme motion of the earth.

Karlin et al. (2004), cataloging and dating turbidite sediments in Lake Washington found one of their triggering events was most likely the 1700 CSZ earthquake (2σ ages of 130 – 400 cal. years B.P. [1550 – 1820]). Schulz et al. (2012), modeling the potential instabilities of several large-scale landslides in southern Oregon, have suggested only a large seismic source (the 1700 earthquake) could have triggered these slides, as no increase in pore water pressure on assumed pre-failure geometries were similarly capable of generating unstable conditions in the slide mass. In total, these studies amount to a small handful of unconfirmed coseismic landslides triggered by a ~M9.0 earthquake along the Cascadia Subduction Zone.

The paucity of 1700 landslides[1] is the likely the product of two independent factors. First, there are so *many* landslides in the coastal regions of the Pacific Northwest that 1700 landslides have either been superimposed and removed from the landscape or are masked by the thousands of precipitation induced landslides that have slowly accumulated over the past few centuries.

[1] i.e. landslides triggered by the 1700 CSZ earthquake

Second, large magnitude subduction zone earthquakes may not trigger as many landslides as equivalent, or much smaller magnitude, crustal earthquakes, meaning we may be searching for a 317-year-old inventory of hundreds or a few thousand landslides, and not tens or hundreds of thousands.

At least two ongoing research and field-work are seeking to find the missing 1700 landslides. LaHusen et al. (2016) are leading an effort to identify landslides clustered in time by calibrating surface roughness derived from bare-earth lidar to known landslide ages. By calibrating a few age-roughness points within the Tyee formation of Oregon they hope to identify many candidate landslides of predicted ages of ~320 years of age. Struble et al. (2017) are focusing on ghost forests in landslide-dammed lakes where an extended dendrochronology-record allows for year-of-death precision dating for the stranding of each tree, and thus the date of the damming landslide.

Simple estimates of the number of expected landslides a M9.0 earthquake could trigger, extrapolated from historic datasets of crustal earthquakes, range from 900k – 1.8m (Keefer, 2002; Malamud et al., 2004; Xu et al., 2014). Such an enormous number of landslides would dramatically reshape the natural landscape, devastate our infrastructure/transportation systems, and impact thousands of dwellings and structures. As discussed in Chapter 2, only ~3,500 landslides were triggered by the M9.0 Tohoku, Japan earthquake, the majority of which occurred in anthropogenically modified terrain. While Native American and First Nation farming and development represent anthropogenic modification exposed to the 1700 CSZ earthquake, the magnitude and severity of change present in modern North American and Japanese landscapes is

incomparable to that present during the last great CSZ earthquake. As such, very few landslides may have been triggered during the 1700 CSZ earthquake if Tohoku is representative, and far fewer may be preserved in the landscape assuming only slides of significant size (e.g. >1,000m^2) could survive several hundred years of intense rainfall and subsequent landslides.

To test the assumption that great earthquakes will produce great numbers of landslides, 38 coseismic landslide inventories from 33 earthquakes were collected to assess the factor correlated to the number of landslides triggered by each earthquake (Appendix B). This suite of coseismic landslide inventories reveals interface (subduction zone) earthquakes have triggered far fewer landslides (Eq. 3.1) than crustal earthquakes (Eq. 3.2) of similar magnitudes (Fig 3.1, based on mapped counts or best available estimates).

$$N = 0.0026e^{1.611M} \qquad \text{Equation 3.1}$$

$$N = 0.0071e^{1.874M} \qquad \text{Equation 3.2}$$

From these data, the empirically expected number of landslides for a M9.0 subduction zone earthquake is 5,160. Far fewer than expected values extrapolated from smaller magnitude crustal earthquakes. Other than earthquake magnitude, no potentially descriptive factor (e.g., area of slopes >20° where Modified Mercalli Index (MMI) $\geq$ 7, mean slope of the meizoseismal area, annual precipitation within the meizoseismal area, mapping methodology, etc.) collected for this work was found to significantly correlate to the reported number of landslides for this set of earthquakes.

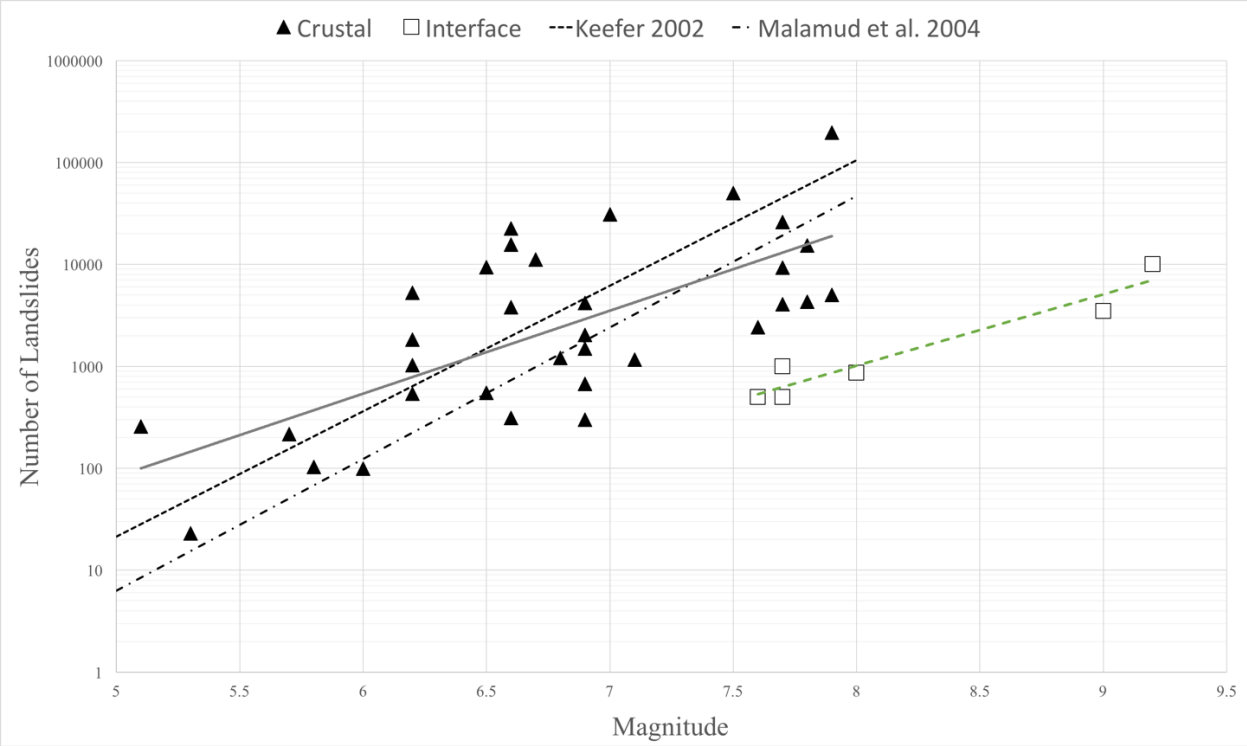

Figure 3.1 Mapped or estimated counts of subaerial coseismic landslides for crustal (black triangles) and interface (squares) earthquakes. Previous estimates (Keefer, 2002; Malamud et al. 2004) describe the trend in crustal data (solid grey line, Eq. 3.2), but do not reflect interface/subduction zone earthquakes (dashed green line, Eq. 3.1) where far fewer landslides have been observed to occur. Data used to construct this figure, and associated references to original inventories are in Appendix B.

The difference between observed landslide counts for crustal and subduction zone (interface) earthquakes has been previously hypothesized to be a function of high-frequency seismic energy attenuation from source to hillslopes for interface earthquakes. During shallow crustal earthquakes, landslides typically occur in high concentrations along, or within 1km, of fault rupture (Jibson et al., 2004; Kargel et al., 2016), whereas the closest subduction zone landslide to fault rupture may be tens of kilometers away. High-frequency energy, which attenuates more rapidly with distance than low-frequency wave energy (e.g. Shearer, 2009), is assumed to control shallow translational coseismic landslide initiation (Jibson et al., 2004; Harp et al., 2014) as it more closely matches the natural period (>10Hz) of shallow, brittle, landslides. Gorum and

Carranza (2015; Gorum et al., 2014) observe a control on the spatial pattern of coseismic landslides from the style of earthquake faulting, suggesting coseismic landslide inventory differences driven by the difference in fault mechanics. Note, only subaerial landslides, due to the availability of coseismic landslide inventories, are considered. Tens of thousands of square kilometers of ocean floor are strongly shaken during large-magnitude subduction zone earthquakes that are not considered here. Were that area of relatively flat ocean floor replaced with steep mountainous topography, many thousands of additional landslides would undoubtedly be triggered.

3.2.2 Mapped landslides of Seattle, WA

The cities of Seattle and Mercer Island are dominated by glacial geology, consisting of a stack of recessional outwash sands, till, and advance outwash deposits overlying thick clay deposits (Lawton clay, Fig. 3.6). Locally to the South, uplift along the Seattle Fault exposes bedrock, primarily volcanoclastic rocks of Eocene to Oligocene age (Troost and Booth, 2008). Glacial topography in this region is expressed as a series of N-S trending drumlins and coastal bluffs along their extensive shorelines along the Puget Sound and Lake Washington. To date, 1,555 known landslides triggered in the last century have been mapped within Seattle (Fig. 3.2, Seattle Public Utilities, 2017; Laprade and Tubbs, 2008). Steep coastal bluffs and glacial drumlin slopes typically fail due to unstable hydrologic conditions or anthropogenic forcing, but have been observed following a local earthquake (e.g. the 2011 M6.8 Nisqually earthquake). Previous studies of landslides in Seattle have focused on precipitation-induced failures (e.g. Harp et al., 2008; Brien and Reid, 2008), or due to a modeled earthquake along the Seattle Fault (Allstadt et al., 2013). Here, we develop probabilistic coseismic landslide hazard estimates, incorporating

uncertainty in published material strengths, groundwater conditions, and shaking intensity, for a M9.0 earthquake along the CSZ and probabilistic coseismic hazard analysis for a seismic hazard level of 10% probability of exceedance in 50-years. Landslides mapped in Seattle, WA show high rates of occurrence along steep coastal bluffs and inland drumlin slopes stretching back nearly a century (Fig. 3.2). Mapped landslides include those triggered by the 2001 Nisqually earthquake. To highlight a point from Ch. 2 on the occurrence of landslides in anthropogenically modified slopes, Fig. 3.3 shows the spatial distribution of Seattle landslides associated with some degree of anthropogenic modification (73%), natural slopes (10%), and unknown (17%). Strength modifications based on findings from the Tohoku landslide inventory (Ch. 2) were not applied to Seattle for this analysis, but may be possible via the future study of case history landslides in Seattle to constrain expected strength change due to anthropogenic modification.

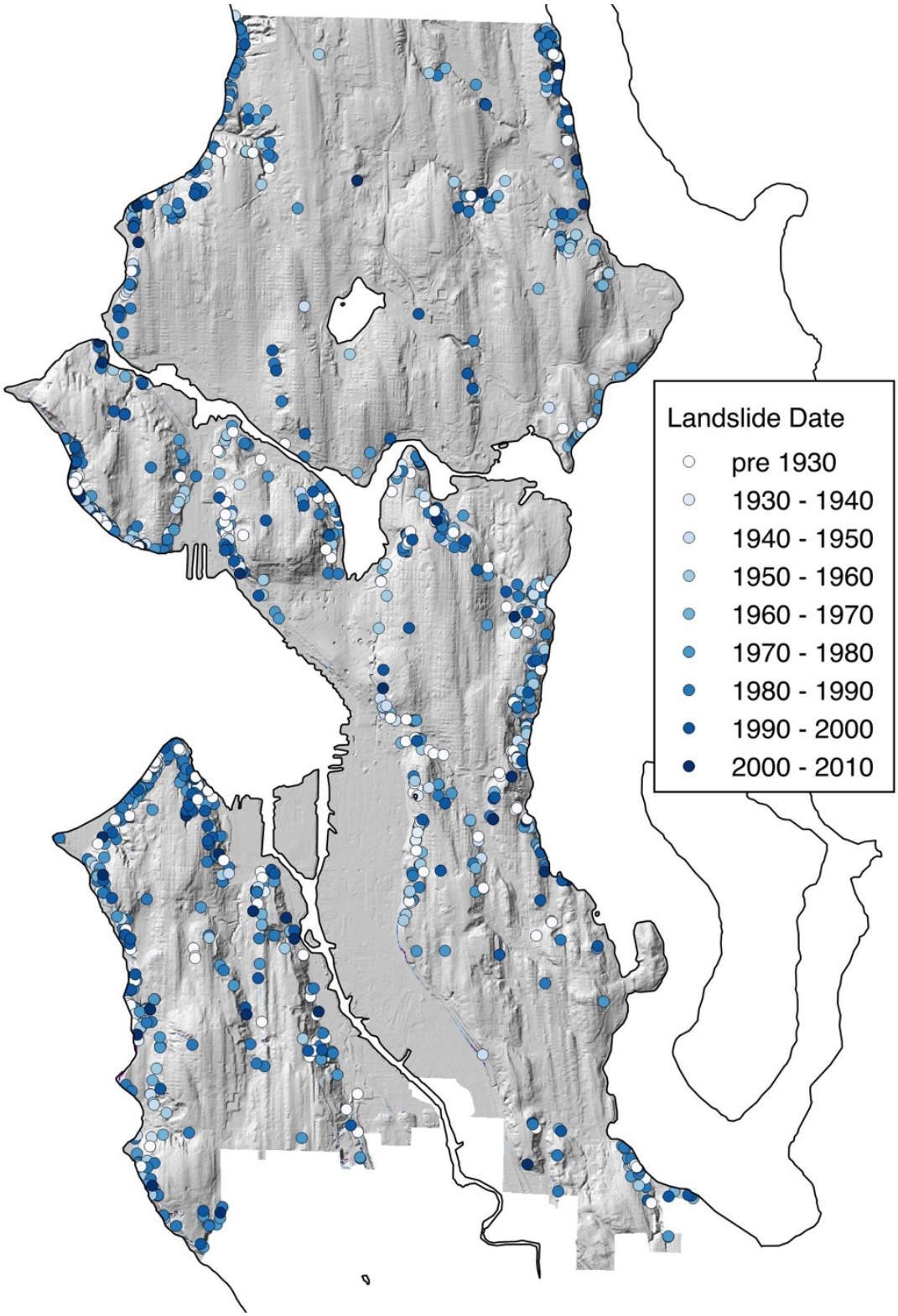

Figure 3.2 Mapped landslides within Seattle (available at https://data.seattle.gov/dataset/City-Of-Seattle-Environmentally-Critical-Areas/zwze-9nv3, last accessed November, 2017). Figure shows 1,555 landslide source regions compiled from written reports and field reconnaissance. Note all types of mapped landslides for all associated triggering events shown.

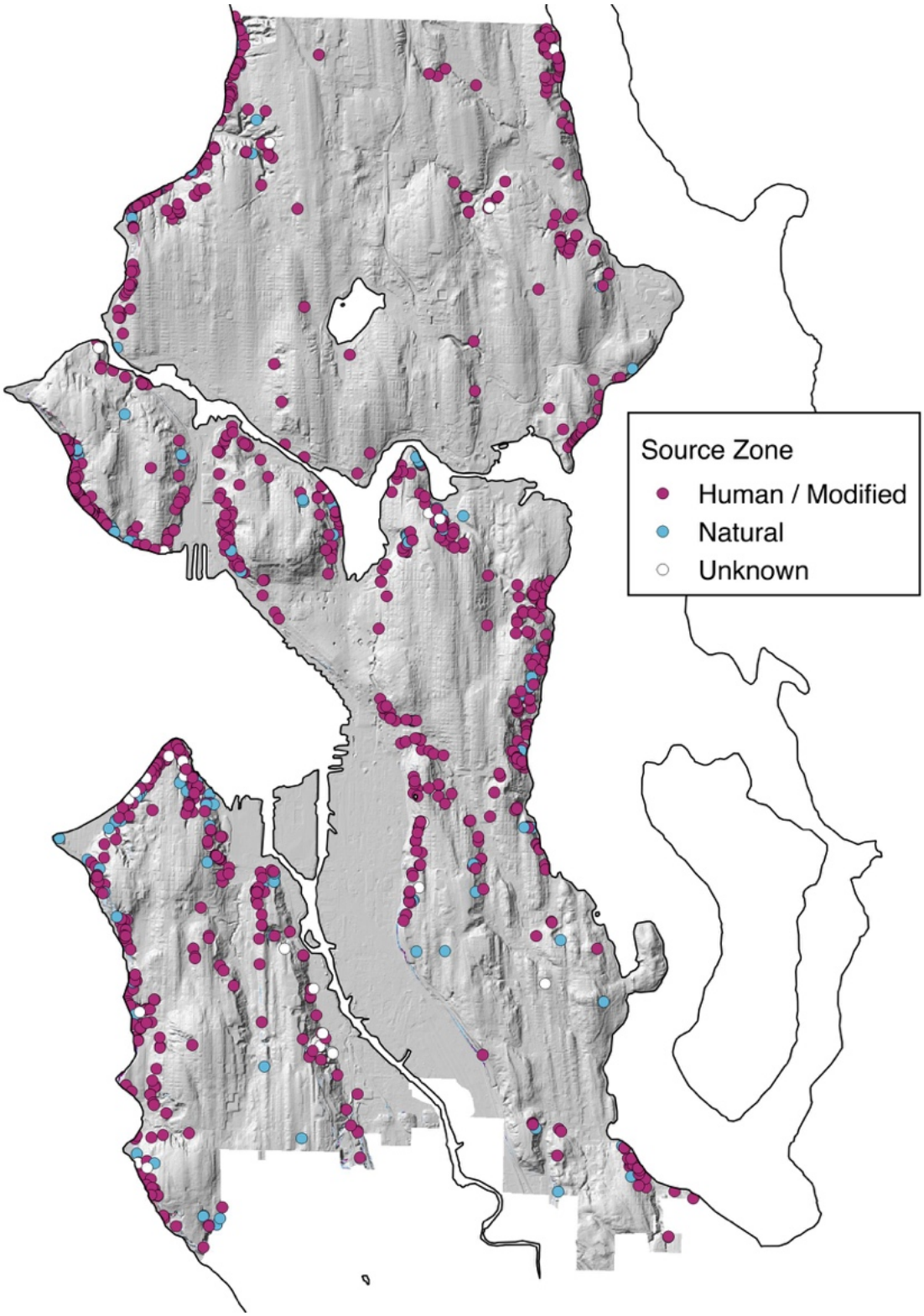

Figure 3.3 The vast majority (73%) of landslides mapped in Seattle have been known to have some degree of human influence on initiation. Just 10% of mapped slides were identified as 'natural', with the remaining 17% unknown.

3.3 Methods

Probabilistic coseismic landslide hazard for Seattle and Mercer Island, WA was conducted for two modes of landslides given a future M9.0 CSZ earthquake. Here landslide hazard is taken to be the probability of landslide occurrence, for each mode of landslide, adopting a triggering threshold of 1cm of expected coseismic landslide displacement. For each of the 30 CSZ M9.0 synthetic earthquakes, displacement was computed based on a stochastic realization of material strength (section 3.3.2), assuming two reasonable end-member conditions for dry and wet hillslope saturation conditions based on local groundwater monitoring data (Smith et al. 2017). The average probabilities of landslide occurrence across the full suite of realizations for dry and wet conditions are reported below (3.4.1).

A second analysis (3.4.6), considering multiple sources of seismicity, was then performed to develop a simplified Probabilistic Coseismic Landslide Hazard Analysis (PCLHA) for the city of Seattle incorporating subduction, crustal, and deep sources of earthquakes affecting Seattle.

3.3.1 Coseismic landslide hazard models

Coseismic landslide hazard was computed for two types of landslide failure, shallow translational slides (debris slides), and deep rotational slumps (rotational slides, or coherent rotational slides). Physics-based models for these failure modes (described below) were updated from the models presented in Chapter 1 (Eqs. 1.4, 1.5). The updated models (Eqs. 3.9, 3.19), allow for the introduction of a watertable (below which the material is assumed fully saturated) that fills some arbitrary fraction *m* of the landslide mass to more realistically model slope stability in a seasonally wet climate. For both landslide types, the stability of the slope is

expressed as a factor of safety (*FS*), where *FS* is equal to the ratio of all resisting stresses reinforcing the slope to all destabilizing driving stresses (Eq. 3.3).

$$FS = \frac{\sum resisting\ stresses}{\sum driving\ stresses} \qquad \text{Equation 3.3}$$

The described models were developed to facilitate stability analysis on a per-pixel (raster cell) basis. As in Chapter 1, the landscape is divided into zones of landslide susceptibility based on slope. Shallow translational slide stability, and later hazard, was computed for all regions in excess of 30° slope, rotational slide stability and hazard were assessed for slopes between 5 – 30°. Lateral spreads and flows omitted here as they are covered within the scope of the M9 project by Greenfield (2017). Rock slope failures are also omitted within Seattle and Mercer Island as no steep exposures of bedrock susceptible to rock slides and falls are found within the focused study area. Sliding-block displacements were adopted as a metric for landslide initiation, adopting a conservative threshold of 1cm predicted sliding-block displacement for landslide initiation for both considered modes of landslide failure. Sliding-block displacement calculations are discussed below in section 3.3.4.

3.3.1.1 Shallow translational slides

Shallow translational slides are most commonly modeled as an infinite 2D slope where some block of uniform thickness sits upon a rigid infinitely long uniform slope (e.g. Selby, 1993, Fig. 3.4).

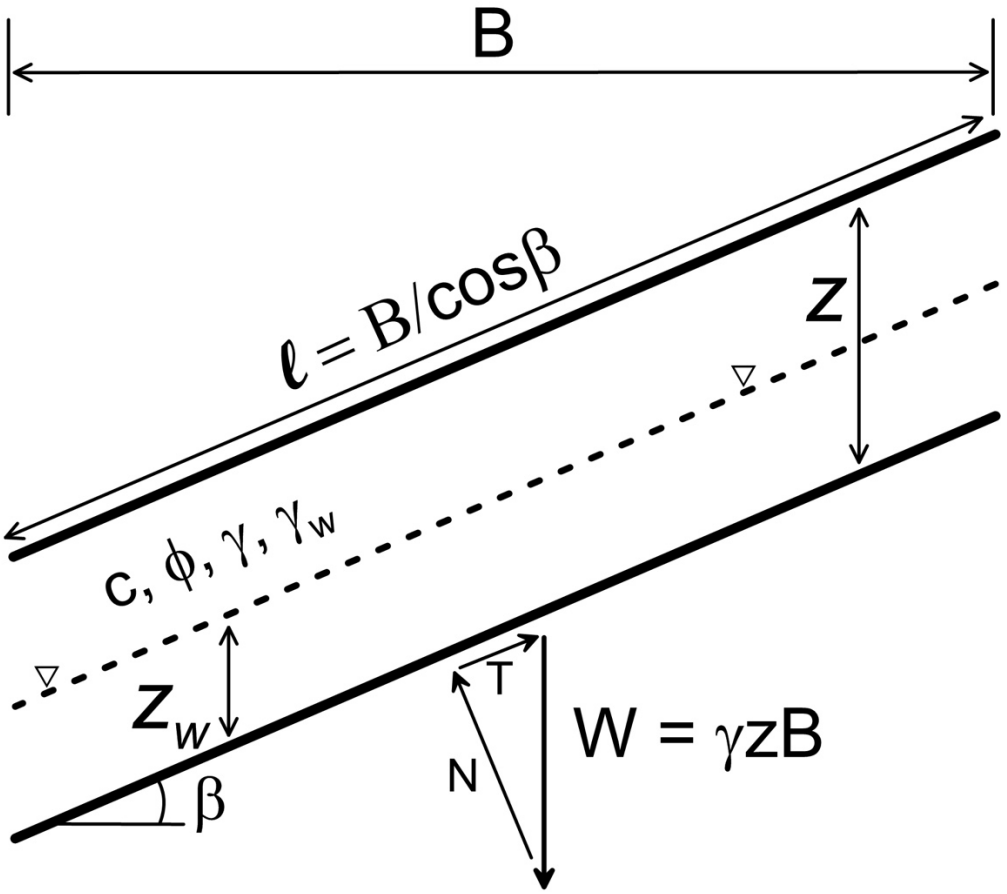

Figure 3.4 Infinite slope geometry adopted for shallow translational landslide stability analysis.

For some slope angle β, and arbitrary block with dimensions B and z with a unit weight γ, the resultant normal (N) and tangential (T) forces acting at the base of the block (assumed failure plane) are:

$$N = W cos\beta = \gamma z B cos\beta \qquad \text{Equation 3.4}$$

$$T = W sin\beta = \gamma z B sin\beta \qquad \text{Equation 3.5}$$

Assuming a Mohr-Coulomb failure criteria:

$$s = c + \sigma' tan\phi$$ Equation 3.6

where s is the resisting stress of the block, c is cohesional strength, ϕ is the internal friction angle, and σ' is the normal effective stress:

$$\sigma' = \sigma - u = \frac{N}{l} - \gamma_w z_w cos^2\beta = \gamma z cos^2\beta - \gamma_w z_w cos^2\beta$$ Equation 3.7

Where l is the failure plane length. The driving stress τ is given by:

$$\tau = \frac{T}{l} = \gamma z sin\beta cos\beta$$ Equation 3.8

Rearranging and combining equations 3.6, 3.7, and 3.8, the ratio of resisting to driving forces (factor of safety) can be expressed as:

$$FS = \frac{c+(\gamma z cos^2\beta - \gamma_w z_w cos^2\beta)tan\phi}{\gamma z sin\beta cos\beta} = \underline{\frac{c}{\gamma z sin\beta cos\beta} + \left(1 - m\frac{\gamma_w}{\gamma}\right)\frac{tan\phi}{tan\beta}}$$ Equation 3.9

where m is the ratio of z_w/z. As in Chapters 1and 2, a yield acceleration, k_y the acceleration above which downslope movement will occur, is computed for both modes of landslide failure as:

$$k_y = (FS - 1)sin\beta$$ Equation 3.10

3.3.1.2 Deep rotational slides

Deep rotational slide stability is computed assuming a circular failure plane acting through a uniform slope centered the raster cell (pixel) being analyzed of some slope angle β and height H (Fig. 3.5). The failure plane length, l is given by the properties of a circular segment:

$$l = 2\delta R \qquad \text{Equation 3.11}$$

where δ is the half angle of the circular segment

$$\delta = \sin^{-1}\frac{H}{2Rsin\beta} \qquad \text{Equation 3.12}$$

and R is the radius of the circle:

$$R = \frac{1}{4}H\left(\frac{cos\beta}{psin^2\beta} + \frac{p}{cos\beta}\right) \qquad \text{Equation 3.13}$$

where p is a depth factor empirically fixed as 0.85 to match resultant factors of safety from rigorous 2D methods (Will Pollock, *personal communication*). Assuming a unit thickness of the 2D slice (no constraining effects from neighboring hillslopes) the weight of the slice can be solved geometrically as:

$$W = \frac{1}{2}\gamma R^2(2\delta - sin2\delta) \qquad \text{Equation 3.14}$$

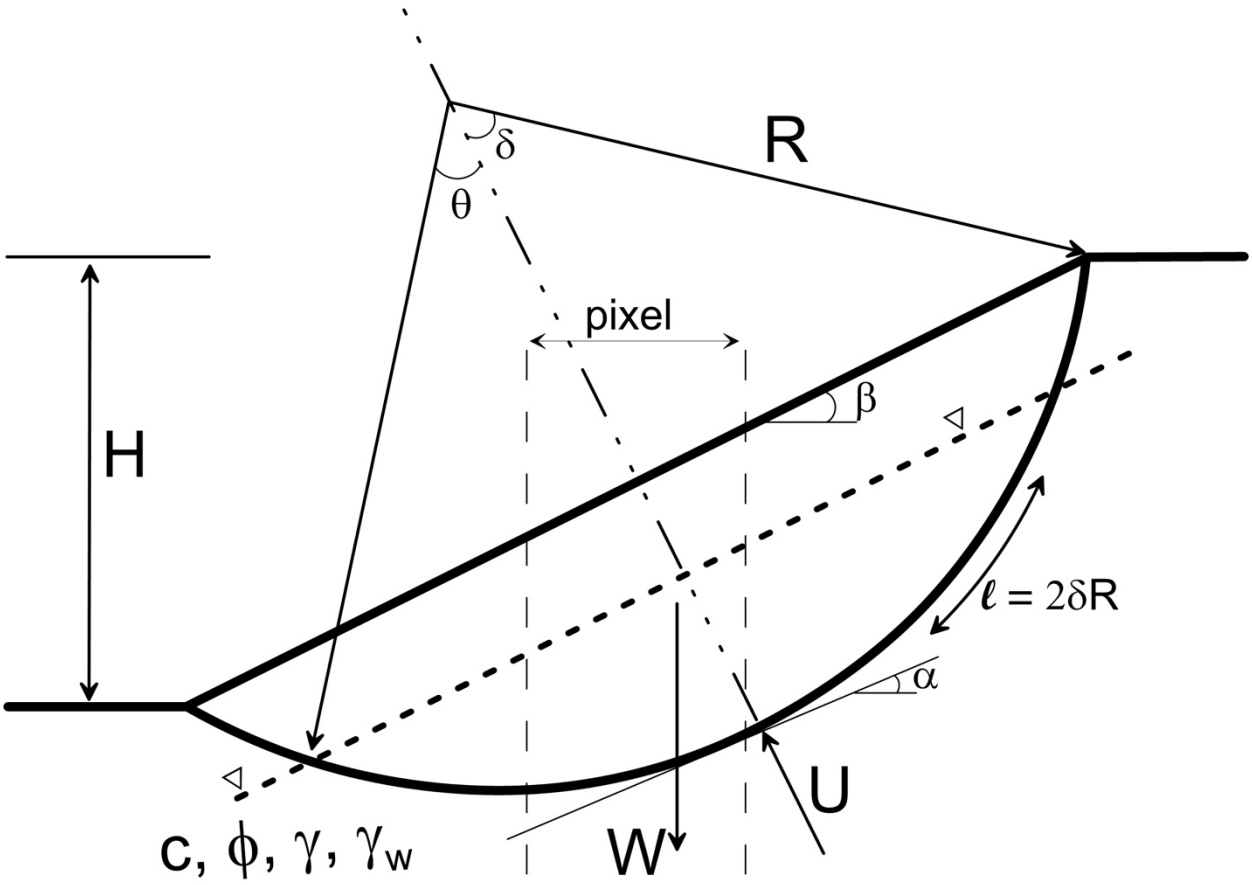

Figure 3.5 Assumed geometry for a deep rotational slide acting along a slope of angle β and height H.

The angle from horizontal at which the resultant normal force acts (intersection of W and the failure surface) α is found by:

$$\alpha = \sin^{-1}\left[\frac{4sin^3\delta sin\beta}{3(2\delta - sin2\delta)}\right] \qquad \text{Equation 3.15}$$

slope normal pore water pressure U, is assumed to act on the same point as the surface normal stress and the angle α. If some arbitrary water table is assumed to be slope-parallel that develops in-slope pore water pressure given by:

$$u = \frac{\gamma_w}{cos\beta}$$ Equation 3.16

the location of the water table can be defined from the circular section origin as the half-angle θ:

$$\theta = \cos^{-1}(1 - m + mcos\delta)$$ Equation 3.17

Where m is the fraction of the hillslope occupied by the water table. The total upward force of water, U, acting on the centroid of the failure mass, is then:

$$U = \frac{\gamma_w R^2}{2cos\beta}(2\theta - sin2\theta)$$ Equation 3.18

For a single pixel in the landscape (treated as a single-slice of an ordinary method of slices analysis), stability of the slope is given by:

$$FS = \frac{c+\sigma' tan\phi}{\tau} = \frac{c+\left(\frac{Wcos\alpha - U}{l}\right)tan\phi}{\frac{Wsin\alpha}{l}} = \frac{cl+(Wcos\alpha - U)tan\phi}{Wsin\alpha}$$ Equation 3.19

This stability model assumes the landslide mass fails as a rigid block along a circular failure plane, the mass of which is expressed as a single vertically acting force through its centroid (single slice assumption.) Dimensions of the landslide mass are governed by the slope angle β, height H, and geometric properties of a circular section. Pore pressures acting along the base of the slope due are assumed to act as a single force U through the centroid of the circle, which

results in slightly conservative (lower) estimates of static factors of safety relative to less-constrained models. For raster-based per-pixel analyses, the weight of the failure mass W and the pore water pressure U are assumed to act at the slope-normal angle α, and are taken as the average stresses across the entire failure plane length. Sensitivity testing of output provided in this model has shown predicted factors of safety similar to 3D slope stability software Scoops3D (Reid et al., 2015) in southwestern Seattle (Brien and Reid, 2008). Scoops3D utilizes Bishop's simplified method on 3D slope surfaces to estimate object-based static factors of safety across a landscape. Scoops3D is not utilized in this work due to the computational difficulties in implementing the code with probabilistic inputs as performed below.

3.3.2 Input parameters and data

Digital elevation data was adopted from the 10m resolution National Elevation Dataset and used to develop topographic slope maps. Material properties critical to landslide modeling (cohesional and frictional strength, unit weight) were adopted from the Harp et al. (2008) study of landslide hazard in Seattle. Shallow translational slide thickness was fixed at a slope-normal 2m. Unit weights of all mapped geologic materials was assumed to be 19kN/m^3 (Harp et al. 2008).

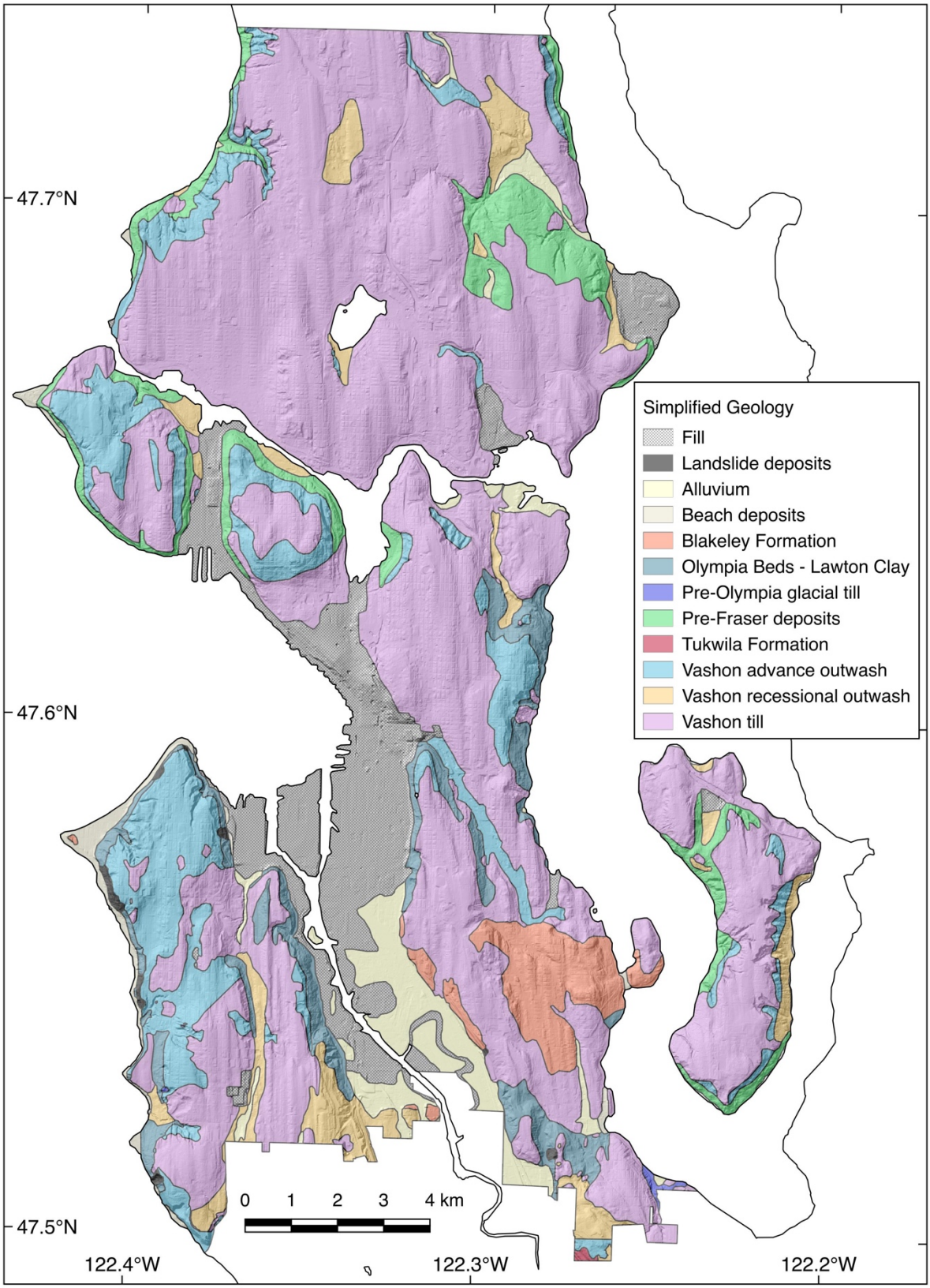

Figure 3.6 1: 100,000 geologic map of Seattle and Mercer Island, WA. Material properties adopted from Harp et al. (2008) for these materials shown in Table 3.1.

Name	Geo.	Age	c (kPa)	phi (deg)
Fill	Qf	Holocene	14	30
Beach deposits	Qb	Holocene	0	34
Alluvium	Qa	Quaternary	0	32
Landslide deposits	Qls	Quaternary	24	30
Vashon recessional outwash	Qvr	Pleistocene	5	32
Olympia Beds - Lawton Clay	Qc	Pleistocene	19	34
Vashon till	Qvt	Pleistocene	96	33
Vashon advance outwash	Qva	Pleistocene	12	34
Pre Olympia glacial till	Qpogt	Pleistocene	96	33
pre-Fraser deposits	Qpf	Pleistocene	19	38
Blakeley Formation	Tb	Oligocene-Eocene	29	40
Tukwila Formation	Tpt	Eocene	48	40

Table 3.1 Material properties adopted from Harp et al., (2008).

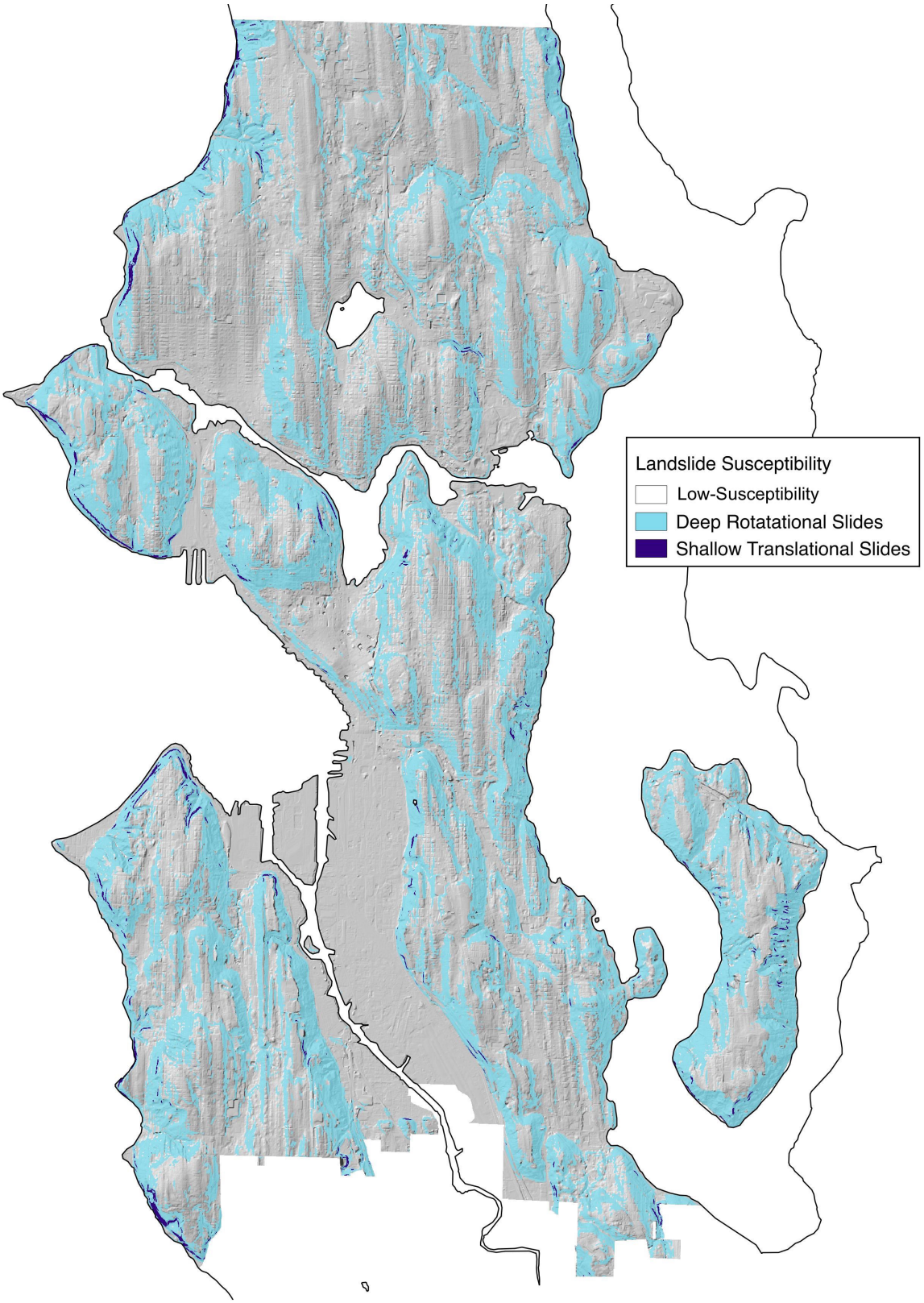

Figure 3.7 Landslide susceptibility zones based on limits of 5 – 30° for deep rotational slides, and >30° for shallow translational slides. As lateral spreads are not considered in this study, <5° is treated as an unconditionally stable, or unsusceptible to landslides, zone.

Pore water pressure data collected by the USGS (Smith et al., 2017) in a vegetated hillslope (Fig. 3.8) in Mukilteo, Washington, just north of Seattle, collected over an annual period of July 2016 – June 2017 were used to develop estimates for saturation conditions in the near surface. Pore water pressures in Fig 3.8 were converted into a fraction of the hillslope that is assumed to be fully saturated, *m*, shown in Fig 3.9.

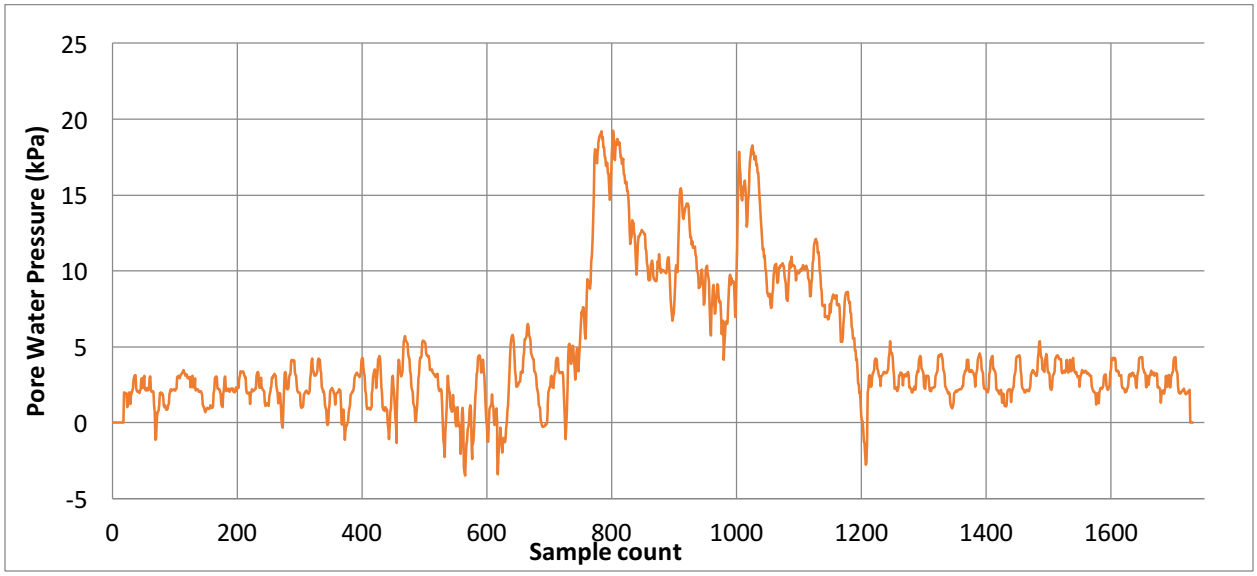

Figure 3.8 Pore water pressure (kPa) recorded at a depth of 300cm in a vegetated hillslope in Mukilteo, WA. Data spans a 12-month period from the beginning of July 2016 – the end of June 2017.

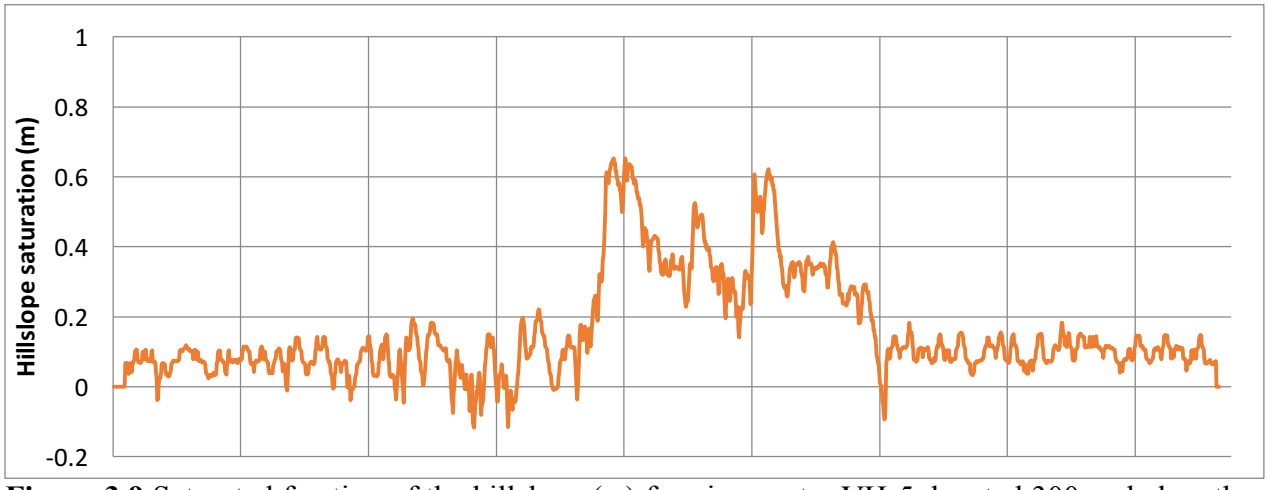

Figure 3.9 Saturated fraction of the hillslope (*m*) for piezometer VH-5, located 300cm below the surface.

Assuming the data of Smith et al. (2017) to be applicable to nearby Seattle and Mercer Island, which are composed of the same glacial deposits as the pore water pressure monitoring site, two saturation regimes were adopted for probabilistic analyses: dry, where m = 0.0 – 0.2, and wet, where m = 0.4 – 0.6. In both cases, a uniform random distribution between the listed upper and lower bounds was used to randomly sample ground saturation conditions.

To simulate the heterogeneities in material properties, random fractal terrain fields, scaled to the assumed coefficients of variation of 10% and 12% for cohesional and frictional strength, respectively, were generated for each realization of the model. Across the full suite of runs used to develop probabilistic landslide hazard, this has the effect of generating a random normal sample of material strength for every location but enforces a more realistic spatial autocorrelation of strengths within each simulation. Fractal random fields were developed using the diamond-square algorithm (Xu, 2012), with fixed roughness. Stochastically generated fractal terrain fields (ranging from -2.0 to 2.0, mean of zero) were then scaled to the coefficients of variability for each strength parameter and added to homogeneous inputs to develop heterogeneous strength estimates (Fig. 3.10, 3.11). Dimensionless roughness coefficients of 1.2 and 1.1 were adopted for cohesion and friction angle, respectively (see Figs. 3.10, 3.11). Variable cohesion and friction angle were computed independently and are not correlated to topographic or climatic factors. Given additional geospatial data on the variability of material strengths and soil thickness across the study region, variability in strength and geometry could be characterized by data rather than theoretical distributions from random fractal fields. While the random fractal field generation produces the same end result as per-pixel random-normal

distribution sampling, spatially coherent randomization (Figs. 3.10, 3.11) is preferred as it more realistically simulates heterogeneous natural materials.

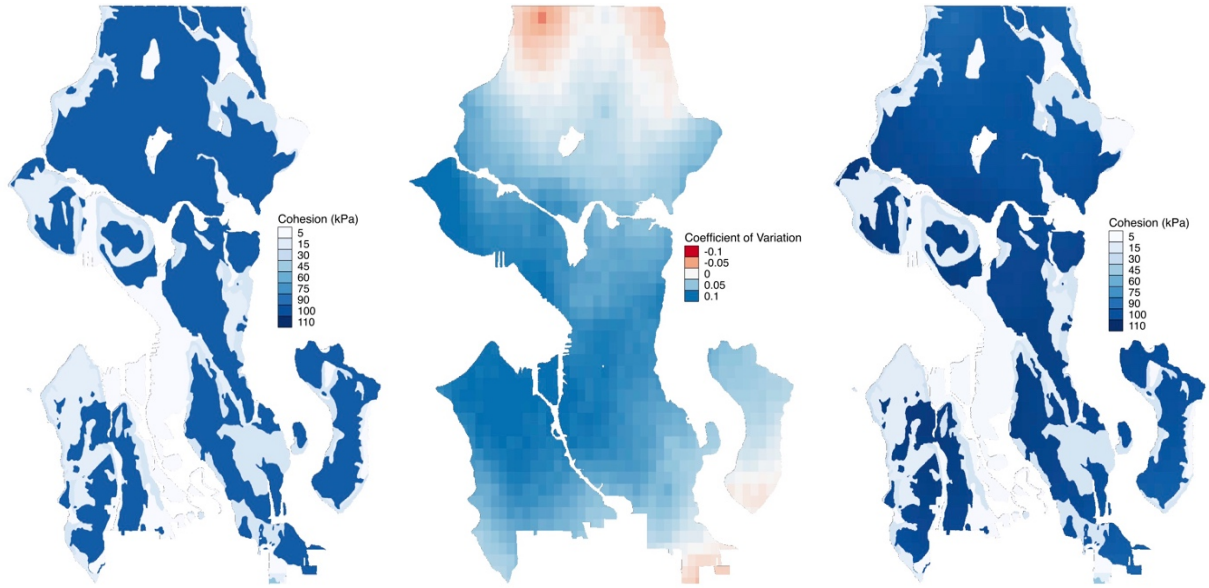

Figure 3.10 Left, homogeneous input to cohesional strength from Harp et al. (2008). Center, example distribution of increased (blue) and decreased strength (red) given by the random fractal field. Right, heterogeneous cohesional values used to compute the probability of landslide occurrence given the mean values (left) and coefficient of variation (center).

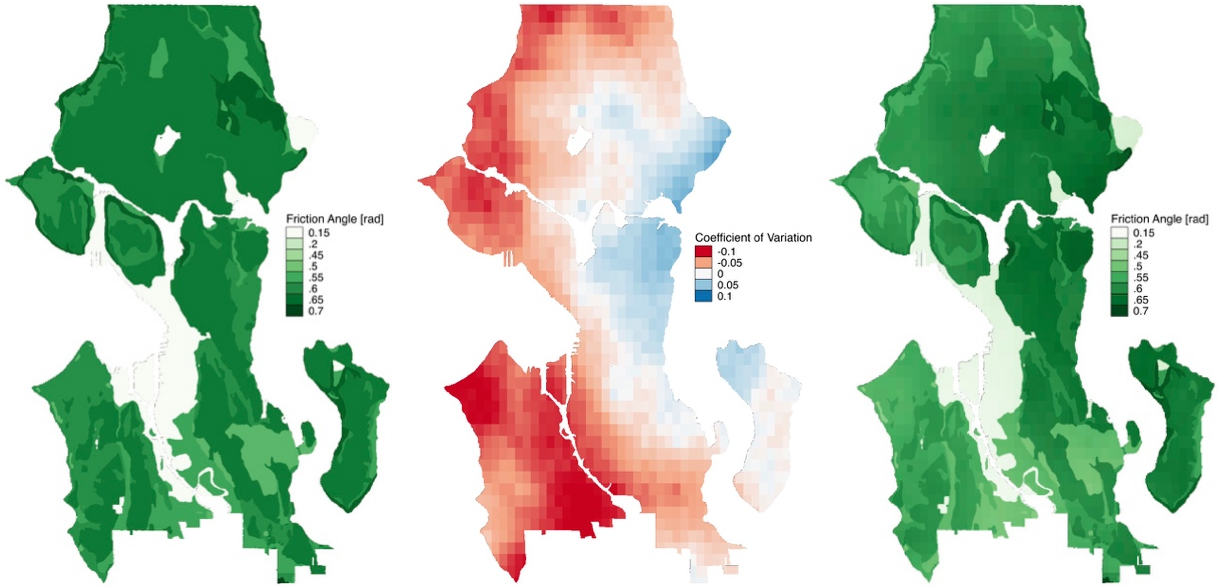

Figure 3.11 Left, homogeneous input to friction angle from Harp et al. (2008). Center, example distribution of increased (blue) and decreased strength (red) given by the random fractal field.

Right, heterogeneous friction angle values used to compute the probability of landslide occurrence given the mean values (left) and coefficient of variation (center).

3.3.3 CSZ synthetic earthquake ground motions

Synthetic ground motions modeling a suite of potential M9.0 CSZ earthquakes, used as triggering inputs for coseismic hazard in this work, were generated by the USGS and the University of Washington (Franket et al., *in review*). Broadband synthetics (0 – 10Hz) were developed via a kinematic hybrid model combining deterministic low frequency (<1Hz) and stochastic high frequency (>1Hz) ground motions utilizing a compound source model (Frankel et al., *in review*) that has been verified against recorded data from the Maule, Chile and Tokachi-Oki, Japan earthquakes (Frankel, 2017; Wirth et al., 2017). The suite of 30 CSZ synthetic earthquakes of Frankel et al. (*in review*), shown as median peak ground accelerations across the Pacific Northwest in Fig. 3.12, were adopted for all analyses.

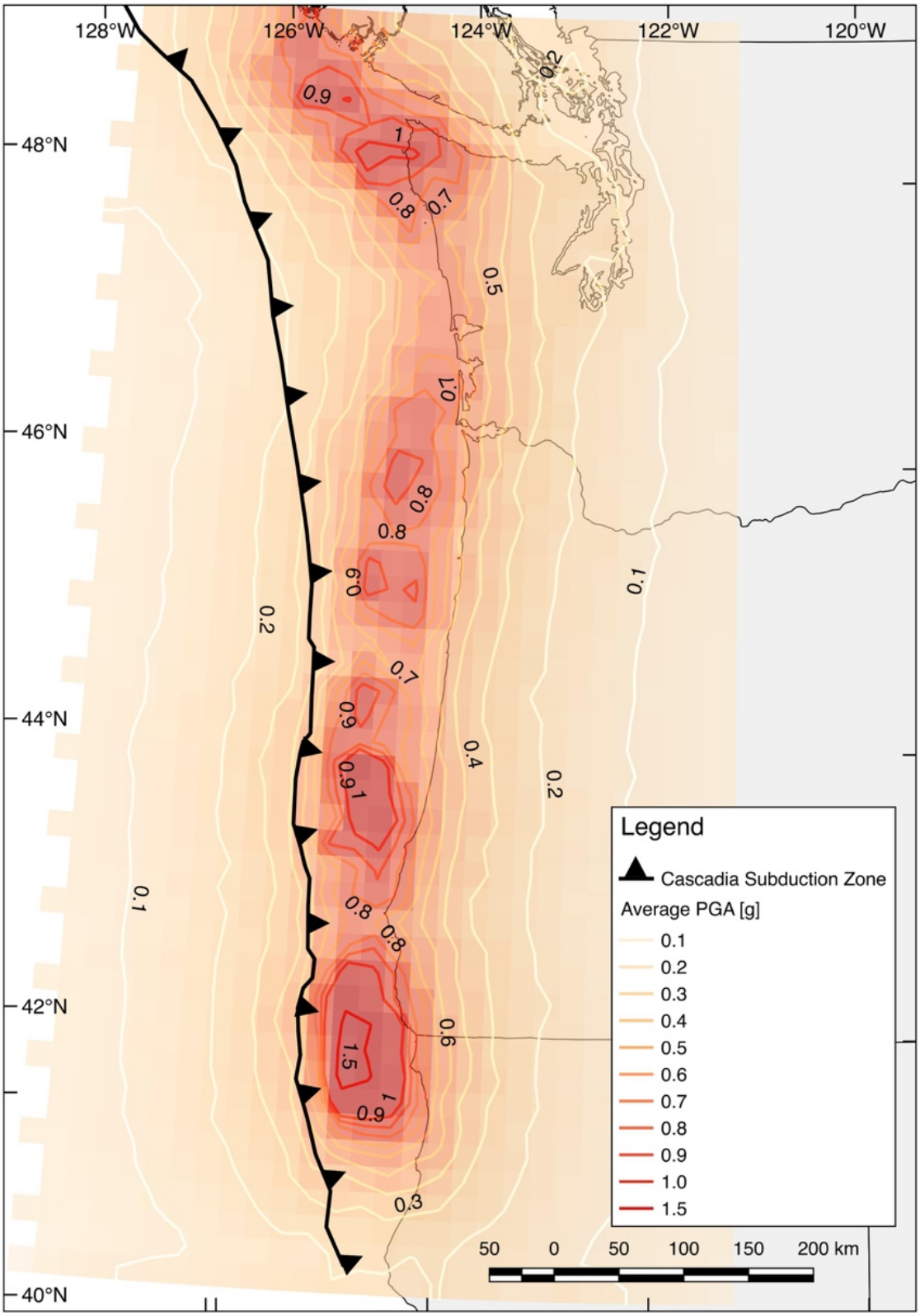

Figure 3.12 Median peak ground acceleration (PGA) values for the M9.0 CSZ synthetic earthquake suite. Individual realizations may deviate significantly from these reported values due to the location of asperities, directivity of motion, and the eastward extent of fault rupture.

3.3.4 Subduction time history database and Newmark sliding-block displacement.

Coseismic sliding displacement is the most common parameter used in the assessment of seismic slope stability and hazard forecasting or zonation (e.g. Wieczorek et al. 1985; Khazai and Sitar, 2000; Jibson et al., 2000; Saygili and Rathje, 2009). Newmark (1965) first published a rigid sliding-block procedure to estimate coseismic displacements of an idealized landslide mass. The Newmark sliding-block procedure assumes a rigid, perfectly-plastic landslide block, with some yield acceleration, k_y, sliding along a rigid base subject to some acceleration time history. Sliding begins when the input acceleration exceeds k_y and continues until the relative velocity of the sliding-block and rigid base are equal. The relative velocities between the sliding-block and base are then integrated over the entire time history to compute a coseismic displacement. In regional-scale studies it is impractical, and often inappropriate, to compute sliding-block displacements, as time histories are not available for every location in the landscape at the resolution of mapping. Coseismic hazard studies utilizing displacement as a hazard metric rely on estimates of sliding-block displacement (D_N) based on geospatially continuous inputs such as peak ground acceleration (PGA), peak ground velocity (PGV), or Arias Intensity (I_a) (e.g. Ambraseys and Menu, 1988; Jibson, 2007; Saygili and Rathje, 2008; Urzúa and Christian, 2013). The most commonly used estimators of D_N (Jibson, 2007; Saygili and Rathje, 2008) were developed using a catalog of time histories from crustal earthquakes of M5.1 – 7.9. These relationships may not be applicable to subduction zone regions where earthquakes in excess of M8.0 may produce ground motions of significantly longer duration, leading to increased coseismic deformation (Urzúa and Christian, 2013). Urzúa and Christian (2013) performed a similar analysis on 18 ground recordings from the Maule, Chile earthquake. While the Urzúa and Christian (2013) regression provides a large magnitude subduction zone earthquake displacement equation, the

volume of data now available beyond what was used at the time of that study motivates a reanalysis of these relationships considering many more large-magnitude earthquake records. Ambraseys and Menu (1988) fit 30 earthquake ground motion records where sliding-block displacement (D_N) is estimated as a function of the ratio between yield acceleration of the slope (k_y) to peak ground acceleration (PGA):

$$logD_N = 0.90 + \log\left[\left(1 - \frac{k_y}{PGA}\right)^{2.53}\left(\frac{k_y}{PGA}\right)^{-1.09}\right] \pm 0.30 \qquad \text{Equation 3.20}^2$$

Utilizing an expanded inventory of 2270 time histories from 30 crustal earthquakes of M5.3 – M7.6, Jibson (2007) updated this relationship to:

$$logD_N = 0.215 + \log\left[\left(1 - \frac{k_y}{PGA}\right)^{2.341}\left(\frac{k_y}{PGA}\right)^{-1.438}\right] \pm 0.51 \qquad \text{Equation 3.21}$$

Rigid sliding-block displacements are applicable to thin soil failures common in natural slopes (Saygili and Rathje, 2008). Additional sliding-block models allowing for strain-dependent changes to block-behavior (e.g. Seed and Martin, 1966; Matasovic et al. 1997) and coupled dynamic behavior of the sliding mass (e.g. Kramer and Smith, 1997; Rathje and Bray, 2000). As in Saygili and Rathje (2008), I compute rigid sliding-block displacements here as they are applicable to the vast majority of naturally occurring coseismic landslides. Additional analyses capturing the dynamic response of soils to long-duration subduction zone earthquake ground

[2] N.B. the ratio k_y/PGA has been expressed elsewhere as k_y/k_{max} and a_c/a_{max}. For the thin, rigid, slopes assumed here these expressions are equivalent and shown only as k_y/PGA for simplicity. In all cases logarithms are base 10.

motions must be performed to accurately assess the effects of liquefaction and lateral spreading across the PNW. These pore-water-pressure generation dependent failures are outside the scope of this work and are discussed in detail by Greenfield (2017).

To develop a model for D_N for use in the forecasting of coseismic landslide hazard across the PNW for a M9.0 CSZ earthquake, a catalog of large magnitude subduction zone acceleration time histories was collected. Newmark displacements were then computed for a suite of k_y values. A subduction-specific regression was then fit to these displacement data to predict D_N, and the probability of D_N exceeding some threshold given some intensity measure (IM). The resultant equations will allow spatially continuous data derived from the M9 synthetics (PGA, PGV, etc.) to be used for coseismic landslide displacement and hazard forecasting.

1,243 acceleration time histories were collected from four large-magnitude (>8.0) subduction zone earthquakes (Table 3.2). For this analysis, only records with peak horizontal ground accelerations in excess of 0.05g were collected. The dataset, compiled from data recorded in Japan, Chile, and Mexico, is heavily skewed towards Japanese recordings (96%), which may affect the results, though no inter-event bias was observed in these data. The maximum recorded ground acceleration in the dataset is 2.75g, with an average peak ground acceleration across all records of 0.23g (median of 0.15g). Seismograms from the Tohoku and Tokachi-oki earthquakes were collected from the National Research Institute for Earth Science and Disaster Prevention (NIED) in Japan. Data were obtained from http://www.kyoshin.bosai.go.jp/ (last accessed September 2017). Seismograms from the Maule, Chile earthquake were collected from the Department of Civil Engineering, University of Chile, from

http://terremotos.ing.uchile.cl/registros/164 (last accessed September 2017). Seismograms from the Michoacan earthquake were collected from the University of Nevada Reno Guerrero Accelerograph network available on the strong motion virtual data center http://www.strongmotioncenter.org/vdc/scripts/event.plx?evt=125 (last accessed September 2017.)

Earthquake	Magnitude	Date	Records
Tohoku, Japan	9.0	3/11/11	855
Maule, Chile	8.8	2/27/10	36
Tokachi-oki, Japan	8.3	9/25/03	335
Michoacan, Mexico	8.0	9/19/85	17

Table 3.2 Earthquake and number of records used in Newmark sliding-block analysis

Utilizing previously developed functional forms relating displacement to ratios of k_y/PGA (e.g., Ambraseys and Menu, 1988; Jibson, 2007; Saygili and Rathje, 2008) and modified functional forms developed for this study, time history solutions for displacement were fit to in Python via nonlinear least-squares curve fitting with soft-l1 loss to account for outliers (Mayorov, 2015).

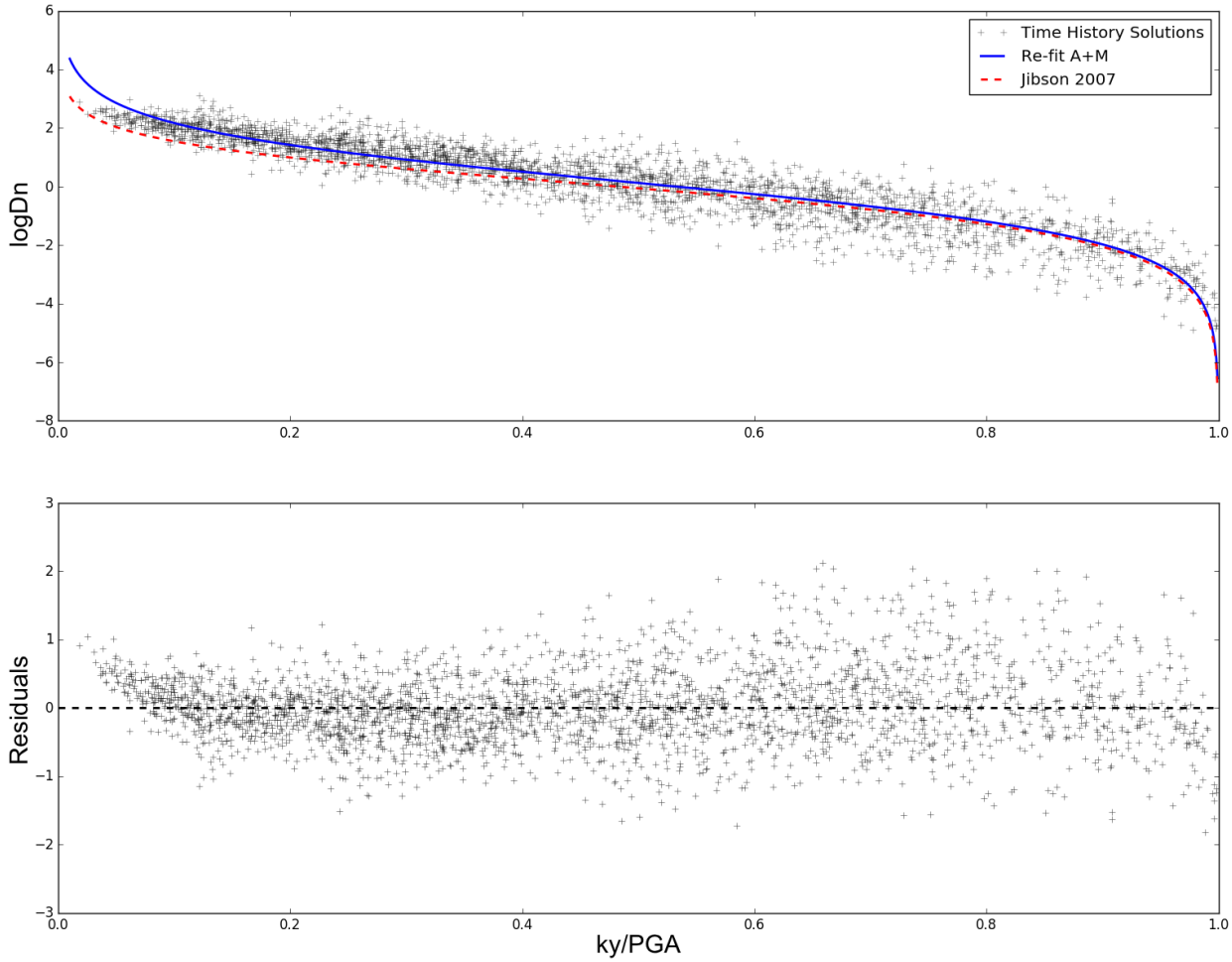

Figure 3.13 Top, Comparison of Jibson (2007) regression line (dashed red) and a refit Ambraseys and Menu functional form (blue line) to time history Newmark sliding-block displacements from subduction zone large-magnitude earthquakes (black ticks). Bottom, residuals shown for the Ambraseys and Menu function form refit to subduction data.

As shown in Fig. 3.13, adopting the Ambraseys and Menu (1988) functional form (Equation 3.22), as done in Jibson (2007), yields positively biased residuals at the lower tail of these data. That is, displacements predicted by the model are higher than the time-history displacement data. Similar errors are seen for polynomial fits following (Saygili and Rathje, 2008) at the upper tail of the data.

$$logD_N = 0.15 + \log\left[\left(1 - \frac{k_y}{PGA}\right)^{2.229}\left(\frac{k_y}{PGA}\right)^{-2.08}\right] \pm 0.57 \qquad \text{Equation 3.22}$$

The preferred model, modified from Ambraseys and Menu (1988) to flatten the lower portion of the curve, $k_y/PGA < 0.2$, (Equation 3.23) was adopted and shown in Fig. 3.14.

$$logD_N = 1.834 - 2.996\frac{k_y}{PGA} + \log\left[\left(1-\frac{k_y}{PGA}\right)^{1.250}\left(\frac{k_y}{PGA}\right)^{-.592}\right] \pm 0.52 \qquad \text{Equation 3.23}$$

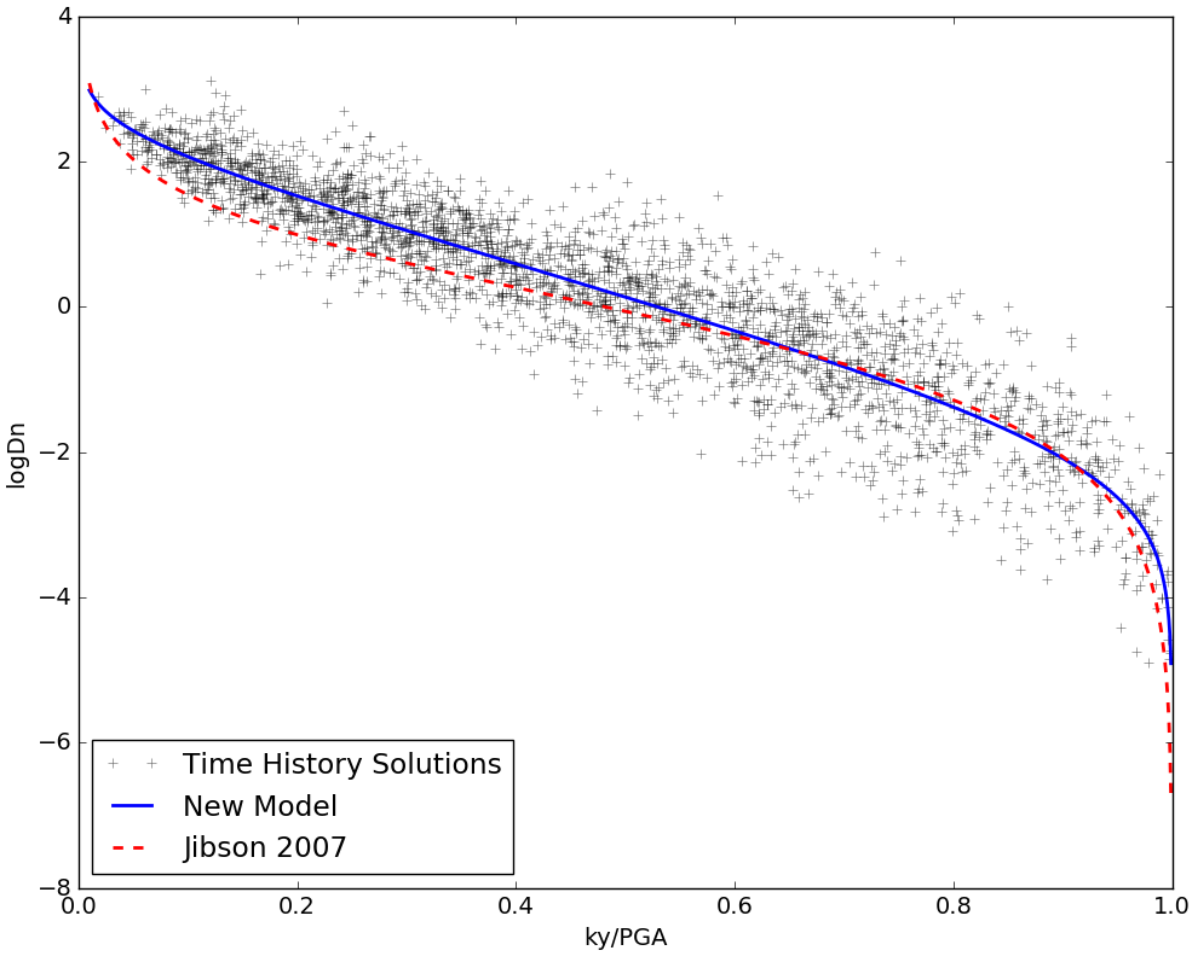

Figure 3.14 Preferred fit to large-magnitude subduction zone sliding-block displacements (solid blue line) compared to a moderate-magnitude crustal earthquake fit (dashed red line). Time history solutions shown as black ticks.

As in previous studies (e.g. Saygili and Rathje, 2008) residuals from the preferred 'new' model are heteroskedastic (Fig. 3.15), that is the variance in Y (displacement) increases with X

(k_y/PGA). The absolute value of residuals was such that a non-stationary standard deviation as a function of k_y/PGA could be developed (Equation 3.24).

$$\sigma = 0.1786 \ln\left(\frac{k_y}{PGA}\right) + 0.6648 \qquad \text{Equation 3.24}$$

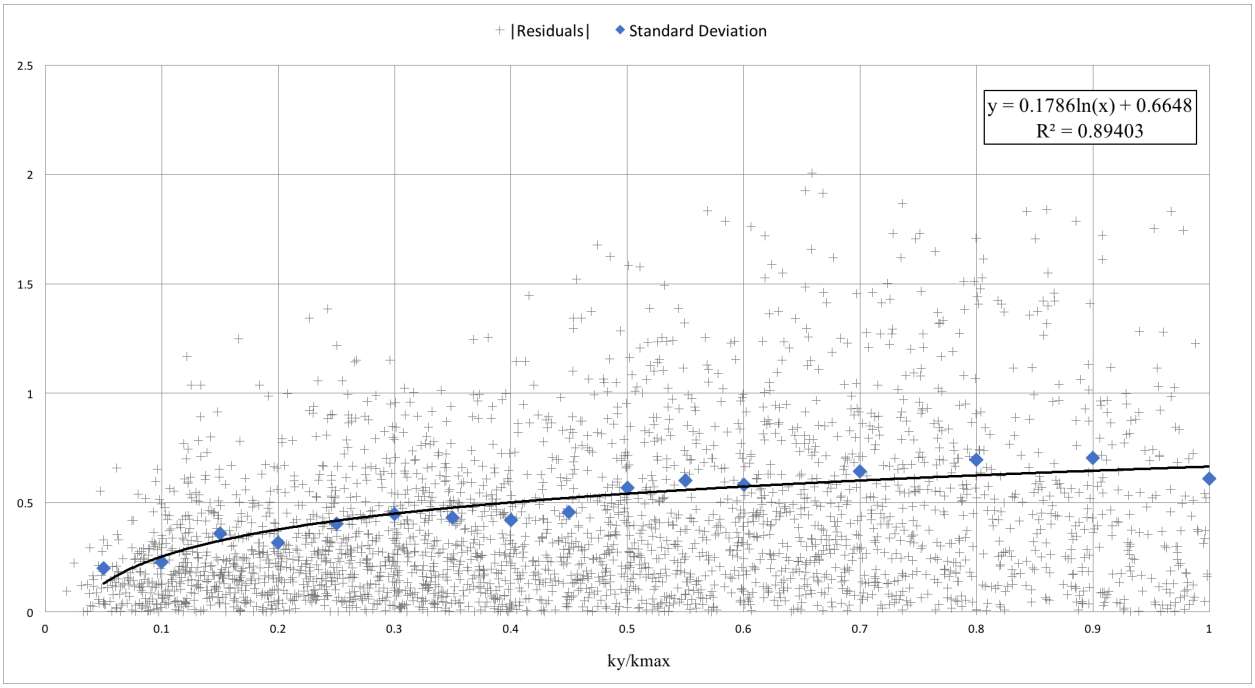

Figure 3.15 Absolute values of residuals of the subduction-specific model (Eq. 3.23). The solid line (Eq. 3.24) shows the heteroskedastic error, fit to binned residuals shown as blue diamonds.

The observed increase in variance with k_y/PGA is likely due to the increased dominance of single acceleration pulses of unknown frequency where k_y/PGA approaches 1.0. However, the increased variance with k_y/PGA is easily accounted for in the utilization of this regression.

Given a normal distribution of data with a mean μ and standard deviation σ (log displacement data in this study are approximately normally distributed), the cumulative distribution function (F(x)) is described as:

$$F(x) = \frac{1}{2}\left[1 + erf\left(\frac{x-\mu}{\sigma\sqrt{2}}\right)\right] \quad \text{Equation 3.25}$$

where *erf* is the error function (Weisstein, 2017). The cumulative distribution function here gives us the probability of an estimated log-transformed displacement (D_N) and is less than or equal to the expected value given some k_y/PGA. As we are interested in the exceedance of some displacement threshold as a proxy for landslide initiation and or hazard (e.g. Jibson and Michael, 2009; Saygili and Rathje, 2009), we can compute the survival function, *SF*, as $SF = 1 - F(x)$, yielding the probability of exceeding some threshold displacement given k_y/PGA. Solving for commonly adopted displacement thresholds of 1, 5, and 15cm (Fig. 3.16) the following conditional probabilities reflect best-fit estimates of large-magnitude subduction zone ground motions:

$$P\left(D_N > log(1)\middle|\frac{k_y}{PGA}\right) = 1 - \frac{1}{2}\left[1 + erf\left(\frac{\frac{k_y}{PGA} - 0.530}{0.091 + .048\frac{k_y}{PGA}\sqrt{2}}\right)\right] \quad \text{Equation 3.26}$$

$$P\left(D_N > log(5)\middle|\frac{k_y}{PGA}\right) = 1 - \frac{1}{2}\left[1 + erf\left(\frac{\frac{k_y}{PGA} - 0.377}{0.067 + .101\frac{k_y}{PGA}\sqrt{2}}\right)\right] \quad \text{Equation 3.27}$$

$$P\left(D_N > log(15)\middle|\frac{k_y}{PGA}\right) = 1 - \frac{1}{2}\left[1 + erf\left(\frac{\frac{k_y}{PGA} - 0.274}{0.049 + .146\frac{k_y}{PGA}\sqrt{2}}\right)\right] \quad \text{Equation 3.28}$$

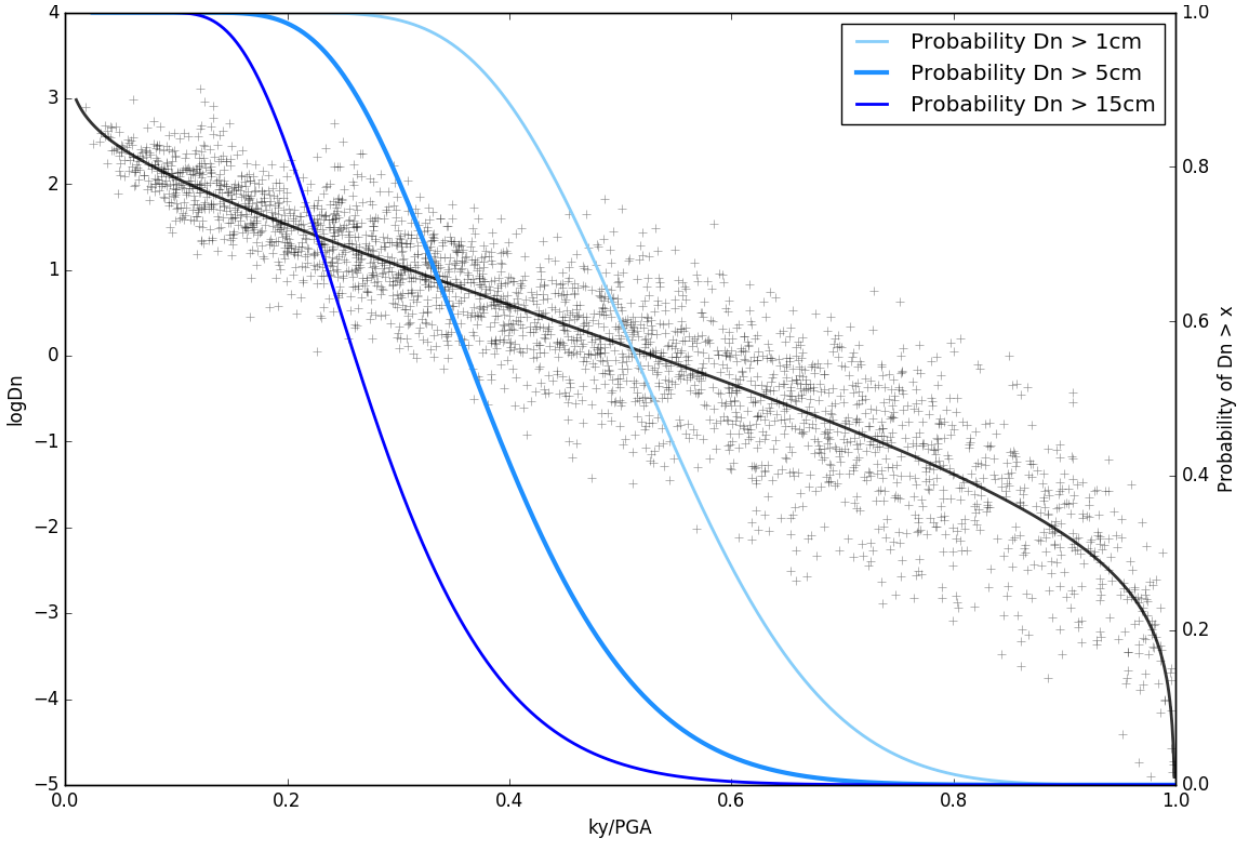

Figure 3.16 Probability of exceedance curves for 1, 5, and 15cm of sliding-block displacement given some k_y/PGA ratio less than 1.0 (unstable). Equations used to generate these curves shown in Eqs. 3.26-.28

3.3.5 Verification of displacement model for synthetics

To test if the displacement prediction equations given in Eqs. 3.26-28 are suitable for use with the CSZ synthetics, a sample of synthetic time histories was generated from 13 locations across Oregon and Washington (Table 3.3). To remove records affected by numerical instabilities each record was processed twice, once with no filtering, and a second time only considering the first 350 seconds of the record. Synthetics where the peak ground acceleration for each case were identical were kept, with unstable or incomplete (PGA1 ≠ PGA2) records removed. Locations were selected to represent population centers distributed across the affected region along the coast and the Puget and Willamette lowlands.

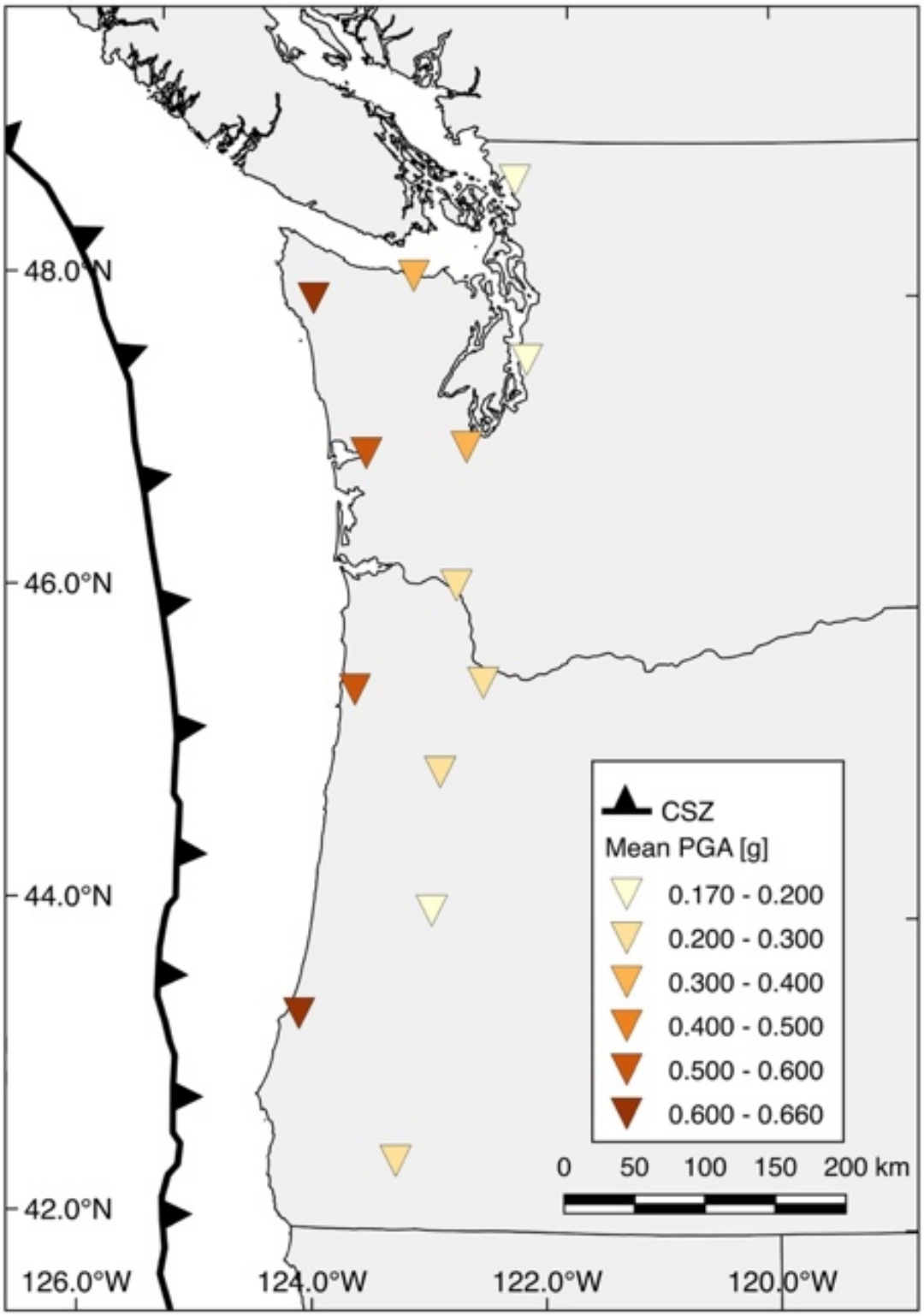

Figure 3.17 Locations and mean horizontal peak ground acceleration ($\overline{PGA}$) sampled from 30 synthetic time histories generated from potential M9.0 earthquakes by the USGS and UW. Locations and ground accelerations shown in this figure are presented in Table 3.3

Location	Latitude	Longitude	PGA Range	$\overline{PGA}$
Forks, WA	47.95	-124.38	0.26 – 1.26	0.66
Coos Bay, OR	43.36	-124.22	0.25 – 1.34	0.65
Aberdeen, WA	46.97	-123.82	0.20 – 1.10	0.57
Tillamook, OR	45.45	-123.84	0.26 – 1.06	0.53
Olympia, WA	47.03	-122.88	0.12 – 0.71	0.32
Port Angeles, WA	48.12	-123.43	0.12 – 0.63	0.31
Longview, WA	46.14	-122.94	0.12 – 0.44	0.26
Grants Pass, OR	42.94	-123.33	0.14 – 0.43	0.24
Salem, OR	44.94	-123.04	0.10 – 0.65	0.22
Portland, OR	45.52	-122.67	0.12 – 0.47	0.21
Seattle, WA	47.60	-122.33	0.10 - 0.34	0.20
Eugene, OR	44.05	-123.08	0.11 – 0.32	0.19
Bellingham, WA	48.75	-122.48	0.07 – 0.36	0.17

Table 3.3 Locations used to generate a representative sample of broadband synthetics. Range of horizontal peak ground accelerations [g] from the suite of M9.0 CSZ synthetic earthquakes

Time history sliding-block displacements were computed for all valid synthetic time histories (k_y < PGA) and plotted against recorded subduction zone time histories and the described best fit (Fig. 3.18). The median time history displacements for synthetic ground motions (Fig. 3.19.) is nearly identical to the preferred model for recorded ground motions. Fig. 3.20 shows these same synthetic displacement data disaggregated by sampled location. In Fig. 3.21 the deviation between Seattle and Olympia (both in the Puget Lowland) and the rest of the data are highlighted. Amplification of ground motions, and the generation of significant surface waves in the Puget lowland and Seattle basin likely drive this increase in computed displacement.

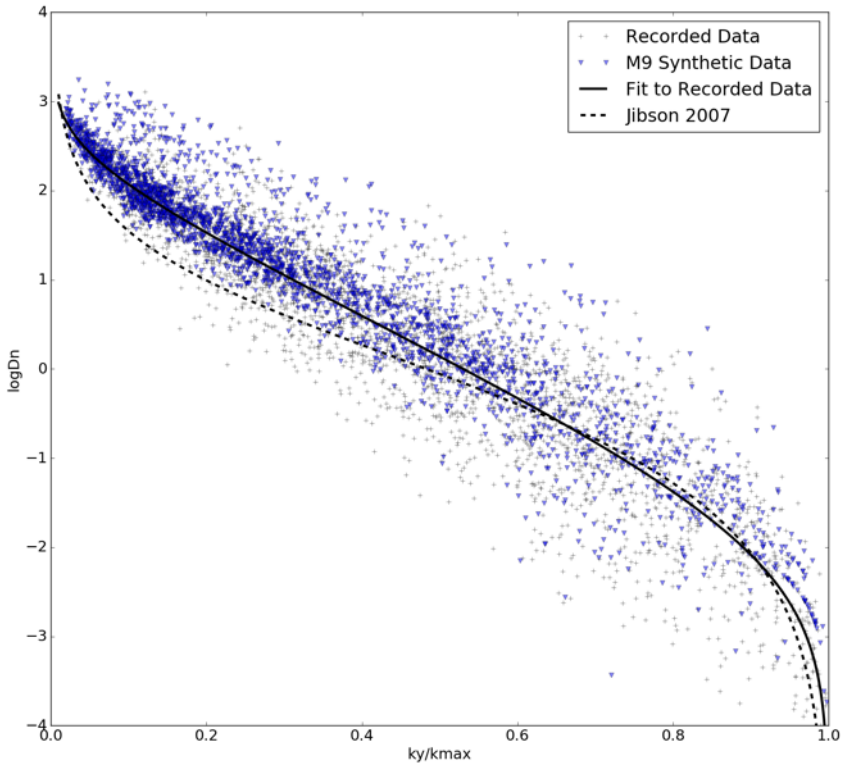

Figure 3.18 Synthetic time history solutions for Newmark sliding displacement (blue triangles)

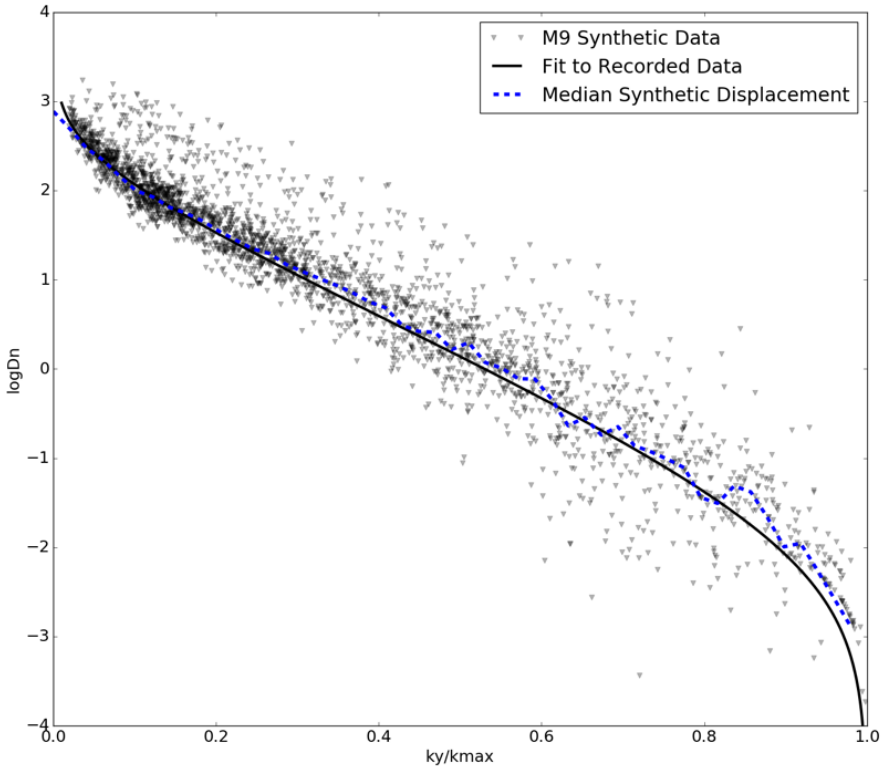

Figure 3.19 Median of the synthetic data (black triangles, blue dashed line) versus the recorded data regression.

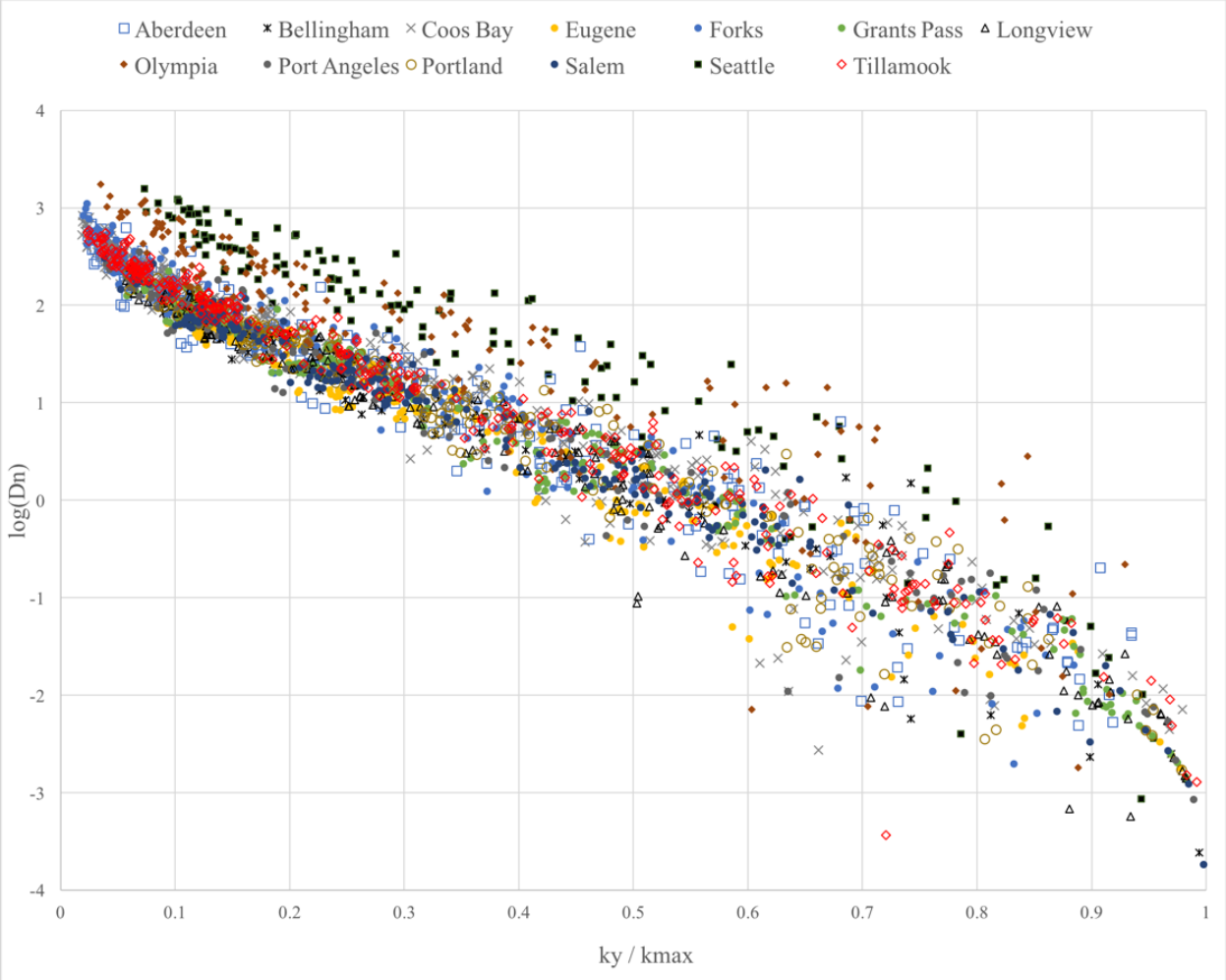

Figure 3.20 Disaggregation of synthetic displacement data by location, bias above the global trend is observed for Seattle and Olympia, WA.

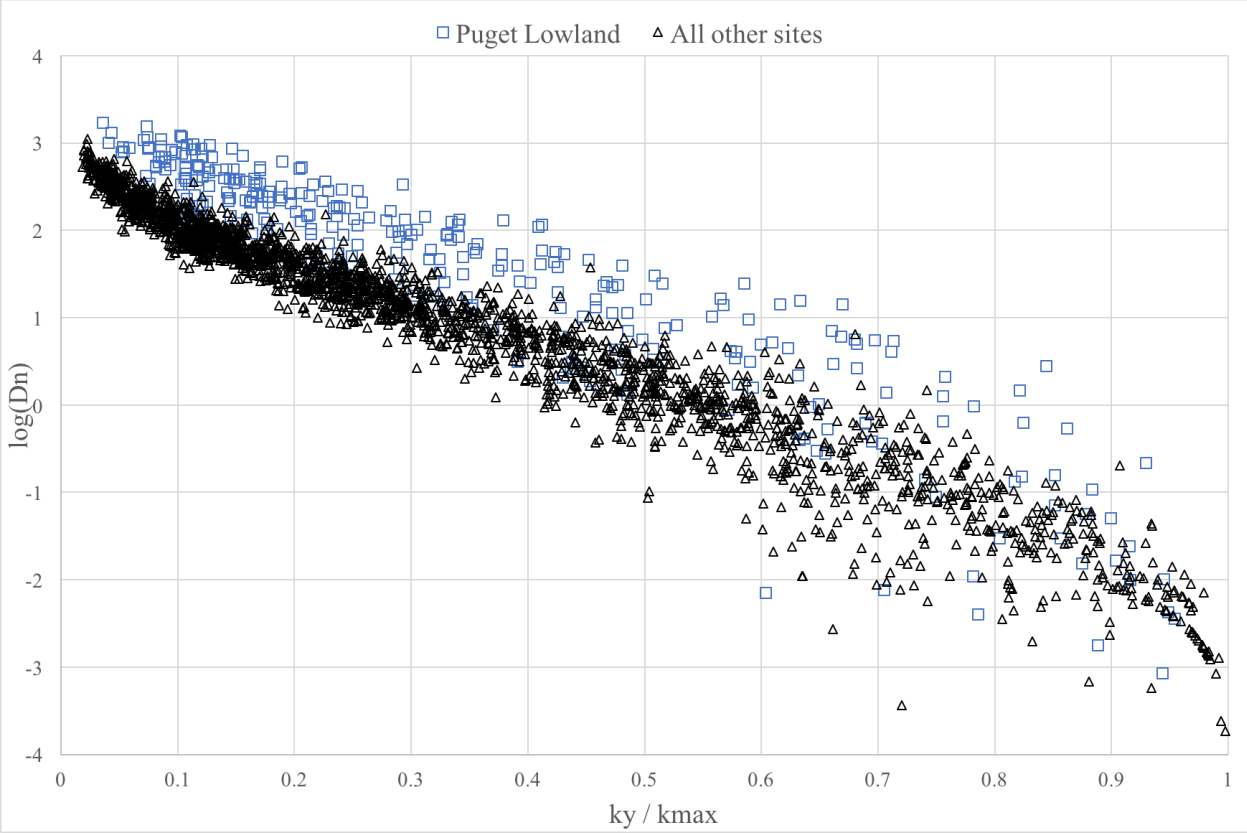

Figure 3.21 Comparison between the Puget Lowland (Seattle and Olympia, blue squares) and the remaining 11 Washington and Oregon locations (black triangles) computed displacements.

In aggregate, the synthetic time history solutions match closely with expected values from recorded ground motions from similar magnitude earthquakes. Thus the newly derived equations for sliding-block displacement, and probabilities of exceeding some threshold displacement, are appropriate for use with the synthetic earthquake data.

3.3.6 Crustal earthquake probability of displacement

To make direct comparisons between crustal and subduction ground motions within this framework, the procedure outlined above for predicting the probability of exceeding some displacement threshold was repeated using the displacement regression of Jibson (2007). (Fig. 3.22) The resultant prediction equation is given by:

$$P\left(D_N > log(1)\middle|\frac{k_y}{PGA}\right) = 1 - \frac{1}{2}\left[1 + erf\left(\frac{\frac{k_y}{PGA} - 0.482}{0.161 - .019\frac{k_y}{PGA}\sqrt{2}}\right)\right] \quad \text{Equation 3.29}$$

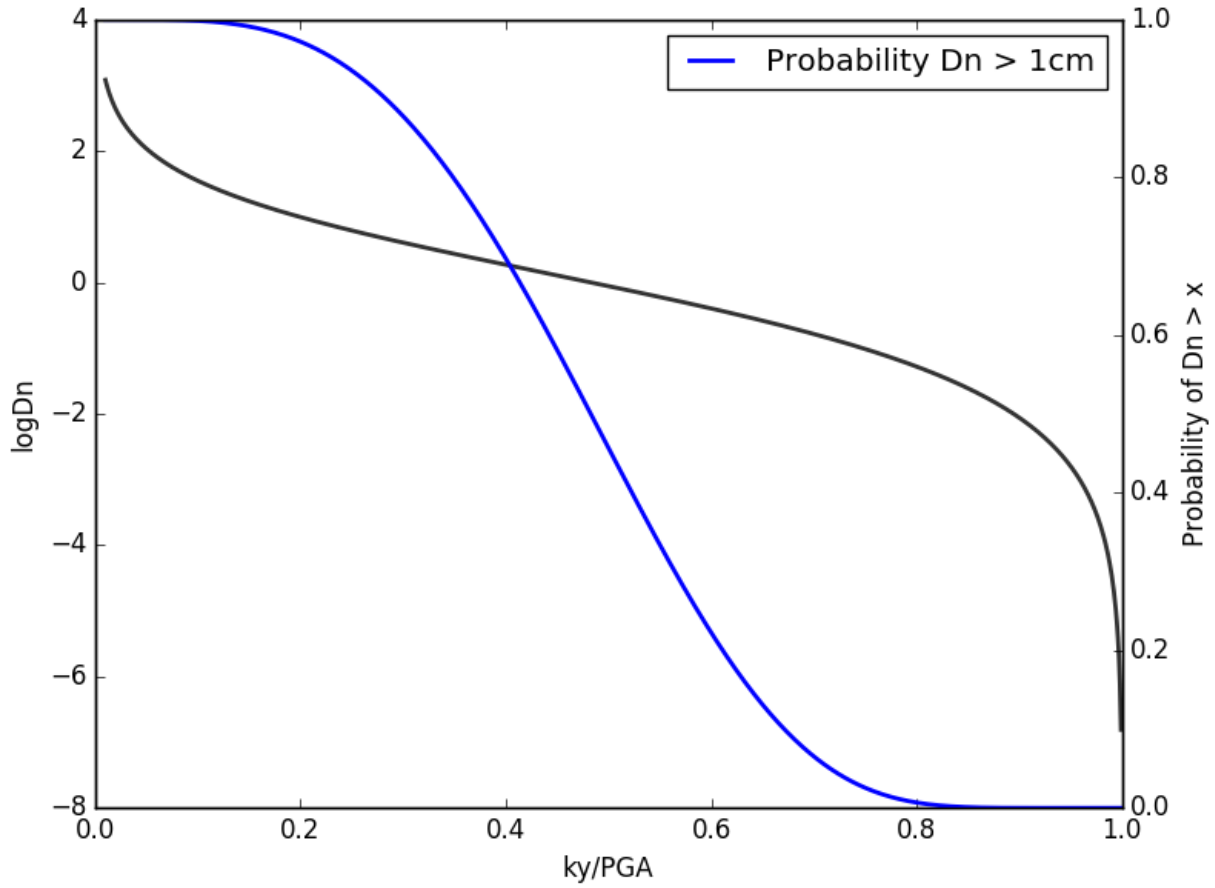

Figure 3.22 Probability of exceedance for a displacement threshold of 1cm (blue line) based on the crustal-earthquake specific regression of Jibson (2007, black line). Used in this work to compute coseismic displacement caused by the Nisqually earthquake and a future earthquake on the Seattle Fault.

To verify the coseismic hazard modeling framework presented here, estimates of coseismic landslide occurrence probabilities (Eq. 3.29), based on wet winter-like ground saturation conditions and homogeneous material strength inputs were made for recorded ground acceleration intensities caused by the Feb 28, 2001 M6.8 Nisqually, WA earthquake. Mapped

landslides in the Seattle landslide inventory (Seattle Public Utilities, 2017) triggered by the Nisqually earthquake were then used to test if predicted landslide hazard matched observed landslides.

3.2.7 Probabilistic Coseismic Landslide Hazard Analysis (PCLHA)

Large magnitude earthquakes along the Cascadia Subduction Zone are an important source of seismic hazard in Seattle, but other local seismic sources such as the Seattle Fault, Whidbey Island Fault, or Benioff Zone earthquakes on the subducted slab are capable of generating more intense ground shaking within Seattle. For example, over a 475-year return period (10% probability of exceedance in 50-years), the CSZ contributes 19% of the total seismic hazard with respect to peak ground acceleration for Seattle. Two scenario earthquakes, the M6.8 2001 Nisqually earthquake that triggered several landslides in Seattle and a synthetic M7.0 Seattle Fault earthquake (Allstadt et al., 2013) were used to compute bimodal coseismic landslide hazard to assess differences between projected CSZ-triggered landslides and other more local sources. Coseismic landslide probabilities of occurrence for the Nisqually and Seattle Fault earthquakes were based on the crustal-earthquake specific Eq. 3.29.

To analyze the total coseismic landslide hazard over a 475-year return period for the city of Seattle, disaggregated probabilistic seismic hazard analysis (Fig. 3.23) weights for three major sources of seismicity, interface earthquakes, crustal faults, and Benioff zone were applied to landslide hazard forecasts from the Cascadia Subduction Zone, Seattle Fault, and Nisqually earthquake. Combining the weighted coseismic landslide output by contribution to overall seismic hazard, a simplified 3-source Probabilistic Coseismic Landslide Hazard Analysis was

performed for Seattle, Washington at a return period of 475-years. To maintain consistency across all model runs, randomization of input parameters (section 3.3.2) was removed during these analyses, adopting homogeneous material properties from Harp et al. (2008). Based on the hydrologic data of Smith et al. (2017), dry (m = 0 – 20%) and wet (m = 40 – 60%) saturation conditions were assigned long-term weights of 0.7 and 0.3, respectively (section 3.3.2). As in the previous analyses, coseismic landslide hazard was expressed as the probability of exceeding 1cm of predicted sliding block displacement via the seismically-appropriate prediction equation (Eq. 3.29: Seattle Fault and Nisqually, Eq. 3.26: Cascadia Subduction Zone). Seattle fault ground motions were adopted from Allstadt et al. (2013) for non-amplified ground motions to be consistent with the CSZ synthetics (Figure 3.24). Allstadt et al. (2013) synthetic ground motions derived from a M7.0 source model using the same 3D finite difference codes as the CSZ synthetics. Nisqually shaking intensities were adopted from the USGS.

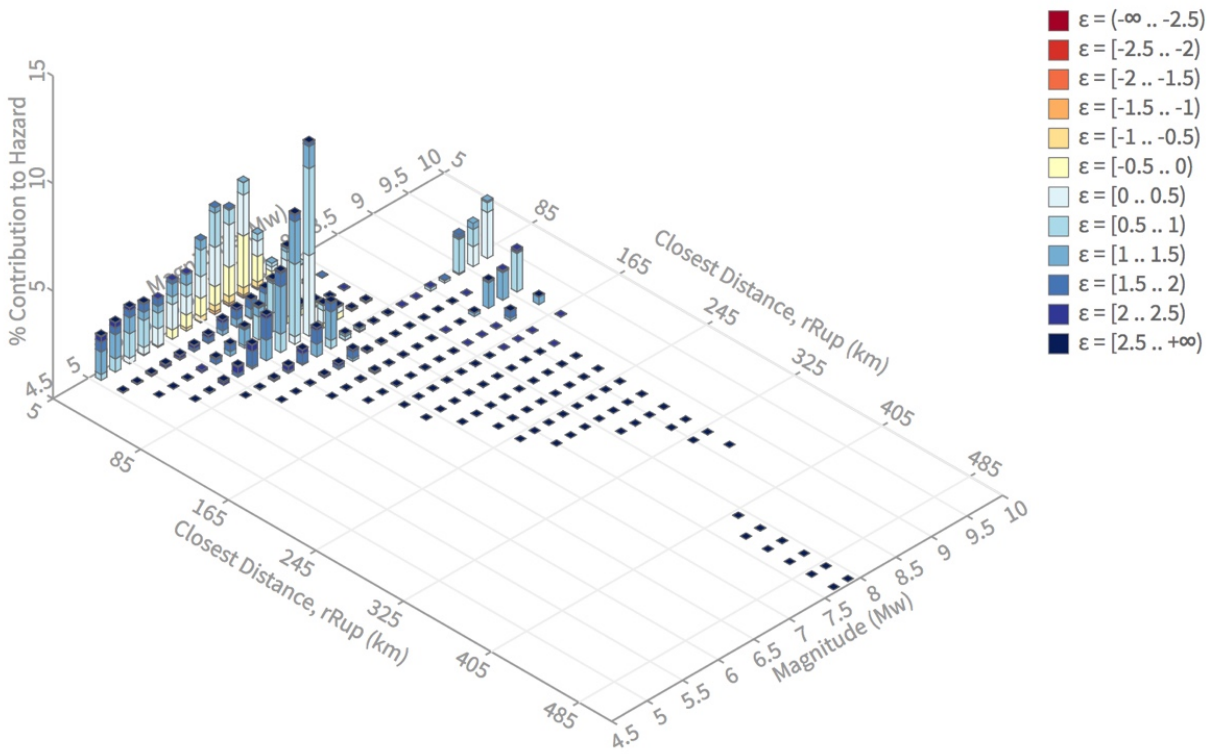

Figure 3.23 Disaggregated probabilistic seismic hazard analysis for Seattle (47.652, -122.305) for a return period of 475-years (10% probability of exceedance in 50-years). Bar height reflects the relative contribution to hazard of each seismic source. Zones of elevated hazard reflect known faults (Seattle Fault, CSZ) and hazard from some future Benioff Zone deep earthquake (e.g. Nisqually, 2001). Bar color, reflecting event epsilon, can be ignored for the purposes of this analysis. Figure by the USGS, accessed at https://earthquake.usgs.gov/hazards/interactive/. Weights were adopted for a PCLHA of Seattle adopting a simplified 3-source model: Cascadia Subduction Zone (Interface, 19%), Seattle Fault (Fault and Grid, 47%) and Nisqually (Slab, 34%).

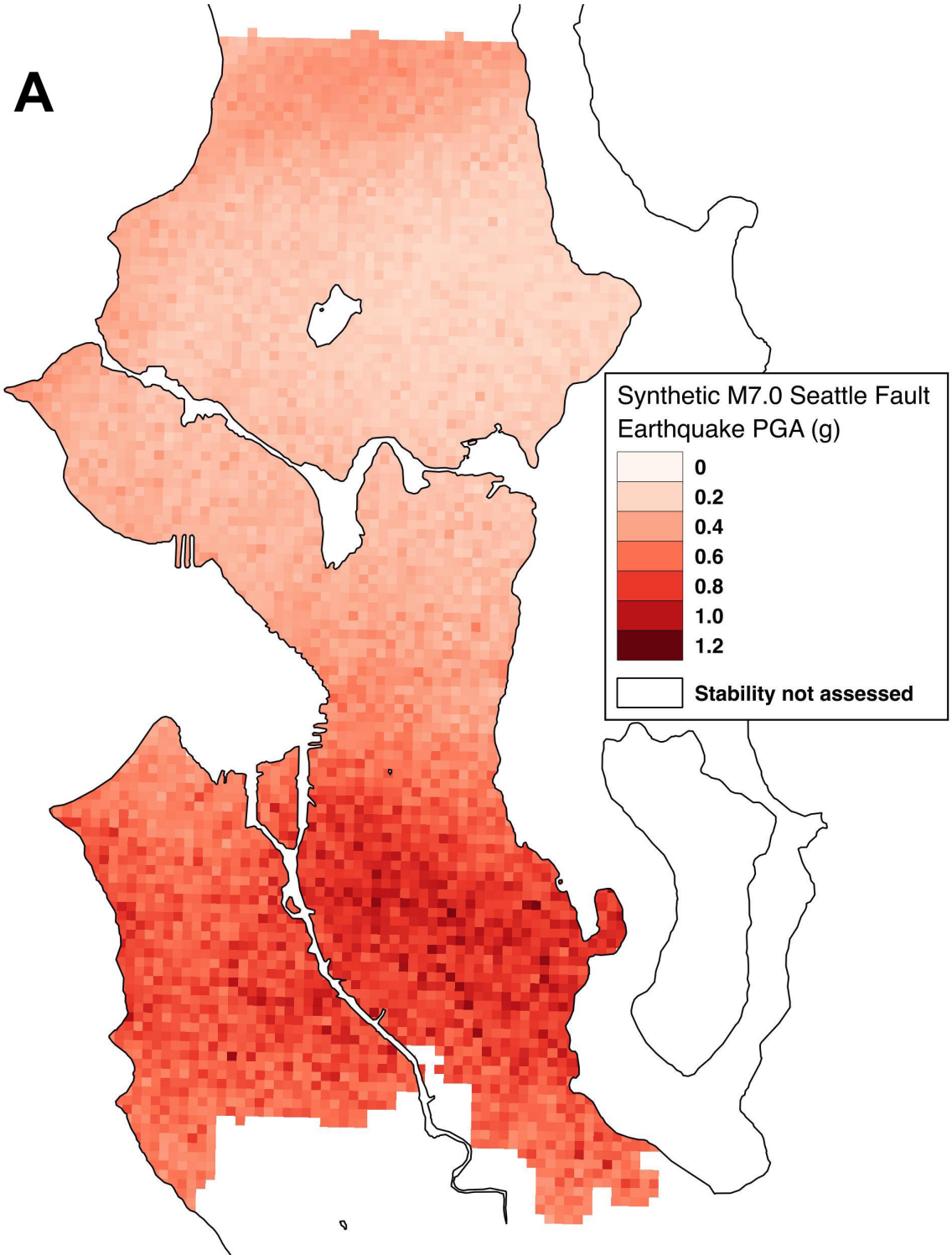
A
Synthetic M7.0 Seattle Fault
Earthquake PGA (g)
0
0.2
0.4
0.6
0.8
1.0
1.2
Stability not assessed

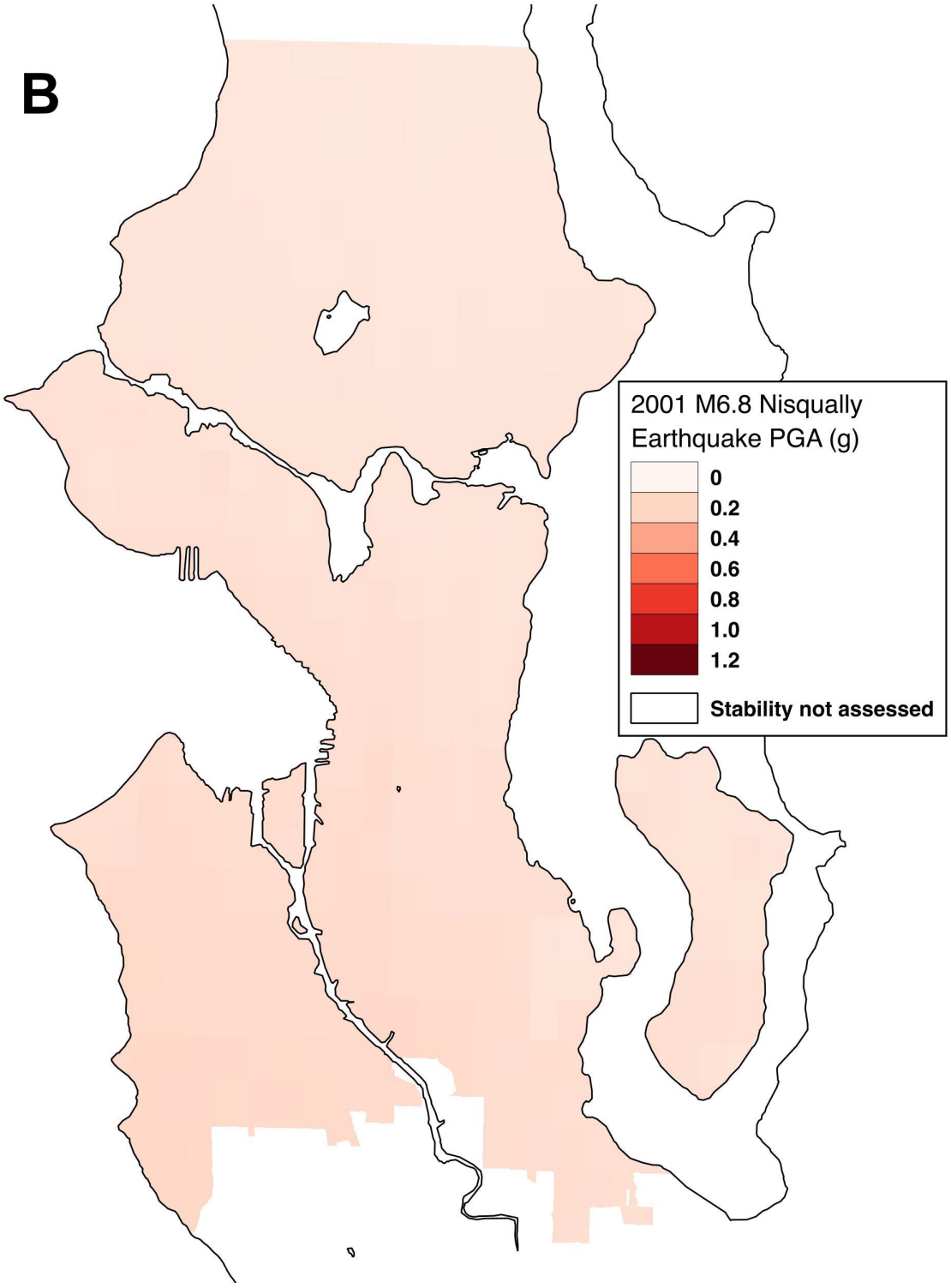
B
2001 M6.8 Nisqually
Earthquake PGA (g)
0
0.2
0.4
0.6
0.8
1.0
1.2
Stability not assessed

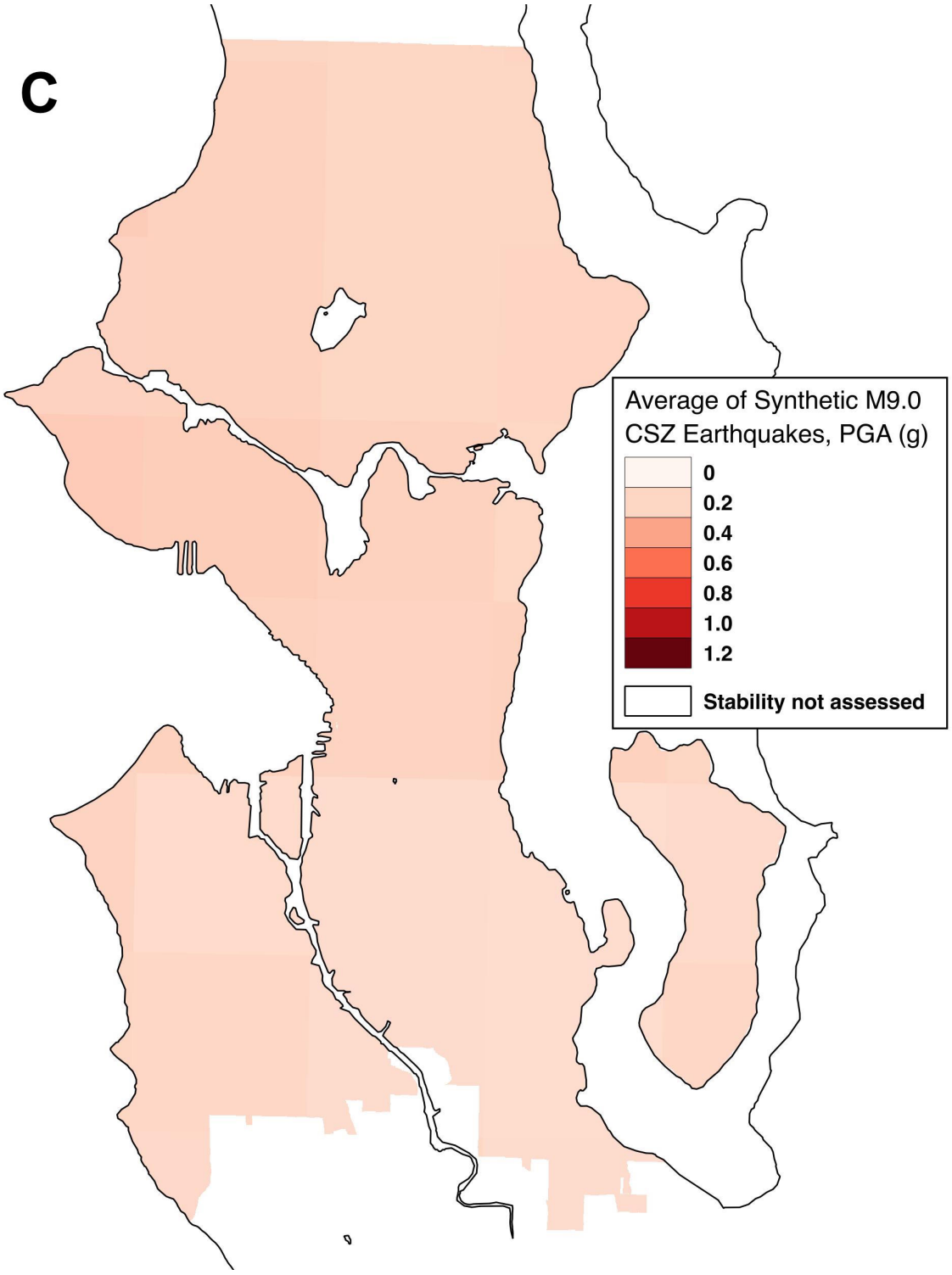

Figure 3.24 Peak ground acceleration, equally scaled, for each considered earthquake source. A: M7.0 synthetic Seattle Fault, B: 2001 M6.8 Nisqually earthquake (deep intra-slab), and C: average accelerations from the M9.0 CSZ suite. For a near-field seismic source like the Seattle Fault, ground motions are approximately 5x higher than more distant deep sourced earthquakes (Nisqually) and the CSZ M9.0 scenarios.

3.4 Results

3.4.1 Probability of coseismic landslides for a M9.0 CSZ earthquake in Seattle and Mercer Island

static stability conditions were computed for shallow translational (Eq. 3.9) and deep rotational (Eq. 3.19) landslides across Seattle and Mercer Island. Material strengths were computed stochastically via fractal random field generation (section 3.3.2), with dry and wet ground water saturation conditions developed from Smith et al. (2017). Expected slope stability with respect to each landslide mode is expressed as yield acceleration (k_y, resistance to coseismic landslide triggering, Eq. 3.10), for dry (Fig. 3.25) and wet (Fig. 3.26) ground saturation conditions. Hillslopes susceptible to failure under strong (k_y < 0.5) and moderate (k_y < 0.2) ground accelerations increase significantly for wet (Fig. 3.26) saturation conditions.

Probabilities of coseismic landslide triggering, reported as the probability of expected coseismic displacement exceeding 1cm, for a suite of 30 synthetic M9.0 CSZ earthquakes are shown in Figs. 3.27 (dry) and 3.28 (wet). Little coseismic landslide hazard is predicted for a summertime CSZ earthquake (observed as the lack of visible hazard in Fig. 3.27), as the relatively dry hillslopes are capable of resisting the moderate levels of shaking developed by the CSZ synthetic suite. For deep rotational slides, the total area with at least 5% probability of occurrence increases 515% from dry to wet conditions, expanding from 0.18km^2 to 1.13km^2. For these 30 synthetic CSZ ground motions, shallow translational slides show almost no change from dry to wet conditions (5% increase, 0.56 to 0.59km^2 dry to wet) as they are focused in a small number of near-critical slopes that are highly susceptible to failure under any seismic loading. Shifts in expected landslide distribution are highlighted in Figure 3.29, showing a detail of predicted probabilistic coseismic landslide hazard West Seattle given a M9.0 CSZ earthquake.

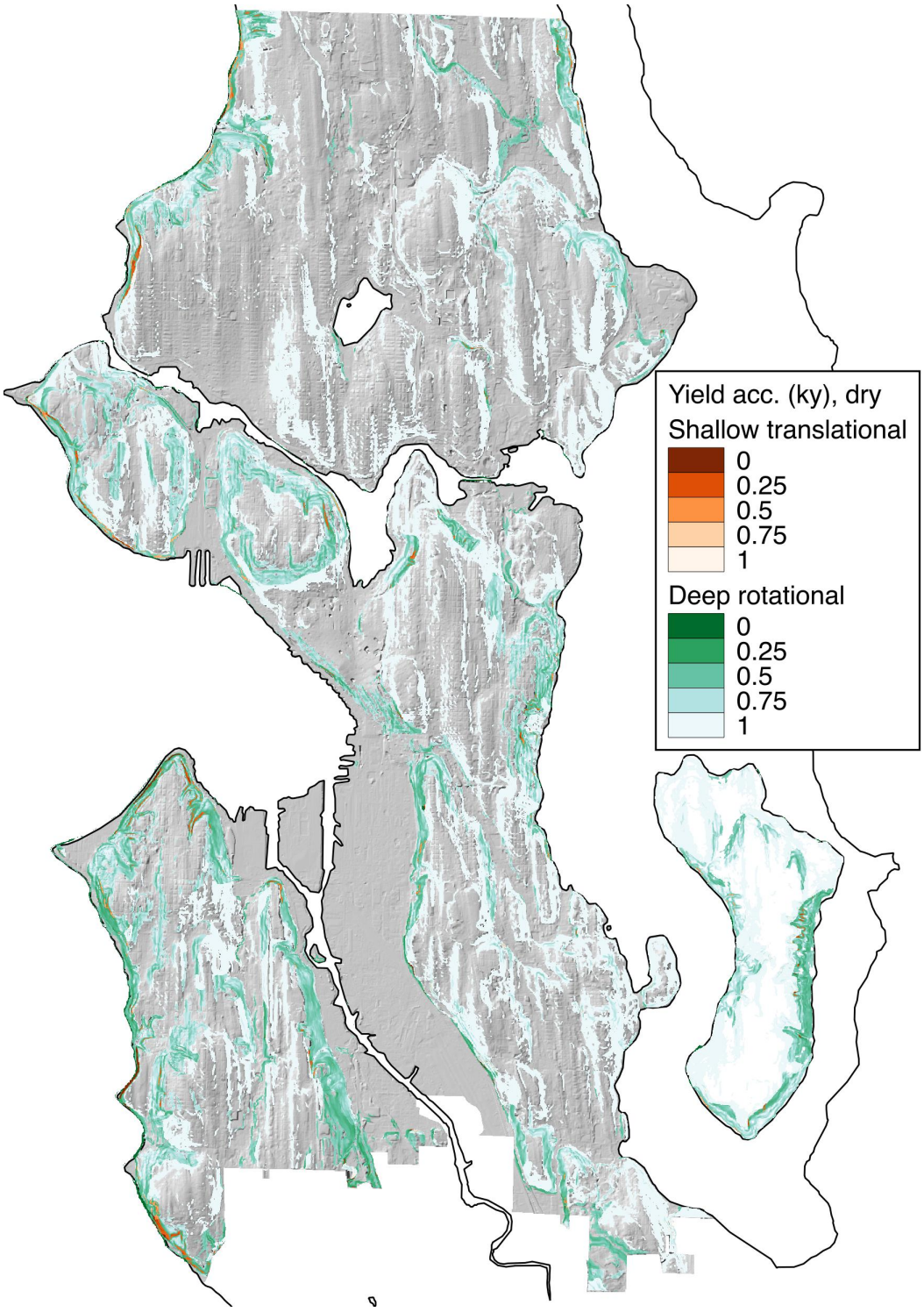

Figure 3.25 Yield accelerations both shallow translational and deep rotational landslides for dry conditions. Decreasing values of k_y indicate higher likelihood of coseismic failure.

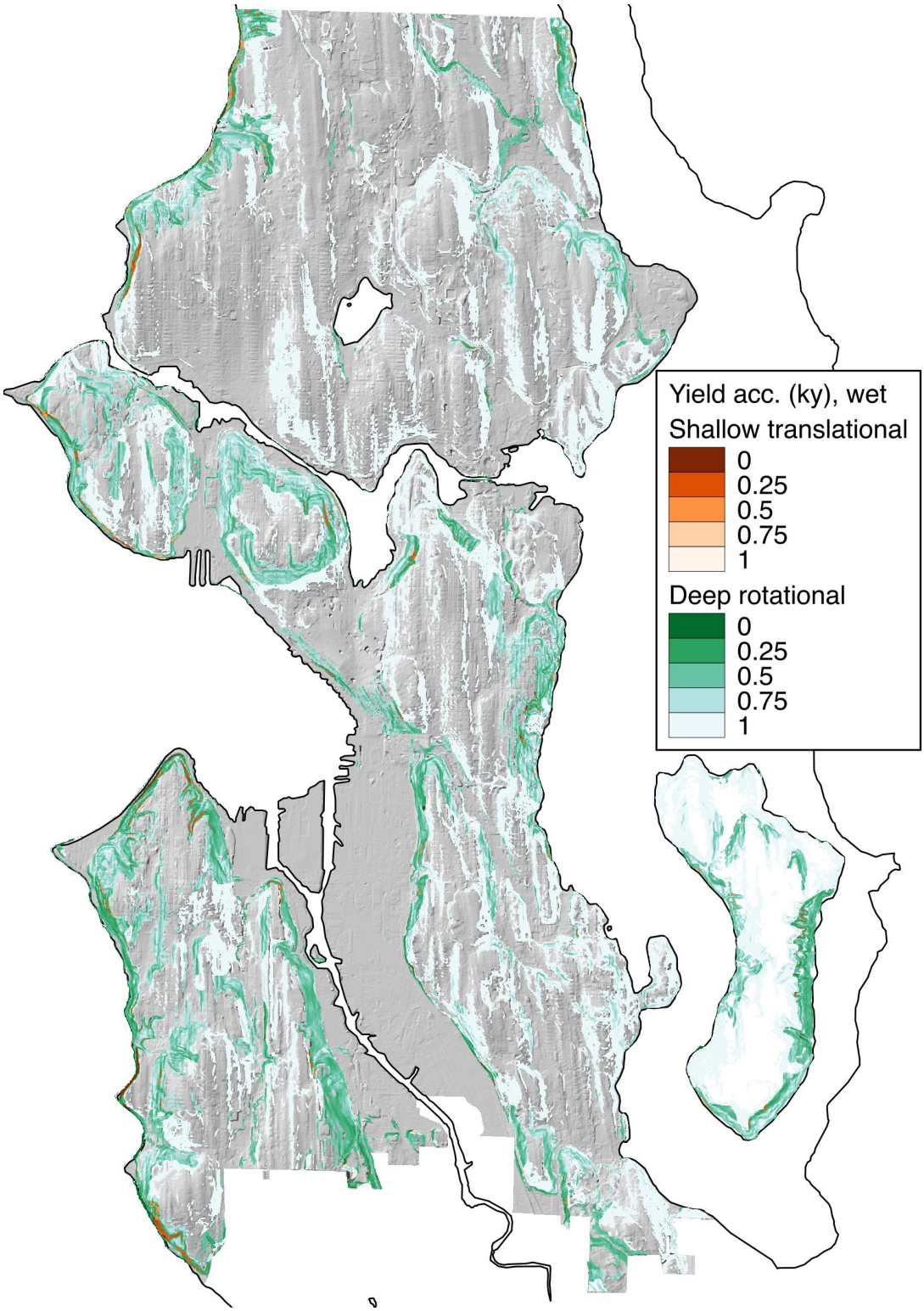

Figure 3.26 Yield accelerations both shallow translational and deep rotational landslides for wet conditions. Decreasing values of k_y indicate higher likelihood of coseismic failure.

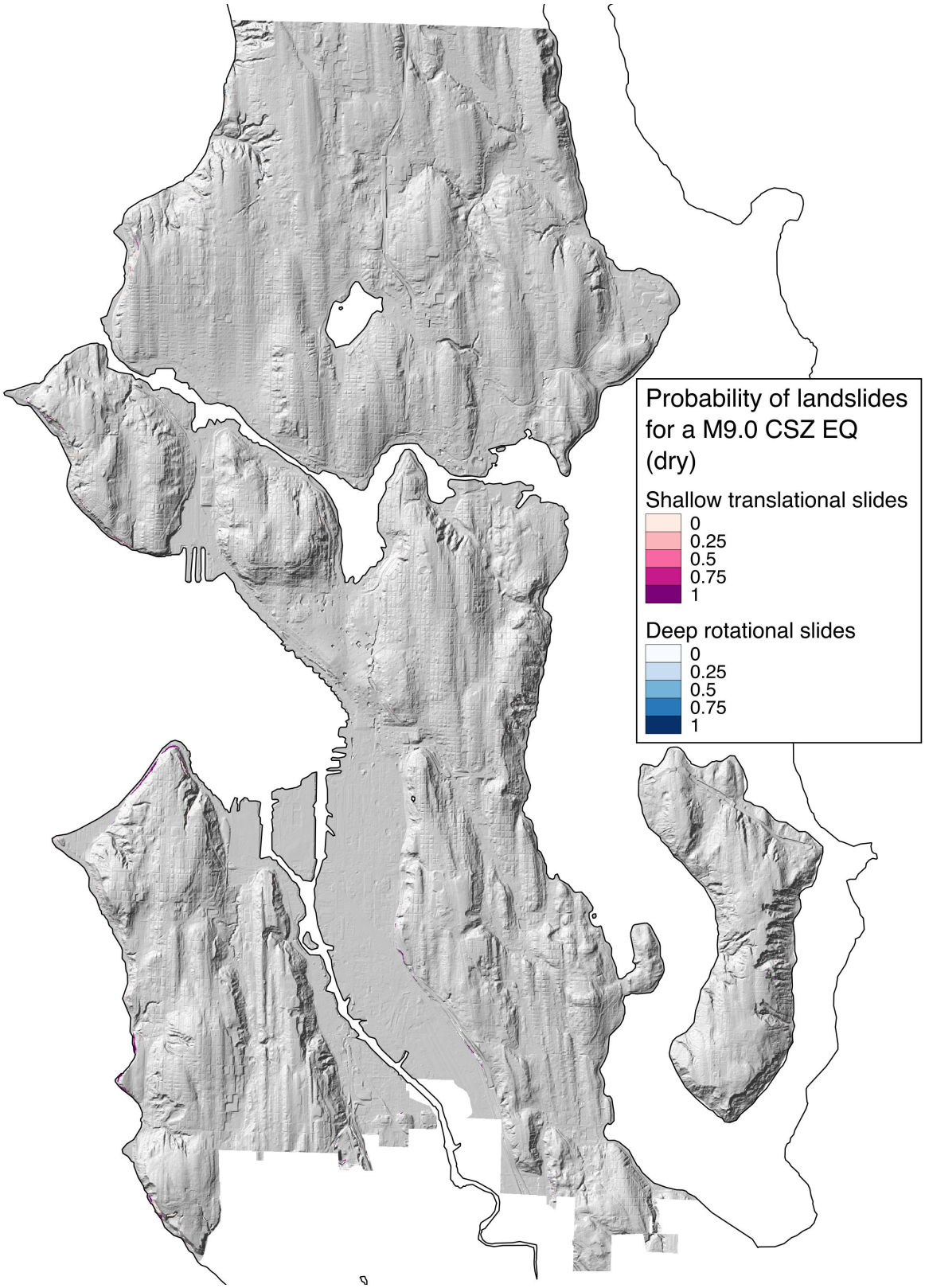

Figure 3.27 Probability of coseismic landslide triggering (D_N > 1cm) given a M9.0 CSZ earthquake for shallow translational (pinks) and deep rotational (blues) landslides during dry, summer-like, ground saturation conditions in Seattle and Mercer Island.

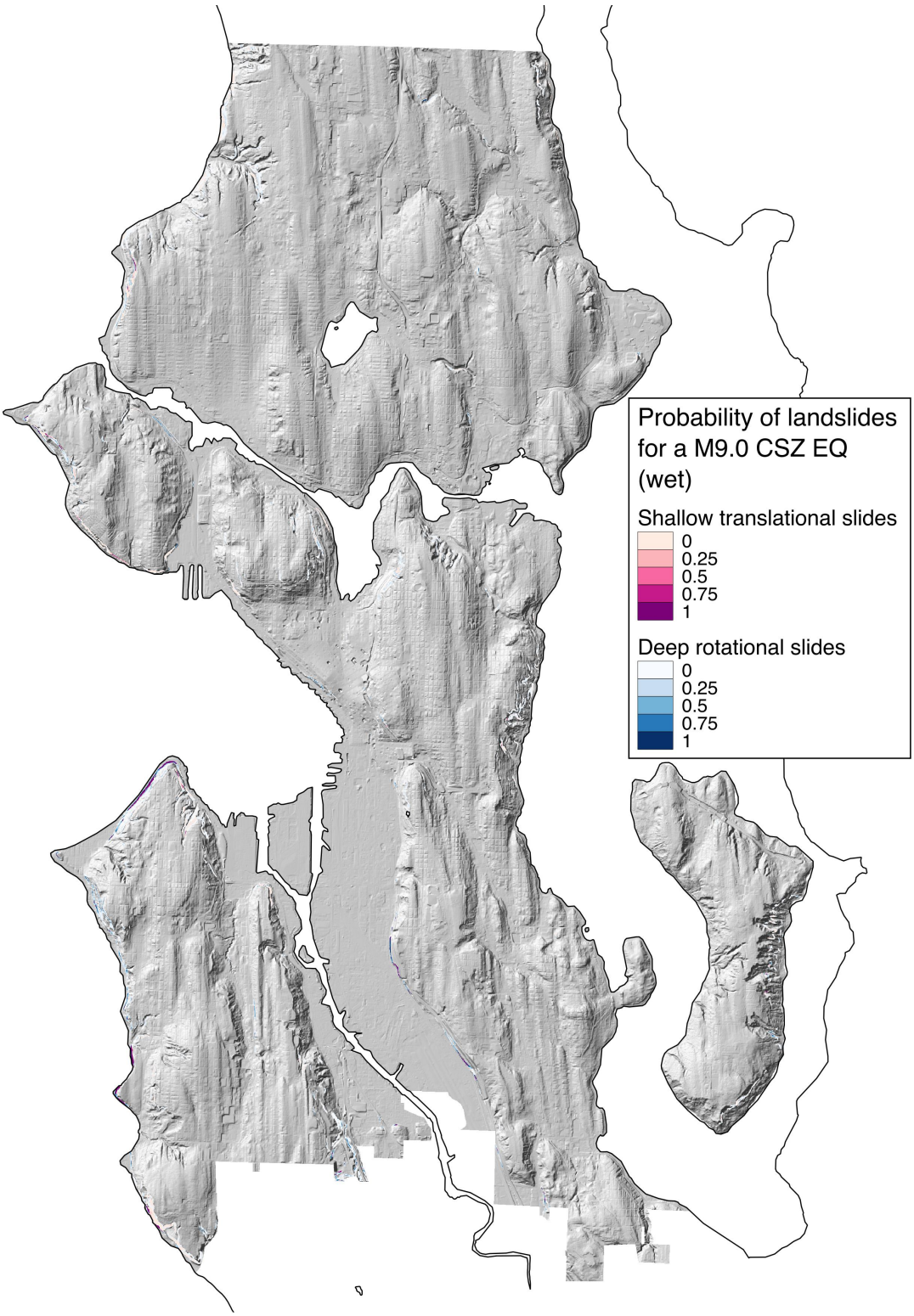

Figure 3.28 Probability of coseismic landslide triggering (D_N > 1cm) given a M9.0 CSZ earthquake for shallow translational (pinks) and deep rotational (blues) landslides during wet, winter-like, ground saturation conditions in Seattle and Mercer Island.

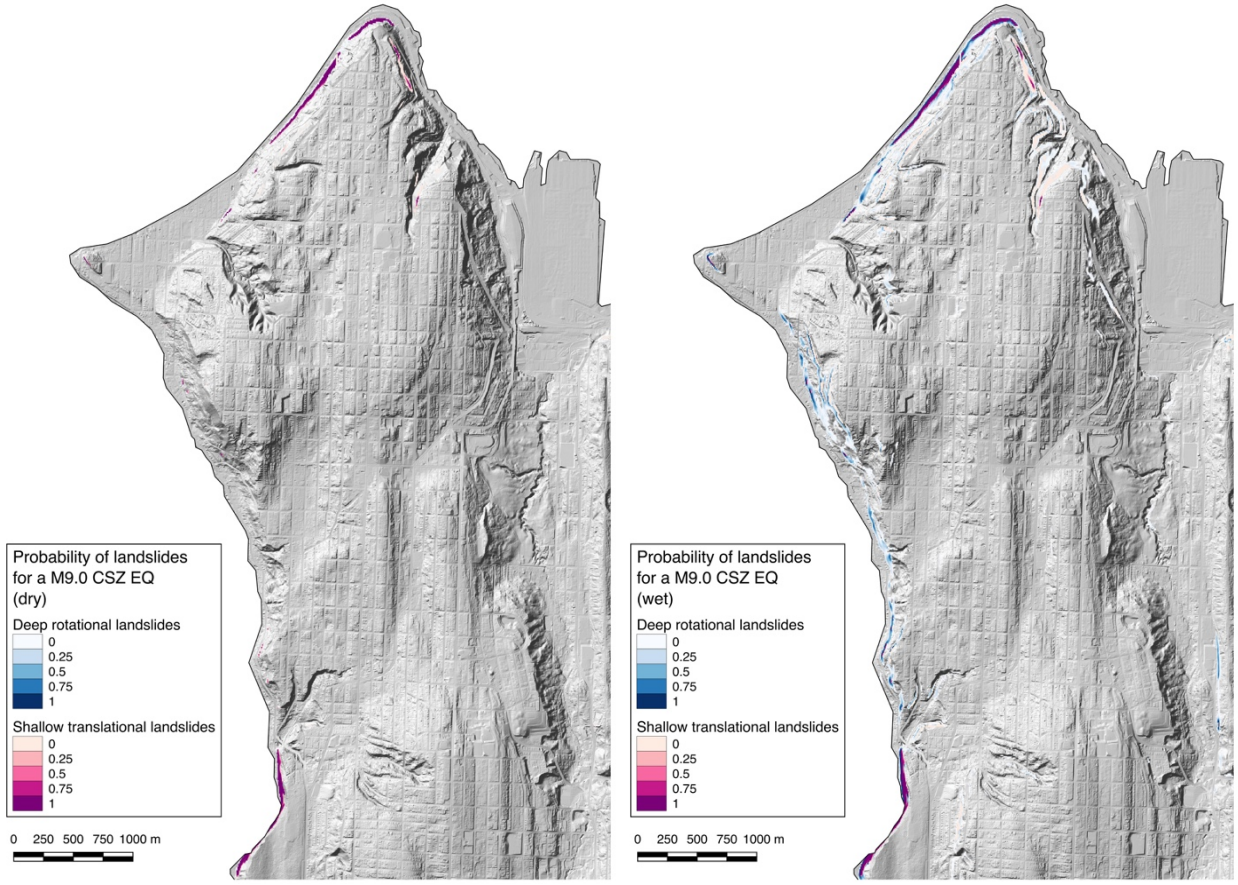

Figure 3.29 Detail of forecasted M9.0 CSZ coseismic landslide hazard for deep rotational (blues) and shallow translational (pinks) slides in West Seattle for dry (m = 0 – 0.2) and wet (m = 0.4 – 0.6) ground saturation conditions.

3.4.2 Coseismic landslide hazard from the 2001 M6.8 Nisqually earthquake

The Feb 28, 2001 M6.8 Nisqually, Washington earthquake triggered at least ten landslides within the city of Seattle (Fig. 3.30). Coseismic landslide hazard estimates, based on observed ground accelerations (USGS, 2017), were computed for wet winter-like conditions to match the time of year of the Nisqually earthquake. Each of the mapped Nisqually landslides is located on, or directly adjacent (5 – 10m) from regions of predicted Nisqually coseismic landslide hazard (Fig 3.30 insets). For Nisqually ground motions, only 0.72km^2 was predicted to have at least a 5% probability of landslide failure. Less than 0.25km^2 is predicted to fail with a probability of at least 25%. The predicted lack of landslide hazard suggests true-negative prediction of landslide

occurrence, given only ten landslides have been mapped within Seattle. Coseismic landslide hazard for Nisqually was computed using unmodified Harp et al. (2008) material strength properties based on the two modes of landslides discussed above. Strong agreement between the historic Nisqually earthquake landslide inventory and blind-prediction coseismic landslide hazard provides verification that these coseismic landslide hazard models, and probabilistic initiation models can accurately predict coseismic landslide hazard developed from synthetic future earthquakes. In general, areas of computed coseismic landslide hazard show lower probabilities, and are of smaller extent for the Nisqually earthquake than the CSZ synthetics, due to the larger expected peak ground accelerations from the CSZ scenarios, and duration effects from the larger magnitude subduction zone earthquake accounted for in the displacement models.

3.4.3 Coseismic landslide hazard for a synthetic M7.0 Seattle Fault earthquake

Adopting the M7.0 Seattle Fault synthetic ground motions of Allstadt et al. (2013), predicted multimodal coseismic landslide hazard is shown in Fig. 3.31 for dry, and Fig. 3.32 for wet ground saturation conditions. Unlike Allstadt et al. (2013), coseismic landslide hazard is presented for two modes of failure, and 'wet' ground saturation is assumed to be equivalent to a water-table of height of 40 – 60% of the total landslide mass (compared to their 100%) based on local piezometer data (Smith et al., 2017). Areas of 5% or greater probability of landslide occurrence during dry conditions increase 85% (shallow translational) and 724% (deep rotational) with respect to a M9.0 CSZ earthquake. For wet ground saturation conditions zones of 5% or greater landslide probability increase the same 85% for shallow translational slides, and 394% for deep rotational slides. Expected ground motions in southern Seattle from the M7.0

synthetic Seattle Fault earthquake are severe enough to predict widespread deep rotational and shallow translational landslides even for dry saturation conditions, and far more widespread coseismic landslide hazard than a larger magnitude CSZ earthquake.

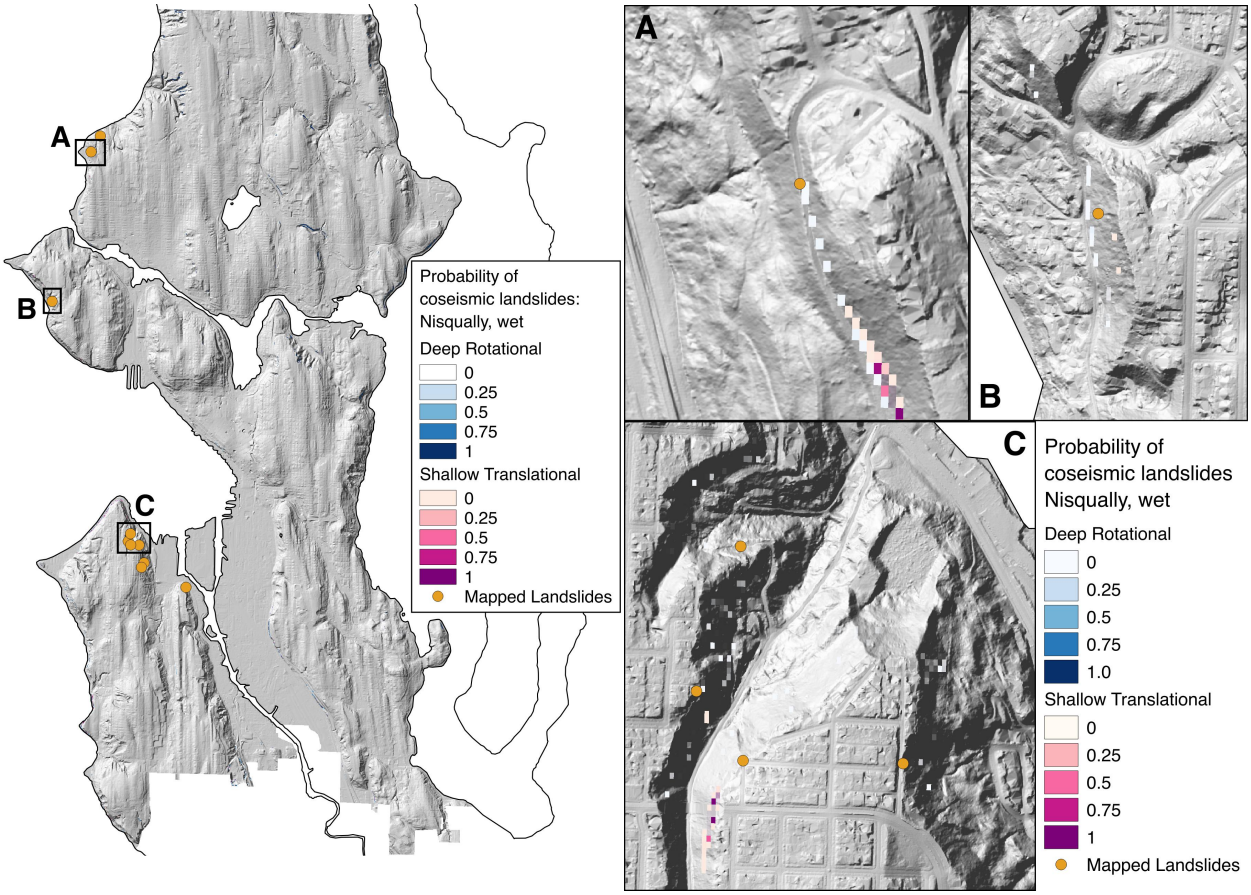

Figure 3.30 Mapped Nisqually landslides from the city of Seattle landslide dataset plotted with wet-season predictions of landslide likelihood given USGS derived Nisqually peak ground accelerations within Seattle. Insets, observed landslides following the Nisqually earthquake map onto, or within several meters (5 – 10m) of predicted zones of coseismic landslide initiation during the Nisqually earthquake.

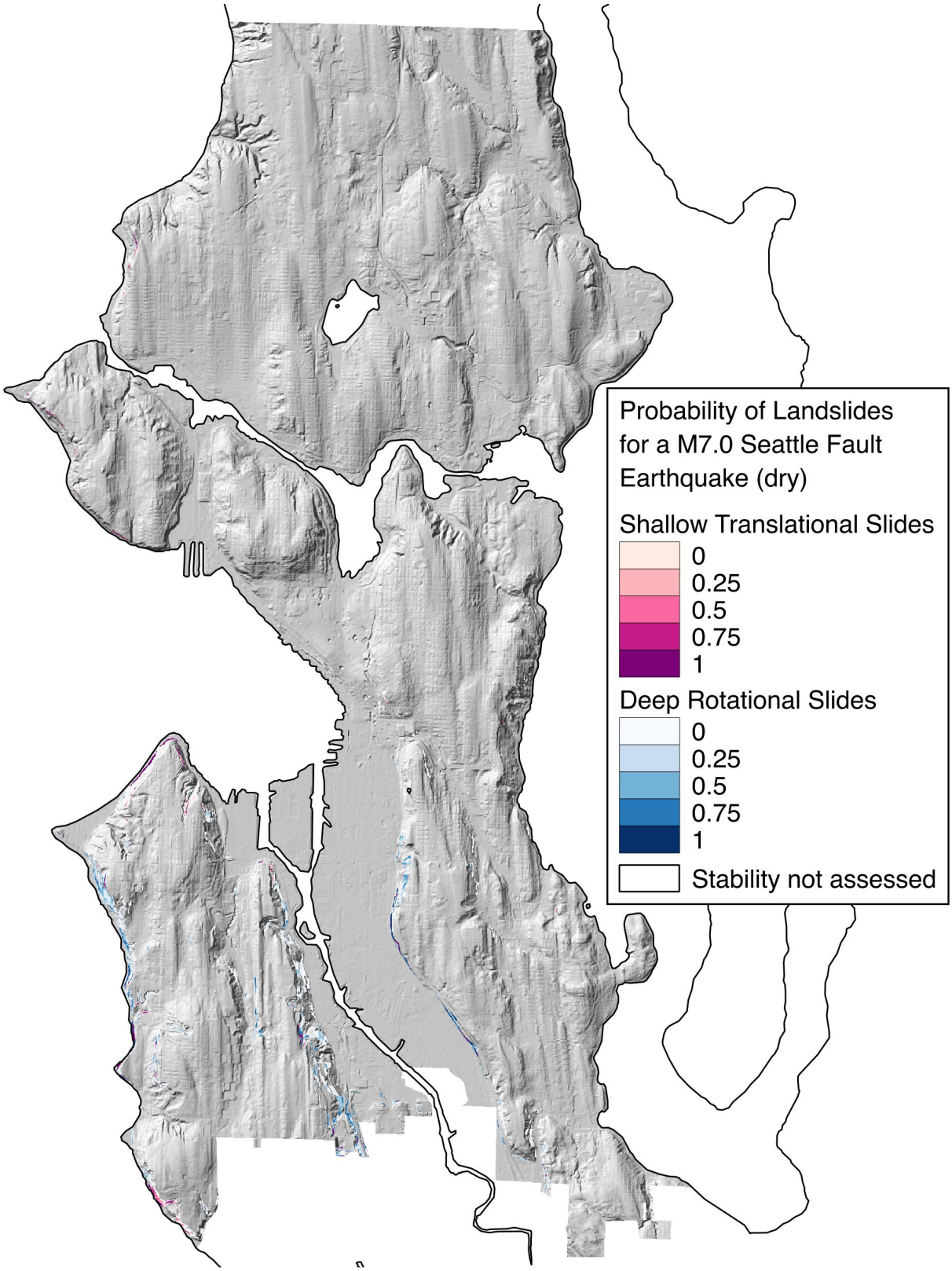

Figure 3.31 Probability of coseismic landslides given a M7.0 Seattle Fault earthquake for shallow translational (pinks) and deep rotational (blues) landslides during dry, summer-like, ground saturation conditions in Seattle.

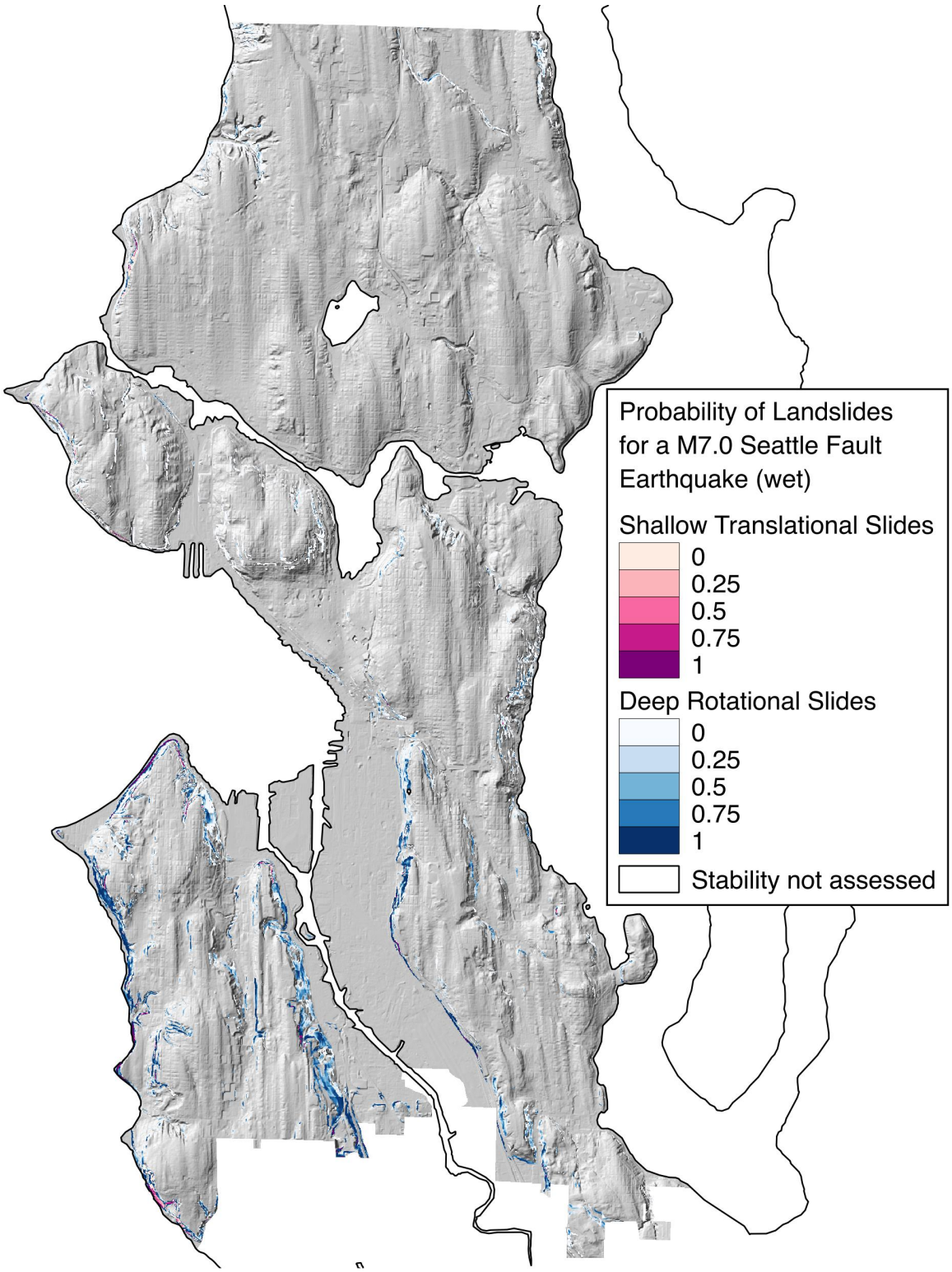

Figure 3.32 Probability of coseismic landslides given a M7.0 Seattle Fault earthquake for shallow translational (pinks) and deep rotational (blues) landslides during wet, winter-like, ground saturation conditions in Seattle.

3.4.4 PCLHA output for Seattle

Based on the relative contribution of hazard to a 475-year probabilistic seismic hazard analysis for Seattle, WA, the three earthquake sources discussed above, Cascadia Subduction Zone (interface earthquakes), Seattle Fault (shallow crustal faults), and Nisqually (slab earthquakes) were combined to develop a simplified Probabilistic Coseismic Landslide Hazard Analysis (PCLHA). Weighted by relative-contribution to seismic hazard, and long-term ground saturation levels, 10% in 50-year PCLHA results for Seattle, WA are shown in Fig. 3.33, with a detail of West Seattle shown in Fig. 3.34. PCLHA output show much lower hazard than an extreme case (midwinter Seattle Fault earthquake), as longer-term seasonality, and lower predicted hazards from earthquakes like the 2001 Nisqually event, balance relatively intense local seismic sources.

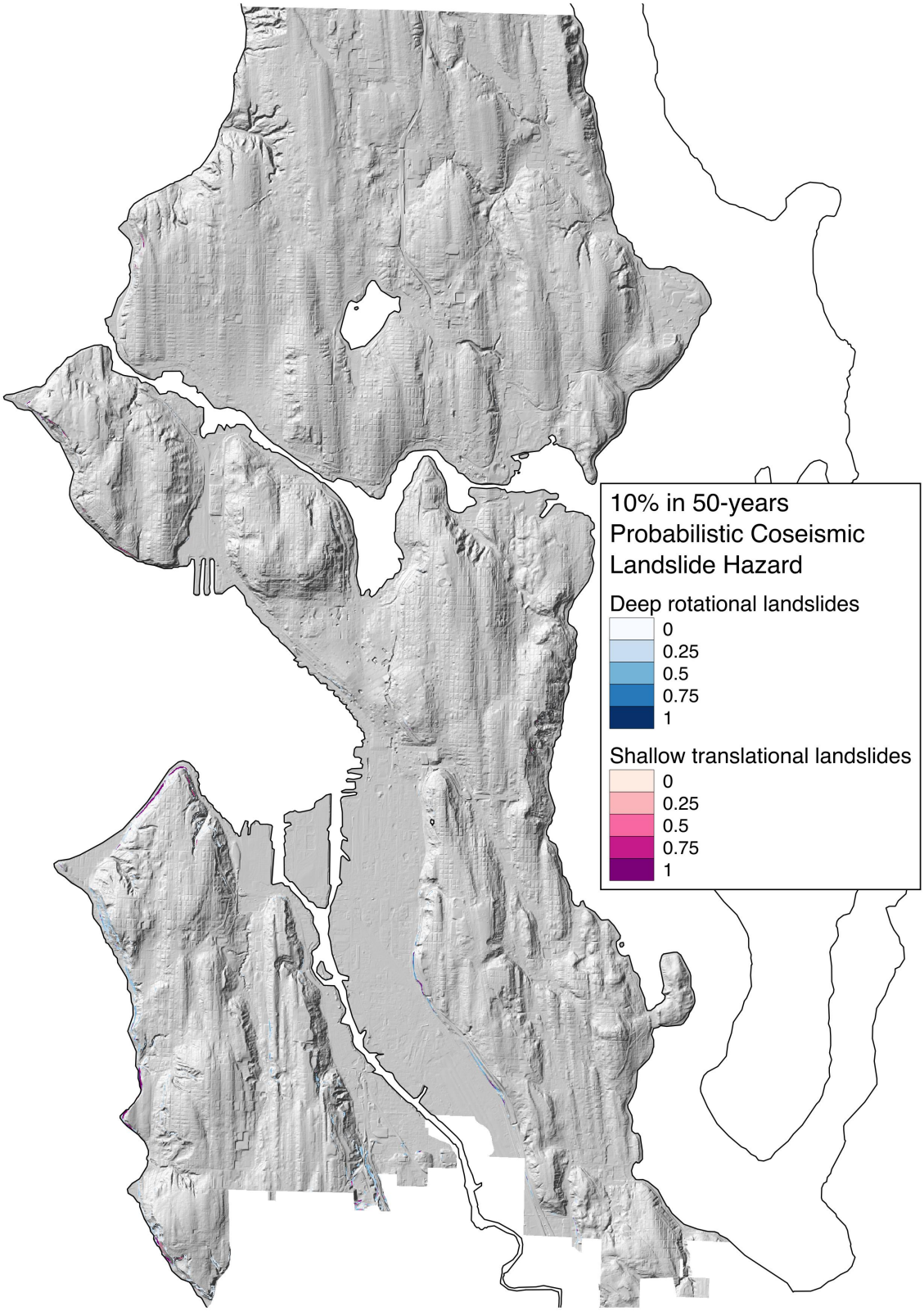

Figure 3.33 Probabilistic coseismic landslide hazard analysis for 10% in 50-year probability of exceedance in Seattle, Washington for two modes of landslides, shallow translational and deep rotational slides.

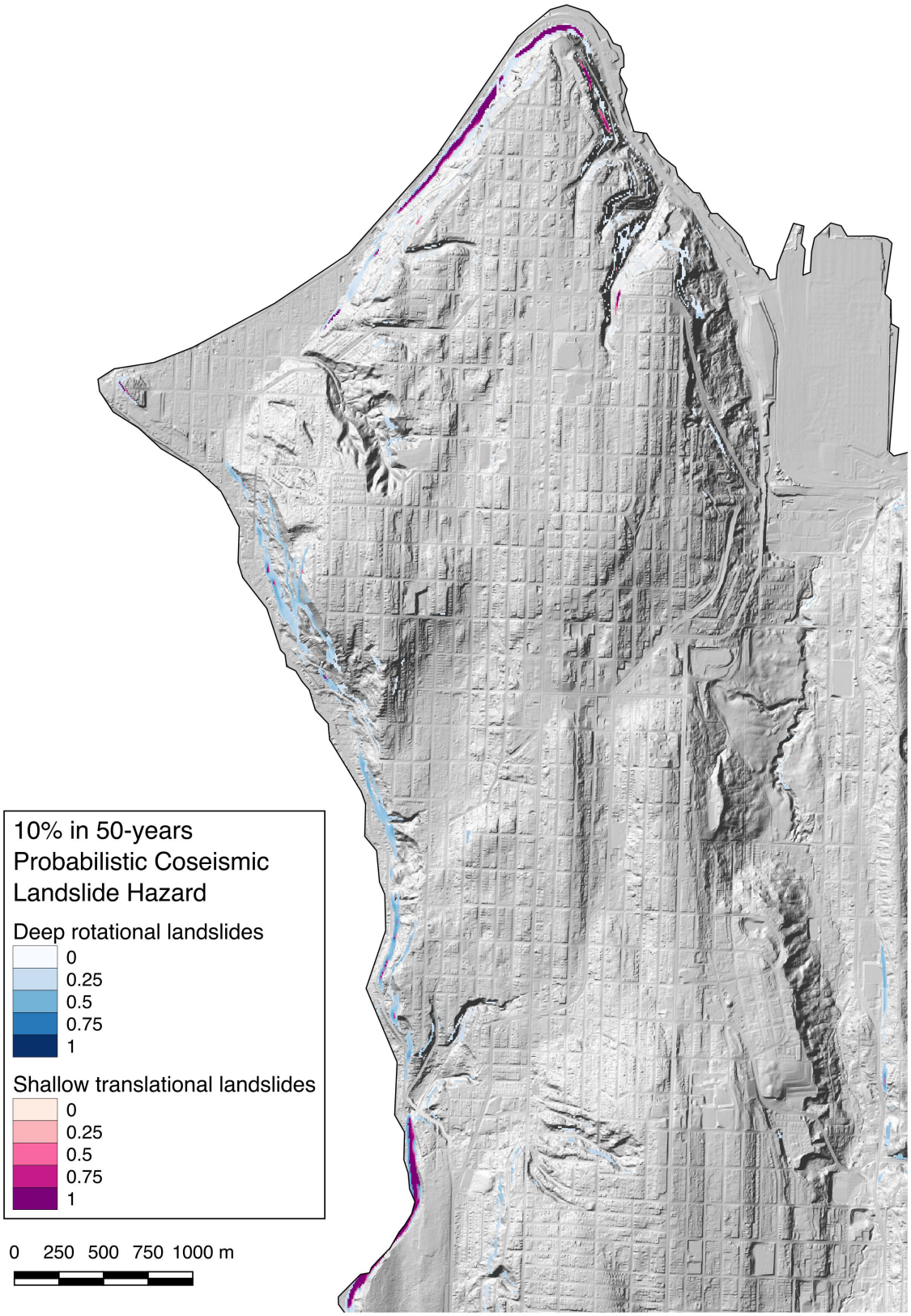

Figure 3.34 Detail of 10% in 50-years probabilistic coseismic landslide hazard analysis showing West Seattle.

3.5 Discussion

3.5.1 Subduction-specific sliding-block displacements

A new model to predict expected sliding-block displacements during large magnitude (M8 – M9) subduction zone earthquakes was presented. This model was developed to better match sliding-block displacement characteristics of recorded large-magnitude earthquakes, where many cycles of loading may develop greater displacements than in equivalent slopes during a crustal earthquake (M5 – 7.5, Fig 3.35). Displacements shown in Fig. 3.35 were computed following Newmark's (1965) sliding-block model, which has been applied around the world to coseismic landslide hazard assessments. Many, e.g. Wartman et al. (2003, 2005), Kramer and Smith (1997), Rathje and Bray (1999, 2000), have shown Newmark sliding-block calculations, assuming rigid perfectly-plastic slope displacement, to be inadequate when modelling larger or more complex landslide movements where dynamic slope response is more significant. However, Newmark sliding-block displacements continue to be a valuable and widely used tool for coseismic landslide hazard assessment, and have been shown to be appropriate for thin shallow translational landslide analysis, as well as providing reasonable estimates of relative coseismic deformations for deep rotational slides as computed here.

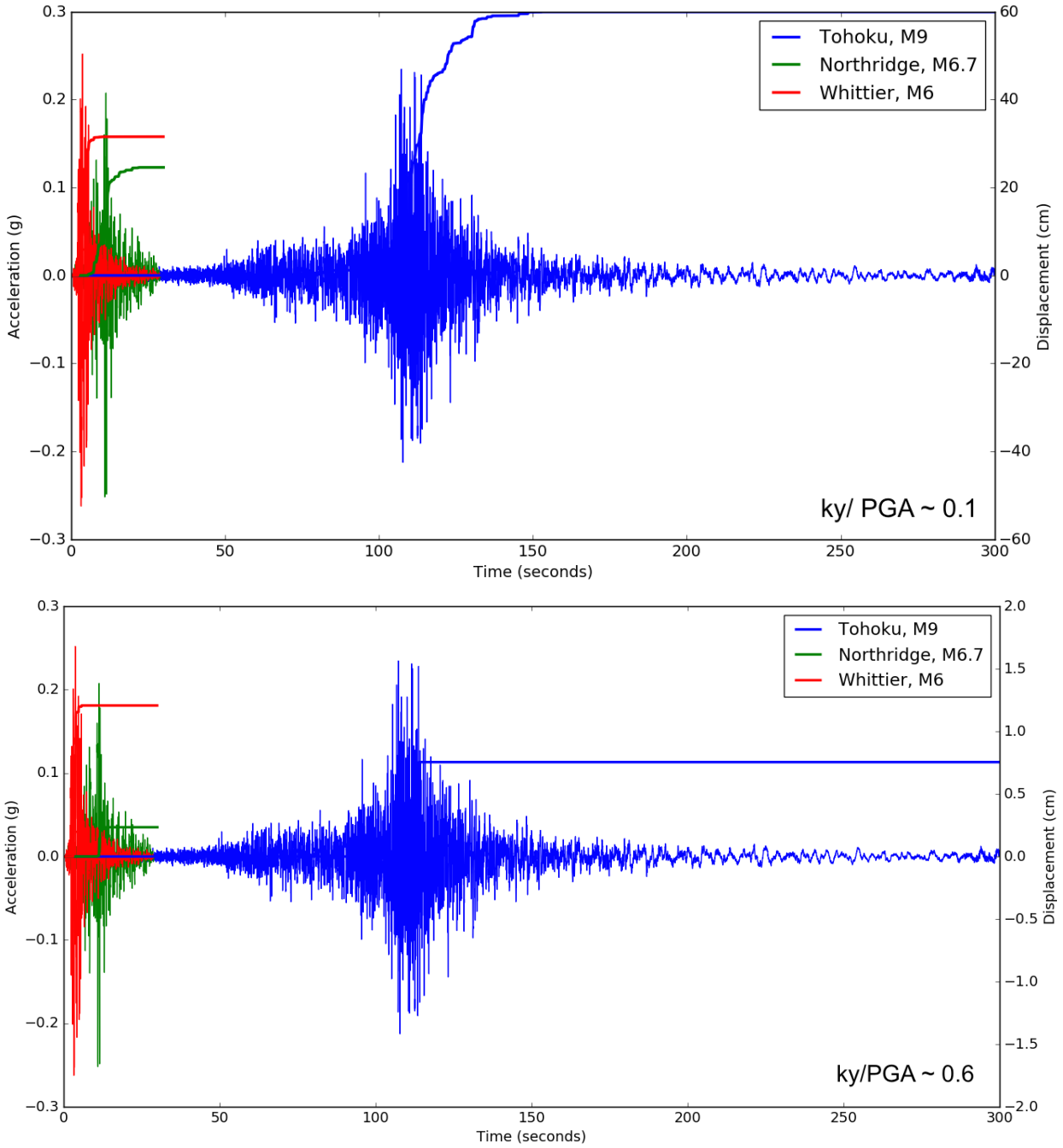

Figure 3.35 Sliding-block displacements computed for three equivalent slopes acted upon by recordings of equivalent PGA from the M9.0 Tohoku, M6.7 Northridge, and the M6.0 Whittier Narrows earthquakes. Top, for very low k_y/PGA ratios (relatively weak slopes), the additional cycles of seismic loading from the larger Tohoku earthquake drive much higher displacement (60cm), than the smaller magnitude events (25 – 30cm), for the same k_y/PGA ratio. Bottom, for more stable slopes ($k_y/PGA \geq 0.6$) sliding-block displacements are controlled by a small number of high acceleration pulses, and little difference is observed for the three recordings (M6 – M9, displacements from 0.2 – 1.4cm).

Synthetic earthquake data for much of the PNW modeling a M9.0 CSZ earthquake tightly fit the distribution of sliding-block displacements from recorded large magnitude subduction earthquakes, suggesting these synthetics are in close agreement with respect to duration and cumulative acceleration with real data. Others (Jibson, 2007) have observed insignificant differences in the resultant models when the recorded data are disaggregated into soil and rock categories to capture first-order site effects, which have been neglected here. However, when synthetic earthquake data is categorized as being within the Puget Lowlands (basin) or non-basin, expected displacements within the basin are 1 - 2σ above the general trend of recorded data and non-basin synthetic data. This suggests basin amplification in the Puget Lowlands may develop more coseismic landslides than an equivalent site just outside the basin due to excitation of the ground motions and potentially increased shaking duration. A more careful analysis of this basin response, for not only rigid-block systems but also coupled and decoupled dynamic analyses and compliant 2D slopes, to assess the significance of basin amplified motions on shallow translational landslides, deep-seated landslides, and lateral spreads should be investigated. Modeling of coseismic displacements for synthetic ground motions should be combined with the subduction time history databases and mapped distributions of coseismic landslides in regions of known sedimentary basins to develop a better understanding of expected coseismic displacement behavior and the realized consequences with respect to triggered landslides within and outside of basins from past earthquakes.

3.5.2 Probabilistic coseismic landslide hazard

Utilizing the newly developed suite of potential M9.0 CSZ synthetic earthquakes developed by the USGS and UW, probabilistic coseismic landslide hazard estimates were made for the cities

of Seattle and Mercer Island. As in Allstadt et al. (2013), we find ground saturation assumptions (seasonality) to have a significant effect on predicted coseismic landslide hazard, resulting in a 515% increase in potential areas of deep-rotational landslides, many of which are within 10m of highways, roads, or homes. When coseismic landslide hazard was predicted for different types and magnitudes of earthquakes affecting Seattle, significant variations were observed (Fig. 3.36). The historic 2001 M6.8 Nisqually earthquake, causing relatively weak ground accelerations across Seattle (< 0.2g) was predicted to generate very limited amounts of coseismic landslide hazard—0.25km^2 with a 5% of greater probability of failure when dry, 0.72km^2 if wet—and triggered only ten mapped landslides within Seattle. Strong ground accelerations, and much longer, predicted ground motions from simulated M9.0 CSZ earthquakes develop greater areas of predicted coseismic landslide hazard than the Nisqually earthquake—0.74km^2 with a 5% of greater probability of failure when dry, 1.72km^2 if wet. Synthetic ground motions for a M7.0 Seattle Fault, occurring directly below southern Seattle are much stronger than either Nisqually or potential CSZ megathrust motions (Fig. 3.24). A M7.0 Seattle Fault earthquake is expected to generate far greater numbers of landslides, and landslide consequences, than either of the other two seismic sources—1.86km^2 with a 5% of greater probability of failure when dry, 5.94km^2 if wet.

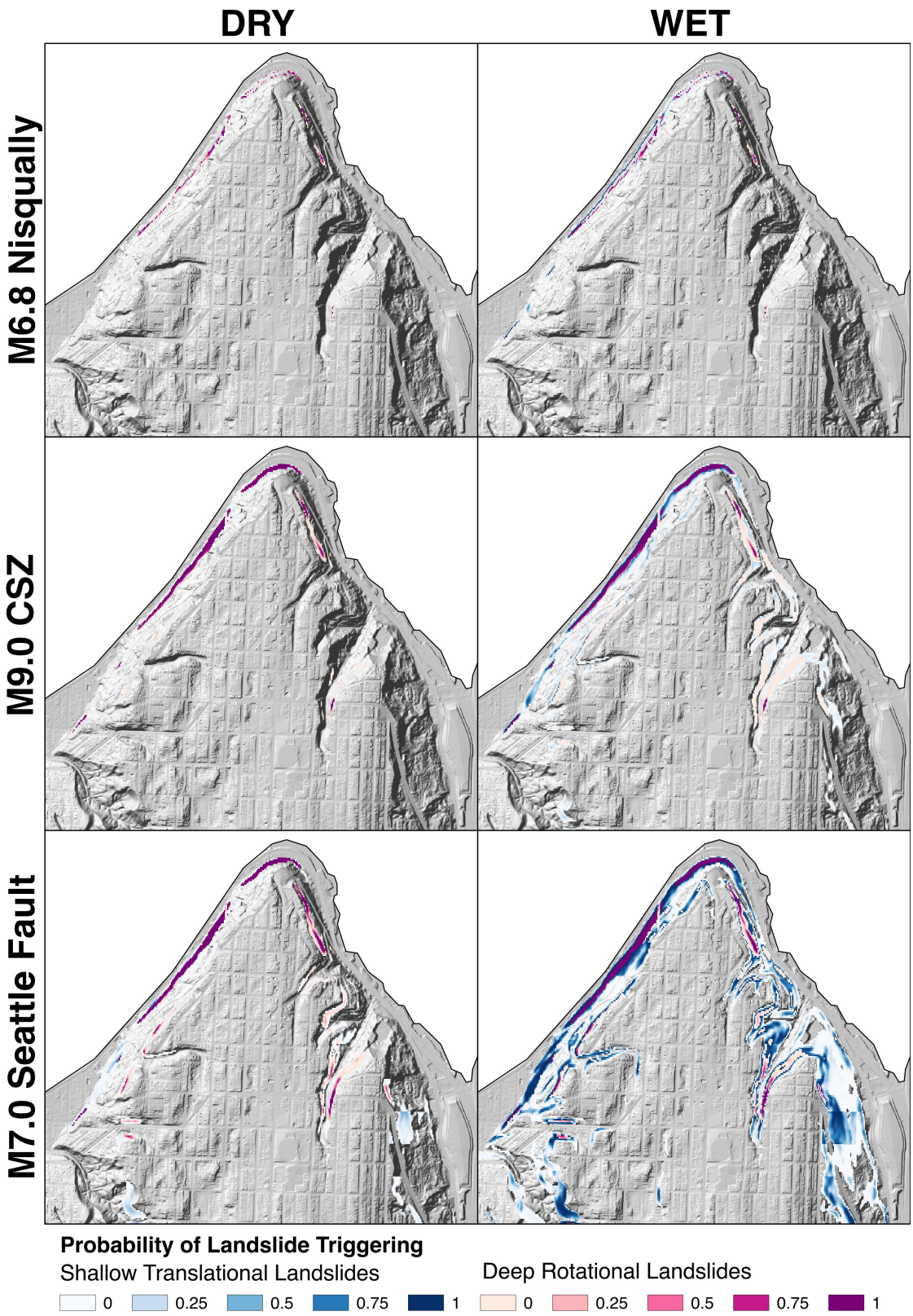

Figure 3.36 Comparison of predicted landslide extents for each considered earthquake scenario, 2001 M6.8 Nisqually earthquake, M9.0 CSZ synthetics, and a M7.0 Seattle Fault synthetic, for dry (left column) and wet (right), simulated ground saturation conditions.

The implications to coseismic landslide risk, in terms of economic and productivity losses, due solely to seasonality are therefore immense and deserve more careful analysis at a more detailed site-specific level to better characterize this effect. To facilitate the analysis of multimodal landslide hazard assessment across Seattle and Mercer Island, assumptions about geologic structure (analyzing only surficial geology), heterogeneities in material strengths (stochastic fractal fields to enable probabilistic hazard calculations in lieu of physically based relationships), and landslide saturation conditions (from monitoring data of Smith et al., 2017) were made. These assumptions reflect the state of the art in regional-scale probabilistic coseismic landslide hazard analyses, where surficial geology, sometimes ascribed distribution of strengths, with no, or heuristically imposed groundwater, are used to predict single-mode coseismic landslide hazard (e.g., Saygili and Rathje, 2009; Allstadt et al., 2013; Lari et al., 2014; Wang and Rathje, 2015). However, at the scale of Seattle, or other cities and townships, improvements to each of these assumptions should be made. 3D subsurface geology, constructed from existing borehole data, could be utilized by programs such as Scoops3D (Reid et al., 2015) to assess local hillslope stability incorporating more realistic geologic conditions. Spatial variability in material strengths could also be inferred from bore-hole data, geotechnical reports, or field work aimed at characterizing material variability. Finally, a comprehensive inventory of city, state, and federal monitoring data collected within the study bounds may also allow for well constrained spatially and temporally-variable groundwater conditions. Simplifications notwithstanding, probabilistic coseismic landslide hazard analysis output, considering a seismic hazard in Seattle for a 10% in 50-years exceedance threshold, closely match observed landslides throughout Seattle (Fig. 3.37). While mapped landslides were primarily triggered by precipitation or human action (Fig. 3.37), the most active hillslopes are generally predicted to be most susceptible to coseismic landslides.

Mapped landslides triggered by the 2001 Nisqually earthquake (Fig 3.30) fit near-perfectly with predicted areas of coseismic landslide hazard based on observed shaking intensities and assumed winter ground saturation conditions. No effort was made to calibrate the model to match Nisqually data, and the predicted coseismic hazard distribution showing virtually no hazard throughout the city save for a few isolated hillslopes (only eight landslides have been mapped as being triggered by the Nisqually earthquake in Seattle) provides strong verification that modeled landslide hazard reflects what may occur in Seattle.

From Chapters 1 and 2, probabilistic coseismic landslide hazard analysis presented are incomplete in their omission of lateral spreads, as well as potential rock slope failures and the development of flow slides. Lateral spreads are particularly important as they have been shown to be a dominant mode of landslide failure with respect to the natural environment (i.e. sediment mobilization, Wartman et al. 2013) and the built environment (Chapter 2.). Lateral spreads and flow slides were omitted from this work as they fall under the scope of Greenfield (2017) within the M9 project, and require time-domain analyses to assess cyclic degradation of strength, development of excess pore water pressures, and mobilization not performed in this regional-scale analysis. Rock slope failures of all modes are omitted due to the geographically limited scope presented. For future analyses in the great PNW where steep exposed rock is present, these analyses will be reincorporated.

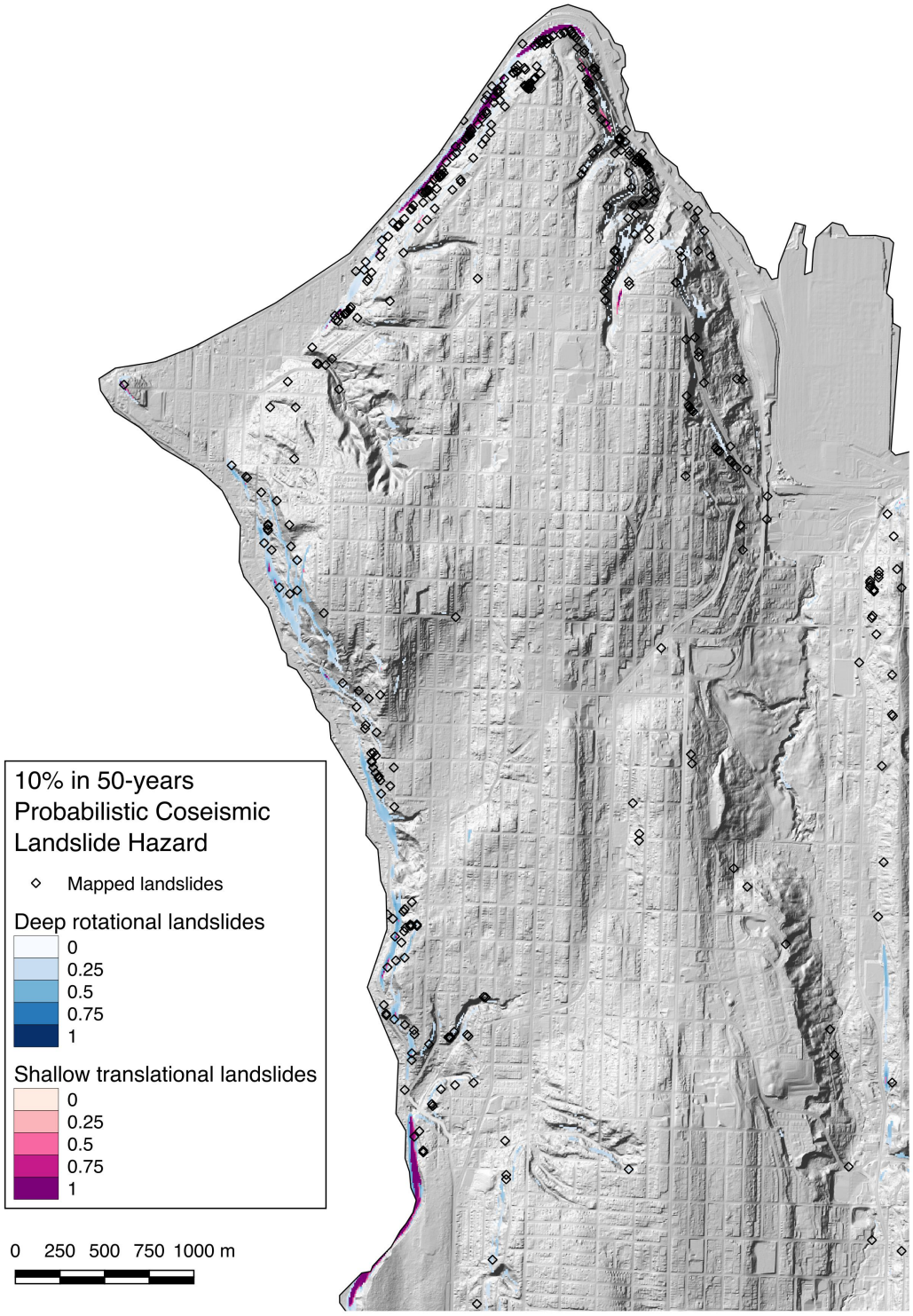

Figure 3.37 Detail of West Seattle showing predicted coseismic landslide hazard for a peak ground acceleration exceedance rate of 10% in 50-years for shallow translational and deep rotational landslides. Black diamonds show points where landslide sources have been mapped in Seattle from historical records and post-event field observations. Note, virtually all mapped landslides were triggered by anthropogenic forcing or precipitation, and many landslides may be omitted in areas not affecting homes or roadways and/or areas difficult to reach by foot.

3.5.3 Extension to the Pacific Northwest

This chapter presents and discusses the framework for analysis implemented for Seattle and Mercer Island, WA that will be carried out over the full extent of the Pacific Northwest affected by a great Cascadia Subduction Zone earthquake. Seattle and Mercer Island were selected as a sub-area due to the availability of high-quality material strength estimates, ground-water recording data, a comprehensive landslide inventory, and the ability to rapidly test these models at such a scale. As part of the M9 project, this work is a component of a larger mission to probabilistically forecast the hazards and consequences of a M9.0 CSZ earthquake across the full PNW. Future areas of high-concern include coastal towns and villages exposed to steep, landslide prone, topography and potentially extreme ground shaking, and additional urban areas, such as Portland, OR and Vancouver, B.C. Particular attention must be paid to coastal regions where the interaction between primary and secondary earthquake hazards (shaking, landslides and tsunamis) will play a critical role in the survival of exposed populations. In many coastal areas of the PNW, tsunami evacuation routes seek to rapidly gain elevation to best protect communities from destructive waves. These evacuation routes in some cases pass along, or across hillslopes highly susceptible to landslides. Understanding which of these evacuation routes are most likely to be cut off by coseismic landslides, and potential damages to the sparse road network connecting our coastal communities, will be critical to reducing losses during the next CSZ earthquake, and a should be priority of future work. Collaboration with researchers seeking to develop an inventory of landslides triggered by the 1700 CSZ earthquake (e.g. LaHusen et al., 2016; Struble et al., 2017), will enable further verification of existing models against CSZ-triggered landslides, and the development of additional modes of coseismic landslide failure in the continuation of this work. Recent synthetic earthquake modeling (Wirth et

al., 2017) suggests a reasonable estimate of the January 26, 1700, ~M9 CSZ earthquake could be developed by matching 1700 coseismic coastal subsidence estimates (Wang et al., 2013). By modeling coseismic landslide hazard expected from a 1700-like CSZ earthquake, we could better facilitate landslide mapping and dating efforts to confirm the triggering date of these landslides, and reciprocally gain further insight on the mechanisms and distribution of landslides triggered by large-magnitude subduction zone earthquakes.

3.6 Conclusions

Probabilistic coseismic landslide hazard analyses are presented for Seattle and Mercer Island for both a M9.0 Cascadia Subduction Zone earthquake, and the cumulative seismic hazard in Seattle for a 10% in 50-year exceedance threshold using a newly developed coseismic displacement model for large-magnitude subduction zone earthquakes. Coseismic landslide hazard is considered for two modes of failure, shallow translational slides, and deep rotational slides or slumps. Model verification, utilizing mapped landslides from the 2001 M6.8 Nisqually earthquake and recorded shaking intensities, shows close agreement between mapped coseismic landslides and predicted regions of hazard. Coseismic landslide hazard predictions in Seattle and Mercer Island were found to be highly susceptible to ground saturation conditions, with far greater portions of the cities exposed to potential landslides during wet, winter-like conditions. Results from this work represent the state of the art in regional-scale coseismic landslide hazard analysis and will be extended to the CSZ meizoseismal region across the PNW to assess potential landslide hazard and consequences due to a future M9.0 earthquake.

Acknowledgements

Financial support for this research was provided by the U. S. National Science Foundation under Grant No. 1331412. The opinions, findings, and recommendation expressed in this chapter are those of the author and do not necessarily reflect the views of these agencies. Large magnitude subduction zone earthquake ground records used in this research were compiled by Michael Greenfield. Synthetic ground motions were developed and provided by Erin Wirth-Moriarty, Arthur Frankel, Kate Allstadt, and Nasser Marafi. Alison Duvall and Sean LaHusen provided additional insight into the nature of landslides triggered in the Pacific Northwest.

References

Allstadt K, Vidale JE, Frankel AD (2013) A scenario study of seismically induced landsliding in Seattle using broadband synthetic seismograms. Bulletin of the Seismological Society of America. 103(6): 2971

Ambraseys, N.N., Menu, J.M., 1988. Earthquake-induced ground displacements. Earthquake Engineering and Structural Dynamics 16, 985–1006.

Atwater, B.F., Musumi-Rokkaku, S., Satake, et al. 2005. The orphan tsunami of 1700; Japanese clues to a parent earthquake in North America: Report U.S. Geological Survey Professional Paper 1707, 133

Brien, D. L., & Reid, M. E. (2008). Assessing deep-seated landslide susceptibility using 3-D groundwater and slope-stability analyses, southwestern Seattle, Washington. Reviews in Engineering Geology, 20, 83-101.

Department of Civil Engineering, University of Chile (2017) strong motion records accessed at http://terremotos.ing.uchile.cl/registros/164 (last accessed September, 2017).

Frankel, A.D. 2011. Summary of November 2010 Meeting to Evaluate Turbidite Data for Constraining the Recurrence Parameters of Great Cascadia Earthquakes for the Update of the National Seismic Hazard Maps, U.S. Geological Survey Open-File Report 2011–1310, 13 pp., http://pubs.usgs.gov/of/2011/1310/.

Frankel, A. (2017). Modeling Strong-Motion Recordings of the 2010 Mw 8.8 Maule, Chile, Earthquake with High Stress-Drop Subevents and Background Slip. Bull. of the Seis.l Soc. of America, 107(1), 372-386.

Goldfinger, C., Nelson, C.H., Johnson, J.E., et al., 2012. Turbidite event history—Methods and implications for Holocene paleoseismicity of the Cascadia subduction zone: Report U.S. Geological Survey Professional Paper 1661-F, 170 p

Gorum, T., Korup, O., van Westen, C. J., van der Meijde, M., Xu, C., & van der Meer, F. D. (2014). Why so few? Landslides triggered by the 2002 Denali earthquake, Alaska. Quaternary Science Reviews, 95, 80-94.

Gorum, T., & Carranza, E. J. M. (2015). Control of style-of-faulting on spatial pattern of earthquake-triggered landslides. International Journal of Environmental Science and Technology, 12(10), 3189-3212.

Grant, A., Wartman, J., & Abou-Jaoude, G. (2016). Multimodal method for coseismic landslide hazard assessment. Engineering Geology, 212, 146-160.

Greenfield, M. (2017) Effects of Long-duration ground motions on liquefaction hazards. Doctoral Thesis, University of Washington.

Harp, E. L., Michael, J. A., & Laprade, W. T. (2008). Shallow landslide hazard map of Seattle, Washington. Reviews in Engineering Geology, 20, 67-82.

Harp, E. L., Hartzell, S. H., Jibson, R. W., Ramirez-Guzman, L., & Schmitt, R. G. (2014). Relation of Landslides triggered by the kiholo bay earthquake to modeled ground motion. Bulletin of the Seismological Society of America, 104(5), 2529-2540.

Hill-Tout, C. (1978). Cowichan traditions of a great flood and earthquake, in R. Maud (editor), The Salish People: The Local Contribution of Charles Hill-Tout: The Sechelt and the South-Eastern Tribes of Vancouver Island, Vancouver: Talonbooks, 157-158.

Jibson RW (2007) Regression models for estimating coseismic landslide displacement. Engineering Geology, 91(2), 209-218

Jibson RW, Harp EL, Michael JA (2000) A method for producing digital probabilistic seismic landslide hazard maps. Engineering Geology 58, 271–289

Jibson, R. W., Harp, E. L., Schulz, W., & Keefer, D. K. (2004). Landslides triggered by the 2002 Denali Fault, Alaska, earthquake and the inferred nature of the strong shaking. Earthquake Spectra, 20(3), 669-691.

Jibson RW, Michael JA (2009) Maps showing seismic landslide hazards in Anchorage, Alaska: U.S. Geological Survey Scientific Investigations Map 3077, scale 1:25,000, 11-p. pamphlet

Kargel, J. S., Leonard, G. J., Shugar, D. H., Haritashya, U. K., Bevington, A., Fielding, E. J., ... & Anderson, E. (2016). Geomorphic and geologic controls of geohazards induced by Nepal's 2015 Gorkha earthquake. Science, 351(6269), aac8353.

Laprade, W. T., & Tubbs, D. W. (2008). Landslide mapping in Seattle, Washington. Reviews in Engineering Geology, 20, 37-54.

Lari, S., Frattini, P., & Crosta, G. B. (2014). A probabilistic approach for landslide hazard analysis. Engineering Geology, 182, 3-14.

Ludwin, R. S., Dennis, R., Carver, D., McMillan, A. D., Losey, R., Clague, J., ... & James, K. (2005). Dating the 1700 Cascadia earthquake: Great coastal earthquakes in native stories. Seismological Research Letters, 76(2), 140-148.

Keefer DK (2002) Investigating landslides caused by earthquakes–a historical review. Surveys in geophysics, 23(6), 473-510

Khazai B, Sitar N (2000) Assessment of seismic slope stability using GIS modeling. Geographic Information Sciences, 6(2), 121-128

Kramer SL, and Smith MW (1997) Modified Newmark model for seismic displacements of compliant slopes.'' J. Geotech. Geoenviron. Eng., 123 (7), 635 - 644

LaHusen, S., Duvall, A., Grant, A., Wartman, J. (2016). Assessing the Impact of Coseismic Landslides during the AD 1700 Cascadia Subduction Zone Megathrust Earthquake along the coastline of the Pacific Northwest (USA). GSA Annual Meeting, Denver

Laprade, W. T., & Tubbs, D. W. (2008). Landslide mapping in Seattle, Washington. Reviews in Engineering Geology, 20, 37-54.

Ludwin, R. S., Dennis, R., Carver, D., et al. (2005). Dating the 1700 Cascadia earthquake: Great coastal earthquakes in native stories. Seismological Research Letters, 76(2), 140-148.

Malamud, B. D., Turcotte, D. L., Guzzetti, F., & Reichenbach, P. (2004). Landslides, earthquakes, and erosion. Earth and Planetary Science Letters, 229(1), 45-59.

Mayorov, N. (2015) Robust nonlinear regression in scipy. Accessed at http://scipy-cookbook.readthedocs.io/items/robust_regression.html (November, 2017)

Matasovic, N., Kavazanjian, E., and Yan, L. (1997) Newmark deformation analysis with degrading yield acceleration. Proc., Geosyn. '97, Long Beach, Calif.
National Research Institute for Earth Science and Disaster Prevention in Japan (2017). Strong Motion records accessed at http://www.kyoshin.bosai.go.jp/ (last accessed September, 2017)

Newmark N, 1965. Effects of earthquakes on dams and embankments. Geotechnique 15, 139–160

Rathje, E. M., and Bray, J. D. (1999). An examination of simplified earthquake-induced displacement procedures for earth structures.'' Can. Geotech. J., Ottawa, 36, 72–87.

Rathje, E.M., Bray, J.D., 2000. Nonlinear coupled seismic sliding analysis of earth structures. Journal of Geotechnical and Geoenvironmental Engineering 126, 1002–1014.
Reid, M. E., Christian, S. B., Brien, D. L., & Henderson, S. (2015). Scoops3D—Software to Analyze Three-Dimensional Slope Stability Throughout a Digital Landscape. In Tech. Rep. US Geological Survey Techniques and Methods, book 14 (p. 218).

Saygili G, Rathje EM (2008) Empirical predictive models for earthquake-induced sliding displacements of slopes. Journal of Geotechnical and Geoenvironmental Engineering. 134(6), 790 - 803

Saygili, G., & Rathje, E. M. (2009). Probabilistically based seismic landslide hazard maps: an application in Southern California. Engineering Geology, 109(3), 183-194.

Shearer, P.M. (2009). Introduction to Seismology. Cambridge University Press. Chicago

Schulz, W. H., Galloway, S. L., & Higgins, J. D. (2012). Evidence for earthquake triggering of large landslides in coastal Oregon, USA. Geomorphology, 141, 88-98.
Seattle Public Utilities (2017) City of Seattle environmentally critical areas, including mapped landslides. https://data.seattle.gov/dataset/City-Of-Seattle-Environmentally-Critical-Areas/zwze-9nv3 (last accessed Nov. 2017)

Seed, H. B., and Martin, G. R. 1966 . "The seismic coefficient in earth dam design." J. Soil Mech. and Found. Div. 92 SM3, 25–58.

Selby, M.J. (1993) Hillslope materials and processes. Oxford: Oxford University Press.

Smith, J.B.; Baum, R.L.; Mirus, Benjamin B.; Michel, Abigail R.; Stark, Ben, 2017, Results of Hydrologic Monitoring on Landslide-Prone Coastal Bluffs Near Mukilteo Washington: U.S. Geological Survey Open-File Report 2017-1095, 50 p., http://dx.doi.org/10.3133/ofr20171095

Struble, W., Roering, J., Burns, W.J., et al. (2017) Propensity for Deep-Seated Landslides in the Oregon Coastal Ranges During Cascadia Megathrust Earthquakes Through Dendrochronological Dating of Landslide-Dammed Lakes. GSA Annual Meeting, Seattle.

Troost, K. G., & Booth, D. B. (2008). Geology of Seattle and the Seattle area, Washington. Reviews in Engineering Geology, 20, 1-36.

United States Geological Survey (2017) shakemap peak ground accelerations for the 2001 Nisqually earthquake last accessed Nov. 2017 at https://earthquake.usgs.gov/earthquakes/eventpage/uw10530748#shakemap

University of Nevada Reno Guerrero Accelerograph network (2017) strong motion accessed at http://www.strongmotioncenter.org/vdc/scripts/event.plx?evt=125 (last accessed September, 2017.)

Urzúa, A., & Christian, J. T. (2013). Sliding displacements due to subduction-zone earthquakes. Engineering Geology, 166, 237-244.

Wang, P. L., Engelhart, S. E., Wang, K., Hawkes, A. D., Horton, B. P., Nelson, A. R., & Witter, R. C. (2013). Heterogeneous rupture in the great Cascadia earthquake of 1700 inferred from coastal subsidence estimates. Journal of Geophysical Research: Solid Earth, 118(5), 2460-2473.

Wang, Y., & Rathje, E. M. (2015). Probabilistic seismic landslide hazard maps including epistemic uncertainty. Engineering Geology, 196, 313-324.

Wartman, J., Bray, J. D., & Seed, R. B. (2003). Inclined plane studies of the Newmark sliding-block procedure. Journal of Geotechnical and Geoenvironmental Engineering, 129(8), 673-684.

Wartman, J., Seed, R. B., & Bray, J. D. (2005). Shaking table modeling of seismically induced deformations in slopes. Journal of Geotechnical and Geoenvironmental Engineering, 131(5), 610-622.

Weisstein, Eric W. (2017) "Normal Distribution." From MathWorld--A Wolfram Web Resource accessed at http://mathworld.wolfram.com/NormalDistribution.html (last accessed September, 2017)

Wieczorek GF, Wilson RC, Harp EL (1985) Map showing slope stability during earthquakes in San Mateo County, California. U.S. Geological Survey Miscellaneous Investigations Map I-1257-e, scale 1:62, 500

Wirth, E. A., Frankel, A. D., & Vidale, J. E. (2017). Evaluating a Kinematic Method for Generating Broadband Ground Motions for Great Subduction Zone Earthquakes: Application to the 2003 Mw 8.3 Tokachi-Oki Earthquake. Bull. of the Seis. Soc. of America.

Xu X. (2012) Random fractal terrain generator, GitHub repository, https://github.com/qiao/fractal-terrain-generator

Xu, C., Shyu, J. B. H., & Xu, X. (2014). Landslides triggered by the 12 January 2010 Port-au-Prince, Haiti, Mw= 7.0 earthquake: visual interpretation, inventory compiling, and spatial distribution statistical analysis. Natural Hazards and Earth System Sciences, 14(7), 1789.

Chapter 4 – The impact of rockfalls on dwellings during the 2011 Christchurch, New Zealand, earthquakes

The content of this chapter was published in:

Grant, A., Wartman, J., Massey, C., Olsen, M. J., O'Banion, M., & Motley, M. (2017). The impact of rockfalls on dwellings during the 2011 Christchurch, New Zealand, earthquakes. *Landslides*, 1-12.

Abstract

Rockfalls and debris avalanches triggered by earthquakes during the 2010-2011 Canterbury earthquake sequence killed five people and caused an estimated US$400 million in damages. In total, about 200 dwellings were directly impacted by some of the ~6,000 rockfalls and debris avalanches that occurred across the Port Hills of Christchurch. This chapter presents the results of the analysis of a high-quality, database of 61 individual rockfall impacts on 29 dwellings in the Port Hills of Christchurch, New Zealand. Dwellings in the Port Hills are typically simple timber framed structures with wooden or unreinforced masonry cladding, comparable to most dwellings across New Zealand, North America, Australia, and elsewhere. Rockfall impacts on dwellings in this study were observed to follow a power-law relationship between kinetic energy and: (1) the runout distance into and through the dwelling; and (2) the impacted area within the dwelling. The results have been quantified and are presented as a "damage proportion," which is defined as the proportion of the area affected by an individual rock-block inside the dwelling divided by the total area of the dwelling. These data provide a fundamental input for rockfall risk analysis and will allow the losses from rockfall impacts to be better constrained.

4.1 Introduction

Rock-slope failures triggered by the moment magnitude (M_W) 6.2, 22 February 2011, Christchurch Earthquake and associated aftershocks resulted in five fatalities and caused ~US$400 million in damages to buildings and infrastructure (Dellow et al. 2011). In total, approximately 200 residential dwellings were impacted by some of the ~6000 rock-slope failures across the Port Hills area of Christchurch (Massey et al. 2014). Although a significant amount of research has been conducted on rockfall hazard and risk assessment (e.g., Cruden and Fell 1997; Leroi 2005; TRB 2012; Lee and Jones 2014; Wang et al. 2014), there has been relatively little work performed on the impacts of rockfalls on dwellings based on field observations and measurements from actual rockfall impacts. Some recent examples of such research are Finlay et al. (1999), Hollenstein (2005), and Corominas et al. (2014). The lack of information on the physical impacts of falling rocks on homes limits our ability to estimate the consequences to people and property (Galli and Guzzetti 2007), as construction details of homes vary between different regions and countries. For example, dwellings in Hong Kong (Finlay et al. 1999) are constructed of different materials to those in New Zealand (Massey et al. 2014). An enhanced understanding of how falling rocks impact homes of different construction materials would both advance quantitative risk assessment and enable improved mitigation and preparedness against losses in future rockfall events (Papathoma-Köhle et al. 2011).

While some previous studies provide numerical estimates of the consequences, typically expressed as "vulnerability"—defined as the degree of loss to a particular element at risk due to a natural phenomenon of a given magnitude (Varnes 1984) —that serve as inputs for risk analysis (e.g., Finlay et al. 1999; Bell and Glade 2004; AGS 2007), these values are rarely based on quantitative

measurements of actual impacts. Bell and Glade (2004) developed heuristic consequence classes for rockfall impacts on structures based on the magnitude (rock-block size) of rockfalls, adopting vulnerability classes ranging from 0.1 – 0.5, based on existing heuristic data for buildings struck by rockfall (e.g., Finlay et al. 1999; BUWAL 1999; Corominas et al. 2005). More recent research studying vulnerability of structures to rockfall and debris flow impacts (e.g., Galli and Guzzetti 2007; Agliardi et al. 2009; Jakob et al. 2012; Du et al. 2013) continue to rely on qualitative assessments of impact (following Cardinali et al. 2002, among others) to characterize the consequences, while refining quantitative measures of landslide intensity. Mavrouli and Corominas (2010a, 2010b) developed an analytically-derived vulnerability curve for reinforced concrete buildings based on numerical modeling of an empty concrete frame impacted by rocks of various sizes and velocities. Although quantitative, this analytic approach is only appropriate for simple concrete structures and does not capture the many softer elements (e.g., walls, furnishings, appliances, etc.) within dwellings that may significantly affect rock impact consequences.

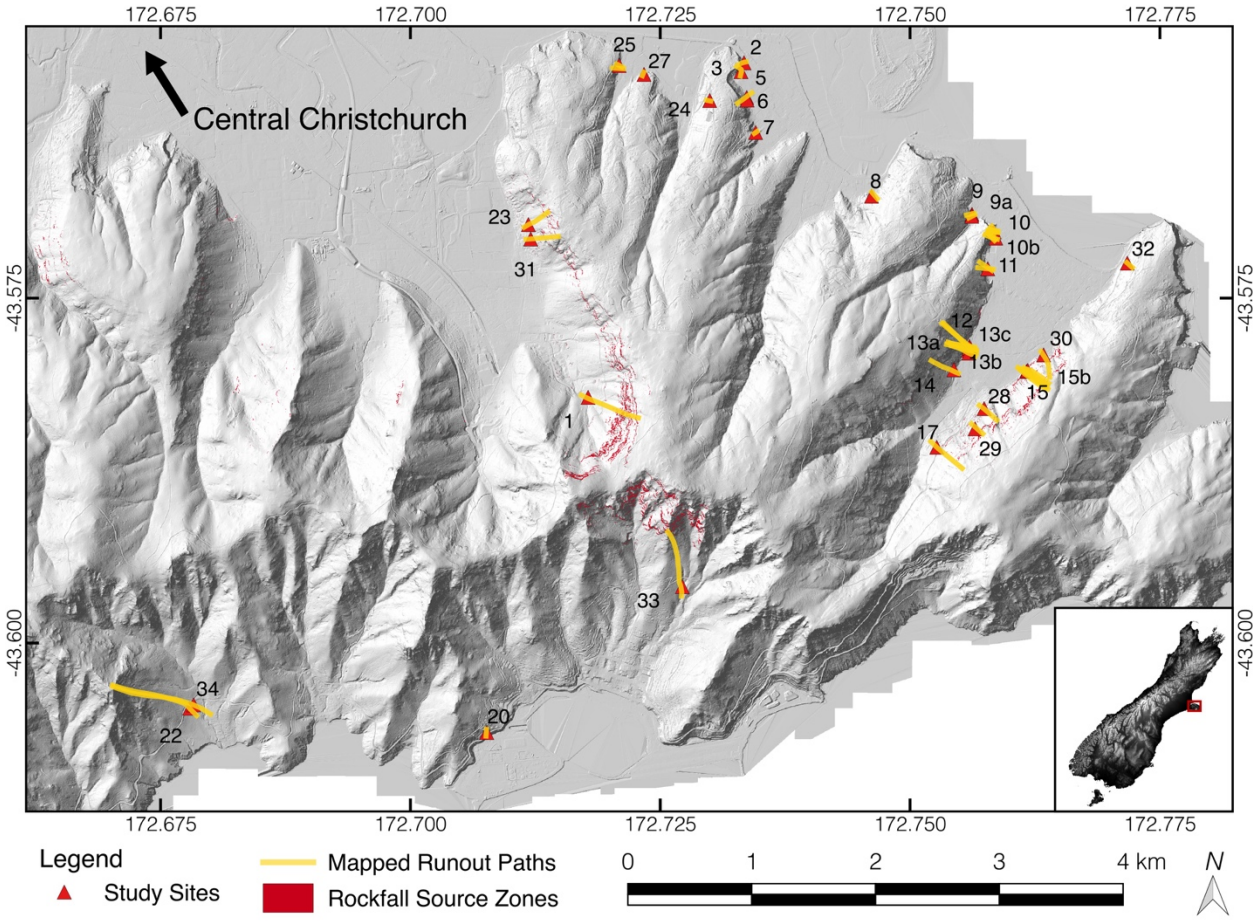

Figure 4.1 Port Hills of Christchurch, New Zealand showing dwellings impacted by rocks (study sites, blue triangles) used in this work, rockfall source zones (red regions), and mapped runout paths for all impacting rocks (yellow lines). Datum: New Zealand Transverse Mercator 2000

In this chapter, I present and analyze data describing the consequences of 61 rock impacts on 29 dwellings (study sites) located in the Port Hills of Christchurch, New Zealand (Fig. 4.1). These data were collected through field reconnaissance, terrestrial LiDAR scans, aerial LiDAR terrain analysis, and high-resolution image acquisition made between 2014 and 2015. The results provide a unique, high-quality database on the consequences of rockfall impacts on these dwellings. Dwellings in this database were primarily light timber-frame construction with and without unreinforced masonry facades. Such building materials and types are typical throughout New Zealand and many other regions including Australia, North America, and Japan, among others

(Arnold 2002; Maki and Tanaka 2002). For the 29 dwellings under study, the consequences of the rockfall impacts ranged from (1) minor "aesthetic" impacts to a dwellings cladding; (2) instances where rockfalls penetrated dwellings and came to rest within the structure; to (3) rockfalls that passed through the dwelling and continued to roll and bounce downslope (Fig. 4.2).

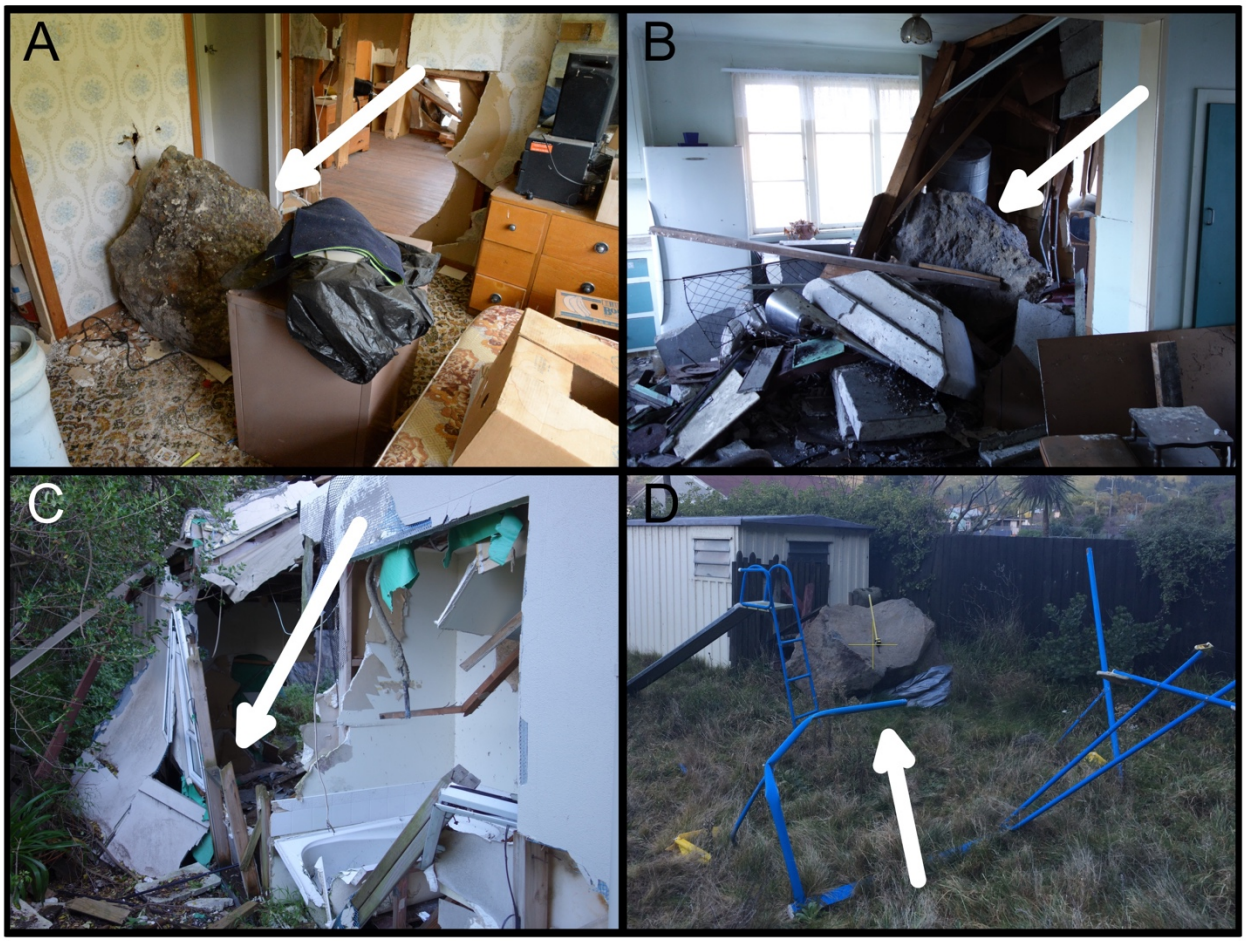

Figure 4.2 Examples of rockfall impacts on dwellings in the Port Hills of Christchurch. **a** and **b** two rock impacts on Site 22 affecting a total of three rooms causing significant damage. **c** and **d** a single rock impacts to sites 9a and 26 respectively that caused limited damage. **e** significant damages to Site 17 caused by a through-going rock. **f** rock impacting a corner of Site 1 causing exterior damages. Boxed annotations in each subfigure refer to impact classifications as described in Tables 1 and 2.

4.2 Study area

4.2.1 Earthquake and consequences

The M_W 6.2 22 February 2011, Christchurch earthquake occurred at 12:51 pm local time with a focal depth of 5 km below the Port Hills of Christchurch (Bradley and Cubrinovski, 2011). Peak horizontal and vertical ground accelerations recorded in the Port Hills region were typically in the range of 0.3– 0.9g but reached values as high as 1.4g (horizontal) and 2.2g (vertical) at the Heathcote Valley School station (Bradley and Cubrinovski 2011; Cubrinovski et al. 2011), located ~750 m northwest of Site 1 (Fig. 4.1). Short distances (Rupture Distance (R_{rup}) < 10 km) between the earthquake fault plane and rock fall sources and the high-frequency nature of ground motions in the Port Hills are thought to have been factors that resulted in a large number of rockfalls and landslides triggered in the region (Cubrinovski et al. 2011).

4.2.2 Geologic and geomorphic setting

The Port Hills are a series of loess-mantled ridges rising approximately 500 m above densely populated valleys. Local bedrock is composed of the Lyttleton Volcanic Group (Forsyth et al. 2008; Hampton 2010), a sequence of weathered Miocene basalt flows, which grade vertically and laterally to breccia, agglomerate, sandy tuff beds, and buried paleosols (Massey et al. 2014). The volcanic bedrock is overlain by wind-blown fine sandy silt (loess) and colluvium (reworked loess, and volcanic clasts) that is typically 1 m thick but varies locally to more than 5 m (Bell and Trangmar 1987). Both the volcanic bedrock and breccia are cliff-forming and are exposed in both isolated outcrops and continuous cliffs (formed from lava flows) that vary in height from a few meters to over 40 m tall (Massey et al. 2014). Both individual outcrops and continuous cliffs were identified as rockfall sources during the 22 February 2011, Christchurch Earthquake and other

earthquakes in the Canterbury sequence. The engineering geological descriptions of the rockfall sources and rock slope failure mechanisms are detailed in Massey et al. (2017).

4.3 Methods

4.3.1 Field reconnaissance methods

The research team collected data during three field reconnaissance visits (24 June – 1 July 2014; 1-2 November 2015; 3-4 December 2015). Field reconnaissance included characterization of the rockfall source area, trajectory (runout) and shape/volume, impact measurement and characterization of the structure impacted (Appendix C.) Each impacted dwelling served as a 'study site' for this case-history database and assigned a numeric identifier (e.g., "Site 1"), in some cases neighboring dwellings were added at a later date with an appended letter (e.g., Sites 13a, 13b, and 13c). Each impacting rock-block was then numbered to make distinctions between multiple impacts on a single study site (dwelling). The database includes only those dwellings whose post-earthquake damage conditions and features were well preserved and unambiguous. In most cases, these dwellings were "red-tagged" (dangerous to inhabit) and secured in the immediate aftermath of the earthquake sequence preventing residents from returning to their homes, which allowed us to capture in situ impact data after the rock impacts occurred. All impacting rocks were physically and or digitally measured using terrestrial laser scan (TLS) generated 3D point clouds or scaled images. Each rock block was assigned a shape classification of equant, flat, or long based on the shape criteria of Sneed and Folk (1958). The TLS surveys were carried out at 19 dwellings, and these data were used to augment physical observations, enabling mm- to cm-scale measurement precision of the fallen rocks, their impacts, and the structural elements of the

dwellings. Where possible, rock-block runout paths field-verified and geo-referenced using the mobile application *Theodolite* (Hunter Research and Technology 2016).

4.3.2 Impact measurement

Basic measurements of rock-block impacts on structures were made for each rock that hit a dwelling. The runout distance (R) into a dwelling was measured, which is defined as the shortest horizontal distance from the initial impact point (either an exterior wall or a roof) to the furthest point on the rock (away from the impact point). The area directly impacted (A_D) was then computed as:

$$A_D = R \times a \qquad \text{Equation 4.1}$$

where A_D is the plan area [m^2] through which the rock-block traveled or occupied within the dwelling and a is the maximum (principal axis) dimension of the rock-block.

At several sites, the rock-blocks upon entering a dwelling caused household objects and broken pieces of the dwelling structure (e.g., wood framing, cladding, and interior walls) to spread out from the area of direct impact (A_D), therefore affecting a larger plan area of the dwelling. To characterize this larger area of impact, the area of "scattered" debris (A_S) was measured in the field at the limited number of sites where scattered debris remained in place and undisturbed. This was based on the maximum extent of scattered debris around the point of entry into the dwelling for each rock, taking care not to confuse debris from shaking damage. Two areas of scattered debris were recorded: A_{S1}, comprising structural debris of timber framing, cladding (from external walls)

cabinets, and appliances, and A_{S2}, comprising non-structural debris such as plaster board, dishes, and other small and light household ornaments. A diagram depicting each of these impact measurements is shown in Fig. 4.3.

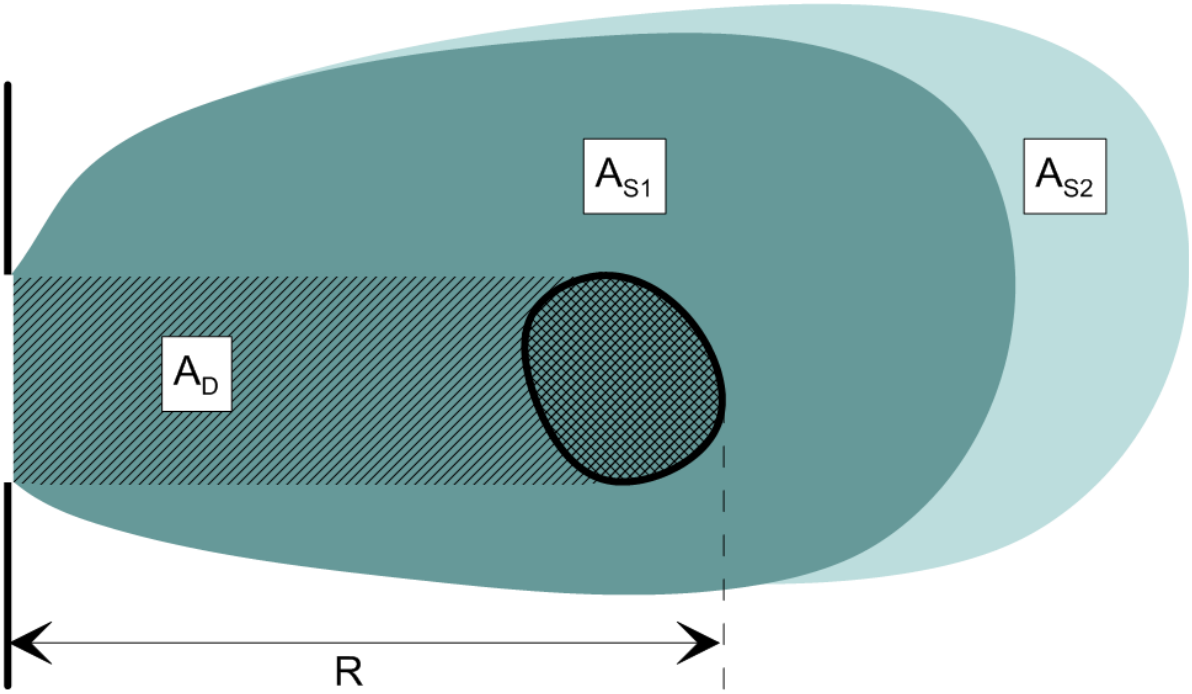

Figure 4.3 Plan view of an example rock impact showing runout distance into the dwelling (R). $\mathbf{A_D}$ area directly impacted by rock runout (hatched area). $\mathbf{A_{S1}}$ area of scattered debris for structural elements and large objects (dark green). $\mathbf{A_{S2}}$ area of scattered debris for interior household items (light green).

4.3.3 Dwelling characterization

Two classification systems were used to categorize the construction type, impacted materials, and location for each rock-block impact (note some dwellings were impacted by more than one rock-block.) First, a primary impact classification (Table 4.1) was assigned, based on dwelling construction and the impact location of the rock-block. These classes distinguish between sites where rocks would have encountered little resistance upon impact (aluminum roofing, windows, Fig. 4.2a-b, e; Figure 4.4) and more robust materials that would have served to absorb more energy (reinforced masonry, and cladded wood frames, e.g. Fig. 4.2c-d, f).

A secondary impact classification scheme was applied to describe the nature of interior household elements within dwellings that were struck by rocks (Table 4.2). Impact classes distinguish between rocks that did not strike interior objects before reaching their final stopping point, those striking minor (e.g., cabinets) or major (e.g., beds) furnishings, those striking or shearing interior walls or floors, and those rocks striking the corner of a dwelling (Table 4.2). In some instances, a dual classification was given for rocks; for example, at Site 17 a rock traveled partially through a window and then impacted an interior wall before shearing through flooring (Fig. 4.2e). This rock-block was assigned an impact classification of 1D-F (Tables 4.1 and 4.2).

Class	Location of impact and dominant structural element impacted
0	Windows or aluminum roofs with minimal timber framing
1	Mixed impacts (e.g., window and wood frame, door and wood frame)
2	Wood frames and unreinforced masonry
3	Reinforced masonry

Table 4.1 Primary impact classification scheme based on dwelling construction type and rock impact locations

Class	Household elements struck by rock-blocks
A	No impacts inside dwelling before resting point
B	Minor Furnishings (e.g., shelves, cabinets)
C	Significant appliances and furnishings (e.g., stoves, refrigerators, beds, sofas)
D	Interior Walls
E	Impact on exterior corner of dwelling
F	Shearing along interior flooring

Table 4.2 Secondary impact classification based on impact geometry and interior materials

Figure 4.4 Impact Classification examples. A, Site 9a: 2A. B, Site 26: 2B. C, Site 17: 1D-F. D, Site 1: 2E

4.3.4 Digital collection

LiDAR is a line-of-sight technology that allows for the digital preservation and analysis of high-resolution 3D point clouds that has been shown to be well suited to rockfall analysis (e.g., Abellán et al. 2014). Detailed terrestrial LiDAR surveys were completed for 19 sites between 24 June 2014 and 1 July 2014, as part of the initial reconnaissance effort. Multiple scans were taken both in and outside the dwellings to capture interior damage, the location and shape of the impacting rock-blocks, entry paths into the dwellings, and surrounding objects and topography. Where possible, scans were collected in a 360° sweeping pattern around impacted dwellings as well detailed scans inside the damaged portions of the dwellings. The scans were collected with a typical point

spacing of ~30 mm on the exterior of the dwellings, <10 mm in locations of significant damage, and ~50 mm for the surrounding terrain or structures. Global Navigation Satellite Systems (GNSS) were used to establish ground control points for geo-referencing the LiDAR scans. A total station linked the strategically placed scan targets to these ground control points as well as helped link exterior and interior scans. To ensure precise leveling for measuring wall and floor tilts, high accuracy (+/-0.008° 1-σ) inclination sensors built in the scanner were employed. The scans were registered in Leica Cyclone 9.1 using a combination of black and white pattern targets and cloud to cloud surface matching constraints. The relative accuracy of the scans was determined statistically from the registration residuals on common target matches between scan positions as well as differences observed between matching surface features within overlapping scans. From these registration results, the relative accuracy was found to be less than 8 mm (3D root mean square [RMS] error) and 4 mm (vertical RMS) at most sites. However, note that measurements (such as rock dimensions and extents of dwelling damages) would be expected to have higher (cm-level) uncertainty because of the additional uncertainty associated with extracting key points for measurements given the cm-level resolution of points on the surfaces. Point clouds developed from LiDAR surveys were then used for rock-block and dwelling damage measurements via manual point selection and measurement.

4.3.5 Runout path mapping

Georeferenced images acquired during the field reconnaissance visits (containing runout and impact trajectories) were combined with high-resolution (10 cm) aerial images and airborne LiDAR-derived digital elevation models (DEMs) to define the runout paths of individual rocks into the dwellings. Pre- and post-earthquake LiDAR change detection, along with field mapping

of rock slope failures were used to define the locations of the rockfall source areas (Massey et al., 2012), which were combined with reconnaissance data and high-resolution aerial images to reconstruct the precise source area and runout path for each rock-block that impacted a dwelling. The high-resolution aerial images, which were collected by New Zealand Aerial Mapping (NZAM) on 24 February 2011, provided a tight constraint on runout paths for large (>2 m^3) rocks where runout path damage was visible (Fig. 4.4). Two aerial LiDAR surveys, collected on 6-9 July 2003 and 8-10 May 2011, were differenced to determine rock-slope failure source areas from areas of elevation loss along steep (>45°) slopes. These were used to develop 1 m by 1 m bare-earth DEMs (in grid format) of the region, which were then differenced to identify changes in the landscape pre- and post- earthquake. Only those grid cells with slope angles ≥45˚ were used in the differencing. Rockfall runout paths for each rock block were extracted from the May 2011 DEM using the software code *QGIS* (QGIS Development Team 2016), to generate two-dimensional profiles along each rockfall runout path. These profiles were exported and used in the two-dimensional numerical rockfall simulations. (Fig. 4.5).

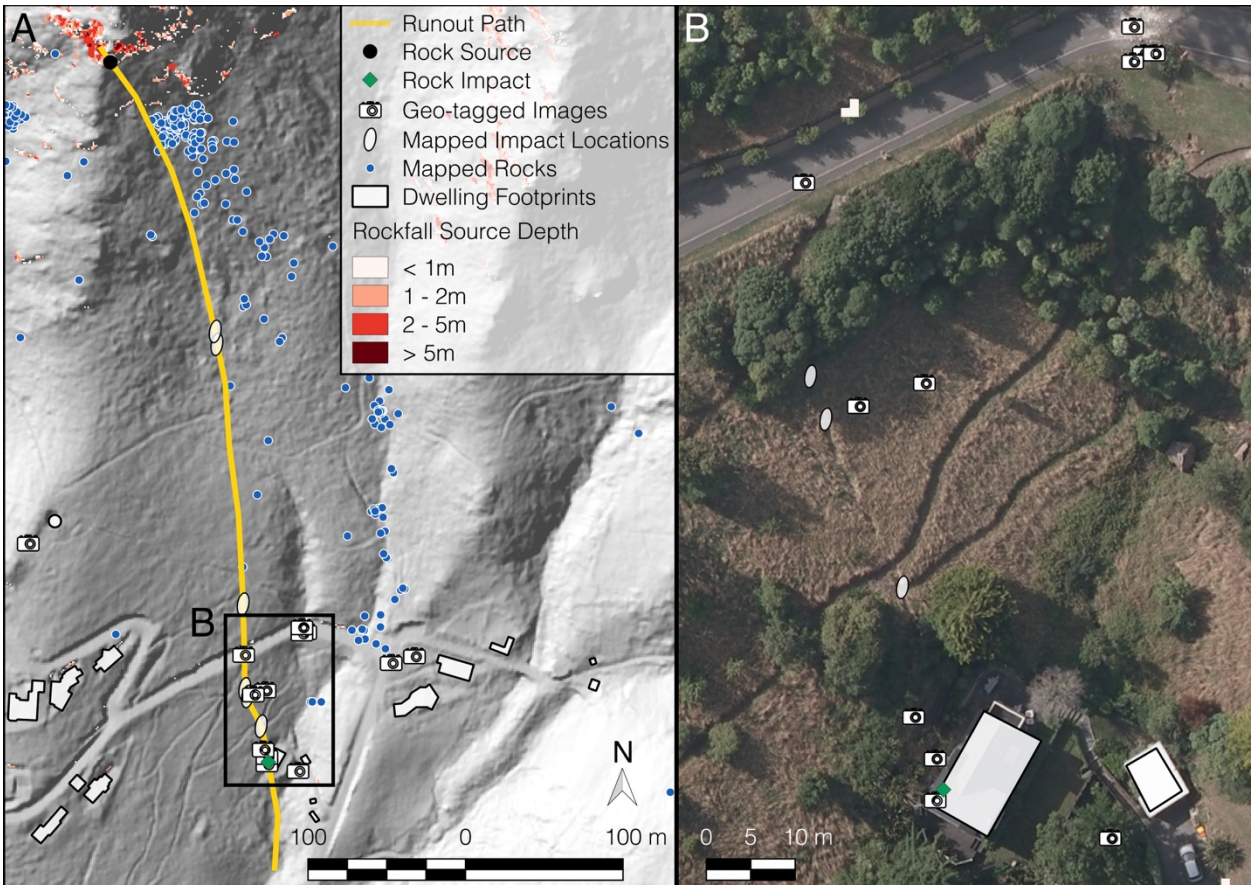

Figure 4.5 Example of runout modeling data availability for Site 33. **a** Runout path from source to dwelling impact location showing known hillslope impact locations, all other modern rockfall and local source areas. **b** Enlargement of Site 33 showing clearly visible runout path from areal images and locations of geo-tagged field reconnaissance photographs used to further constrain the runout path

Class	Rockfall impact data quality
1	Source unknown, no images, no change detection, runout path unclear
2	Source inferred, LiDAR/geomorphology only, no substantiating field data.
3	Source inferred, mapped from runout paths based on rock-block impacts on the slope and the geomorphology only. Source areas may be relatively uncertain (modeled sources 5-10m long)
4	Source mapped, and LiDAR change detection shows a single well-defined source and where the runout paths are visible in aerial photographs.
5	Source mapped, and LiDAR change detection shows a single well-defined source. Runout paths have been walked and mapped in the field and are clearly visible, including rockfall impact locations on the slope surface, in the aerial photographs.

Table 4.3 Those impacted dwellings where the rockfall data quality classes were 1 and 2 were omitted from the analyzed data set. Source zone location uncertainty ranged from 2 –10 m for level 3 sites, 1 – 5 m for level 4 sites, and was typically 1 m or less for level 5 sites

Rock impacts on dwellings were classified into five data quality levels (Table 4.3). These data quality levels were based on my ability to constrain the source area of each rockfall, the runout path, and any other available supporting data. For all analyses, I have omitted rock impacts that were deemed to be of low quality (i.e. levels 1-2) to ensure the results of this work were not governed by uncertainty in the inputs to impact energy back-analysis. Five dwellings impacted by more than ten rocks were removed from this analysis due to the high degree of uncertainty associated with the source areas and runout paths of each rock-block. Two additional dwellings were removed from the database as they were impacted by debris avalanches (comprising many rock-blocks), and not individual rock-blocks. Acceptable levels of data quality (3, 4, and 5), represent increasing certainty in the source area location and runout path (Table 4.3). Using this classification scheme, 27% (16) of the reported impacts are level 5, 34% (21) level 4, and the remainder (24) classified as level 3.

4.3.6 Runout analysis

I estimated kinetic energies at the point of impact for each rock striking a dwelling using the two-dimensional software RocFall 5.0 (RocScience 2016). RocFall uses a lumped mass, physics-based modeling approach to compute rock velocities and bounce heights for any point along a selected runout path based on a topographic profile. In this study, I adopted RocFall input parameters based on an independent analysis of unimpeded rock runout paths by Massey et al. (2012) for rockfalls triggered by the Canterbury earthquake sequence in the Port Hills (Table 4.4). These calibrated RocFall input parameters (coefficient of normal restitution *Rn*, coefficient of tangential restitution *Rt*, friction angle *Phi*, and roughness of the slope) based on the geomorphic mapping of Townsend and Rosser (2012) were used with mapped runout paths and impact locations to compute kinetic

energies at the point each of the mapped rock blocks impacts the structure. For each rockfall runout path, I simulated 10,000 rock blocks initiating from the field identified source point or region, and recorded the simulated translational and rotational velocity of each rock at the known point of impact with the dwelling. Model parameters and initial conditions for each rockfall simulation were adopted from Massey et al. (2012, see Appendix D) The velocity distribution of the simulated rock blocks at the point of impact was then used to compute a distribution of impact kinetic energy on each dwelling.

ID	Material	Rn	Rt	Phi	Roughness
A	Clean Hard Bedrock	0.53 ± 0.04	0.99 ± 0.04	40° ± 2	5
B	Talus with vegetation or surficial rock covered in part by talus	0.5 ± 0.04	0.85 ± 0.04	20° ± 2	5
C	Colluvial loess with rough vegetation	0.3 ± 0.03	0.85 ± 0.03	8° ± 2	11
D	Colluvial loess with smooth vegetation	0.3 ± 0.03	0.85 ± 0.03	4° ± 2	0
E	Asphalt (RocFall Default)	0.4	0.9	30	0

Table 4.4 Model parameters used for back-analysis of impact kinetic energy adopted from Massey et al. (2012) and geomorphic mapping of the Port Hills by Townsend and Rosser (2012).

An example runout profile with simulated rock paths and impact energies is presented in Appendix D. The total kinetic energy of an object can be expressed as the sum of the translational energy, as a function of its mass M and translational velocity V, and its rotational energy, as a function of its moment of inertia I and rotational velocity ω. Rock-block volumes were estimated as being 80% of the product of the three principal axes measured in the field to adjust for the irregularity of the rock shape. Rock masses were computed using unit weights of 27kN/m^3 for basalt and 18 kN/m^3 for Breccia (Massey et al. 2012). The simulated rocks were assumed to roll or bounce along the axis of minimum moment of inertia (I), which was computed assuming ellipsoidal rocks as:

$$I = \frac{M(b^2+c^2)}{5}$$ Equation 4.2

where a, b, and c are the measured maximum, secondary, and minimum principal dimensions of the rock, respectively and M is the mass of the rock-block (AISC, 2001).

Impact kinetic energies (KE) were then computed based on the measured dimensions and mass of each rock as:

$$KE = \frac{1}{2}(MV^2 + I\omega^2) \quad \text{Equation 4.3}$$

where M is the rock-block mass, V is its translational velocity, I is its moment of inertia, and ω is its rotational velocity. For rocks entering through the roof of a dwelling, the trajectory angle (θ) from vertical was measured from LiDAR scans, collected images, and the source and final resting location of the rock. To be consistent with my measurement of runout distance (R) for roof impacts, the horizontal component of kinetic energy was computed as:

$$KE_h = KE sin\theta \quad \text{Equation 4.4}$$

4.3.7 Impedance effect of dwellings on runout distance

Field observations of rockfall impacts within dwellings suggest that in some cases a dwelling can impede the overall runout distance of a rock-block. This is thought to be due to a reduction (damping) in the kinetic energy of the rock caused by its interaction with the dwelling structure (shearing through the floor) and household furnishings and appliances (e.g., sofas, refrigerators) as it travels through the dwelling. To estimate the impedance effect of dwellings on the runout distance I developed a set of modified runout profiles that isolate the effect of dwellings on the

simulated rockfall runout distance. I then compared the recorded rockfall runout distance into the dwellings (R) with the simulated rockfall runout. Modified profiles used in this analysis were identical to the runout profiles used for impact energy analysis based on the LiDAR DEM. The length of the profile occupied by the dwelling, downslope from the point of impact, was assumed to be flat, and the surface was given uniform material properties. This was done for each of the simulated profiles to remove profile-specific differences in the downslope morphology. Modified profiles were analyzed using 10,000 simulated rocks, and all other parameters remained unchanged. The modal runout distance of all simulated boulders downslope from the point of impact with the structure was recorded. The runout reduction caused by dwellings (Δ), was then computed as the difference between this modal unimpeded runout distance and the actual (measured) runout into the dwelling.

4.3.8 Dwelling loss due to rock impacts

Qualitative assessment of loss is often necessary due to the lack of economic or quantitative structural damage data required to perform a purely quantitative analysis. Fuchs et al. (2007) and Totschnig et al. (2011) used the ratio of the cost of repair to dwelling value as a direct measure of loss from debris flow impacts, while Mavrouli and Corominas (2010a, 2010b) proposed a building damage index based on the proportion of structural elements (e.g. reinforced concrete columns and beams) impacted by rockfall.

Information on economic losses due to rock impacts was not available for the dwellings in this study, which, as residential structures, lacked well-defined structural systems (i.e. steel or concrete framing). Indeed, observed damage to the dwellings was highly localized around individual rock

impacts, with little evidence of propagation through a structural system. Therefore, to construct a quantitative physical vulnerability curve for dwellings impacted by rocks, I defined the damage proportion (D) as the ratio of the area affected by a rock (A_D) to the total footprint area of the dwelling.

4.4 Results

This database contains 42 impacts to walls (and window systems) of dwellings and 19 impacts to roofs. Back-analyzed impact energies ranged from 0.15 kJ to 1412 kJ, with a median impact energy of 49 kJ. The volume of rocks ranged from 0.0015 m^3 to 14.4 m^3, with a median value of 0.26 m^3. Rockfall runout distances into dwellings ranged from ~0.01 m (minor impact where the rock failed to penetrate through the cladding and enter the dwelling) to complete dwelling penetrations (in the back and out the front) with final resting positions more than 75 m beyond the initial impact with the dwelling. The median runout distance was 2 m into a dwelling.

Fig. 4.6 shows both runout distance (R) (Fig. 4.6a) into dwellings and impact area (A_D) (Fig. 4.6b) as a function of kinetic energy. The error bars in Fig. 4.5 indicate +/- 1 standard deviation in the back-analyzed impact energy. Vertical error bars (uncertainty in measurement of consequences) are omitted from Fig. 4.6 as field and lidar measurement uncertainty is smaller than the displayed symbology for nearly all impacts (approx. 1 – 3cm). For external wall and window impacts, regression of the data using a power-law function reveals a strong correlation between kinetic energy and area impacted ($A_D = 0.023KE^{0.97}$, $R^2 = 0.84$), but a slightly weaker relationship between kinetic energy and runout distance ($R = 0.064KE^{0.75}$, $R^2 = 0.71$). Similarly, for roof impacts, we found a stronger relationship between kinetic energy and area impacted (A_D =

$0.10KE^{0.69}$, R^2 = 0.79) than for kinetic energy and runout distance (R =$0.35KE_h^{0.45}$, R^2 = 0.53). When combining the wall and roof impact data, I a found a strong correlation (A_D = $0.029KE^{0.92}$, R^2 = 0.82) between kinetic energy and area impacts, with slightly less correlation (R = $0.083KE^{0.72}$, R^2 = 0.68) between kinetic energy and runout distance. Overall, the data show that for an order of magnitude increase in impact energy, an 8-fold increase in impact area is expected while runout distance increased 5.5-fold over the same range.

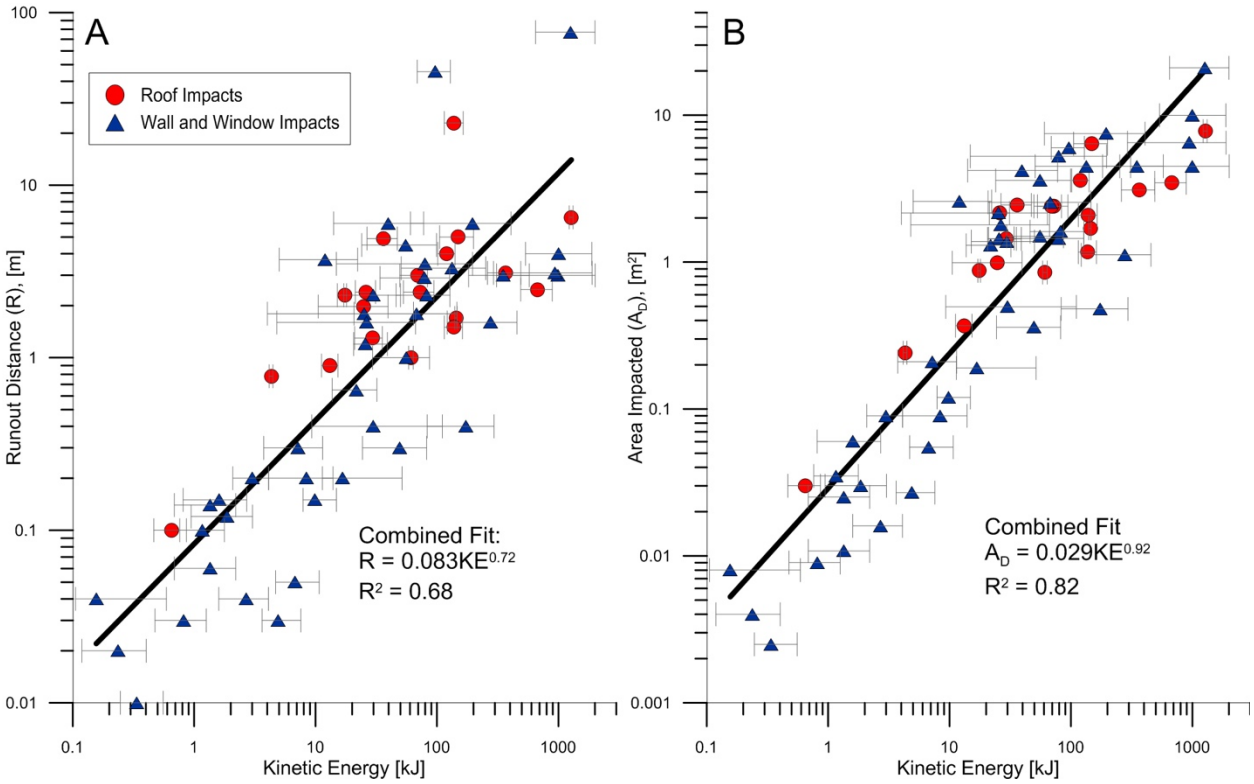

Figure 4.6 a Runout distance into dwellings as a function of kinetic energy. **b** area directly impacted by rocks as a function of kinetic energy. The three upper data points on the runout distance diagram (**a**) correspond to rock impacts that traveled through and beyond dwellings. Correlation equations for the disaggregated data are presented above in text. Error bars in the figures show +/- 1 standard deviation of impact kinetic energy

4.4.1 Area of scattered debris

Data describing the total area affected by both the rock and resulting scatter debris (A_D + A_S, Fig. 4.3) were collected for six dwellings whose interior damage patterns remained exceptionally well

preserved. Data on seven wall and nine roof impacts with scattered structural debris (A_{S1}) that ranged from 1.5 - 49 m^2 were collected. Areas impacted by scattered debris were normalized by the affected room dimensions to estimate the percentage of each room or rooms affected. Roof impacts, regardless of impact energy or rock size, created debris throughout almost all (90 – 100%) of rooms they impacted. Debris spread by wall impacts completely filled rooms in some instances (~90%), while having a significantly less spatial impact in others (20% - 60% of impacted room affected by debris). Overall, there is little sensitivity to the proportion of room(s) filled with scattered debris to rock size or impact energy (Fig. 4.7a). Non-structural scattered debris (A_{S2}) exhibits similar patterns of room filling and randomness for roof and wall impacts, respectively.

4.4.2 Rock-block shapes, structural class, primary impact, and dwelling impedance

Rock shape, classified as equant, flat, or long following Sneed and Folk (1958), was not found to significantly affect dwelling impact consequences. The majority (75%) of rocks in this study were roughly spherical or cubic (equant) and closely follow a power-law distribution of impact area with kinetic energy (Fig. 4.7b). Irregular rocks (flat and long) follow a similar trend to equant rocks but with more scatter, likely caused by the angle at which they entered the dwelling. Other rock and particle shape measurements, such as aspect ratio and Wadell sphericity (Wadell 1933) show a similar pattern of increased scatter for irregular rocks with no clear shift from the overall relationship between kinetic energy and impacted area or runout distance.

No significant relationship between primary and secondary impact classification (Tables 4.1 and 4.2) and impacted area or runout distance was observed (Fig. 4.7c). Where rocks entered dwellings partially through windows (primary impact class 1) slightly larger directly impacted areas (A_D)

were observed than comparable impacts in classes 2 and 3 (higher resistance wall impacts). Due to the limited number of observations (4) in this impact class, we cannot statistically express this difference, but it does follow intuitive sense that window points of entry would facilitate larger in-dwelling impacts than exterior walls. Rocks impacting dwellings through light aluminum roofing (class 0) did not exhibit statistically different areas directly impacted than rocks impacting exterior walls by my standardized metrics. Note roof impacts are measured from their point of entry, and not the rear of the dwelling, and in many cases affect portions of the dwelling further downslope than a comparable wall impact.

The modified profile analyses indicate that dwellings had a significant effect on runout distance (or "stopping power") as a function of median translational impact velocity (v) for wall and window impacts (Fig. 4.7d). The runout reduction caused by dwellings (Δ), computed as the difference between estimated and actual (measured) distance beyond impact follows a linear trend with translational velocity at impact:

$$\Delta = 1.71v - 3.24 \qquad \text{Equation 4.5}$$

Rocks impacting dwellings were not correlated with any of the impact measures considered in this work. No clear relationship between runout reduction and other impact measurements, such as momentum or kinetic energy, or rotational velocity were observed.

4.4.3 Damage proportion

Directly impacted areas (A_D) in dwellings ranged from 0.000025 m^2 to 21 m^2, with a mean value of 2.3 m^2, shown in Fig. 4.8. Dwellings included in this study ranged from 76 – 559 m^2 in area, resulting in an average damage proportion (D) of 0.0002 with a maximum of 0.16, per individual rock-block impact. For all impacts on dwellings, the observed damage proportion was found to follow a power-law relationship with impact energy:

$$D = 0.00019KE^{0.88} \qquad \text{Equation 4.6}$$

with a coefficient of determination (R^2) of 0.77. To ensure this relationship was not overly influenced by the one case of major damage (D = 0.16) in these data, we repeated this analysis without that data point and found virtually no change in the predicted power-law relationship between impact energy and observed damage proportion ($D = 0.0002KE^{0.88}$, $R^2 = 0.75$). Area of scattered debris, discussed above, were not included as "impacted areas" as I was not able to collect these data for all rock impacts considered in this study.

Damage proportions were found to be negligible (< 0.005) for all rock impacts of less than 10 kJ (Fig. 4.7). Above 10 kJ of impact kinetic energy, damage proportions for individual rock impacts range from ~ 0.001 – 0.16 with a mean of 0.02.

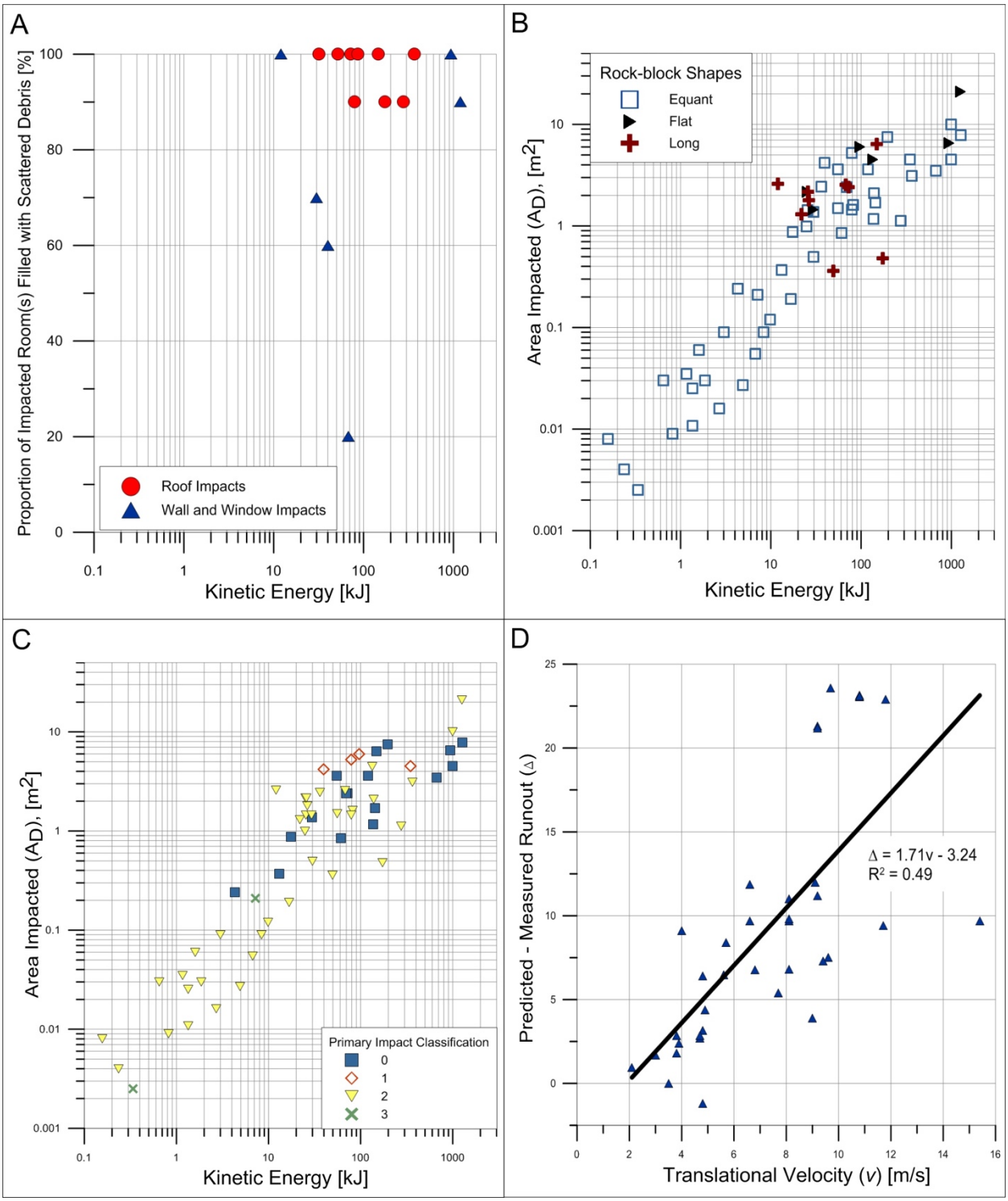

Figure 4.7 a Proportion of impacted rooms filled with structural or large household object scattered debris (A_{SI}). **b** Rock shape effects on impact area as a function of kinetic energy. **c** Primary impact classification effects on impact area. Symbols: 0 – Windows and aluminum roofs; 1 – Mixed Impacts (e.g., window and wood frame); 2 – wood frames and unreinforced masonry; and 3 – reinforced masonry. **d** Difference between predicted and measured runout distance as function of the median back-analyzed translational velocity at impact for all simulated rocks

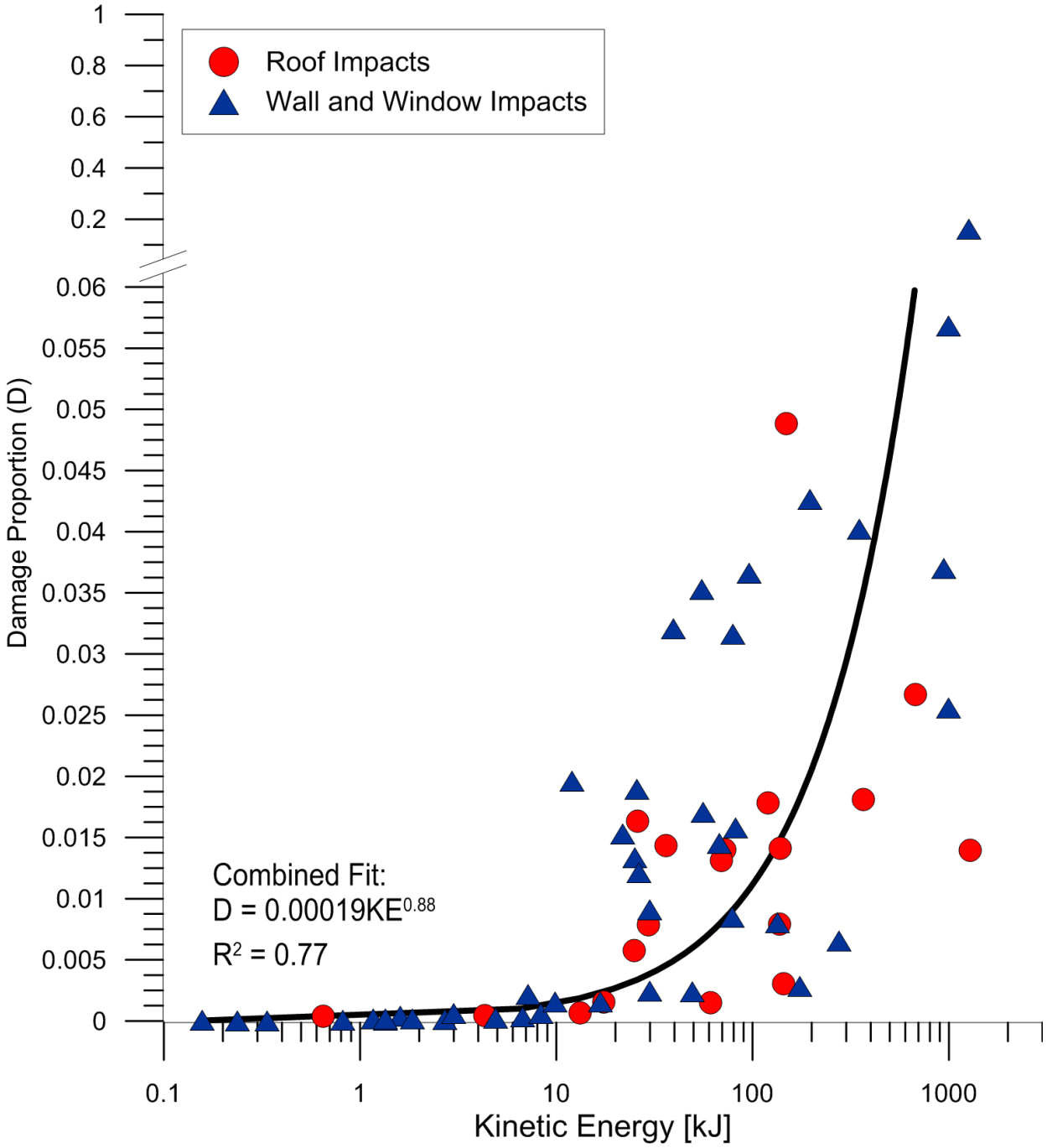

Figure 4.8 Damage proportion for dwellings in the Port Hills due to rock impacts as a function of kinetic energy. Damage proportion (D) is given the by the proportion of area directly affected by rock impacts (A_D) to the total footprint area of the dwelling

4.5 Discussion

The data presented in Fig. 4.6b indicate that areas directly impacted by rocks (A_D) are largely a function of kinetic energy (*KE*). Previous studies have found that rockfall source and debris characteristics such volume and rock shape can affect *unobstructed* runout distances (e.g. Corominas 1996; Dade and Huppert 1998; Okura et al. 2000; Leine et al. 2014). However, in this chapter no direct correlation between rock-block characteristics (volume and shape) and runout distance for rocks traveling into and *through* dwellings is found. I believe that variability in the in the A_D-KE relationship (Fig. 4.6b) is related to dwelling-specific damping factors involving collision and shearing through different types of hard (timber framing, flooring, and masonry) and soft materials (furnishings, appliances). Variability in the A_D-KE relationship may also result from differences in the relative location of rock impact (e.g. building corners tend to have more structural resistance than walls). While additional data collection, especially for irregularly shaped rocks and low-energy impacts, may further reduce uncertainty the A_D-KE relationship, rock trajectory and impact location are inherently stochastic and therefore difficult to predict in practice. Nevertheless, this data may be used to estimate A_D for similar timber-frame dwellings and structures in other settings and thus support quantitative rockfall risk assessment.

Fig. 4.8 presents the relationship between *D* and *KE*, which can be used in risk assessment analysis to help quantify the probability of a person being hit by a rock-block (provided they are present) and also the financial losses caused by rock impact to a dwelling. The results of this research also suggest that rock-blocks at impact kinetic energies of < 2 kJ are unlikely to penetrate more than 0.1 m into a dwelling, which are similar to the typical thickness of the timber framed wooden dwellings we studied. The data presented in Fig. 4.8 suggest a threshold may exist at ~10 kJ, a

kinetic energy below which very small ($D < 0.5\%$) portions of each dwelling were affected, but above which significant consequences are possible ($D > 5\%$). Data points in Fig. 4.7 lying to the right of the best fit (i.e. having high impact energies for relatively low damage proportions) were most likely shifted by vegetation effects along the runout path, which were not captured in these numerical simulations (Perret et al. 2004). The coefficients of restitution used in my simulations were developed for unimpeded rockfall runouts. However, many of these high energy, low impact rock-blocks travelled through thick brush and trees located directly behind each dwelling (and the point of rockfall impact) not observed at other locations, and therefore the kinetic energy associated with these rock-blocks is likely to have been lower than the values derived from these simulations.

4.6 Conclusions

Currently, few rockfall risk assessments have been based on quantitative impact analysis using case-study data. This research presents the results of the analysis of a high-quality, database of 61 individual rockfall impacts on 29 dwellings in the Port Hills of Christchurch, New Zealand. Dwellings in the Port Hills are typically simple timber framed structures with wooden or unreinforced masonry cladding, and they are comparable to most dwellings in New Zealand, North America, Japan, Australia, and elsewhere. Rockfall impacts on the dwellings in this chapter were observed to follow a power-law relationship between kinetic energy and: (1) the runout distance into and through the dwelling; and (2) the impacted area within the dwelling. Rock-block shape or the location of where the rock struck the dwelling did not appear to be driving factors in observed impacts. The variability in observed consequences (rock runout and area impacted) due to rock impacts on dwellings is primarily accounted for by back-analyzed impact kinetic energy. The

results have been quantified and are presented as a "damage proportion," which is defined as the proportion of the area affected by an individual rock-block inside the dwelling divided by the total area of the dwelling. These data provide a fundamental input for rockfall risk analyses and will better constrain future estimates of loss from rockfall impacts.

Acknowledgements

Financial support for this research was provided by the U.S. National Science Foundation under grants Nos. 1439773 and 1439883. Any opinions, findings, and conclusions or recommendations expressed in this material are those of the authors and do not necessarily reflect the views of the National Science Foundation. The authors also acknowledge the support of Leica Geosystems, David Evans and Associates, and Maptek I-Site in providing equipment and software used in this study. Lisa Dunham (UW) and Patrick Burns (OSU) assisted with the field effort. Catherine Burchard (OSU) and Jenny DiGiulio (OSU) assisted with processing the terrestrial lidar datasets. David Hanson (UW) and John Henderson assisted with processing the visual images. C. Massey's research was supported by the Natural Hazards Research Platform (New Zealand), Landslide Hazards Programme.

References

Abellán A, Jaboyedoff M, Oppikofer T, Rosser NJ, Lim M, Lato, M (2014) State of science: terrestrial laser scanner on rock slopes instabilities. Earth Surf Process Landf 39 (1):80–97

Agliardi F, Crosta GB, Frattini P (2009) Integrating rockfall risk assessment and countermeasure design by 3D modelling techniques. Nat Hazards and Earth Syst Sci 9(4):1059

American Institute of Steel Construction Manual Committee (2001) Load and resistance factor design: manual of steel construction. 3rd Edition. Published by American Institute of Steel Construction, USA

Arnold C (2002) Wood Frame Single Family House. World Housing Encyclopedia (www. worldhousing. net). Earthquake Engineering Research Institute and International Association for Earthquake Engineering, USA/Report, 65

Australian Geomechanics Society (2007) Practice note guidelines for landslide risk management. J and News of the Australian Geomechanics Society 42, 63–114

Bell R, Glade T (2004) Quantitative risk analysis for landslides? Examples from Bíldudalur, NW-Iceland. Nat Hazards and Earth Syst Sci 4(1):117-31

Bell DH, Trangmar BB (1987) Regolith materials and erosion processes on the Port Hills, Christchurch, New Zealand. In Fifth International Conference and Field Workshop on Landslides, Christchurch, New Zealand, Aug., 1987

Bradley BA, Cubrinovski M (2011) Near-source strong ground motions observed in the 22 February 2011 Christchurch earthquake. Seismological Research Letters Nov 1;82(6):853-65

Bundesamt für Umwel, Wald, und Landschatf (1999) Risikoanalyse bei gravitativen Naturgefahren, Fallbeispiele und Daten. Umwelt-Materialien Nr, 107

Cardinali M, Reichenbach P, Guzzetti F, Ardizzone F, Antonini G, Galli M, Cacciano M, Castellani M, Salvati P (2002) A geomorphological approach to the estimation of landslide hazards and risks in Umbria, Central Italy. Nat Hazards and Earth Syst Sci 2(1/2):57-72

Corominas J (1996) The angle of reach as a mobility index for small and large landslides. Canadian Geotech J, 33(2):260-271

Corominas J, Copons R, Moya J, Vilaplana JM, Altimir J, Amigó J (2005) Quantitative assessment of the residual risk in a rockfall protected area. Landslides 2(4):343-57

Corominas J, Van Westen C, Frattini P, Cascini L, Malet JP, Fotopoulou S, Catani F, Van Den Eeckhaut M, Mavrouli O, Agliardi F, Pitilakis K (2014) Recommendations for the quantitative analysis of landslide risk. Bull of Eng Geol and the Environ 73(2):209-63

Cruden D, Fell R (1997) Landslide Risk Assessment. Proceedings of the International Workshop on Landslide Risk Assessment, Honolulu, Hawaii, USA. 19-21 Feb., 1997

Cubrinovski M, Bradley B, Wotherspoon L, Green R, Bray J, Wood C, Pender M, Allen J, Bradshaw A, Rix G, Taylor M (2011) Geotechnical aspects of the 22 February 2011 Christchurch earthquake. Bull of the New Zealand Society for Earthq Engineering 44(4), 205-226

Dade WB, Huppert HE (1998) Long-runout rockfalls. Geology 26(9):803-6

Dellow G, Yetton M, Massey C, Archibald G, Barrell DJ, Bell D, Bruce Z, Campbell A, Davies T, De Pascale G, Easton M (2011) Landslides caused by the 22 February 2011 Christchurch

earthquake and management of landslide risk in the immediate aftermath. Bull of the New Zealand Society for Earthq Engineering 44(4):227-38

Du J, Yin K, Nadim F, Lacasse S (2013) Quantitative vulnerability estimation for individual landslides. In 18th International Conference on Soil Mechanics and Geotechnical Engineering, 2181-2184, Paris, 2013

Finlay PJ, Mostyn GR, Fell R (1999) Landslides: Prediction of travel distance and guidelines for vulnerability of persons. In Proceedings 8th Australia New Zealand Conference on Geomechanics: Consolidating Knowledge: 105

Forsyth PJ, Barrell DJ, Jongens R (2008) Geology of the Christchurch Area, Institute of Geological & Nuclear Sciences 1: 250000 geological map 16. Lower Hutt, New Zealand

Fuchs S, Heiss K, Hübl J (2007) Towards an empirical vulnerability function for use in debris flow risk assessment. Nat Hazards and Earth Syst Sci 7(5):495-506

Galli M, Guzzetti F (2007) Landslide vulnerability criteria: a case study from Umbria, Central Italy. Environmental management 40(4):649-65

Hampton SJ (2010) Growth, Structure, and Evolution of the Lyttelton Volcanic Complex, Banks Peninsula, New Zealand, Ph.D. Thesis, University of Canterbury, Christchurch, NZ

Hollenstein K (2005) Reconsidering the risk assessment concept: Standardizing the impact description as a building block for vulnerability assessment. Nat Hazards and Earth Syst Sci 5(3):301-7

Hunter Research and Technology (2016) Theodolite (Version 5.0) [Mobile Application Software] Retrieved from http://itunes.apple.com

Jakob M, Stein D, Ulmi M (2012) Vulnerability of buildings to debris flow impact. Nat Hazards 60(2):241-61

Lee ME, Jones DKC (2014) Landslide risk assessment. 2nd Edition. Published by the Institute of Civil Engineering, UK

Leine RI, Schweizer A, Christen M, Glover J, Bartelt P, Gerber W (2014) Simulation of rockfall trajectories with consideration of rock shape. Multibody Syst Dyn. 32(2):241-71

Leroi, E (2005) Global rockfalls risk management process in 'La Désirade 'Island (French West Indies). Landslides 2(4):358-365

Maki N, Tanaka S (2002) Single-family wooden house, World Housing Encyclopedia (www.db.world-housing.net). Earthquake Engineering Research Institute and International Association for Earthq Engineering, USA/Report, 86

Massey CI, McSaveney MJ, Lukovic B, Heron D, Ries W, Moore A, Carey J (2012) Canterbury earthquakes 2010/11 Port Hills slope stability: life-safety risk from rockfalls (boulder rolls) in the Port Hills. GNS Science Consultancy Report 2012/123

Massey CI, McSaveney MJ, Taig T, Richards L, Litchfield NJ, Rhoades DA, McVerry GH, Lukovic B, Heron DW, Ries W, Van Dissen RJ (2014) Determining rockfall risk in Christchurch using rockfalls triggered by the 2010–2011 Canterbury earthquake sequence. Earthq Spectra 30(1):155-81

Massey C, Della Pasqua F, Holden C, et al. (2017) Rock slope response to strong earthquake shaking. Landslides 14: 249. doi:10.1007/s10346-016-0684-8

Mavrouli O, Corominas J (2010a) Vulnerability of simple reinforced concrete buildings to damage by rockfalls. Landslides 7(2):169-80

Mavrouli O, Corominas J (2010b) Rockfall vulnerability assessment for reinforced concrete buildings. Nat Hazards and Earth Syst Sci 10(10):2055

Okura Y, Kitahara H, Sammori T, Kawanami A (2000) The effects of rockfall volume on runout distance. Eng Geol 58(2):109-24

Papathoma-Köhle M, Kappes M, Keiler M, Glade T (2011) Physical vulnerability assessment for alpine hazards: state of the art and future needs. Nat Hazards 58(2):645-80

Perret S, Dolf F, Kienholz H (2004) Rockfalls into forests: analysis and simulation of rockfall trajectories—considerations with respect to mountainous forests in Switzerland. Landslides 1(2):123-30

QGIS Development Team (2016) QGIS Geographic Information System. Open Source Geospatial Foundation Project. http://www.qgis.org/

Rocscience Inc. (2016) RocFall-computer program for risk analysis of falling rocks on steep slopes. Version 5.0. Toronto

Sneed ED, Folk RL (1958) Pebbles in the lower Colorado River, Texas a study in particle morphogenesis. The J of Geology 66(2):114-50

Totschnig R, Sedlacek W, Fuchs S (2011) A quantitative vulnerability function for fluvial sediment transport. Nat Hazards 58(2):681-703

Townsend DB, Rosser B (2012) Canterbury Earthquakes 2010/2011 Port Hills slope stability: Geomorphology mapping for rockfall risk assessment. GNS Science Consultancy Report. 2012;15

Transport Research Board (2012) Rockfall characterization and control. Turner KE, Schuster RL (editors) Transport Research Board miscellaneous publication

Varnes DJ (1984) Landslide hazard zonation: a review of principles and practice. UNESCO Press, Paris 63 pp.

Wadell H (1933) Sphericity and roundness of rock particles. The Journal of Geology 41(3):310-31.

Wang X, Frattini P, Crosta GB, Zhang L, Agliardi F, Lari S, Yang Z (2014) Uncertainty assessment in quantitative rockfall risk assessment. Landslides 11(4):711-22

Chapter 5: Conclusions and Future Research

Coseismic landslide hazard and the analysis of earthquake-induced landslide inventories should consider multiple modes of landslide failure, as presented in Chapters 1, 2, and 3. Coseismic landslides have been observed to occur in a wide range of mechanistically-distinct modes of failure (e.g. Keefer, 1984; Rodríguez et al., 1999; Bommer and Rodríguez, 2002; Dai et al., 2011; Wartman et al., 2013). A multimodal approach to coseismic landslides facilitates the application of more appropriate assumptions about failure mechanisms (Chapters 1 & 3), clarifies observed relationships with causal factors in landslide inventories (Chapter 2), and improves future risk analyses by disaggregating consequences by landslide type (Chapters 2 & 4).

In Chapter 1, I presented a new multimodal landslide hazard assessment methodology that considers four common modes of coseismic failure: rock-slope failures, disrupted soil slides, coherent rotational slides, and lateral spreads. Susceptibility to a specific landslide mode was determined by topographic slope, which is shown to correspond closely with observed landslide activity across Lebanon. Geotechnical models specific to each mode of failure were then used to assess stability and estimate coseismic displacements based on probabilistic or deterministic seismic scenarios. Across Lebanon, field verification of ~30 sites showed close agreement between the landslide susceptible terrain and hazard mapping, and the expected seismic performance of slopes. Direct applications of this work to coseismic landslide risk are underway in Lebanon, where mode-specific runout modeling and consequences are being assessed for permanent populations, Syrian refugee settlements and camps, and infrastructure.

Over 3,500 landslides triggered by the 2011 M9.0 Tohoku, Japan earthquake were mapped and analyzed in Chapter 2. Lateral spreads and flow slides were found to occur predominantly in anthropogenically modified portions of the landscape and drove observed consequences. Debris slides (alternatively shallow translational slides or disrupted soil slides), often considered the dominant mode of coseismic landslides, made up just half of the observed landslides, and were primarily triggered in natural terrain, leading to a disproportionately small impact to the built environment. Driven by differences in triggered modes of landslides, and the heavy influence of anthropogenic modification, commonly observed relationships for landslide concentration triggered by shallow crustal earthquakes (e.g., sharply increasing landslide concentration with peak ground acceleration, slope, or decreasing concentration with distance from faulting) were not observed. A physically-based landslide likelihood framework, based on quantitative estimates of resisting and triggering forces, was developed to explain the distribution of mapped coseismic landslides, of all modes, triggered by the Tohoku earthquake. This physically-based framework was then verified using an independently mapped coseismic landslide inventory from the M6.6 Iwaki earthquake within the Tohoku landslide study region, finding a nearly identical distribution of landslide concentrations strongly correlated to k_y/PGA, the ratio of a slope's yield acceleration to peak ground acceleration loading, suggesting that coseismic landslide concentrations are better and more universally described with classical slope stability analysis frameworks than single-variate correlations such as distance from the seismic source (e.g. Marc et al., 2016).

In Chapter 3, a new model to predict expected sliding-block displacements during large magnitude (M8 – M9) subduction zone earthquakes was presented to facilitate the extension of the multimodal coseismic landslide hazard modeling to the Pacific Northwest. Utilizing a suite of

synthetic M9.0 CSZ earthquakes (Frankel et al., *in review*) probabilistic coseismic landslide hazard estimates were made for the cities of Seattle and Mercer Island. These analyses, incorporating heterogeneities in material strengths and ground saturation conditions (Smith et al., 2017), different modes of landslide failure, and multiple seismic inputs, reflect the state of the art in regional-scale probabilistic coseismic landslide hazard analyses. Coseismic landslide hazard predictions were verified against mapped landslides triggered by the 2001 M6.8 Nisqually earthquake which coincided or are in close proximity to the very limited extent of predicted landslide hazard zones.

While probabilistic estimates of coseismic landslide hazard for a M9.0 CSZ earthquake show the potential for limited (dry) or widespread (wet) landslides throughout Seattle, projected coseismic landslide probabilities and extents are far greater for a M7.0 Seattle Fault earthquake, due to intense near-source ground motions. Results from these three earthquake source scenarios, Nisqually, Seattle Fault, and CSZ, allow for a direct comparison of conditional landslide occurrence probabilities (hazard) to assess their relative impact on Seattle, while their combination into a probabilistic coseismic landslide hazard analysis highlights portions of the city most susceptible to future coseismic landslide occurrence for the two considered landslide types.

Currently, few rockfall or landslide risk assessments have been based on quantitative impact analysis using case-study data. Chapter 4 presents the results of the analysis of a high-quality database of 61 individual rockfall impacts on 29 dwellings in the Port Hills of Christchurch, New Zealand that can be used to develop empirical physical vulnerability curves for risk analyses. Dwellings in the Port Hills are typically simple timber-framed structures with wooden or

unreinforced masonry cladding, and they are comparable to most dwellings in New Zealand, North America, Japan, Australia, and elsewhere. Rockfall impacts on the dwellings in Chapter 4 were observed to follow a power-law relationship between kinetic energy and: (1) the runout distance into and through the dwelling; and (2) the impacted area within the dwelling. Results were quantified presented as a "damage proportion," which was defined as the proportion of the area affected by an individual rock-block inside the dwelling divided by the total area of the dwelling. These data provide a fundamental input for rockfall risk analyses and will better constrain future estimates of loss from rockfall impacts.

Future Research

The complexities of forecasting the initiation, distribution, type, and ultimately risk posed by coseismic landslides has resulted in reliance on relatively rudimentary physical models over regional scales. While the work presented here provides critical improvements to these regional scale coseismic landslide hazard models, a number of critical issues remain.

All geological and geotechnical analyses are limited by our ability to characterize and implement heterogeneities of natural materials into our models. In regional-scale coseismic landslide hazard modeling, homogeneous material strength inputs and depth to failure inputs are typically adopted in the absence of more spatially detailed information. Even relatively small variations in strength can have an outsized effect on predicted landslide stability, and real zones of weakness in and around population centers could have dramatic risk implications for coseismic landslides. The goal of this research should be to better understand meso-scale (~0.1 – ~10km) heterogeneities of natural materials, and predict their spatial extents for the application of hazard and risk analyses

based on the correlation on readily available geospatial data (lidar-derived roughness, kilometer-scale average slope, etc.) with spatially-distributed field and laboratory measurements of strength.

The models presented here, and elsewhere, for coseismic landslide hazard are static, produced once for a single (or probabilistic) set of assumed parameters and conditions. As shown in Chapter 3, predicted coseismic landslide hazard is far greater for wet winter-like conditions than dry summer-like ground saturation. Current live precipitation-induced landslide models (Kirschbaum et al., 2015) should ultimately be coupled to rapid (e.g. Godt et al., 2008) or forecasting (e.g. Chapter 3) coseismic landslide models to provide realistic estimates of not only scenarios (Chapters 1 and 3), but current and near-future dynamic conditions. Post-fire dynamic vegetation and increased mobility modeling (e.g. Staley et al., 2015) could also be incorporated into 'live' coseismic landslide hazard prediction based on empirical data on temporal changes in root cohesion post fire or intensive logging (e.g. Schmidt et al., 2001).

Debris slide data from the Tohoku, Japan earthquake suggests a relationship between the age of parent material and the effect, strengthening or weakening, of anthropogenic modification. Future research, utilizing the newly-developed global coseismic landslide inventory (Tanyaş et al., 2017) and inventories of precipitation-induced landslides (e.g. Kirschbaum et al., 2016), should investigate potential strength modification between unmodified and modified hillslopes where landslides occurred. Research linking regionally-available anthropogenic proxies (e.g. distance to roadways) to potential modification-strength change relationships are also necessary to make any future findings applicable to coseismic landslide studies.

Newmark sliding block displacements for in-basin synthetic ground motions were observed to be greater than outside-of-basin synthetics or recorded data for equivalent 'hillslopes'. Further examination of these data, including coupled/decoupled dynamic analyses for compliant systems and 2/3D dynamic numerical modeling of slope deformation, should be conducted to examine the expected effects of basin ground motions on more complex landslide systems. These numerical findings should be substantiated with a detailed site-specific set of analyses of landslides triggered by similar earthquakes (e.g. Tohoku) both inside and outside of deep sedimentary basins to determine if the observed increase in sliding block displacements from simulations corresponds with increased triggering, or deformation of coseismic landslides.

Rockfall vulnerability data developed in Chapter 4 is applicable to many regions where timber-frame structures/dwellings are exposed to future rock impacts from seismic or aseismic sources. Expanding development along the Wasatch front in Utah, or Yosemite National Park (3.7M visitors per year, NPS, 2017) provide two candidate sites, in addition to work in Christchurch and Wellington, NZ, for new or improved quantitative risk assessments. Such quantitative risk assessments will enable decisions about zonation where risk to life are unacceptably high, and/or mitigation efforts to reduce predicted losses to life and property, and can be repeated in many regions.

Probabilistic coseismic landslide hazard for the Pacific Northwest, based on the collection of material strength properties from published reports and additional field reconnaissance and synthetic M9.0 CSZ earthquake ground motions, must be predicted to better prepare for the next great CSZ earthquake. Particular attention should be paid to coastal regions where the interaction

between primary and secondary earthquake hazards (shaking, landslides and tsunamis) will play a critical role in the survival of exposed populations. For example, understanding which tsunami evacuation routes are most susceptible to destruction due to shaking and landslide damage, and either reinforcing or abandoning high-susceptibility routes, will be critical to reducing losses during the next CSZ earthquake. In collaboration with researchers seeking to develop an inventory of landslides triggered by the 1700 CSZ earthquake (e.g. LaHusen et al., 2016; Struble et al., 2017), verification of the landslide models presented here, and additional modes of coseismic landslide failure should be made. Recent synthetic earthquake modeling (Wirth et al., 2017) suggests that a reasonable estimate of the January 26, 1700, ~M9 CSZ earthquake could be developed by matching 1700 coseismic coastal subsidence estimates (Wang et al., 2013). By modeling coseismic landslide hazard expected from a 1700-like CSZ earthquake, we could better facilitate landslide mapping and dating efforts to confirm the triggering date of these landslides, and reciprocally gain further insight on the mechanisms and distribution of landslides triggered by large-magnitude subduction zone earthquakes. Ultimately improving our ability to predict coseismic landslides and anticipate their consequences will allow for the reduction of future losses.

References

Godt, J., Sener, B., Verdin, K. L., Wald, D. J., Earle, P. S., Harp, E. L., & Jibson, R. W. (2008, November). Rapid assessment of earthquake-induced landsliding. In *Proceedings of the First World Landslide Forum, United Nations University, Tokyo* (Vol. 4, pp. 3166-1).

Kirschbaum, D. B., T. Stanley, and J. Simmons (2015), A dynamic landslide hazard assessment system for Central America and Hispaniola, Nat. Hazards Earth Syst. Sci., 15(10), 2257–2272, doi:10.5194/nhess-15-2257-2015. See: https://pmm.nasa.gov/precip-apps

Kirschbaum, D.B., Psaltakis, J., Stanley, T. (2016) Spatiotemporal properties of landslides in the Pacific Northwest. GSA Annual Meeting 2016, Denver.

National Park Service (2017) Yosemite National Park annual visitation statistics (2001 – 2016) https://www.nps.gov/yose/planyourvisit/visitation.htm

Schmidt KM, Roering JJ, Stock JD, Dietrich WE, Montgomery DR, Schaub T (2001) The variability of root cohesion as an influence on shallow landslide susceptibility in the Oregon Coast Range. Canadian Geotechnical Journal, 38(5), 995-1024

Staley, D. M., Gartner, J. E., and Kean, J. W., 2015, Objective Definition of Rainfall Intensity-Duration Thresholds for Post-fire Flash Floods and Debris Flows in the Area Burned by the Waldo Canyon Fire, Colorado, USA, in Lollino, G., Giordan, D., Crosta, G. B., Corominas, J., Azzam, R., Wasowski, J., and Sciarra, N., eds., Engineering Geology for Society and Territory - Volume 2, Springer International Publishing, p. 621-624. See: https://landslides.usgs.gov/hazards/postfire_debrisflow/)

Tanyaş, H., Westen, C. J., Allstadt, K. E., Anna Nowicki Jessee, M., Görüm, T., Jibson, R. W., ... & Hovius, N. (2017). Presentation and Analysis of a Worldwide Database of Earthquake-Induced Landslide Inventories. *Journal of Geophysical Research: Earth Surface*.

Appendix A Coseismic landslides of the M9.0 2011 Tohoku Japan earthquake

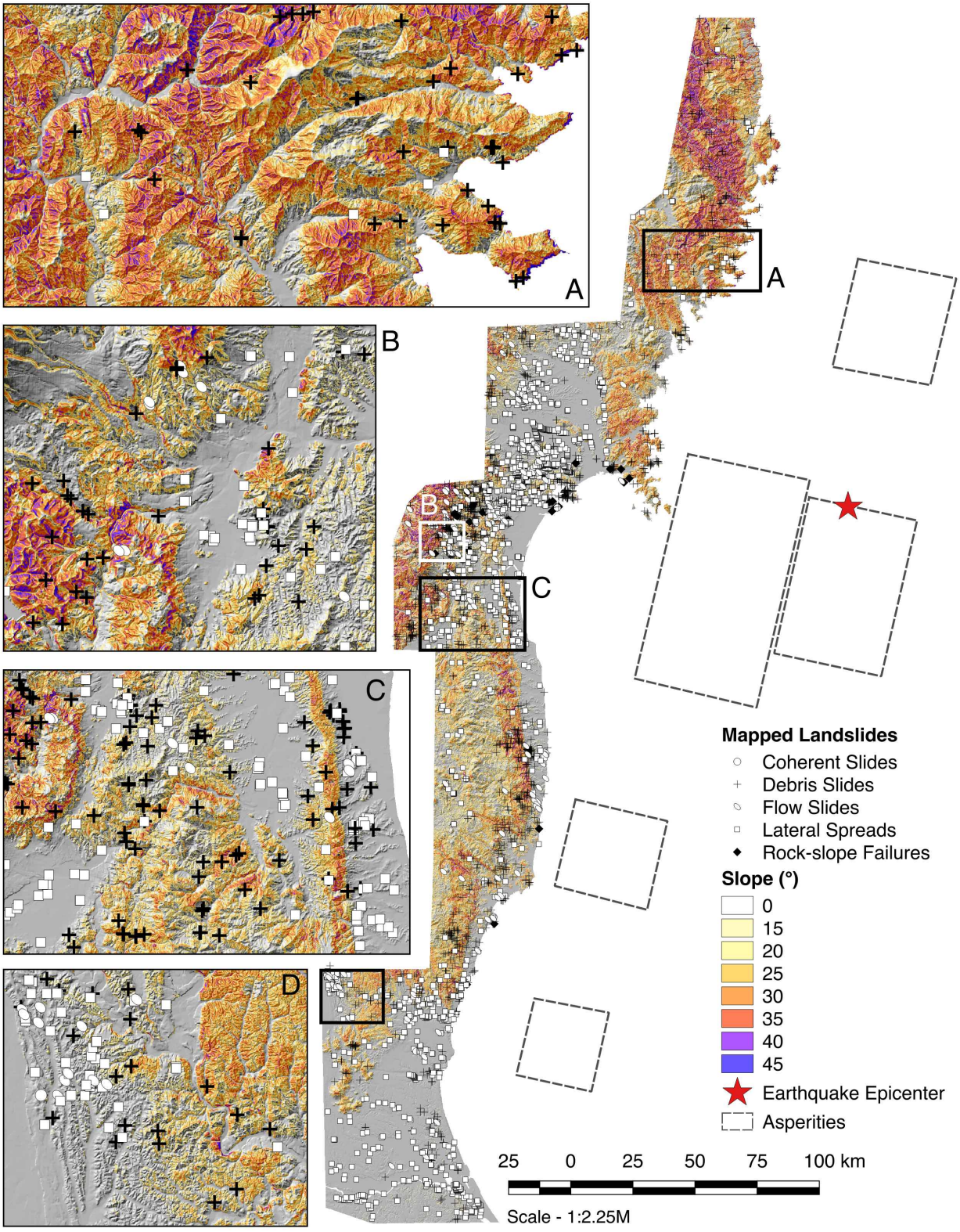

Figure A1 Mapped distribution of coseismic landslides with topographic slope (°) Details show divergence in source location between debris slides (black crosses, steep slopes) and lateral spreads (white squares, flat regions)

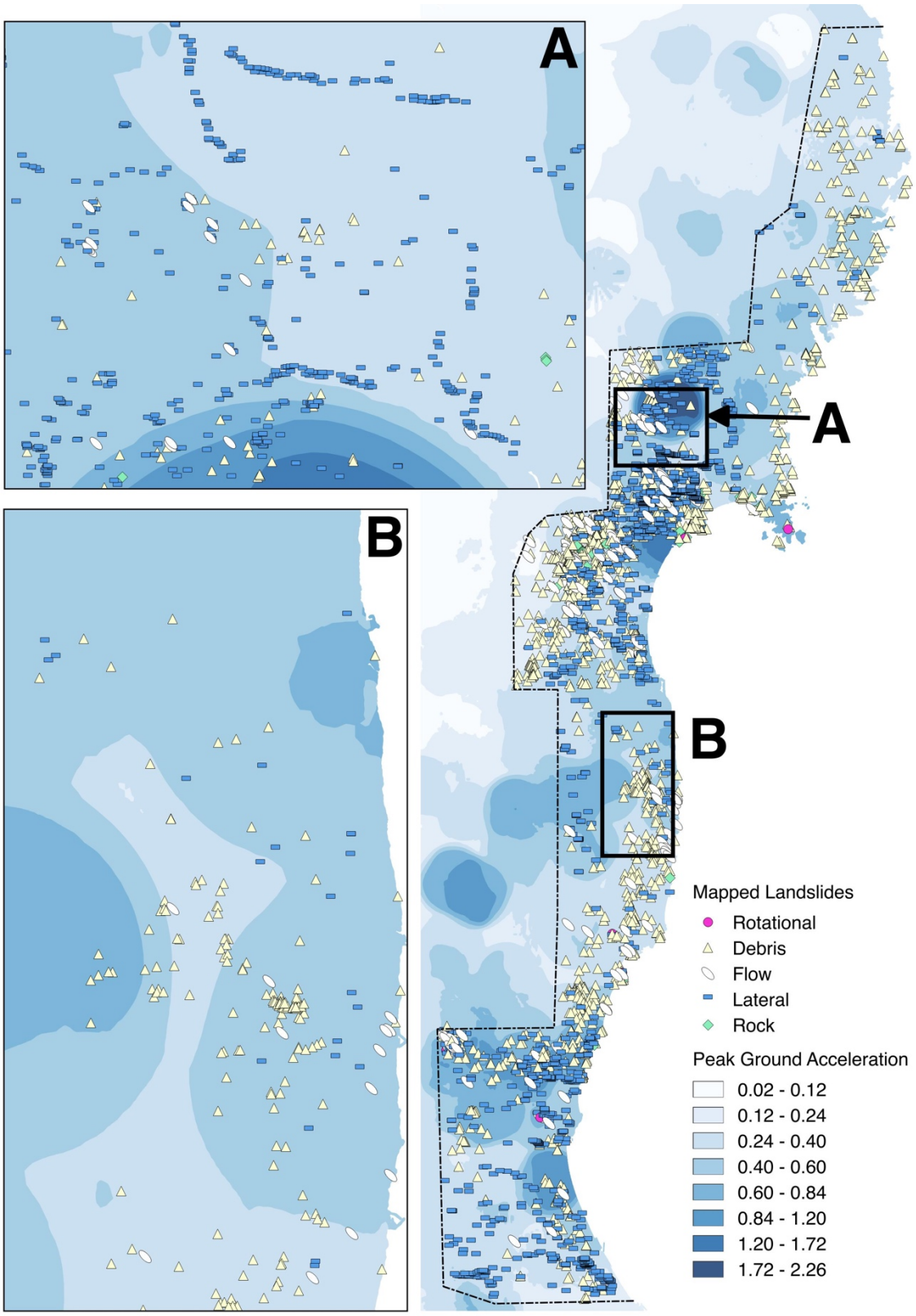

Figure A2 Mapped distribution of landslides with observed peak ground accelerations (g). Insets show concentrations of landslides do not strictly correspond to regions of high ground acceleration.

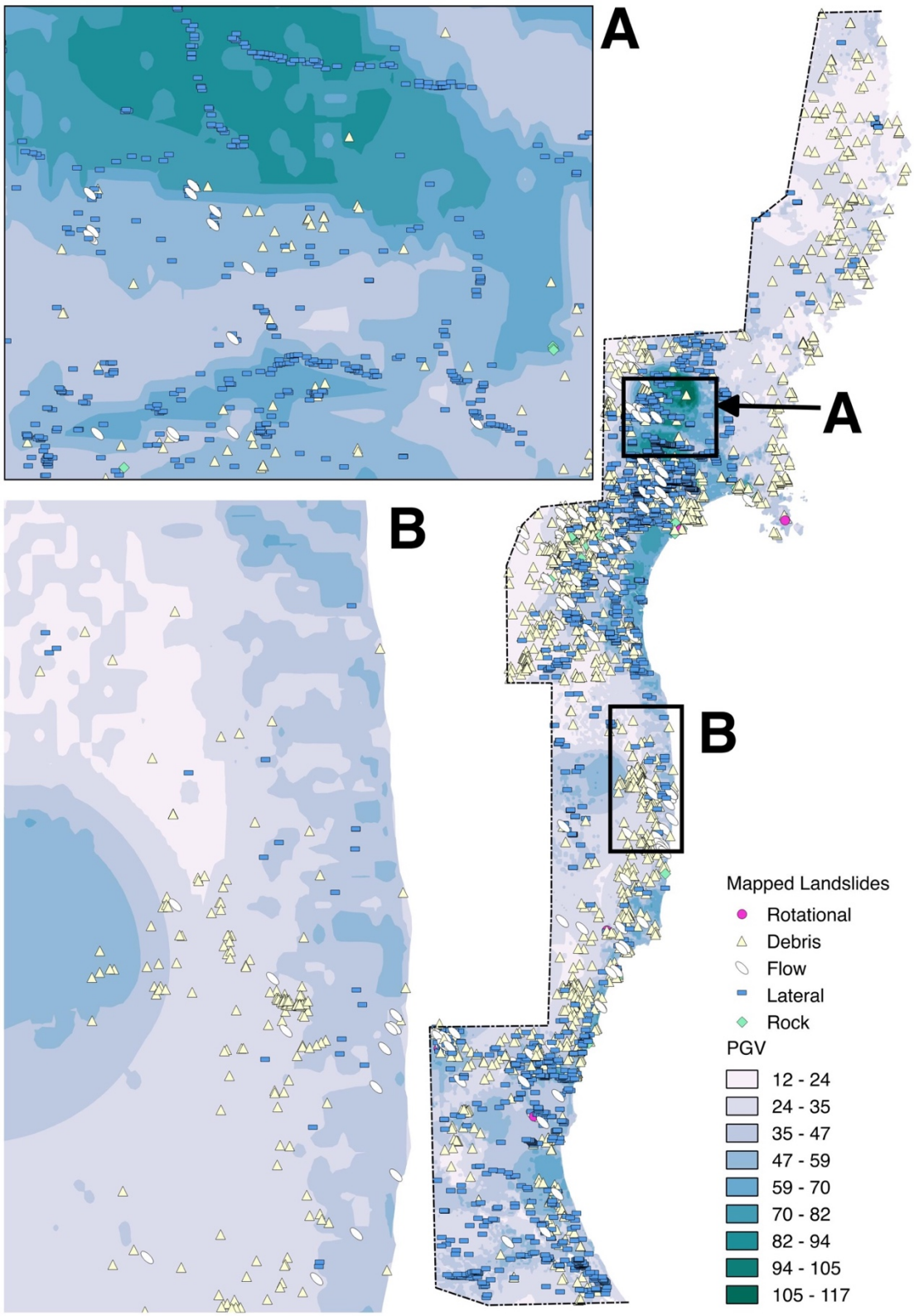

Figure A3 Mapped distribution of landslides with observed peak ground velocities (cm/s). A, lateral spread patterns generally follow trend of increased PGV patches, but in B, debris slides occur in greatest concentrations in relatively weakly shaken zones.

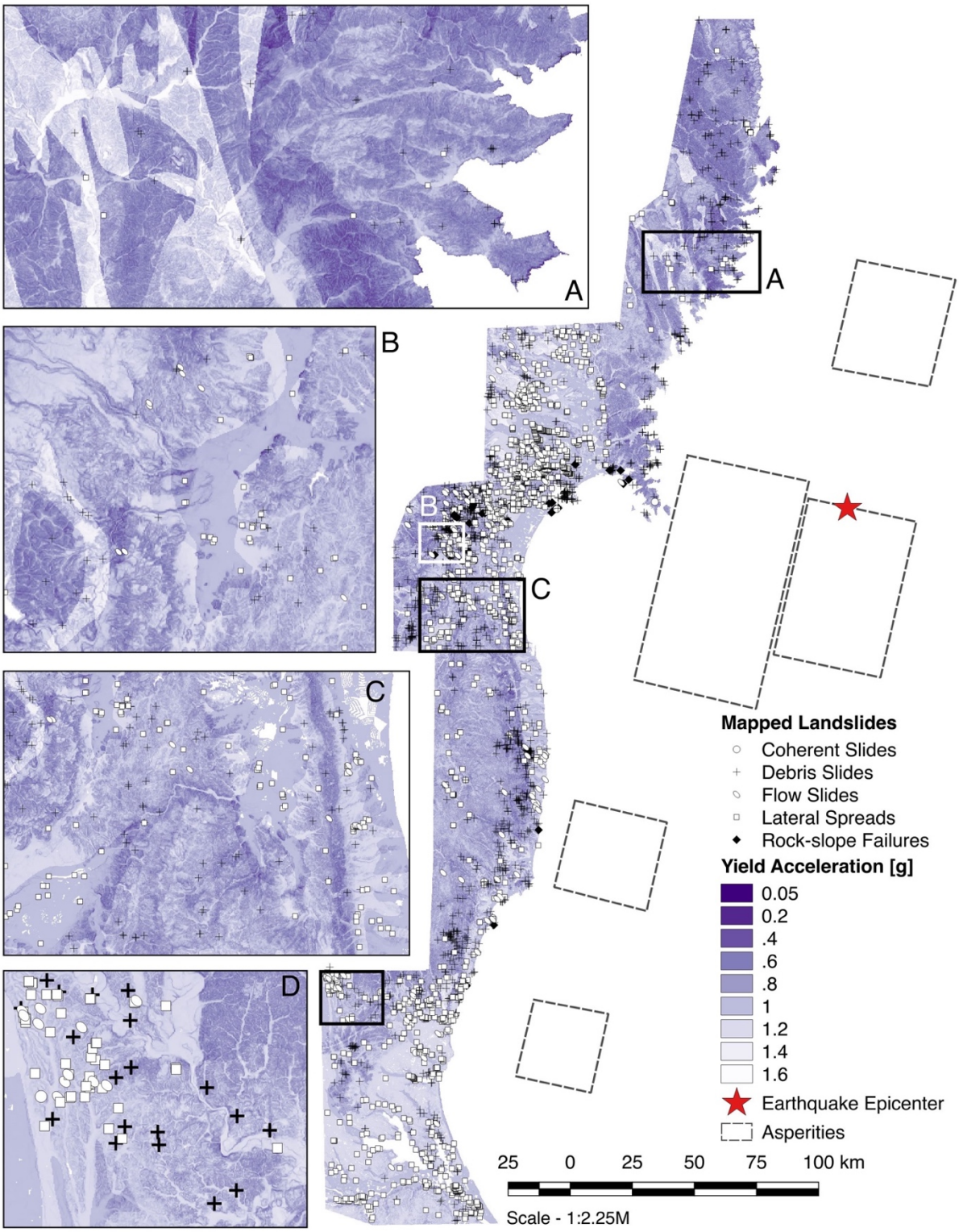

Figure A4 Mapped distribution of landslides with computed yield acceleration based on estimated material strength, topographic slope, and landslide geometric assumptions.

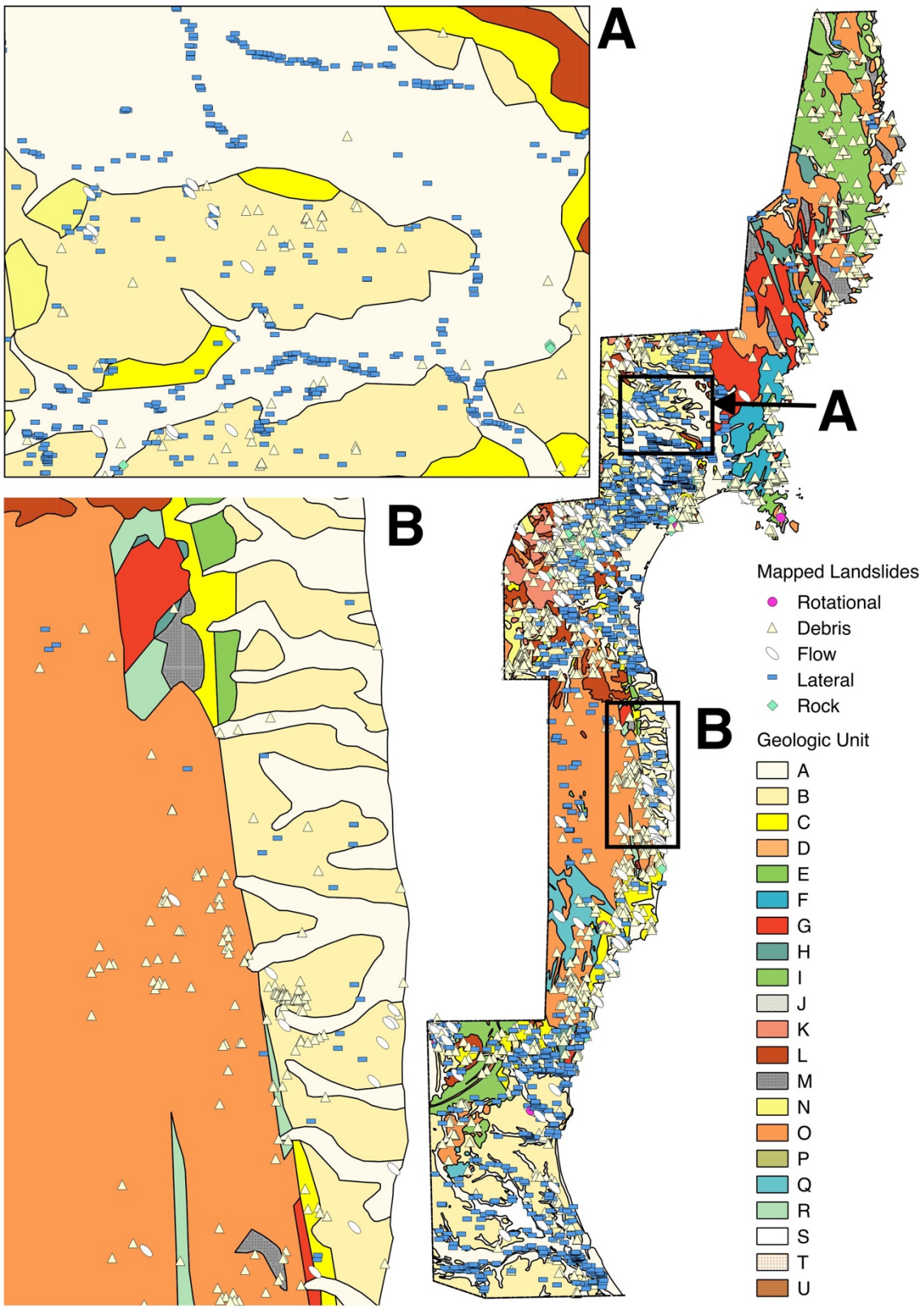

Figure A5 Mapped landslide distribution with geologic unit. See Table 2.7 for descriptions of each mapped geologic unit, landslide counts, and assigned cohesional strength.

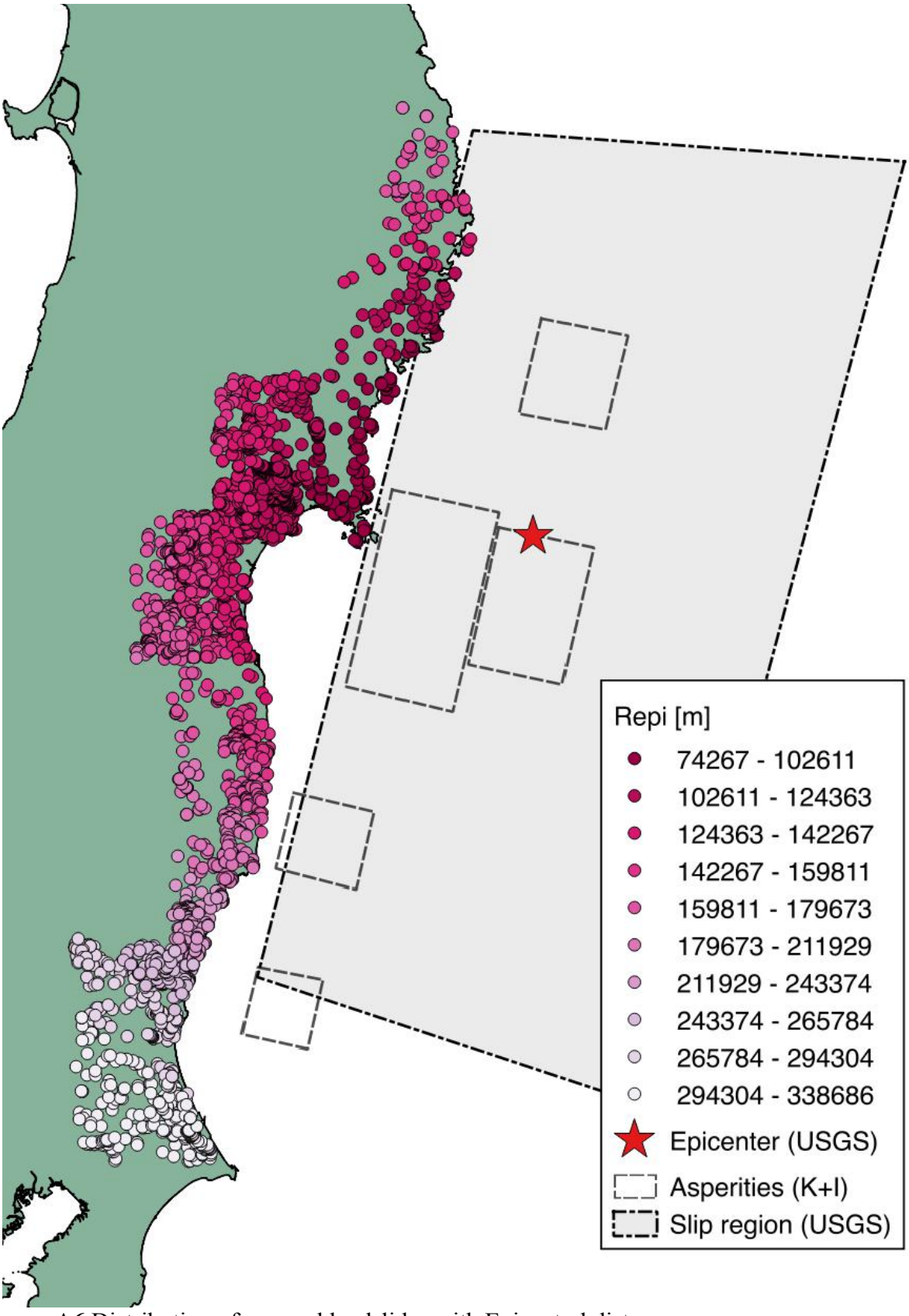

Figure A6 Distribution of mapped landslides with Epicentral distance.

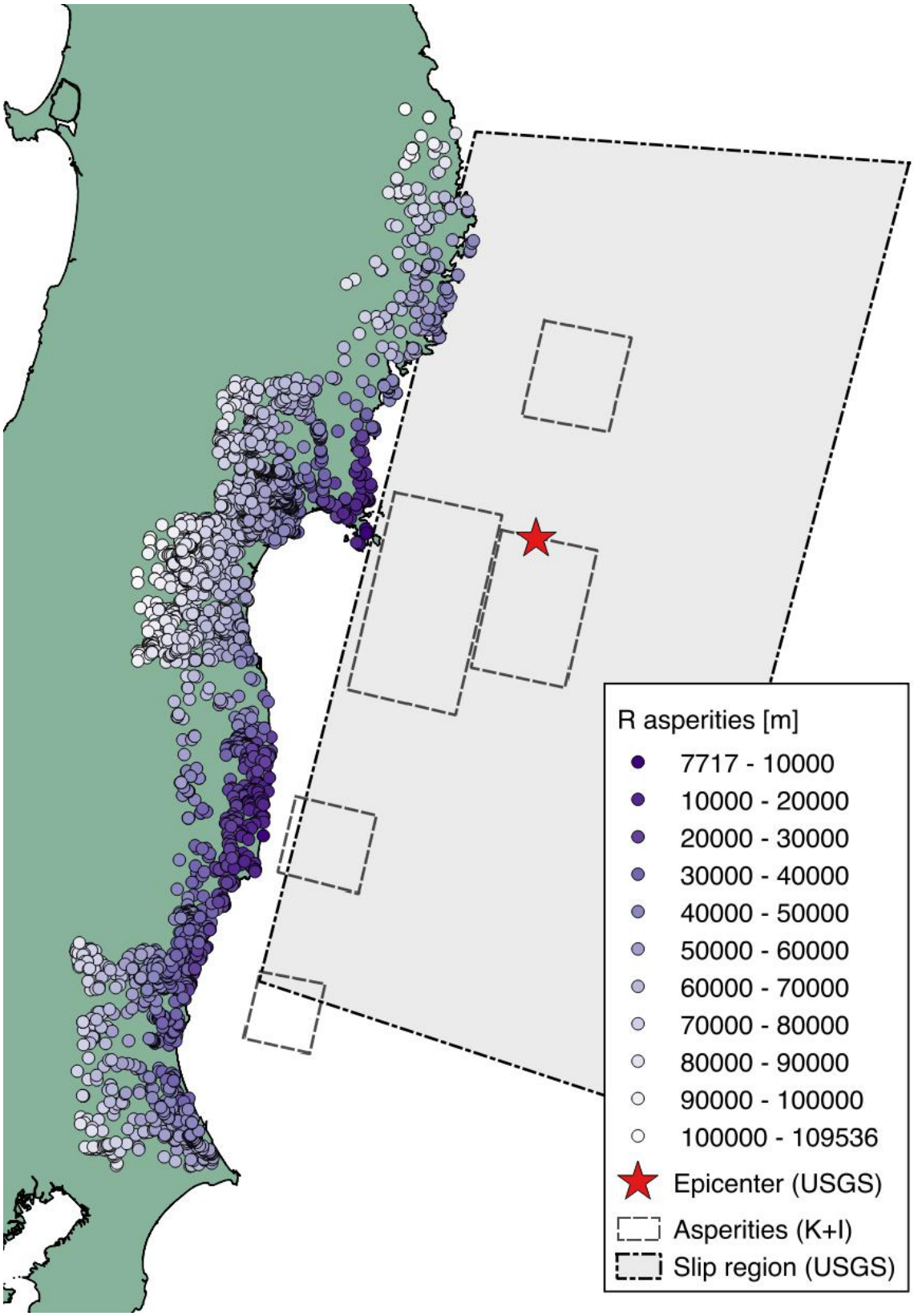

Figure A7 Distribution of mapped landslides with distance to asperities (strong motion generation areas) from Kurahashi and Irikura (2011).

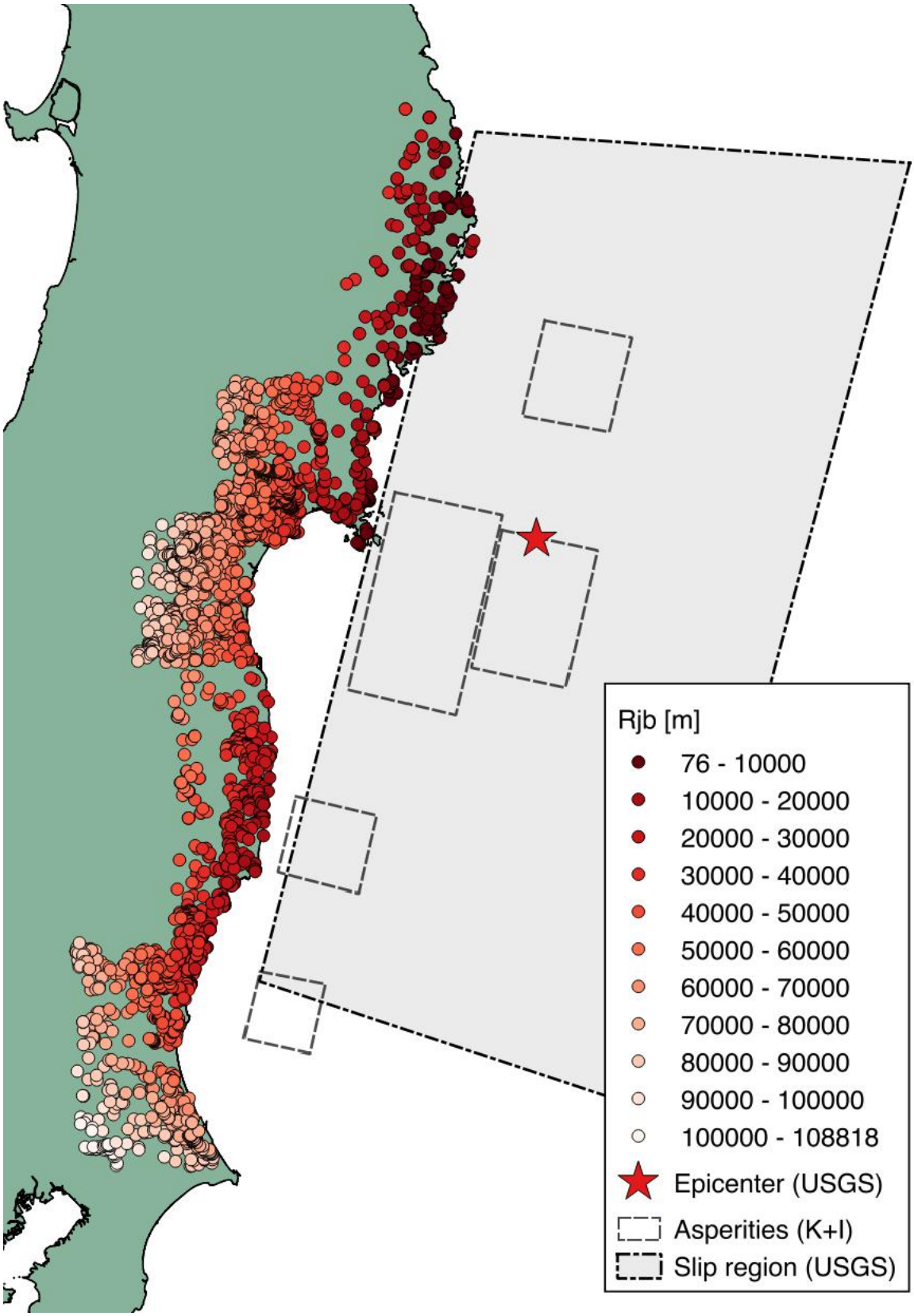

Figure A8 Mapped distribution of landslides with R_{jb}, closest surface projection distance to fault rupture.

Appendix B Global coseismic landslide inventories

Earthquake	Date	M	**Landslides**	Area Affected (km**2)	Type	Minimum Size (m^2)	Disrupted (%)	Coherent (%)	Lateral Spreads and Flows (%)	Reference	Notes
Daly City, CA	22-Mar-57	*5.3*	**23**	-	Strike-slip	*100*	48	30	22	Bonilla, 1960	Richter Local Magnitude
San Salvador, El Salvador	10-Oct-86	5.7	***216***	200	Strike-slip	50	*93*	*5*	*2*	Rymer, 1987; Rymer and White, 1989	"hundreds" 216 low est.
Mt Diablo, CA	24-Jan-80	*5.8*	**103**	1000	Strike-slip	-	83	17	0	Wilson et al., 1985; Keefer and Wilson, 1989	Richter surface-wave
Umbria-Marche, Italy	26-Sep-97	6	**99**	700	Normal	-	*75*	*22*	*3*	Esposito et al., 2000	
Aysen Fjord, Chile	21-Apr-07	6.2	**538**	400	Strike-slip	*100*	Most	-	~1%	Sepulveda et al., 2010	
Avaj, Iran	22-Jun-02	6.5	***600***	3600	Thrust	*100*	*98*	*2*		Mahdavifar et al., 2006	Est. 600 total slides
Niigata Chuetsu	16-Jul-07	6.6	***312***	*250*	Thrust	*50*	84	15	1	Collins et al. 2012	uncertainty over true number of slides, some triggered by Typhoon. Omit numerous small roadside slides
Mid-Niigata, Japan	23-Oct-04	6.8	***1212***	275	Thrust	-	Most	-	-	Wang et al., 2007	
Yushu, China	14-Apr-10	6.9	**2036**	1455	Strike-slip	15	Most	-	-	Xu et al., 2013a	

Appendix B Global coseismic landslide inventories

Borah Peak, ID	28-Oct-83	6.9	***300***	4200	Normal	*50*	Most	-	-	Keefer et al., 1985	"a few hundred." No exact number given
Loma Prieta, CA	17-Oct-89	6.9	***1,500***	*15000*	Oblique	*50*	74	26	0	Keefer and Manson, 1998	
Kobe, Japan	17-Jan-95	6.9	***674***	700	Strike-slip	-	82	14	4	Fukuoka et al., 1997	Slide count may be higher: 674-747
Inangahua, NZ	24-May-68	7.1	**1159**	4288	Thrust	10000	*Most*	-	-	Parker et al., 2015	
Iwate-Miyagi, Japan	14-Jun-08	6.9	**4161**	600	Thrust	-	91	5	4	Yagi et al., 2009	JMA magnitude
Kashmir	8-Oct-05	7.6	***2,424***	*7,500*	Thrust	*10*	Most	-	-	Sato et al., 2007; Owen et al., 2008	
Buller, NZ	16-Jun-29	7.7	***4,074***	*10000*	Thrust	*10,000*	-	-	-	Parker et al., 2015	omits medium and small slides. Total area affected 7k - 15k
Chi-Chi, Taiwan	21-Sep-99	7.7	**9272**	11000	Thrust	*50*	85	11	4	Khazi and Sitar, 2004	
Chi-Chi, Taiwan	21-Sep-99	7.7	**26000**	11000	Thrust	-	-	-	-	Wang et al., 2002	
Gorkha, Nepal	25-Apr-15	7.8	**4312**	*58125*	Thrust	-	-	-	-	Kargel et al., 2016	
Gorkha	25-Apr-15	7.8	**15338**		Thrust	-	-	-	-	Martha et al., 2017	

Appendix B Global coseismic landslide inventories

Denali fault, AK	3-Nov-02	7.9	**5000**	9000	Oblique	*100*	-	-	-	Jibson et al., 2004	1000-10000, unable to perform detailed inventory
Lorca, Spain	11-May-11	5.1	**256**	300	Strike-slip	*5*	97	3	-	Alfaro et al., 2012	
Ludian, China	3-Aug-14	6.2	**1024**	368	Strike-slip	-	-	-	-	Xiaoli et al., 2015	
Ludian, China	3-Aug-14	6.2	**1826**	735	Strike-slip	75	-	-	-	Zhou et al., 2014	Greater number than est. by Xu et al 2014 (chinese) cited by Xiaoli et al., 2015. vast majority of slides larger than 1000m^2, total landslide area of 19km^2
Mammoth Lakes, CA	25-May-80	*6.2*	**5,253**	2,500	Normal	*50*	*98*	*1*	*1*	Harp et al., 1984	Sequence of Earthquakes (4 >M6)
Coalinga, CA	2-May-83	6.5	**9389**	650	Thrust	-	*97*	*2*	*1*	Harp and Keefer, 1990	
Lushan, China	20-Apr-13	6.6	**3810**	13323	Thrust	*25*	-	-	-	Tang et al., 2015	
Lushan, China	20-Apr-13	6.6	**22528**	5400	Thrust	*10*	-	-	-	Xu et al., 2015	
Northridge, CA	17-Jan-94	6.7	**11,111**	*10000*	Oblique	25	90	9	1	Harp and Jibson, 1995, 1996	
Port au Prince, Haiti	10-Jan-10	7	**30828**	3000	Oblique	1	-	-	-	Xu, et al., 2012	

Appendix B Global coseismic landslide inventories

Guatemala	4-Feb-76	7.5	***50,000***	*1,000*	Strike-slip	*100*	Most	-	-	Harp et al., 1981 ; *Harp Unpub. Data (Keefer, 2002)*	
Wenchuan, China	12-May-08	7.9	**196007**	44031	Oblique	-	-	-	-	Xu et al., 2014	
Tecoman, Mexico	21-Jan-03	7.6	***500***	*8,000*	Interface	*5*	Virtually all	-	-	Keefer et al., 2006	*"several hundreds"*
El Salvador	13-Jan-01	7.7	***500***	*12000*	Interface	-	-	-	-	Bommer et al., 2002	*"more than 500 landslides"*
El Salvador	13-Jan-01	7.7	***1,000***		Interface	-	-	-	-	Jibson and Crone, 2001	*'Thousands': original unofficial report by Ed Harp*
Pisco, Peru	15-Aug-07	8	**866**	27000	Interface	100	-	-	-	Lacroix et al., 2013	minimum, incomplete coverage near coast.
Tohoku, Japan	11-Mar-11	9	**3508**	*40000*	Interface	4	63	3	34	This report	Est. area impacted including slides not mapped in this study
Anchorage	28-Mar-64	9.2	***10000***	-	Interface	-	-	-	-	Keefer and Wilson 1989	

Table B1 Global coseismic landslide inventories with reported triggered landslide counts from mapping or well-informed estimates from field reconnaissance, with or without distributions by landslide type.

References

Alfaro, P., Delgado, J., García-Tortosa, F. J., Lenti, L., López, J. A., López-Casado, C., & Martino, S. (2012). Widespread landslides induced by the Mw 5.1 earthquake of 11 May 2011 in Lorca, SE Spain. *Engineering Geology*, *137*, 40-52.

Bommer, J.J., Benito, M.B., Ciudad-Real, M., Lemoine, A., López-Menjívar, M.A., Madariaga, R., ... & Rodríguez-Pineda, C.E. (2002). The El Salvador earthquakes of January and February 2001: context, characteristics and implications for seismic risk. *Soil dynamics and earthquake engineering*, *22*(5), 389-418.

Appendix B Global coseismic landslide inventories

Bonilla, M. G. (1960). *Landslides in the San Francisco South Quadrangle, California* (No. 60-15). US Geological Survey.

Collins, B. D., Kayen, R., & Tanaka, Y. (2012). Spatial distribution of landslides triggered from the 2007 Niigata Chuetsu–Oki Japan Earthquake. *Engineering geology*, *127*, 14-26

Esposito, E., Porfido, S., Simonelli, A. L., Mastrolorenzo, G., & Iaccarino, G. (2000). Landslides and other surface effects induced by the 1997 Umbria–Marche seismic sequence. *Engineering geology*, *58*(3), 353-376.

Fukuoka, H., Sassa, K., & Scarascia-Mugnozza, G. (1997). Distribution of landslides triggered by the 1995 Hyogo-ken Nanbu earthquake and long runout mechanism of the Takarazuka Golf Course landslide. *Journal of Physics of the Earth*, *45*(2), 83-90.

Harp, E. L., Wilson, R. C., & Wieczorek, G. F. (1981). *Landslides from the February 4, 1976, Guatemala earthquake*(No. 551.3 HAR). US Government Printing Office.

Harp E.L., and Keefer, D. K. (1990) Landslides Triggered by the Earthquake. *In The Coalinga, California, Earthquake of May 2, 1983 Rymer, M.J. and Ellsworth, W.L. (eds.)* IS Geological Survey Prof. Paper 1487.

Harp, E. L., & Jibson, R. W. (1996). Landslides triggered by the 1994 Northridge, California, earthquake. *Bulletin of the Seismological Society of America*, *86*(1B), S319-S332.

Harp, E.L., Tanaka, K., Sarmiento, J., & Keefer, D.K. (1984) Landslides from the May 25 – 27, 1980 Mammoth Lakes, California, earthquake sequence. Miscellaneous Investigations Map I-1612. US Geological Survey.

Jibson, R. W., & Crone, A. J. (2001). *Observations and recommendations regarding landslide hazards related to the January 13, 2001 M-7.6 El Salvador earthquake*. US Department of the Interior, US Geological Survey.

Jibson, R. W., Harp, E. L., Schulz, W., & Keefer, D. K. (2004). Landslides triggered by the 2002 Denali Fault, Alaska, earthquake and the inferred nature of the strong shaking. *Earthquake Spectra*, *20*(3), 669-691.

Kargel, J. S., Leonard, G. J., Shugar, D. H., Haritashya, U. K., Bevington, A., Fielding, E. J., ... & Anderson, E. (2016). Geomorphic and geologic controls of geohazards induced by Nepal's 2015 Gorkha earthquake. *Science*, *351*(6269), aac8353.

Keefer, D. K. (2002). Investigating landslides caused by earthquakes–a historical review. *Surveys in geophysics*, *23*(6), 473-510.

Keefer, D.K., Wilson, R.C., Harp, E.L., Lips, E.W. (1985). The Borah Peak, Idaho Earthquake of October 28, 1983—Landslides. *Earthquake Spectra*, *2*(1), 91-125.

Appendix B Global coseismic landslide inventories

Keefer, D. K., & Wilson, R. C. (1989). Predicting earthquake-induced landslides, with emphasis on arid and semi-arid environments. *Landslides in a semi-arid environment*, *2*(PART 1), 118-149.

Keefer, D.K., Manson, M.W., 1998. Regional distribution and characteristics of landslides generated by the earthquake. In: Keefer, D.K. (Ed.), The Loma Prieta, California earth- quake of October 17, 1989 — landslides, US Geol. Survey Prof. Paper 1551-C, C7–C32.

Keefer, D. K., Wartman, J., Ochoa, C. N., Rodriguez-Marek, A., & Wieczorek, G. F. (2006). Landslides caused by the M 7.6 Tecomán, Mexico earthquake of January 21, 2003. *Engineering Geology*, *86*(2), 183-197.

Khazai, B., & Sitar, N. (2004). Evaluation of factors controlling earthquake-induced landslides caused by Chi-Chi earthquake and comparison with the Northridge and Loma Prieta events. *Engineering geology*, *71*(1), 79-95.

Lacroix, P., Zavala, B., Berthier, E., & Audin, L. (2013). Supervised method of landslide inventory using panchromatic SPOT5 images and application to the earthquake-triggered landslides of Pisco (Peru, 2007, Mw8. 0). *Remote Sensing*, *5*(6), 2590-2616.

Mahdavifar, M. R., Solaymani, S., & Jafari, M. K. (2006). Landslides triggered by the Avaj, Iran earthquake of June 22, 2002. *Engineering geology*, *86*(2), 166-182.

Martha, T. R., Roy, P., Mazumdar, R., Govindharaj, K. B., & Kumar, K. V. (2017). Spatial characteristics of landslides triggered by the 2015 Mw 7.8 (Gorkha) and Mw 7.3 (Dolakha) earthquakes in Nepal. *Landslides*, *14*(2), 697-704.

Owen, L. A., Kamp, U., Khattak, G. A., Harp, E. L., Keefer, D. K., & Bauer, M. A. (2008). Landslides triggered by the 8 October 2005 Kashmir earthquake. *Geomorphology*, *94*(1), 1-9.

Parker, R. N., Hancox, G. T., Petley, D. N., Massey, C. I., Densmore, A. L., & Rosser, N. J. (2015). Spatial distributions of earthquake-induced landslides and hillslope preconditioning in the northwest South Island, New Zealand. *Earth Surface Dynamics*, *3*(4), 501.

Rymer, M. J. (1987). The San Salvador earthquake of October 10, 1986—geologic aspects. *Earthquake Spectra*, *3*(3), 435-463.

Rymer, M. J., & White, R. A. (1989, July). Hazards in El Salvador from earthquake-induced landslides. In *Landslides: extent and economic significance, Proceedings of 28th international geological congress, Washington, DC* (pp. 105-109).

Sato, H. P., Hasegawa, H., Fujiwara, S., Tobita, M., Koarai, M., Une, H., & Iwahashi, J. (2007). Interpretation of landslide distribution triggered by the 2005 Northern Pakistan earthquake using SPOT 5 imagery. *Landslides*, *4*(2), 113-122.

Appendix B Global coseismic landslide inventories

Sepúlveda, S. A., Serey, A., Lara, M., Pavez, A., & Rebolledo, S. (2010). Landslides induced by the April 2007 Aysén fjord earthquake, Chilean Patagonia. *Landslides*, *7*(4), 483-492.

Tang, C., Ma, G., Chang, M., Li, W., Zhang, D., Jia, T., & Zhou, Z. (2015). Landslides triggered by the 20 April 2013 Lushan earthquake, Sichuan Province, China. *Engineering Geology*, *187*, 45-55.

Wang, W.N., Nakamura, H., Tsuchiya, S., & Chen, C.C. (2002). Distributions of landslides triggered by the Chi-chi Earthquake in Central Taiwan on September 21, 1999. *Landslides*, *38*(4), 318-326.

Wang, H. B., Sassa, K., & Xu, W. Y. (2007). Analysis of a spatial distribution of landslides triggered by the 2004 Chuetsu earthquakes of Niigata Prefecture, Japan. *Natural Hazards*, *41*(1), 43.

Wilson, R. C., Wieczorek, G. F., Keefer, D. K., Harp, E. L., & Tannaci, N. E. (1985). *Map showing ground failures from the Greenville/Mount Diablo earthquake sequence of January 1980, Northern California* (No. 1711). US Geological Survey.

Xiaoli, C., Qing, Z., & Chunguo, L. (2015). Distribution pattern of coseismic landslides triggered by the 2014 Ludian, Yunnan, China Mw6. 1 earthquake: special controlling conditions of local topography. *Landslides*, *12*(6), 1159-1168.

Xu, C., Xu, X. W., & Yu, G. (2012). Earthquake triggered landslide hazard mapping and validation related with the 2010 Port-au-Prince, Haiti earthquake. *Disaster Adv*, *5*(4), 1297-1304.

Xu, C., Xu, X., & Yu, G. (2013). Landslides triggered by slipping-fault-generated earthquake on a plateau: an example of the 14 April 2010, Ms 7.1, Yushu, China earthquake. *Landslides*, *10*(4), 421-431.

Xu, C., Xu, X., Yao, X., & Dai, F. (2014). Three (nearly) complete inventories of landslides triggered by the May 12, 2008 Wenchuan Mw 7.9 earthquake of China and their spatial distribution statistical analysis. *Landslides*, *11*(3), 441-461.

Xu, C., Xu, X., & Shyu, J. B. H. (2015). Database and spatial distribution of landslides triggered by the Lushan, China Mw 6.6 earthquake of 20 April 2013. *Geomorphology*, *248*, 77-92.

Yagi, H., Sato, G., Higaki, D., Yamamoto, M., & Yamasaki, T. (2009). Distribution and characteristics of landslides induced by the Iwate–Miyagi Nairiku Earthquake in 2008 in Tohoku District, Northeast Japan. *Landslides*, *6*(4), 335.

Zhou, S., Chen, G., & Fang, L. (2016). Distribution pattern of landslides triggered by the 2014 Ludian earthquake of China: Implications for regional threshold topography and the seismogenic fault identification. *ISPRS International Journal of Geo-Information*, *5*(4), 46.

Appendix C New Zealand Rock Impact Data

Site	Dwelling Footprint Area [m**2]	Rock #	Boulder Axis a [cm]	Boulder Axis b [cm]	Boulder Axis c [cm]	Simple Shape (Sneed and Folk, 1989)	Boulder Volume [m**3]	Data Quality Score	Median Translational Velocity [m/s]	Median Rotational Velocity [rad/s]	Mass [kg]	Min. I [kgm**2]	Total KE [kJ]	KE +std	KE -std	Primary Impact Resistance	Secondary Impact Resistance	Modelled Runout Beyond Dwelling	Runout Distance within Dwelling [m]	Impact Angle [deg]	Total Runout Distance, R [m]	Area Impacted, Ad [m**2]	Damage Ratio (D)
1	201	1	124	102	94	equant	0.95	**4**	4	7	1712	659	**30**	111	9	2	E	9.50	0.4		**0.4**	**0.496**	**0.0025**
3	176	1	250	200	200	equant	8.00	**5**	9.1	5.9	14400	23040	**997**	1888	537	2	A	16	4		**4**	**10**	**0.0568**
7	98	1	70	60	50	equant	0.17	**5**	4.9	7.9	454	55	**7**	11	4	3	A	4.7	0.3		**0.3**	**0.21**	**0.0021**
14	130	1	140	130	110	equant	1.60	**4**	15.2	19.0	4324	2508	**952**	1260	693	0	D	19.7	2.48	45	**2.48**	**3.472**	**0.0267**
17	164	1	80	80	40	flat	0.20	**3**	14.3	30.0	553	88	**96**	129	69	1	D-F	23.6	7.5		**45.5**	**6**	**0.0366**
23	206	1	35	35	15	equant	0.01	**3**	4.8	35.0	40	1	**1.2**	1.8	0.8	2	A	6.5	0.1		**0.1**	**0.035**	**0.0002**
24	161	1	20	15	10	equant	0.00	**5**	6.8	64.0	6	0	**0.2**	0.4	0.1	2	A	6.8	0.02		**0.02**	**0.004**	**0.0000**
27	125	1	90	60	60	equant	0.26	**5**	3	5.9	700	101	**5**	8	4	2	A	1.7	0.03		**0.03**	**0.027**	**0.0002**
29	156	1	25	15	5	equant	0.00	**3**	9.7	120.0	4	0	**0.3**	0.6	0.2	3	A	23.6	0.01		**0.01**	**0.0025**	**0.0000**
31	202	1	90	75	75	equant	0.41	**5**	12.7	20.2	1094	246	**138**	163	117	0	C	24	4	60	**4**	**3.6**	**0.0178**
33	88	1	150	120	120	equant	1.73	**5**	3.5	4.5	4666	2687	**56**	87	30	2	A	1	1		**1**	**1.5**	**0.0170**
10-1	559	1	38	32	30	equant	0.03	**3**	26.7	40.2	79	3	**31**	31	30	0	A	2.8	2.3	35	**2.3**	**0.874**	**0.0016**
10-2	559	2	41	40	36	equant	0.05	**3**	24	21.7	128	7	**38**	45	33	0	A	4.3	0.9	20	**0.9**	**0.369**	**0.0007**
10-3	559	3	31	27	25	equant	0.02	**3**	25.6	55.1	45	1	**17**	17	16	0	A	2.7	0.78	15	**0.78**	**0.2418**	**0.0004**
10-4	559	4	100	60	60	equant	0.29	**3**	24.6	17.0	778	112	**251**	255	244	0	A	5.2	1.7	35	**1.7**	**1.7**	**0.0030**
10-5	559	5	120	120	120	equant	1.38	**3**	25.5	13.6	3732	2150	**1412**	1459	1356	0	F	5.6	6.5	65	**6.5**	**7.8**	**0.0140**
10-6	559	6	136	120	78	flat	1.02	**3**	7.7	9.6	2750	1126	**133**	253	51	2	A	8.7	3.3		**3.3**	**4.488**	**0.0080**
10-7	559	7	85	63	45	equant	0.19	**3**	26.7	40.2	521	62	**236**	247	226	0	A	2.8	1	15	**1**	**0.85**	**0.0015**
10b-1	148	1	112	51	38	long	0.17	**3**	9	19.8	469	38	**26**	67	5	2	A	5.5	1.6		**1.6**	**1.792**	**0.0121**
10b-2	148	2	78	70	64	equant	0.28	**3**	19.7	37.1	755	136	**240**	283	200	0	B	12.1	1.5	35	**1.5**	**1.17**	**0.0079**
10b-3	148	3	110	60	50	equant	0.26	**3**	21.6	33.6	713	87	**215**	256	179	0-2	A	19.4	1.9	40	**22.9**	**2.09**	**0.0141**
10b-4	148	4	45	30	30	equant	0.03	**3**	5.7	31.7	87	3	**3**	4	2	2	A	8.6	0.2		**0.2**	**0.09**	**0.0006**
11-1	176	1	142	70	60	long	0.48	**3**	8.1	15.2	1288	219	**68**	146	21	2	F	12.8	1.8		**1.8**	**2.556**	**0.0145**
11-2	176	2	125	110	85	equant	0.94	**3**	8.1	15.2	2525	976	**196**	408	60	0	D	12.8	6		**6**	**7.5**	**0.0426**
11-2a	176	2a	150	150	150	equant	2.70	**3**	8.1	15.2	7290	6561	**997**	2011	310	0	C	12.8	3		**3**	**4.5**	**0.0256**
11-3	176	3	210	200	75	flat	2.52	**3**	8.1	15.2	6804	6209	**940**	1896	292	0	D	12.8	3.1		**3.1**	**6.51**	**0.0370**
11-4	176	4	110	90	70	equant	0.55	**3**	2.1	4.2	1497	389	**7**	11	5	2	A	1	0.05		**0.05**	**0.055**	**0.0003**
12-1	102	1	80	60	60	equant	0.23	**5**	9.6	24.4	622	90	**55**	99	24	0	D	12	4.5		**4.5**	**3.6**	**0.0353**
12-2	102	2	70	60	40	equant	0.13	**5**	15.4	45.5	363	38	**82**	128	46	2	C	12	2.3		**2.3**	**1.61**	**0.0158**
13a-1	162	1	120	110	50	flat	0.53	**3**	3.9	8.3	1426	416	**25**	64	4	2	A	4.2	1.8		**1.8**	**2.16**	**0.0133**
13b	166	1	150	140	70	equant	1.18	**3**	4.8	7.4	3175	1556	**79**	196	15	1	D-F	2.3	3.5		**3.5**	**5.25**	**0.0316**
13c-1	152	1	60	60	90	equant	0.26	**4**	6.6	17.0	700	101	**30**	50	15	0	F	12	2.3		**2.3**	**1.38**	**0.0091**
13c-2	152	2	40	35	20	equant	0.02	**4**	6.6	17.0	60	2	**2**	3	1	2	A	12	0.15		**0.15**	**0.06**	**0.0004**
13c-3	152	3	45	40	35	equant	0.05	**4**	9.2	26.0	136	8	**8**	14	4	2	E	21.5	0.2		**0.2**	**0.09**	**0.0006**
13c-4	152	4	120	50	50	long	0.24	**4**	9.2	26.0	648	65	**49**	82	24	2	A	21.5	0.3		**0.3**	**0.36**	**0.0024**
15-1	171	1	18	18	17	equant	0.00	**4**	10.8	94.8	12	0	**1**	2	1	2	A	23.2	0.06		**0.06**	**0.0108**	**0.0001**
15-2	171	2	18	18	17	equant	0.00	**4**	10.8	94.8	12	0	**1**	2	1	2	A	23.2	0.14		**0.14**	**0.0252**	**0.0001**
15-3	171	3	70	70	70	equant	0.27	**4**	20.4	41.0	741	145	**276**	456	121	2	A-F	23.2	1.6		**1.6**	**1.12**	**0.0065**
15-3a	171	3a	50	50	50	equant	0.10	**4**	20.4	41.0	270	27	**79**	128	34	2	A-F	23.2	2.9		**2.9**	**1.45**	**0.0085**
15-4	171	4	120	80	70	long	0.54	**4**	11.8	21.0	1452	328	**173**	295	83	2	A-F	23.3	0.4		**0.4**	**0.48**	**0.0028**
15-5	171	5	50	40	30	equant	0.05	**4**	20.4	41.0	130	6	**32**	52	14	2	F	23.2	1.98	50	**1.98**	**0.99**	**0.0058**
15-6	171	6	50	50	50	equant	0.10	**4**	19.3	40.4	270	27	**72**	94	53	2	C	18.7	4.9	30	**4.9**	**2.45**	**0.0143**
15-6a	171	6a	100	70	70	equant	0.39	**4**	19.3	40.4	1058	207	**366**	491	260	2	C	18.7	3.1		**3.1**	**3.1**	**0.0181**
15-7	171	7	25	20	15	equant	0.01	**4**	10.8	94.8	16	0	**2**	3	1	2	A	23.2	0.12		**0.12**	**0.03**	**0.0002**
15-9	171	9	100	50	50	long	0.20	**4**	19.3	40.4	540	54	**145**	189	106	0	F	18.7	2.4	30	**2.4**	**2.4**	**0.0140**
15b-1	132	1	90	40	35	long	0.10	**4**	17.4	37.0	272	15	**52**	62	43	2	D	11	2.4	30	**2.4**	**2.16**	**0.0164**
15b-2	132	2	70	40	30	long	0.07	**4**	9.4	29.7	181	9	**12**	22	5	2	F	11	3.7		**3.7**	**2.59**	**0.0196**
20-1	80	1	30	30	30	equant	0.02	**5**	7.3	18.1	58	2	**2**	3	1	2	A	6.9	0.1	20	**0.1**	**0.03**	**0.0004**
22-1	131	1	128	68	40	long	0.28	**3**	15.4	42.0	752	94	**172**	231	122	0	C-D	36.2	5	60	**5**	**6.4**	**0.0489**
22-2	131	2	70	55	40	equant	0.12	**3**	11.7	33.1	333	31	**40**	78	14	1	C	15.4	6		**6**	**4.2**	**0.0321**
25-1	146	1	40	40	30	equant	0.04	**5**	5.6	20.3	104	5	**3**	4	2	2	A	6.5	0.04		**0.04**	**0.016**	**0.0001**
25-2	146	2	30	30	20	equant	0.01	**5**	5.6	20.3	39	1	**1**	1	0	2	A	6.5	0.03		**0.03**	**0.009**	**0.0001**
26-1	76	1	80	70	70	equant	0.31	**5**	3.8	6.7	847	166	**10**	15	8	2	B	3	0.15		**0.15**	**0.12**	**0.0016**
26-2	76	2	120	90	80	equant	0.69	**5**	3.8	6.7	1866	541	**26**	39	21	2	B	3	1.2		**1.2**	**1.44**	**0.0189**
28-1	122	1	95	60	60	equant	0.27	**4**	4.7	12.7	739	106	**17**	52	11	2	A	2.9	0.2		**0.2**	**0.19**	**0.0016**
28-2	122	2	20	20	15	equant	0.00	**4**	4.7	12.7	13	0	**0.2**	1	0	2	A	2.9	0.04		**0.04**	**0.008**	**0.0001**
32-1	183	1	80	70	70	equant	0.31	**5**	11.6	18.2	847	166	**84**	102	60	0	A	9.6	3	55	**3**	**2.4**	**0.0131**
32-2	183	2	111	90	40	flat	0.32	**5**	11.6	18.2	863	167	**86**	104	61	2	E	9.6	1.3	20	**1.3**	**1.443**	**0.0079**
34	131	1	300	300	200	flat	14.40	**3**	3.5	4.5	38880	101088	**1262**	2002	649	2	C-D	15.4	7		**77**	**21**	**0.1603**
5	112	1	150	130	100	equant	1.56	**5**	9.2	12.3	4212	2266	**350**	576	182	1	D	14.2	3		**3**	**4.5**	**0.0402**
9a	85	1	200	60	60	long	0.58	**4**	4.8	5.9	1555	224	**22**	32	14	2	A	3.8	0.65		**0.65**	**1.3**	**0.0153**

Appendix D

RocFall 5.0 modeling parameters used in Grant et al. (2017), Chapter 4.

Parameter	**Assigned Value**
No. of boulders modelled	5,000 – 10,000
Unit weight of Rock	18kN/m^3 - 27kN/m^3
Initial Horizontal Velocity	1.5 m/s
Initial Vertical Velocity	1 m/s
RN scaling	Velocity, K = 9.144 m/s
Velocity Cutoff	0.1 m/s
Friction Angle	From Material Editor
Angular Velocity	Considered

Table D.1 Model parameters